Synthesis and Characterization of Carbonaceous- and Layered-material based Hybrids for Drug Delivery and Catalysis

A Thesis Submitted for the Degree of

DOCTOR OF PHILOSOPHY

By

Piyush Chaturbedy

Chemistry and Physics of Materials Unit

Jawaharlal Nehru Centre for Advanced Scientific Research

(A Deemed University)
Bangalore, India

March 2015

Dedicated To my family

DECLARATION

I hereby declare that the matter embodied in the thesis entitled **"Synthesis and Characterization of Carbonaceous- and Layered-material based Hybrids for Drug Delivery and Catalysis"** is the result of investigations carried out by me at the Chemistry and Physics of Materials Unit, Jawaharlal Nehru Centre for Advanced Scientific Research, India under the supervision of Professor Muthusamy Eswaramoorthy and that it has not been submitted elsewhere for the award of any degree or diploma.

In keeping with the general practice in reporting the scientific observations, due acknowledgement has been made whenever the work described is based on the findings of other investigators. Any omission that might have occurred due to oversight or error in judgement is regretted.

Piyush Chaturbedy

CERTIFICATE

I hereby certify that the work described in this thesis entitled **"Synthesis and Characterization of Carbonaceous- and Layered-material based Hybrids for Drug Delivery and Catalysis"** has been carried out by Mr. Piyush Chaturbedy under my supervision at the Chemistry and Physics of Materials Unit, Jawaharlal Nehru Centre for Advanced Scientific Research, India and that it has not been submitted elsewhere for the award of any degree or diploma.

Professor Muthusamy Eswaramoorthy

(Research Supervisor)

ACKNOWLEDGMENTS

First and foremost, I would express my sincere gratitude to Professor Muthusamy Eswaramoorthy, my research supervisor, for his constant guidance throughout the PhD. The scientific and non-scientific interactions with him were extremely insightful and great learning experience. Most importantly, the freedom for pursuing research and learning one gets in his laboratory is worth acknowledging. I would be ever thankful to him for encouraging and supporting me, financially and morally, during the tough phases of the PhD. I would always cherish memories of working with him.

I would like to thank Professor Tapas K Kundu, for all the discussion meetings which were great occasion for me to learn basic concepts and a few skills of cell biology. The research work for two of my thesis chapters were conducted in collaboration of Prof. Kundu's group and I thank him for generously allowing me to carry out experiments in his laboratory. More than that, Prof. Kundu has always inspired me with his hard work, dedication, and enthusiasm for science.

I thank Prof. CNR Rao for being a constant source of inspiration and I consider myself very fortunate to have worked directly with him on a few research problems.

I am thankful to all my collaborators namely, Prof. Tapas Kundu, Prof. Tapas Maji, Prof. Aanat B Patel, Prof. Ranga Uday Kumar, Dr. Dinesh jagadeesan, Dr. B R Selvi, Snehajyoti Chatterjee, Dr. Manoj Kumar, Dr. Sarmistha Kundu, Dr. Sadhan Das, Dr. Vivek Tiwari, Akshay Bhat, Krishnachary Salikolimi, Prabhu, Dr. Rakesh, Dr. Ramakrisha Matte, Dr. Subramanian, Dr. Nitesh Kumar, and Dr. Leela Srinivas for their help and all the learning I got while working with them.

I thank past and present chairmen of CPMU, Prof. G. U. Kulkarni, Prof. Balasubramanian Sundaram, for allowing to me use the various facilities.

I thank the following faculties namely Prof. G. U. Kulkarni, Prof. S. Balasubramanian, Prof. A. Sundaresan, Prof. S. M. Shivaprasad, Prof. N. Chandrabhas, Prof. T. K. Maji, Prof. Eswaramoorthy and Prof. K. S. Narayan of CPMU, Prof. T. Govindaraju and Prof. S. J. George of NCU, Prof. S. K. Pati, Prof. Umesh V. Waghmare, Prof. S. Narasimhan and Dr. N. S. Vidhyadhiraja of TSU and Prof. S. Ranganathan of Materials Engineering (IISc) for the

insightful courses and discussions. I very much want to thank all the faculty members of JNC for creating such vibrant and friendly environment for research.

I am grateful to my past and present labmates, Dr. Dinesh, Dr. Sai Krishna, Dr. Datta, Dr. Kalyan, Josena, Dr. Pavan, Amrit, Dheeraj, Sisir, Sonu, Suchi, and Sahana for providing very conducive and interactive atmosphere in the lab. I also acknowledge all the visiting scientists and students (POCE and SRF) for their contributions.

I acknowledge the timely help of the technical staff of JNC, Usha madam and Mr. Joy Ghatak (TEM), Mrs. Selvi (FESEM), Mr. Vasu (TGA, IR, UV, PL), Mrs. B. S. Suma (Confocal), Mr. Anil (XRD), Mr. Mahesh (SEM), Mr. Kishore (XPS), Mr. Srinath, Mr. Srinivas, Mr. A Srinivas, Mr. Sunil (Gas Cylinders).

I thank JNC Library, Complab, Hostel, Academics, Administration, and Dhanwantari staff members for all their help during my stay here.

The cheerful company, constant help, encouragement, and support of all my friends at JNC would always be cherishable.

I would like to remember all my teachers for their teachings, encouragement, and support as well.

At the end, its my family and their believe in me, which always have stood by me. This thesis is my humble dedication to them.

PREFACE

This thesis presents synthesis and characterization of hybrids based on carbonaceous and layered materials. It is divided into five chapters. Chapter 1 briefly introduces hybrid materials, which are generally defined as a material that includes two or more moieties blended on the molecular scale. A major emphasis has been given to hybrid materials which find applications in drug delivery and catalysis. Also, it discusses the key challenges in the field of drug delivery and catalysis, with more stress given to ones relevant to this thesis. Chapter 2 presents, surface modifications of glucose derived carbon nanospheres with magnetic (Prussian blue and its nickel-chromium analogues) nanoparticles and luminescent (lanthanide) probes. These multifunctional carbon spheres showed enhanced magnetic and luminescent behaviour as compared to their native elements. These hybrids were biocompatible, have the ability to cross the blood-brain barrier and could be used as brain theranostics. Chapter 3 discusses about synthesis of hybrid nanoparticles made up of magnetic iron oxide materials of different shapes (spheres, spindles, biconcaves and nanotubes) coated with glucose derived carbon. Depending on their shape, these nanoparticles could compartmentalize inside the brain cells in the in vivo conditions. Biconcave shape of nanoparticles showed preferential nuclear entry, whereas nanotube morphology was restricted to the cytoplasm. Also, shape dependent compartmentalized delivery of an activator of an epigenetic enzyme was demonstrated.

Chapter 4 describes about a smart hybrid material made up of layered amino-clay, magnesium phyllo(organo)silicate, sheets/bundles and polyelectrolytes. These organic-inorganic hybrids were synthesized by coating the colloidal polystyrene spheres with polyelectrolyte protected amino-clay layers in a layer-by-layer method. The clay layers are sandwiched between the polyelectrolyte layers. The amino-clay swells in water due to protonation of amino groups and the degree of swelling depends on the pH of the medium. As

a result, the hybrid spheres undergo a size increase up to 60 % as the pH is changed from 9 to 4. The stimuli responsive property of the hybrid spheres was used for the release of ibuprofen and eosin at different pH. Chapter 5 demonstrates catalytic behaviour of layered boron nitride and boron nitride supported metals towards oxidative dehydrogenation of propane. Boron nitride (a generally accepted inert material) catalysed the propane oxidative dehydrogenation reaction. The catalytic activity was found to improve with increasing surface area of the catalyst. The catalytic activity was stable for nearly six hours and could be regenerated easily.

TABLE OF CONTENTS

Chapter 1

A Brief Introduction to the Hybrid Materials

Summary:

Organic-inorganic hybrids are new class of materials bestowed with unusual properties independent of their counterparts and find applications in extremely diverse fields. In this chapter, we present brief introduction to hybrid materials with emphasis on definition, synthetic strategies, and applications. The applications of hybrids were restricted to drug delivery and catalysis in the discussions, as the work of this thesis span in these areas only. The major challenges in the field of drug delivery and catalysis were briefly mentioned and the use of hybrid materials to overcome these challenges were also noted here.

Adapted with permission from reference 5. Copyright 2011, Royal Society of Chemistry.

1.1 Introduction:

Recent technological breakthroughs in materials synthesis and the growing aspiration for new and unique functions in materials have generated enormous demand for the novel materials. However, as single components, materials such as metals, ceramics, plastics *etc.* cannot fulfill all technological aspects required for the various new applications.[1] For example, ceramics are typically strong but not tolerant to surface flaws and cracks, whereas most polymers are flaw-tolerant but deform extensively at rather low applied stresses.[1] Unfortunately, these two properties (strength and toughness) tend to be mutually exclusive, and attaining optimal mechanical performance is always a compromise often achieved through the empirical design of microstructures.[1] Such bottlenecks drives the development of hybrid materials which could nearly accomplish all technological requirements for various applications.

A hybrid material is generally defined as a material that includes two moieties blended on the molecular scale i.e. atomic or nanometer-level mixture of materials gives rise to hybrid materials.[1,2] Hybrids are either homogeneous systems derived from monomers and miscible organic and inorganic components, or heterogeneous systems (nanocomposites) where at least one of the component domains has a dimension ranging from few Å to several nanometers.[3] A wide range of materials, such as crystalline, highly ordered coordination polymers, amorphous sol-gel compounds, materials with and without interactions between the inorganic and organic units are covered under the name hybrid materials.[4] The term hybrid materials is often interchangeably used with nanocomposites. There is no clear borderline between inorganic-organic hybrid materials and inorganic-organic nanocomposites materials. Nanocomposite is used if one of the

structural units, either the organic or the inorganic, is in the size range of 1-100 nm.[1] Commonly, the term nanocomposites is used if discrete structural units in the respective size regime (nanoparticles, nanorods, carbon nanotubes and galleries of clay minerals) are formed in situ by molecular precursors, for example applying sol-gel reactions.[1]

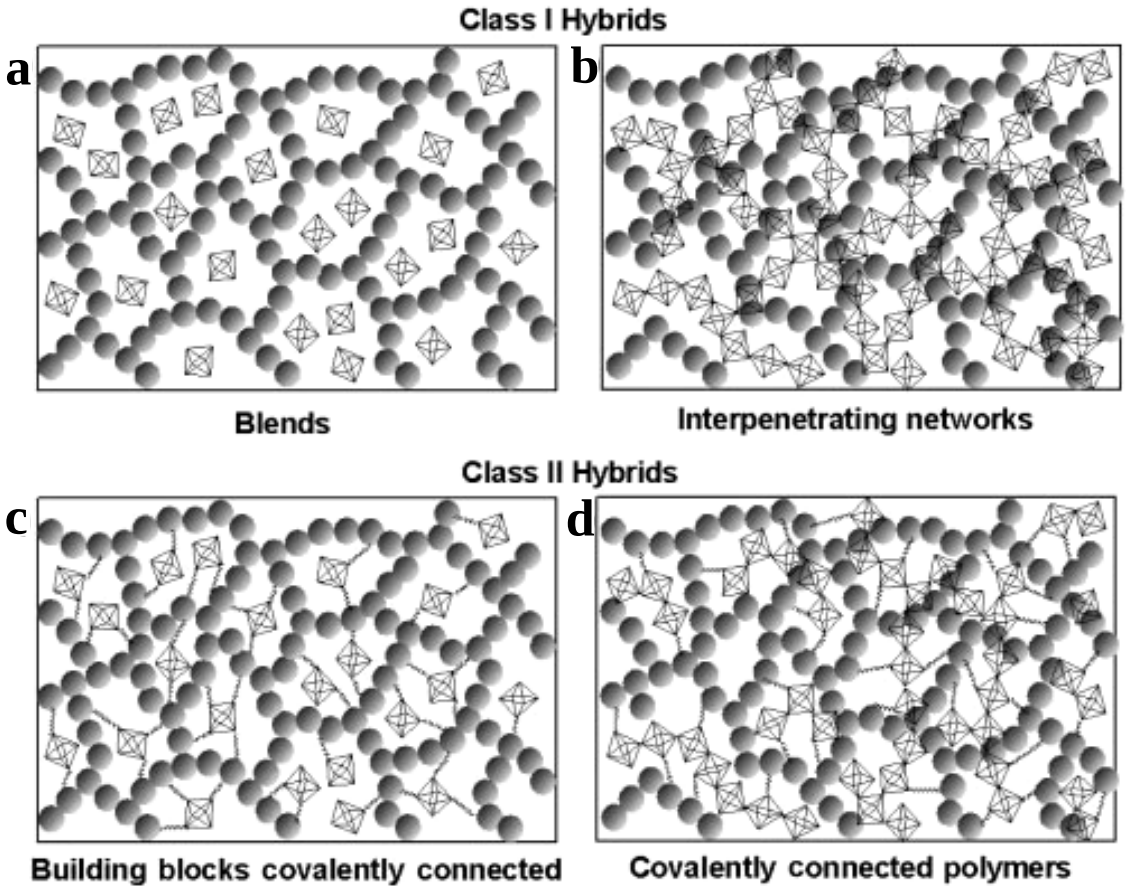

Figure 1: Classification of hybrid materials. Adapted with permission from reference 1. Copyright 2007, John Wiley and Sons.

The properties of hybrid materials are not only the sum of the individual contributions of organic and inorganic phases, but often the interface between the dissimilar phases play significant role in determining the properties of the hybrid.[1,3,5,6] The nature of the interface has been used to grossly divide these materials into two distinct classes (Figure 1).[1] ***Class I*** hybrid materials are those that show weak interactions

between the two phases, such as van der Waals, hydrogen bonding or weak electrostatic interactions. Blends and interpenetrating networks (Figure 1a, 1b) comes under Class I materials when interaction between organic and inorganic building blocks is weak, e.g. materials formed by the combination of inorganic particles and organic polymers which lacks strong interactions. ***Class II*** hybrid materials are those that show strong chemical interactions between the components. They are formed when discrete inorganic blocks are covalently linked to organic polymers or inorganic and organic polymers are covalently connected to each other (Figure 1c, 1d).

The most obvious advantage of organic-inorganic hybrids is that they can favorably combine the dissimilar properties of organic and inorganic components in one material (Table 1).[1,3] This field provides the opportunity to invent new materials with a large spectrum of known and as yet unknown properties. Another driving force in this area is the possibility to create multifunctional materials possessing diverse qualities in a single material. The properties of hybrid materials can be altered by changing the composition at the molecular scale.[1,7] If, for example, more hydrophobicity of a material is desired, the amount of hydrophobic molecular components is increased. Mechanical properties such as toughness or scratch resistance are tailored if hard inorganic nanoparticles are included in the polymer matrix. Because the compositional variations are carried out on the molecular scale a gradual fine tuning of the material properties is possible.[1] This also opens up the way to synthesize smart materials.

Smart materials is one of the hot topics in materials chemistry as they react to environmental changes or switchable systems, and find applications in sensors, membranes, catalysis, and biomedicine areas.[1,3,5,6] The desired function can be derived

Table 1: Comparison of general properties of typical inorganic and organic materials. Adapted with permission from reference 3. Copyright 2005, Royal Society of Chemistry.

Properties	Organics (polymers)	Inorganics (SiO_2, TMO)
Nature of bonds	covalent [C–C] (+ weaker van der Waals or H bonding)	ionic or iono-covalent [M–O]
T_g (glass transition)	low (−100 °C to 200 °C)	high (>200 °C)
Thermal stability	low (<350 °C, except polyimides, 450 °C)	high (≫100 °C)
Density	0.9–1.2	2.0–4.0
Refractive index	1.2–1.6	1.15–2.7
Mechanical properties	elasticity	hardness
	plasticity	strength
	rubbery (depending on T_g)	fragility
Hydrophobicity, permeability	hydrophilic	hydrophilic
	hydrophobic	low permeability to gases
	± permeable to gases	
Electronic properties	insulating to conductive	insulating to semiconductors (SiO_2, TMO)
	redox properties	redox properties (TMO)
		magnetic properties
Processability	high:	low for powders (needs to be mixed with polymers or dispersed in solutions)
	• molding, casting	
	• machining	
	• thin films from solution	high for sol–gel coatings (similar to polymers)
	• control of the viscosity	

from organic or inorganic or from both the components. One of the advantages of hybrid materials in this context is that the functional organic molecules as well as biomolecules often show better stability and performance if introduced in an inorganic matrix.[1]

1.2 General strategies for the design of functional hybrids:

The origin of hybrid materials did not take place in a chemical laboratory but in nature. Many natural materials consist of inorganic and organic building blocks distributed on the molecular or nanoscale. In most cases, the inorganic part provides mechanical strength and an overall structure to the natural objects while the organic part delivers bonding between the inorganic building blocks and/or the soft tissue.[1] Typical examples of such materials are bone, and nacre. The concepts of bonding and structure in such materials are intensively studied by many scientists to understand the fundamental processes of their formation and to transfer the ideas to artificial materials in a so-called biomimetic approach.[8] The fascination of complex geometries produced by biological

hybrid materials under ambient temperature, aqueous environment, and neutral pH inspired the scientists to replicate such structures in the beaker.

The main chemical routes that are used to design a given hybrid materials are schematically represented in figure 2.[3]

Path A corresponds to very convenient soft chemistry based routes including conventional sol–gel chemistry (***Route A$_1$***), the use of specific bridged and polyfunctional precursors (***Route A$_2$***), and hydrothermal synthesis (***Route A$_3$***).

Route A$_1$ produces amorphous hybrid networks through hydrolysis of organically modified metal alkoxides or metal halides condensed with or without simple metallic alkoxides. The solvent may or may not contain specific organic molecules such as, a bio-component or a poly-functional polymer that can be crosslinkable or that can interact or be trapped within the inorganic components through a variety of interactions (H-bonds, p–p interactions, van der Waals). These strategies are simple, low cost and produce amorphous nanocomposite hybrid materials which exhibit infinite microstructures and present many interesting properties and give rise to many commercial products shaped as films, powders or monoliths.

In ***Route A$_2$*** bridged precursors such as silsesquioxanes $X_3Si–R–SiX_3$ (R is an organic spacer, X = Cl, Br, OR) are used which allows the formation of homogeneous molecular hybrid organic–inorganic materials with a better degree of local organization. In recent work, the organic spacer has been complemented by using two terminal functional groups (urea type). The combination within the organic bridging component of aromatic or alkyl groups and urea groups allows better self-assembly through the capability of the organic moieties to form both strong hydrogen bond networks and efficient packing via π–π or hydrophobic interactions.

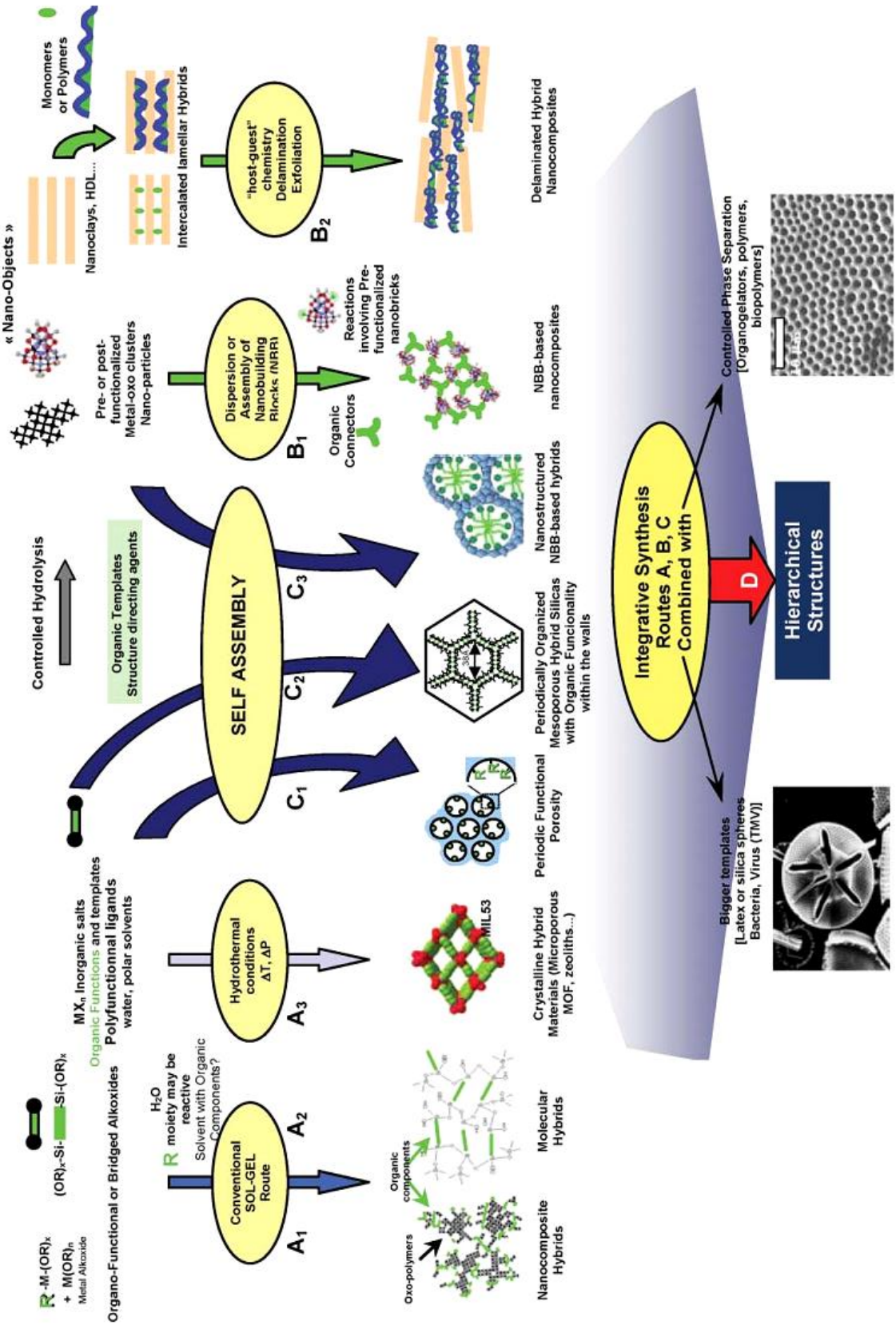

Figure 2: Scheme of the main chemical routes for the synthesis of organic–inorganic hybrids. Adapted with permission from reference 3. Copyright 2005, Royal Society of Chemistry.

Route A_3 is hydrothermal synthesis in polar solvents (water, formamide, etc.) in the presence of organic templates leading to numerous zeolites with a large scale applications in the domain of adsorbents or catalysts. More recently, a new generation of crystalline microporous hybrid solids known as metal organic frameworks (MOF) have been discovered by several groups. These hybrid MOF materials possess very high surface area from 1000 to 4500 m^2g^{-1} and are promising candidates for catalysis and gas adsorption.

Path B corresponds to the *assembling/dispersion (**Route B_1**)* or the *intercalation (**Route B_2**)* of well-defined *nanobuilding blocks (NBB)*. These NBB can be clusters, organically functionalized nanoparticles (metallic oxides, metals, chalcogenides, *etc.*), and layered materials (clays, layered double hydroxides, lamellar phosphates, oxides or chalcogenides) capable of intercalating organic components. The NBB can be capped with polymerizable ligands or connected through organic spacers, like telechelic molecules or polymers, or functional dendrimers. The variety found in the nanobuilding blocks (nature, structure, and functionality) and the linkers allows synthesis of a wide range of architectures and organic-inorganic interfaces, associated with different assembling strategies. Moreover, the step-by-step preparation of these materials usually allows high control over their semi-local structure.

Path C, self-assembling procedures, corresponds to the organization of growing inorganic or hybrid networks over *templates formed by organic surfactants (*Figure 2, ***Route C_1***). In this field, hybrid organic-inorganic phases are very interesting due to the versatility they demonstrate in the building of a whole range of nanocomposites. A recent strategy developed by several groups consists of *templated growth (with surfactants) of mesoporous hybrids by using bridged silsesquioxanes as precursors (*Figure 2, ***Route C_2***).

This approach yields a new class of periodically organized mesoporous hybrid silicas with organic functionality within the walls. These nanoporous materials present a high degree of order and their mesoporosity is available for further organic functionalization through surface grafting reactions. ***Route C_3***, is *combination of self-assembly and NBB approaches*. Strategies combining the nanobuilding block approach with the organic templates to control the assembling step are also appearing (Figure 2). The combination between the "nanobuilding block approach" and "templated assembly" will have paramount importance in exploring the theme of "synthesis with construction". They exhibit a large variety of interfaces between the organic and the inorganic components (covalent bonding, complexation, electrostatic interactions, etc.).

Path D explains *Integrative synthesis* approach (lower part of Figure 2). The strategies reported above mainly offer the controlled design and assembly of hybrid materials in the 1 Å to 500 Å range. Recently, micro-molding methods have been developed, in which the use of controlled phase separation phenomena, emulsion droplets, latex beads, bacterial threads, colloidal templates or organogelators leads to controlling the shapes of complex objects in the micron scale. The combination between these strategies and those above described along paths A, B, and C allow the construction of hierarchically organized materials in terms of structure and functions.

1.3 Applications of hybrids:

Organic-inorganic hybrid materials, for their versatile properties find applications in many areas: optics, electronics, ionics, mechanics, energy, environment, biology and medicine, *etc*. (Figure 3).[3,5] This chapter however, discusses on the utility of the hybrid materials in the fields of drug delivery and catalysis. At first, the major challenges involved in drug delivery and the use of hybrid nanomaterials in circumventing some of these problems is discussed. Later the relevance of hybrid materials in catalysis is highlighted.

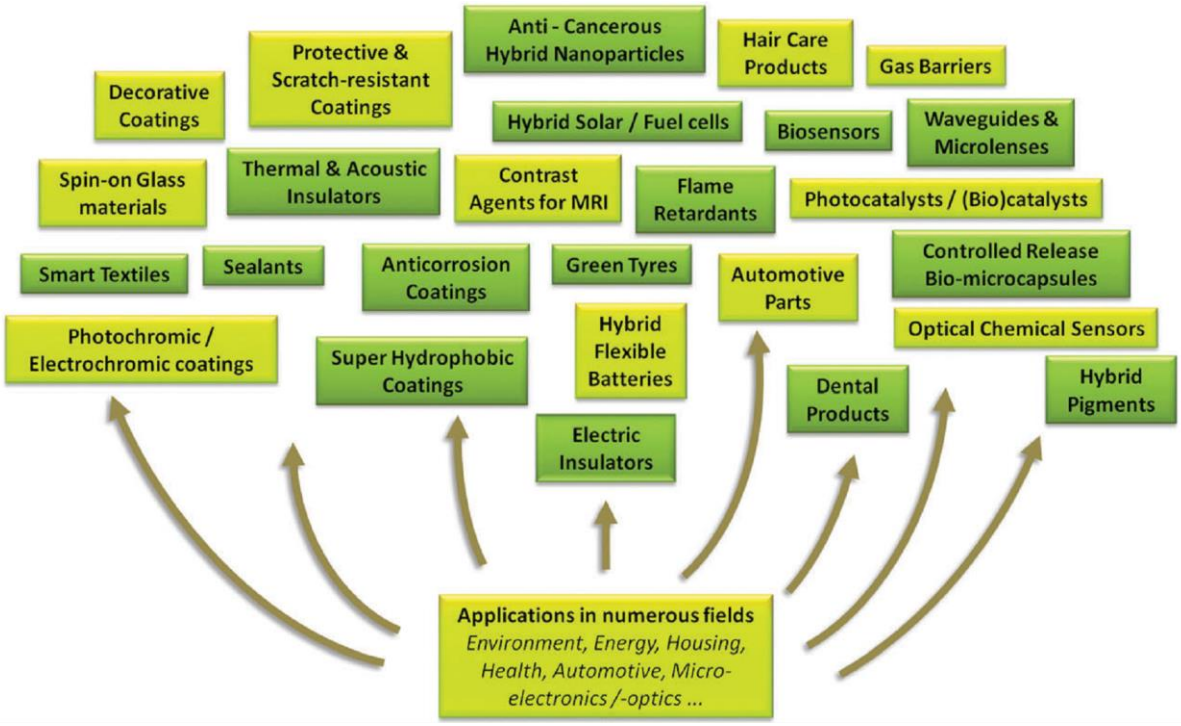

Figure 3: Applications of hybrid materials. Adapted with permission from reference 5. Copyright 2011, Royal Society of Chemistry.

1.3.1 Challenges in Drug delivery:

Conventional ("free") therapeutic agents, poses several concerns including their poor water solubility (at least, for most anticancer drugs), lack of targeting capability, nonspecific distribution, systemic toxicity, and low therapeutic index (Table 1).[9]

Problem	Implication	Effect of DDS
Poor solubility	A convenient pharmaceutical format is difficult to achieve, as hydrophobic drugs may precipitate in aqueous media. Toxicities are associated with the use of excipients such as Cremphor (the solubilizer for paclitaxel in Taxol).	DDS such as lipid micelles or liposomes provide both hydrophilic and hydrophobic environments, enhancing drug solubility.
Tissue damage on extravasation	Inadvertent extravasation of cytotoxic drugs leads to tissue damage, e.g., tissue necrosis with free doxorubicin.	Regulated drug release from the DDS can reduce or eliminate tissue damage on accidental extravasation.
Rapid breakdown of the drug in vivo	Loss of activity of the drug follows administration, e.g., loss of activity of camptothecins at physiological pH.	DDS protects the drug from premature degradation and functions as a sustained release system. Lower doses of drug are required.
Unfavourable Pharmacokine-tics (PK)	Drug is cleared too rapidly, by the kidney, for example, requiring high doses or continuous infusion.	DDS can substantially alter the PK of the drug and reduce clearance. Rapid renal clearance of small molecules is avoided.
Poor biodistributio n	Drugs that have widespread distribution in the body can affect normal tissues, resulting in dose-limiting side effects, such as the cardiac toxicity of doxorubicin.	The particulate nature of DDS lowers the volume of distribution and helps to reduce side effects in sensitive, nontarget tissues.
Lack of selectivity for target tissues	Distribution of the drug to normal tissues leads to side effects that restrict the amount of drug that can be administered. Low concentrations of drugs in target tissues will result in suboptimal therapeutic effects.	DDS can increase drug concentrations in diseased tissues such as tumors by the EPR effect. Ligand-mediated targeting of the DDS can further improve drug specificity.

Table 1: Non-ideal properties of drugs and their therapeutic implications. Adapted with permission from reference 9.

Colloidal drug carriers (such as nano- and micro-particles) have emerged as promising systems which could overcome these challenges.[9-14] The potential advantages of these drug carriers includes: 1) improved delivery of hydrophilic drugs; 2) protecting drugs from harsh environments (e.g., acidic environment in the stomach or the lysosomes, and the high levels of proteases or other enzymes in the blood stream) before reaching their targets, leading to an extended plasma half-life of the drug in the systemic circulation; 3) targeted delivery of drugs in a tissue- or cell-specific manner to maximize the treatment efficacy while systemic side effects are alleviated; 4) controlled release of drugs over a controllable period of time at precise doses and even realization of on-demand release using a more sophisticated, stimuli-responsive system; and 5) co-delivery of multiple types of drugs and/or diagnostic agents (e.g., contrast agents) for combination therapy and real-time readout of the treatment efficacy.[9-14] Despite their enormous potential and extensive scientific efforts, only a few drug delivery systems have been able to enter the market.[15-19] This is because for a successful therapy, the drug carriers are expected to have a set of optimal biological behaviors: i) biocompatibility and biodegradability, ii) longer blood-circulation, iii) extravasation (escape from the blood-vessel) in the target tissue, iv) accumulation and distribution in the target tissue, v) binding and endocytosis in the targeted cells, vi) endosomal escape, vii) therapeutic action and viii) clearance (get cleared from the body) (Figure 4).[20] Each one of these characteristics are critical, however most drug carriers poses not all of them.[11] The above listed, expected behaviors of the drug carriers are mainly due to the biological barriers they encounter on their way to the target site.[21-23] In a typical systemic[24] administration (a route of administration into the circulatory system, such as oral, intravenous, intramuscular, subcutaneous, *etc*., so that the entire body is affected) following are the general biological barriers that drug carriers

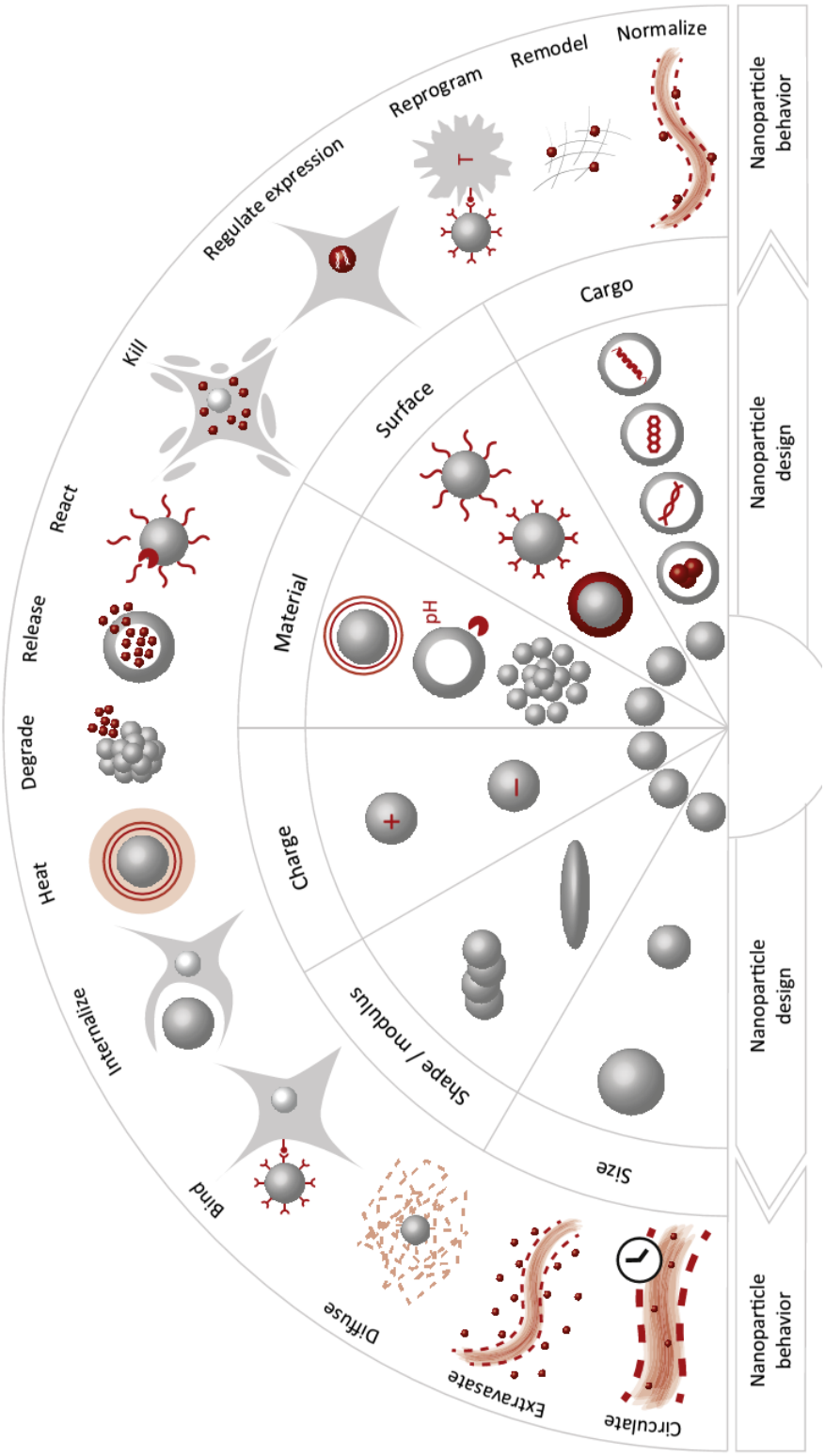

Figure 4: Nanoparticle behaviors. Nanoparticle designs, in terms of size, shape, modulus, charge, material, surface, and cargo, as well as their interactions in the body, determine their individual behavior. Adapted with permission from reference 20. Copyright 2014, Elsevier.

encounter[25,26]:

A. Intestinal epithelial barrier (to enter the circulatory system).

B. Clearance mechanisms of the blood circulation (such as immune clearance and non-targeted tissue accumulation) and the endothelial barrier (to enter the target organ).

C. Diffusion barriers for distribution in the tissue interstitium.

D. Barriers for internalization into the cells and intracellular trafficking.

One of the key benefits of the nano- or micro-particles based delivery systems is availability of a range of handles, such as size, shape, surface charge and chemistry, and material composition, to design/engineer carriers for different therapeutic cargoes, in order to overcome various hurdles (Figure 4).[11,20] In the following subsections, different biological barriers would be discussed briefly with examples of how the diverse carrier design parameters helps overcome these obstacles.

A. Transport across the epithelial barrier:

The transport across the intestinal epithelium, after which the drug carriers reach the blood circulation, is limited by two barriers.[25] The first one is mucosal barrier, which using polyvalent interactions with the drug carriers traps and clears them. In order to penetrate mucus, synthetic drug carriers must avoid adhesion to mucin fibers and be small enough to avoid significant steric inhibition by the dense fiber mesh. Nanoparticles as large as 500 nm have been shown to rapidly diffuse across human mucus after coating with polyethylene glycol.[27] The second barrier comprises the monolayer of the epithelial cells whose tight junctions offer a particularly strong barrier for entry of nanoparticles.

Nanoparticles comprising various materials have been synthesized and used to deliver macromolecules, particularly insulin and vaccines.[28]

B. Drug carriers in the blood circulation:

Once in the bloodstream it is critical for the drug carriers to be stable and hold the cargo without leakage or degradation by enzymes in the blood.[29,30] More importantly, the therapeutic carriers should circulate for longer durations of time to maximize their accumulation in the targeted organ or cells.[21,23,29] However, the circulation of drug carriers in the bloodstream faces various hurdles including, glomerular excretion by the kidney, opsonization followed by immune clearance by the reticuloendothelial system (RES) (macrophages/monocytes, liver, and spleen) and non-specific tissue accumulation.[30] Rapid clearance from the circulation with a consequent over-accumulation in the liver and spleen is regarded as the main cause of side effects and insufficient delivery of nanocarriers to target sites.[30]

In the bloodstream, the nano-bio interfacial reactions between the drug carriers and its surroundings (bio-environment) may lead to change in their surface properties (Figure 5).[31-32] The newly formed nano-bio interface comprises kinetic, and thermodynamic exchanges between the nanosurfaces and the biological components (biological fluids, membranes, cell components, proteins, DNA, etc.).[31-32] Protein adsorption to the carrier surface is one of the interfacial reactions, leading to a protein corona which gives biological identity to the drug carrier and greatly influences their blood circulation and biodistribution.[31-32] A prominent consequence of coating with proteins is opsonization of drug carriers, which allows RES macrophages to easily recognize and remove these carriers.[30] The biomolecular corona is also relevant to

nanoparticles with grafted antibodies, proteins and peptides that are specifically designed for targeting in nanomedicine (Figure 5).[31-32] Their presence may lead to more subtle and poorly understood biological issues possibly related to current struggles in achieving

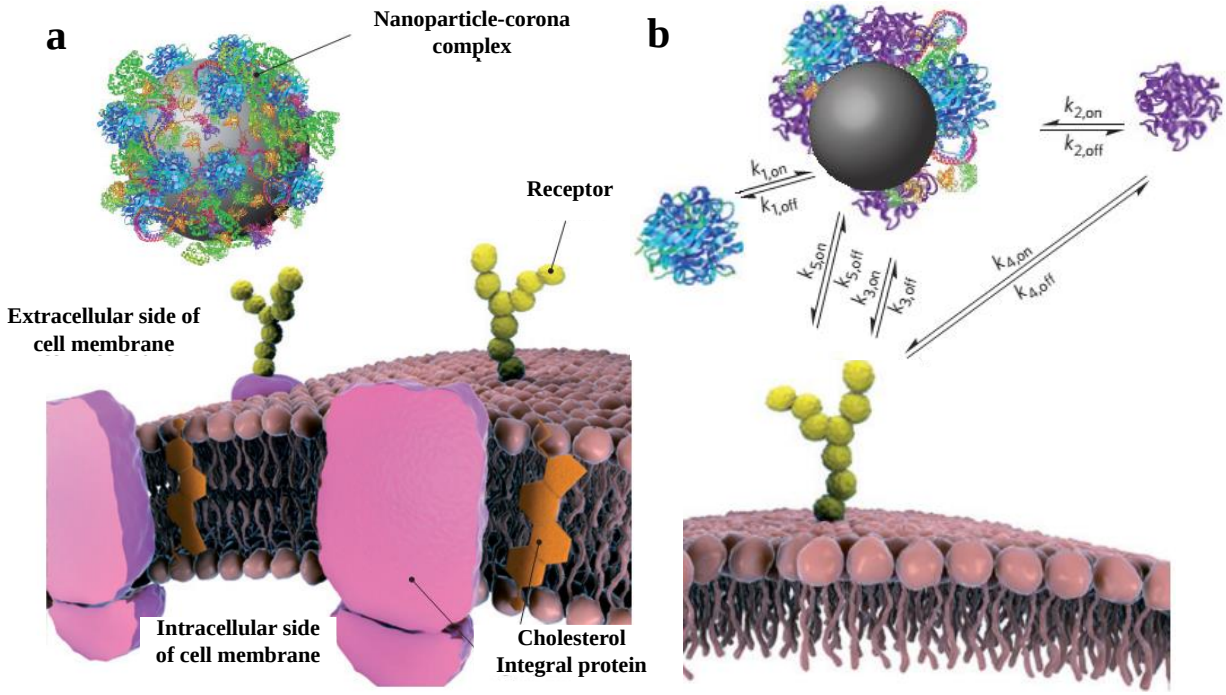

Figure 5: The nanoparticle–corona complex in a biological environment. a) It is the nanoparticle–corona complex, rather than the bare nanoparticle, that interacts with biological machinery, in this example with a cell membrane receptor. b) Relevant processes (arrows), in both directions (on/off), for a nanoparticle interacting with a receptor. Biomolecules in the environment adsorb strongly to the bare nanoparticle surface (k_1), forming a tightly bound layer of biomolecules, the 'hard' corona, in immediate contact with the nanoparticle. Other biomolecules, the 'soft' corona, have a residual affinity to the nanoparticle-hard-corona complex (primarily to the hard corona itself), but this is much lower, so those molecules are in rapid exchange with the environment (k_2). If sufficiently long-lived in the corona, a biomolecule may lead to recognition of the nanoparticle-corona complex as a whole by a cell membrane receptor (k_3). The same biomolecule alone can also be recognized by the receptor (k_4). If present, the bare surface of the nanoparticle may also interact with cell surface receptors (k_5) or other constituents of the cell membrane. Proteins adapted from Protein Data Bank (http://www.pdb.org). Adapted with permission from reference 31. Copyright 2012, Nature publishing group.

efficient targeting of nanomedicines in vivo.[31-32] Surface modification of drug carriers with chemical and biological agents, such as poly(ethylene glycol) (PEG) can create a hydrophilic protective layer around the drug carriers, which sterically hinders absorption of opsonin proteins, thereby blocking the opsonization process (Figure 6).[21]

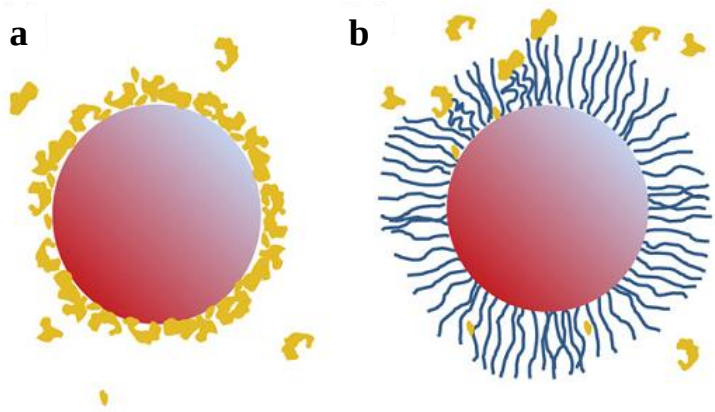

Figure 6: Protein adsorption onto nanoparticle. a) PEGylation of nanoparticles helps to slow the adsorption of proteins to the nanoparticle surface. The exposed surface of a non-PEGylated nanoparticle quickly develops a protein corona. The opsonized surface then promotes phagocytosis by MPS cells leading to rapid clearance of the nanoparticles. b) The hydrophilic polymers grafted onto the nanoparticle form a brush-like barrier that repels most proteins before it can bind to the surface and thus significantly slows the clearance of the nanoparticles. Adapted with permission from reference 21. Copyright 2012, Elsevier.

The circulation of drug carriers in the blood and their exchange between tissue (target or non-target) vasculature and interstitium is a multifaceted process.[29-30] One decisive factor is the vascular physio-anatomy. As shown in Figure 7, in some tissues including liver, spleen, and kidney, the extravasation of carriers is quite efficient due to the openings in discontinuous or fenestrated capillaries.[30] Fenestrated capillaries are also found around tumors due to rapid construction of new vascular structures. These structures possess enhanced permeability, a phenomenon referred to as enhanced

permeation retention (EPR) effect.[33] On the other hand, extravasation of drug carriers is restricted in some important organs. For example, in brain the endothelium is nearly impermeable due to the presence of blood-brain barrier (BBB), an enzymatic and physical barrier, which prevents the entry of toxins from blood to the brain and maintain brain homeostasis.[34-37] The brain endothelium presents most intimate cell to cell connections

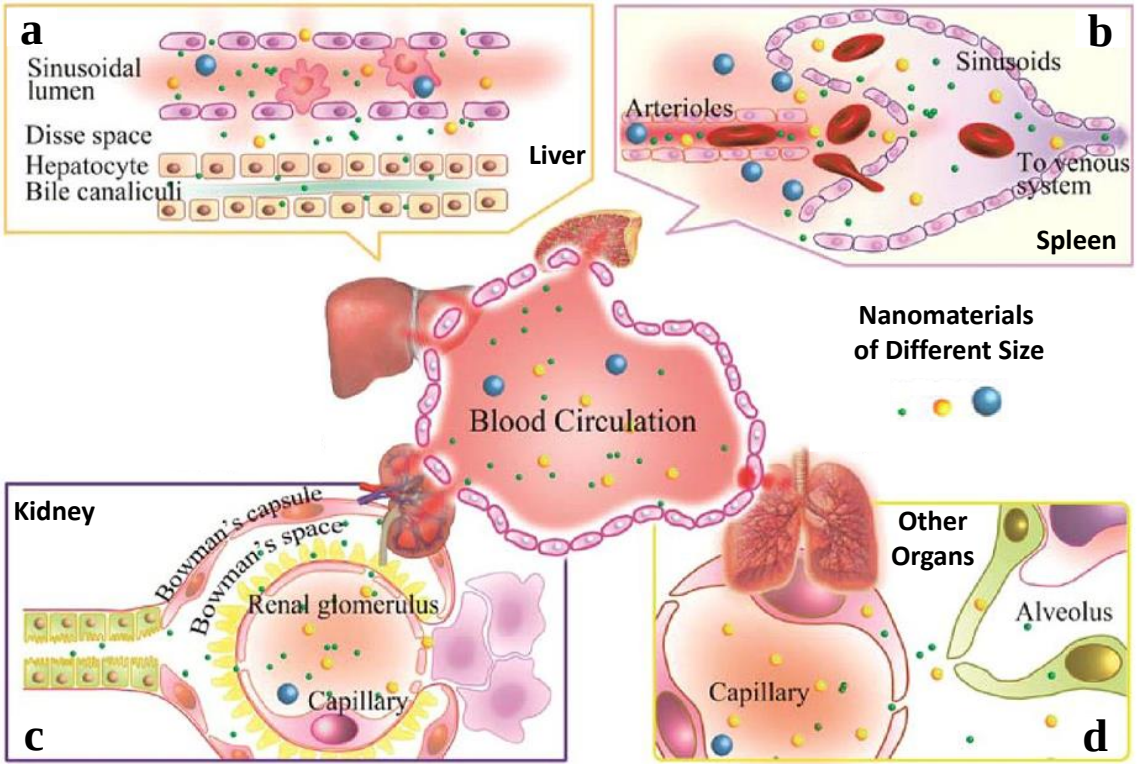

Figure 7: The tissue-specific extravasation of drug carriers. a) In liver, the hepatic sinusoidal endothelial cells possess open fenestraes sized 100-200 nm that facilitate the nanoparticle diffusion. Smaller carriers (10-20 nm) are removed from blood via rapid liver uptake, whereas larger drug carriers (≥200 nm) are effectively cleared by Kupffer cells. b) In sinusoidal spleen (as in rat and human), blood flows through the discontinuous capillary into splenic venous system. Non-deformable entities sized above 200 nm may be cleared from blood by splenic filtration. c) The capillary fenestraes in the glomeruli have size between 10 and 100 nm, but the basal lamina can block the penetration of particles larger than 5 nm. d) The endothelia of lung, muscle, and bone capillaries are generally characterized by a continuous morphology that allows only small particles sized below 3 nm to cross the inter-endothelial cell slits. Adapted with permission from reference 30. Copyright 2013, American Chemical Society.

because of the presence of tight junctions between adjacent endothelial cells (Figure 8).[38] The tight junctions are further strengthened and maintained by the interaction or communication of astrocytes and pericytes with brain endothelial cells.[38] Apart from acting as a physical barrier, BBB possess multiple functions as transport barrier (p-glycoprotein), metabolic or enzymatic barrier (specialized enzyme systems), and immunological barrier.[38] Thus, the paracellular transport across BBB is highly restricted.

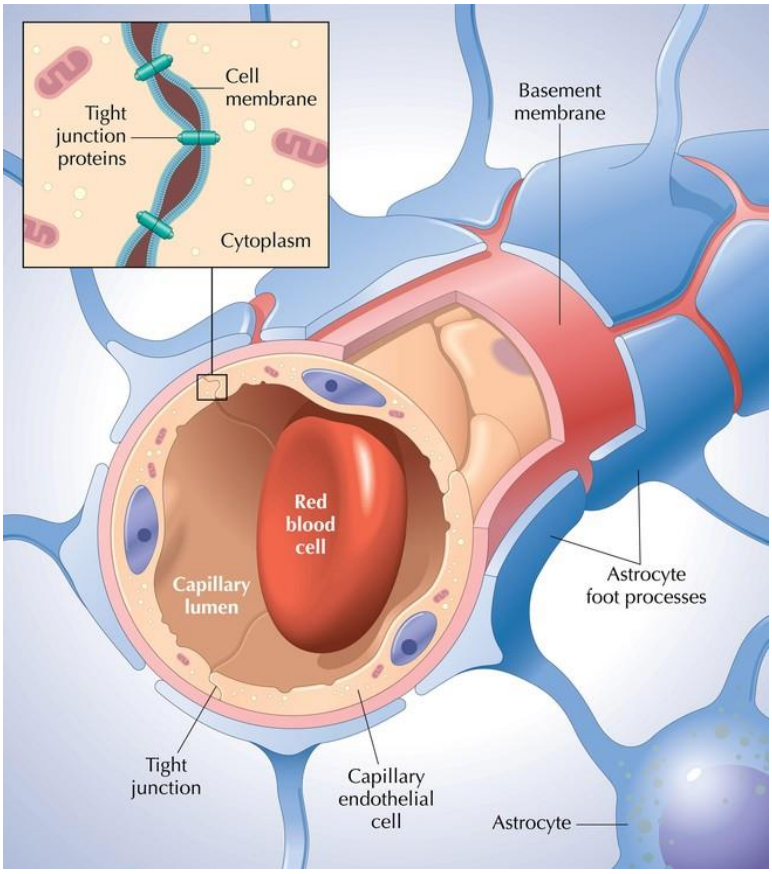

Figure 8: Schematic representation of the blood–brain barrier (BBB). The tight junctions between adjacent endothelial cells is formed by an intricate complex of transmembrane proteins (junctional adhesion molecule-1, occludin, and claudins) with cytoplasmic accessory proteins (zonula occludens-1 and -2, cingulin, AF-6, and 7H6). They are linked to the actin cytoskeleton, thereby forming the most intimate cell to cell connection. Physiologically, in addition to brain capillary endothelial cells, extracellular base membrane, adjoining pericytes, astrocytes, and microglia are all integral parts of the BBB supporting system. Adapted from https://cias.rit.edu/faculty-staff/101/faculty/340.

The near impermeability of several potential drugs, 100% of the large molecules and >98% of small molecules, into the brain limits their use in the treatment of brain diseases like Alzheimer's, Parkinson's, and Brain tumors.[34] Nanoparticle based delivery systems have proven to be promising and are being extensively explored for the delivery across the BBB.[35-36]

The blood circulation and site-specific extravasation of drug carriers is also dependent on physicochemical characteristics of the carriers, which have been thoroughly investigated to understand the mechanisms of toxicology and to develop nanomedicines.[30] For example, size of the nanocarriers affects their removal from the circulation. Small

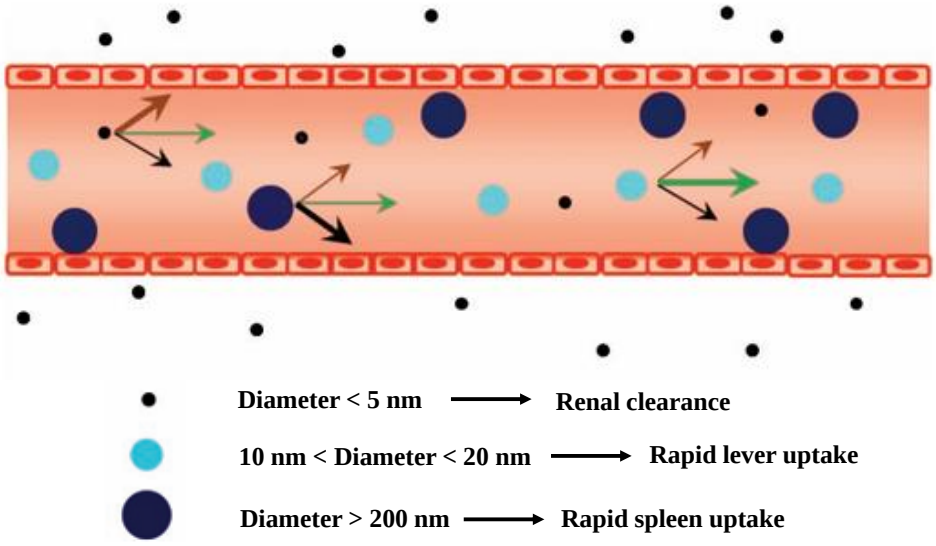

Figure 9: Size of the spherical nanoparticles determines the mechanism and rate of clearance. Spheres which are smaller than 5 nm, readily pass through the tight endothelial junctions, resulting in a relatively rapid rate of clearance from the circulation. For large particles (e.g., >200 nm), momentum forces begin to dominate and wall collisions become more common, resulting in rapidly uptake by the reticuloendothelial system. However, when the particle size falls between two extremes, all of these clearance mechanisms are minimized and circulation times are prolonged (the thickness of arrows represents the strength of the force). Adapted with permission from reference 42. Copyright 2013, John Wiley and Sons.

carriers might be removed from the blood by renal clearance (<5 nm) or rapid liver uptake (10-20 nm)[39], whereas large carriers are filtered in the sinusoidal spleen (>200 nm)[40], or are recognized and cleared by RES (Figure 9).[30] Therefore, drug carriers between 20 and 200 nm can remain in the circulation for an extended period of time.[30] However, these lower and upper boundaries of the nanoparticle size, are not strictly defined and even particles larger than 200 nm are able to circulate for significant durations as result of complex interplay between various physicochemical characteristics of the nanoparticles, such as size, shape, surface charge *etc.*, on their biological behavior.[41-44]

Additionally, recent results indicate that particle shape and surface properties may play important roles in biological half-life, biodistribution, and cellular (endothelial) binding and internalization.[43-45] Internalization kinetics of cylindrical nanoparticles with high aspect ratios have been shown to be significantly faster than those with low aspect ratios.[46] The design of nonspherical or flexible nanoparticles can dramatically extend circulation time in vivo. Furthermore, it is established that nanoparticles with neutral or negatively charged surfaces have a reduced plasma protein adsorption and low rate of nonspecific cellular uptake, while positively charged drug carriers are expected to have a high nonspecific internalization rate and short blood circulation half-life.[47] Blood circulation patterns of drug carriers may also be further influenced by surface ligands and surface chirality.[48]

C. Transport in the interstitium:

Following their extravasation in the target tissue the drug carriers needs to get distributed throughout the tissue for effective and thorough delivery of its payload.

However, the tissue interstitium is a highly heterogeneous and structurally complex medium through which nanoparticles have to diffuse in order to reach the target cell membranes.[49] For example, the tumor interstitial matrix consists of a highly interconnected network of collagen fibers that interact with other molecules, such as proteoglycans and glycosaminoglycans.[21,26] This collagen matrix poses a significant obstacle in nanoparticle diffusion. In the absence of sufficient diffusion through the interstitium, particles that extravasate from blood vessels may just localize on the periphery of the tumor.[50] Diffusion of drug carriers within the tumor depends on their size, shape, and charge as well as on the physicochemical properties of the interstitial matrix. Small molecules diffuse fairly rapidly in the tumor interstitial matrix. However, the diffusion coefficient of nanoparticles and liposomes is dramatically reduced by high viscosity, low porosity and matrix interactions. Particle charge may also play a significant role. Collagen fibers carry a slightly positive charge at neutral pH, and hence negatively charged nanoparticles may interact with the collagen matrix and aggregate.[51]

Several innovative strategies are being developed to enhance the nanoparticle penetration into the solid tissues. For example, collagenase treatment increases the porosity, which may in turn increase nanoparticle penetration.[52] In vitro studies using tumor spheroids, supplemented by mathematical models, have shown that nanoparticles of 20 and 40 nm in diameter are able to accumulate in the interior of the spheroid after treatment with collagenase, while 100 nm particles exhibited poor penetration in untreated spheroids with minor increase in penetration with collagenase treatment. Shape of the nanoparticles has also been shown to enhance interstitial transport. In a recent study, rod-shaped nanoparticles have shown enhanced diffusion in tumor interstitium compared to spherical particles.[53] In another example, a multistage approach has been

proposed where nanoparticles change their size to facilitate transport through interstitium. In this approach, the original 100-nm nanoparticles extravasate from the leaky regions of the tumor vasculature and shrink to 10 nm, thus facilitating their penetration into the tumor parenchyma.[54] Deep penetration into target tissues remains a significant hurdle. While a significant focus has been given to penetration into tumors, several other targets, in particular, brain suffer from the same limitation.[21,26] Accordingly, new materials that are able to enhance penetration of nanoparticles into solid tissues are required.

D. Internalization and intracellular trafficking within target cells:

Post tissue distribution the drug carriers needs to enter the cells and deliver their payload. However, the cell membrane is a formidable barrier to drug delivery.[21] While small, hydrophobic molecules can easily diffuse into the membrane, large or hydrophilic molecules or nanoparticles, cannot passively diffuse through the lipid bilayer membrane and instead must enter via other active uptake mechanisms such as receptor-mediated endocytosis or pinocytosis.[21] Pinocytosis is a relatively haphazard way for cells to engulf their surroundings by enveloping large quantities of surrounding fluid (Figure 10).[21] Receptor-mediated endocytosis is a more controlled method for bringing specific substances into the cell and is generally governed by receptor-ligand interactions at the cell surface (Figure 10).[21] Increasing the strength and probability of these interactions at the tumor cells has become a popular strategy to increase cell uptake at the tumor site.[55]

Following the endocytosis, most active endocytotic pathways direct the endocytosed material through the lysosome for cellular digestion before it is released to the cytoplasm (Figure 10).[21] The cellular digestion process serves the dual purpose of breaking down any potentially dangerous pathogens before they can access the cell and

freeing material for use in cell processes. During endocytosis, a portion of the outer membrane is pinched off inside the cell to form a vesicle containing the endocytosed material which is fused with interior vesicles to form a mildly degradative endosome

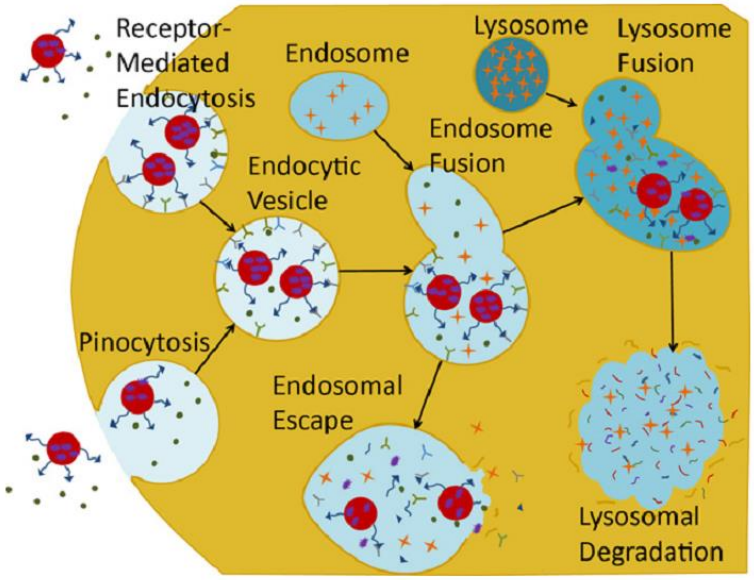

Figure 10: Active cell uptake. The major methods of nanoparticle cell uptake are receptor mediated endocytosis and pinocytosis. Both draw the particles into interior vesicles which eventually fuse with lysosomes to undergo cellular digestion which can neutralize some or all of the drug. Releasing the drug from the endosome before the lysosomal phase can increase the availability of drug in the cytoplasm. Adapted with permission from reference 21. Copyright 2012, Elsevier.

(Figure 10). These vesicles eventually fuse with the lysosome, which is highly acidic and filled with powerful proteases to break down any material contained inside.[56-57] The lysosome is generally capable of degrading organic nanoparticles and even rendering drugs inert.[58] If the nanoparticle can escape the endocytic vesicles during the endosomal phase, the lysosomal degradation of the carrier and drug may be avoided. Further, targeting of specific intracellular compartments including nucleus, mitochondria, cytoplasm using nanoparticles is very actively explored as the site of the action of various drugs are located in these precise organelles.[59-60]

Internalization of particles by cells is a complex process. There are some established thumb rules with respect to particle internalization into cells; particles >1 μm are internalized by phagocytosis and those between diameters of 0.2 μm and 1 μm are internalized by endocytosis (Figure 11). However, recent findings suggest that particles as large as 5 μm can be endocytosed through receptor mediated endocytosis.[46] The extent of internalization of particles depends on various parameters including surface chemistry, size and shape.[61] Among these, surface chemistry is the most studied parameter. Association of carriers with cell membranes depends extensively on surface hydrophobicity and charge. Hydrophobic particles are known to better associate with cell membranes, although such association is non-specific. The same is also true about surface charge. Positively charged particles have higher affinity with negatively charged cell membranes. In spite of their strong association with cell membranes, hydrophobic and positively charged particles are not actively used due to their non-specific association with cells.[26]

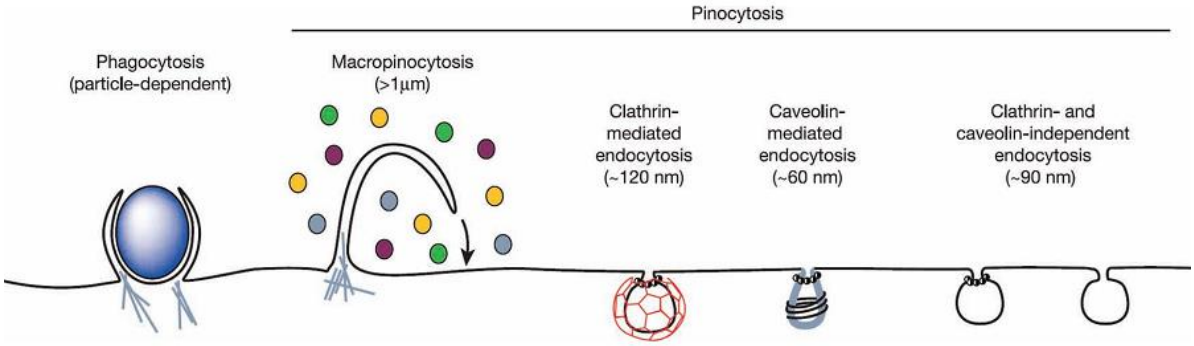

Figure 11: Entry pathways for mammalian cells. The endocytic pathways depend on the size of the endocytic vesicle, the nature of the cargo (ligands, receptors, and lipids) and the mechanism of vesicle formation. Adapted with permission from reference 41. Copyright 2003, Nature Publishing Group.

Shape of nanoparticles has also been engineered to enhance intracellular drug delivery. For example, needle shaped particles have been shown to enhance intracellular

delivery of siRNA compared to spherical particles due to shape-induced membrane permeation.[62-63] Rod shaped nanoparticles have been shown to exhibit enhanced intracellular uptake compared to spherical particles.[46] Particle geometry has been shown to influence the cellular uptake mechanisms of the drug carriers.[64] For a given duration of incubation with cells, silica cylindrical nanoparticles were internalized more compared to spherical and worm like silica nanoparticles in immortalized RAW 264.7 macrophages

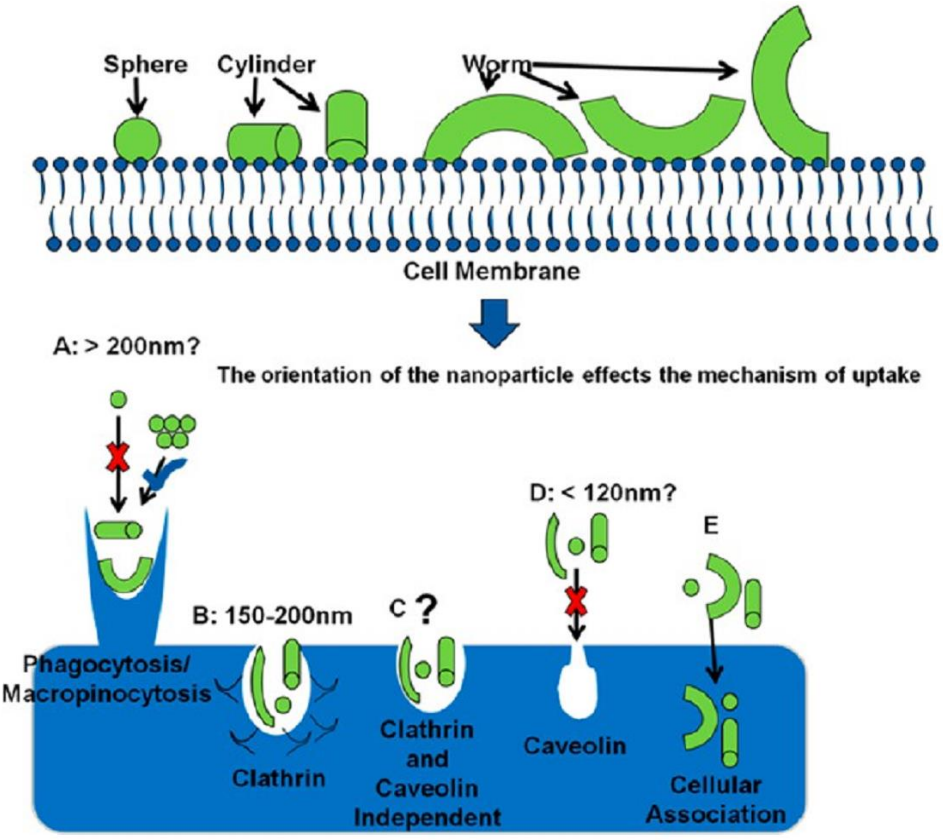

Figure 12: Cartoon depicting the hypothesis that the orientation of the nanoparticle influences the mechanism of uptake. (A) Macropinocytosis has been shown to occur at the microscale, fitting with one dimension of cylinders and worms. However, spheres, unless aggregated, do not fit this criterion. (B) Theoretically if oriented properly, all particles could be taken up via clathrin-mediated mechanisms. (C, E) Other mechanisms of uptake not readily identifiable are plausible. (D) Caveolin-mediated invaginations are theoretically much too small for the nanoparticle size range tested here. Adapted with permission from reference 64. Copyright 2013, American Chemical Society.

(Figure 12).[64] The uptake mechanisms operating for these silica particles were shown to be reliant on the way these varied shape particles orient themselves at the cell surface (Figure 12). Silica spheres have one dimension of approximately 200 nm, which may be expected to be within the size range of clathrin-mediated endocytosis, unless it clusters to form bigger size particles which may utilize phagocytosis/macropinocytosis pathways.[64] Worms and cylinders however had one dimension of approximately 200 nm, within the clathrin limits, and another dimension (~400 and 1300 nm) that was within the limits of macropinocytosis and phagocytosis.[64] Thus, it is possible that both the end of the particle and the longitudinal rotation of the particle could interact with the cell surface, effectively harnessing both mechanisms of uptake.[64]

1.3.2 Hybrid materials in drug delivery:

Hybrid nanomaterials are been extensively explored for drug delivery.[64-66] This is because these materials combine multiple functionality, which could perform diagnostics as well as therapeutic functions, in one component.[64-66] The hybrid delivery systems follow on the concept of a "theranostic" device, in which both diagnostic and therapeutic functions can be administered in a single dose.[67-71] The most relevant application of theranostic nanomedicines is their use for validating and optimizing the properties of drug delivery systems.[67-71] For theranostic systems, it can be non-invasively visualized that how well the carrier materials are able to deliver pharmacologically active agents to the pathological site, and how they are able to prevent them from accumulating in potentially endangered healthy tissues.[67-71] So, important information can be obtained for optimizing the basic properties of drug delivery systems, as well as for improving the balance between the efficacy and the toxicity of targeted therapeutic interventions.[67-71] Further,

using theranostics systems the pre-screening of the nanomedicine could be carried out for every individual.[67-71] To patients showing high levels of target site accumulations and responding well to the first couple of treatment cycles only the targeted therapy should be continued, and those who do not respond well to a particular therapy, other therapeutic options should be considered. Thus, development of theranostic nanomedicines could contribute substantially to realizing the potential of personalized medicine.[67-71]

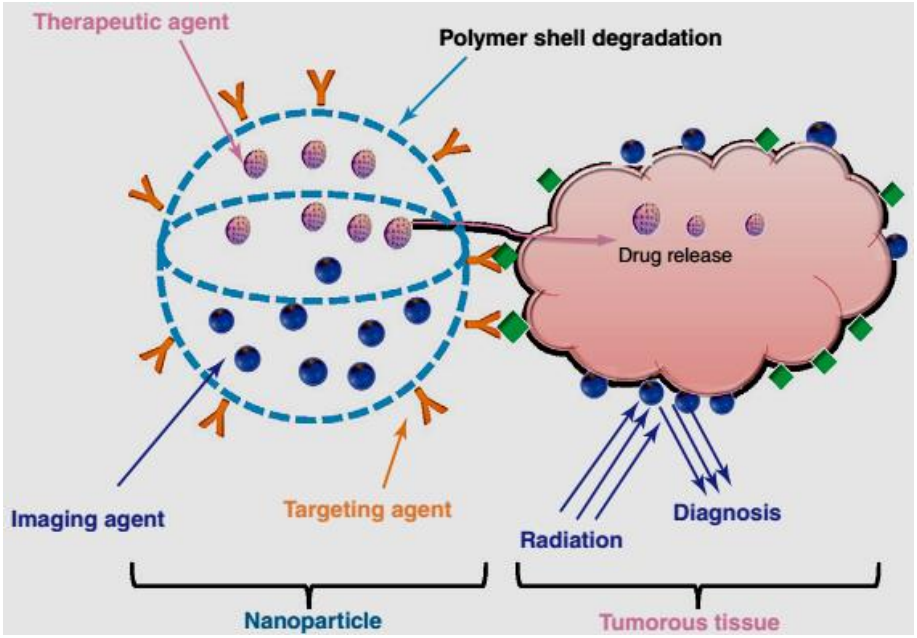

Figure 13: Schematic illustration of cancer theranostics (therapy and diagnosis) with nanoparticles. Adapted with permission from reference 69. Copyright 2012, Elsevier.

For example, Park and co-workers developed a liposomal system, in which anti-HER2 antibody and luminescent quantum dots were chemically linked to functional PEG groups on the liposome surface, and the interior of the liposomes contained a DOX payload (Figure 14).[71] The antibody was used to provide specific molecular targeting for the tumor site, quantum dots were used for imaging, and doxorubicin was a chemotherapeutic. The researchers were able to verify localization at tumor sites both in vitro and in vivo by observation of luminescence from the quantum dots. This study

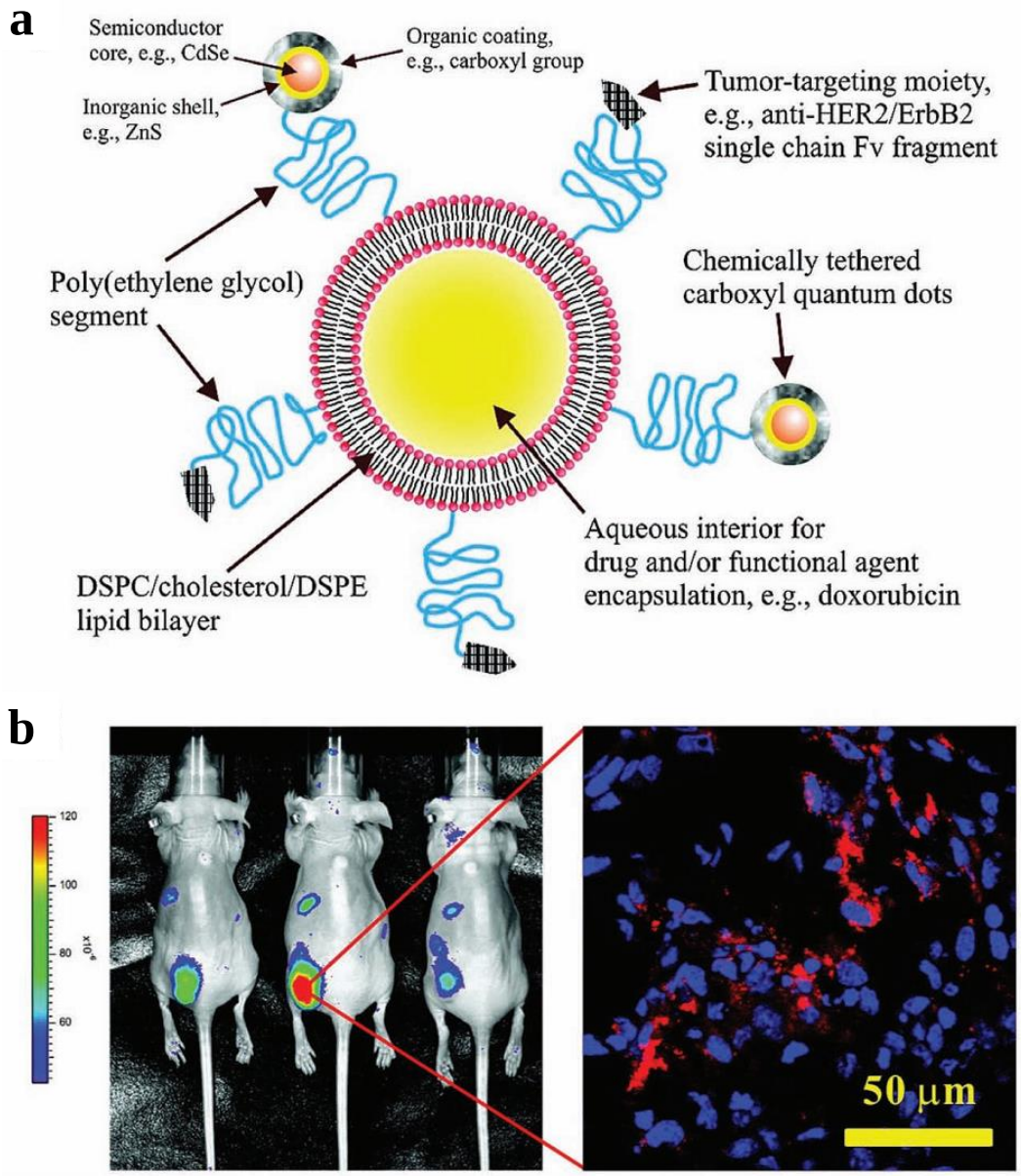

Figure 14. a) Schematic showing a liposomal hybrid nanoparticle containing antibody and quantum dot functionalities (QD-immunoliposomes). The pendant antibody provides a targeting capability, while the quantum dot exhibits bright photoluminescence to enable *in vivo* or *in vitro* imaging. b) (Left panel) *In vivo* fluorescence images of mice bearing MCF-7/HER2 xenograft tumors implanted in the lower back, 30 h after intravenous injection with QD-immunoliposomes. Fluorescence intensity is displayed in false colour; the high intensity at the tumor site demonstrates that the liposomes accumulate prominently in tumors. (Right panel) Confocal fluorescence image of a tumor slice from the mouse, 48 h post-injection. Red and blue indicate QD-immunoliposomes and cell nuclei (DAPI stain), respectively. The QD-immunoliposomes appear to internalize into the cytosol of MCF-7/HER2 tumor cells *in vivo*. Adapted with permission from reference 71. Copyright 2008, American Chemical Society.

demonstrated the feasibility of real-time observation of the dynamics of drug delivery to a targeted tumor site.

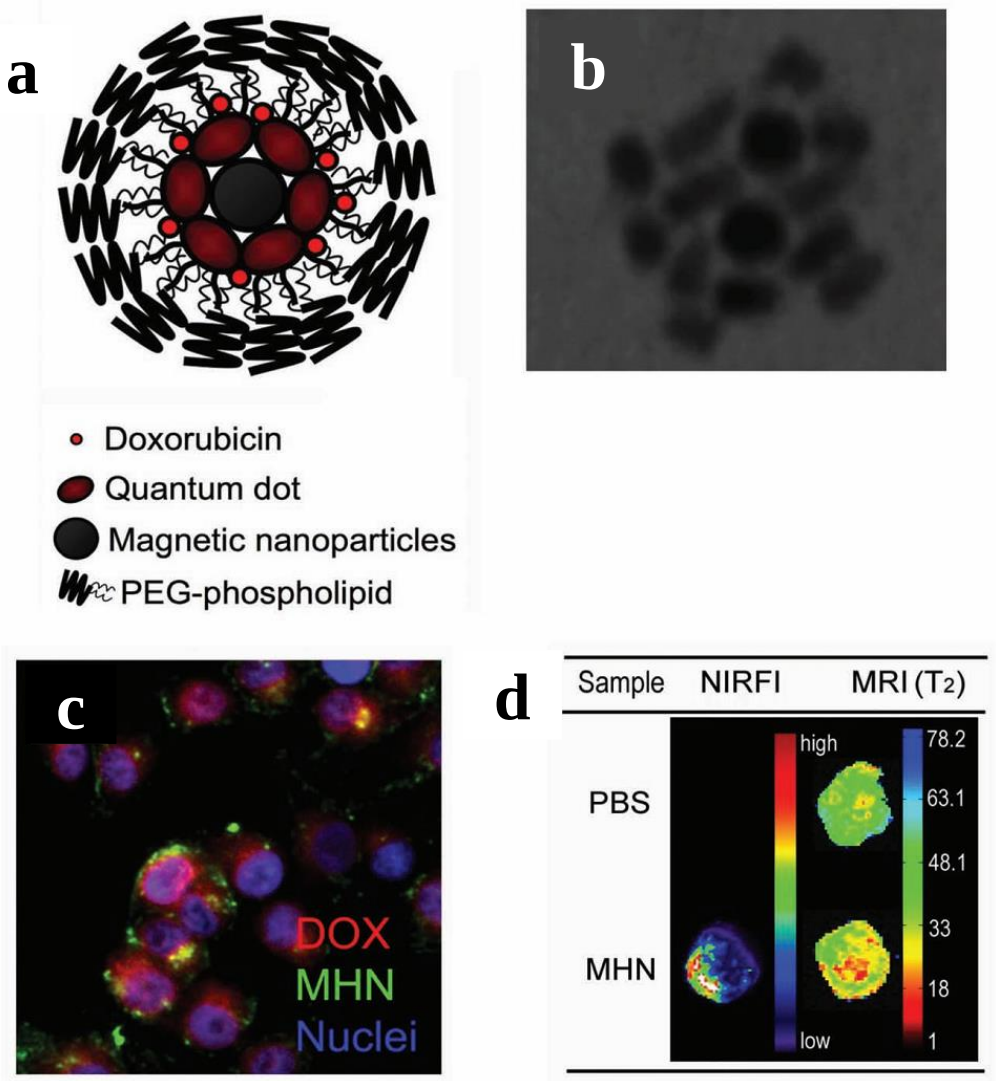

Figure 15: a) Schematic representation of micellar hybrid nanoparticles containing two different types of nanoparticles and a molecular drug. b) Transmission electron microscope (TEM) image of a micelle containing a mass ratio of 1 magnetic nanoparticle for every 3 quantum dots. In these formulations the quantum dots are elongated and the magnetic nanoparticles are spherical. c) Fluorescence microscope image showing targeted delivery of doxorubicin (DOX)-incorporated micelles to MDA-MB-435 human carcinoma cells. The micelles have peptide targeting groups attached to their surface. d) MRI and NIR fluorescence images of tumors harvested from mice 20 h after injection with the micellar nanostructures. Control is injection with phosphate buffered saline. Adapted with permission from reference 72. Copyright 2008, John Wiley and Sons.

Hybrid nanoparticles that contain magnetic nanocrystals, quantum dots and a molecular anti-cancer agent within a single poly(ethylene glycol)-phospholipid micelle (Figure 15) were synthesized.[72] The two different types of hydrophobic nanocrystals were incorporated with doxorubicin during synthesis, and their targeted delivery to tumor cells was demonstrated using a pendant targeting peptide. The dual-mode imaging (by MRI and fluorescence) of a xenografted tumor in a mouse was demonstrated. The work illustrated the ability to combine optical with magnetic resonance imaging, to obtain

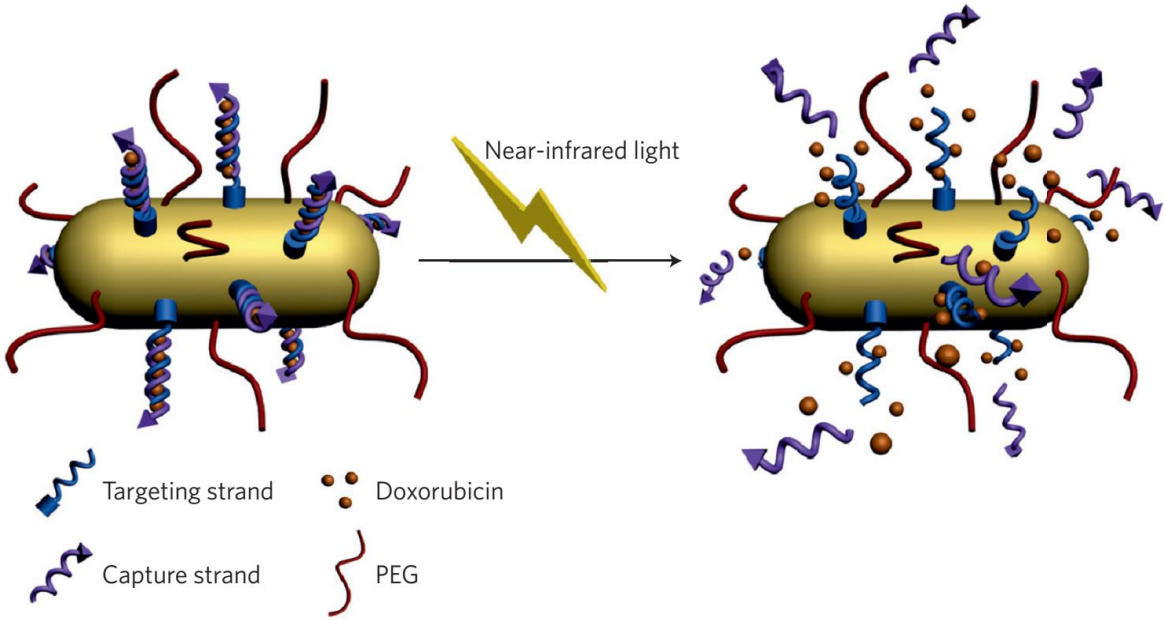

Figure 16: DNA assembly of a targeted, NIR-responsive delivery platform. This platform comprises gold NRs (50 nm x 10 nm), PEG layers, and complementary DNA oligonucleotides consisting of capture strands and targeting strands. Consecutive CG base pairs provide binding sites for doxorubicin (Dox) loading. The capture strands are conjugated to gold NRs for NIR response. The targeting strands are complementary to the capture strands and conjugated with ligands for molecular targeting. The delivery platform is assembled through the hybridization of capture strands attached on the NRs and targeting stands. The resulting double-stranded DNA structures form scaffolds for Dox intercalation. Upon NIR irradiation, the heated gold NRs result in DNA denaturation and the release of drugs (Dox) at the target site. Adapted with permission from reference 73. Copyright 2013, Nature Publishing Group.

microscopic resolution at the tumor site by fluorescence, and full anatomical distribution by MRI.

Stimuli-responsive hybrid materials which in response to a specific stimulus (exogenous or endogenous), undergo a protonation, a hydrolytic cleavage or a (supra)molecular conformational change and deliver its payload drug in spatial-, temporal- and dose-controlled fashions are very promising.[73] This is because, on-demand drug delivery is becoming feasible through the design of stimuli-responsive systems that recognize their microenvironment and react in a dynamic way, mimicking the responsiveness of living organisms.[73] For example, light-to heat transduction mediated by NIR irradiation of gold nanorods caused a rapid rise in the local temperature, which was exploited to induce dehybridization of DNA helices conjugated at the gold surface, allowing the release of doxorubicin molecules bound to consecutive cytosine–guanine base pairs (Figure 16).[74]

1.3.3 Hybrid materials in catalysis:

Hybrid materials find applications as heterogeneous-, homogeneous-, photo-, electro-, and bio-catalysts for various reactions.[75-78] This is because making hybrids impart stability, higher activity, and multi-functionality to the catalysts.[75-78] Metal nanoparticles having high surface area or higher surface atoms, show improved catalytic activity which could be tuned by varying their size, shape, and the surface properties.[79-80] However, owing to their high surface energy, nanoparticles tend to rapidly sinter into larger clusters, especially under the conditions typically used in heterogeneous catalysis.[76] This sintering process leads to the reduction of the active surface area, and also to the loss of the unique properties of the nanostructured catalysts.[76] Making intelligent hybrids of

catalytically active nanoparticles with their supports were shown to improve the catalyst stability.[76] For example, catalyst in which platinum nanoparticles of size 2-3 nm were dispersed on the surface of ~100-nm-diameter silica beads, when calcined at 1075 K, the Pt nanoparticles were seen to sinter into a few large crystalline particles ~10-20 nm in

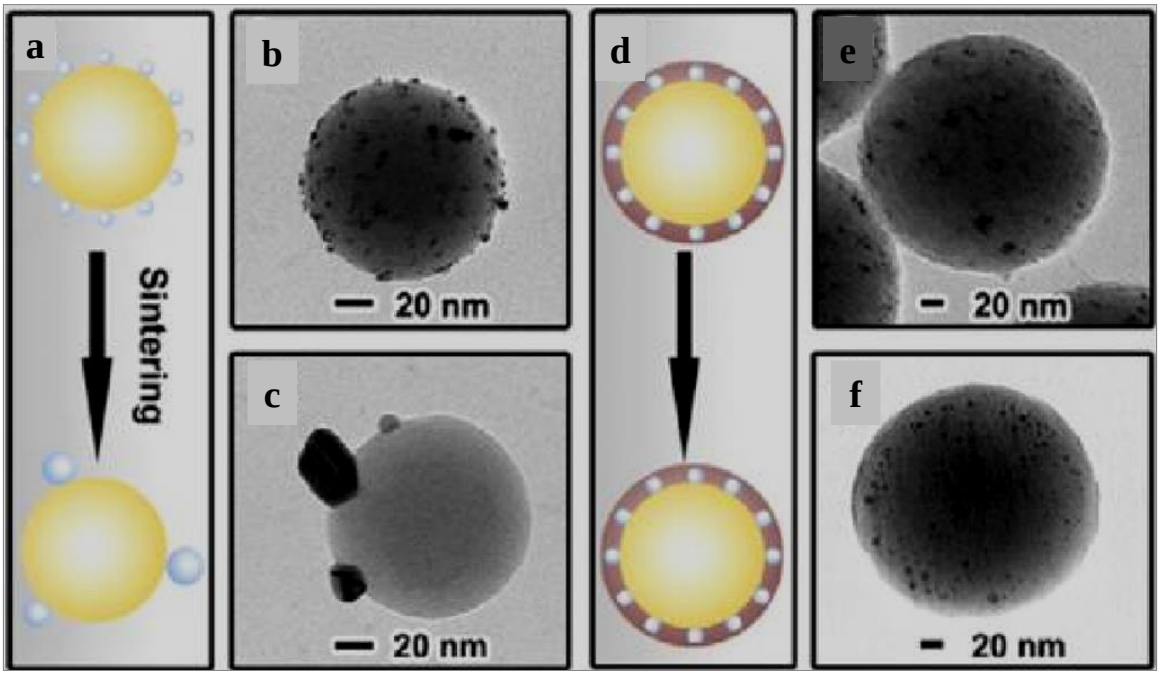

Figure 17: Illustration of the use of mesoporous silica layers for protection against sintering of dispersed metal nanoparticles. As shown schematically in panel (a), the original small Pt nanoparticles supported on SiO_2 beads (panel (b)) coalesce into a few larger structures (panel (c)) upon calcination at 1075 K. The corresponding TEM images from a catalyst coated with a mesoporous SiO2shell, shown in panels (e) and (f), prove the enhanced stability afforded by such treatment (panel (d)). Adapted with permission from reference 76. Copyright 2012, American Chemical Society.

size (Figure 17b,c).[81] A thin layer of silica deposited on the original silica-bead/Pt catalyst however, prevents the sintering of Pt nanoparticles and forms a core-shell structure (Figure 17).[81] As shown in the images in Figure 17e and f, this treatment completely suppresses sintering of the metal nanoparticles.

Yin *et.al.* prepared core-shell hybrid catalyst in which ~15 nm gold particles were coated with silica shell.[82] The silica shell was then etched with NaOH using a surface protected (with PVP, poly(vinyl pyrrolidone)) etching method. The extent of etching could be controlled by varying duration of NaOH etching which in turn resulted in tunable porosity of the silica shell. The size of the hybrid nanocatalysts was around 150 nm. The catalytic property of the Au-encapsulated catalyst was tested for the catalyzed reduction of 4-nitrophenol (4-NP) by $NaBH_4$.[82] The non-etched SiO_2 shells were proven to be impenetrable by 4-NP, as no measurable catalytic activity was detected (Figure 18).

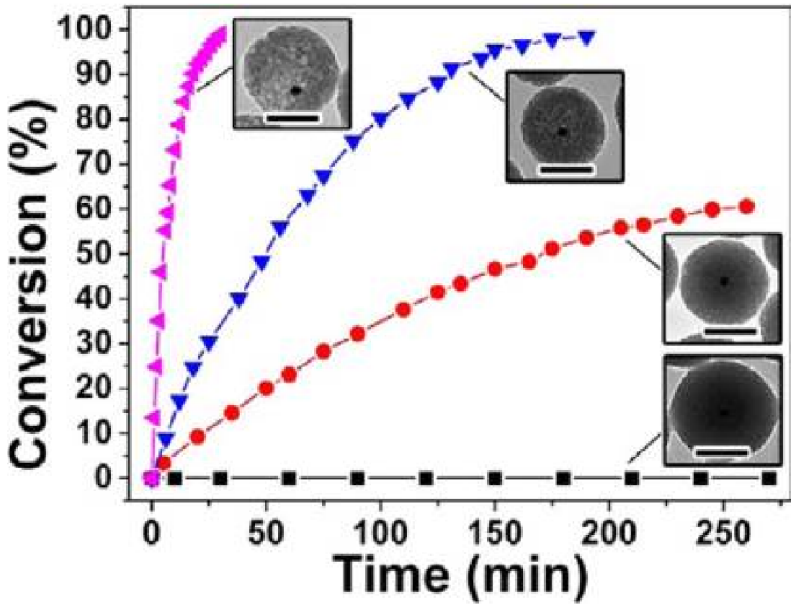

Figure 18: Conversion of 4-NP promoted by Au@SiO2 catalysts which were prepared by etching for different period of time: 0 min (black square); 90 min (red circle); 150 min (blue down-pointing triangle); and 180 min (pink left-pointing triangle). The corresponding TEM images show different porosities of the as-prepared product. All scale bars are 100 nm. Adapted with permission from reference 76. Copyright 2012, American Chemical Society.

However, by using our surface-protected etching process, the size of the pores in the silica shell could be increased systematically (from ~1.5 nm after 10 min of etching to a wide distribution of pores with diameters well in excess of ~15 nm after 180 min of

etching), to allow for the 4-NP molecules to access the center of the nanostructures and increase the catalytic performance. Indeed, as shown in Figure 18, the catalytic activity was observed to increase consistently in these nanocatalyst systems with increased etching time. Importantly, BET measurements indicated comparable surface areas for all samples etched more than 10 min (between approximately 220 and 270 m^2g^{-1}).

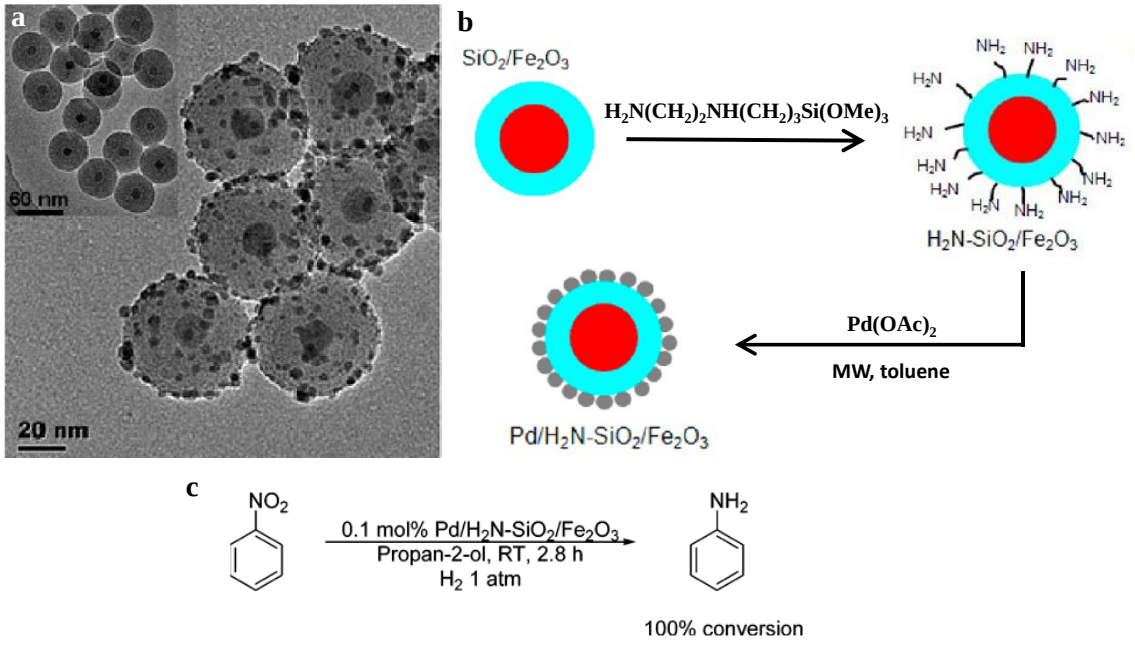

Figure 19: a) TEM micrographs of as-prepared SiO_2/Fe_2O_3 (left inset), Pd/HS-SiO_2/Fe_2O_3 (left), and Pd/H_2N-SiO_2/Fe_2O_3 (right). b) Synthesis of Pd/SiO_2/Fe_2O_3 nanocomposites and c) chemical equation for the reduction of 4-NP with alcohol. Adapted with permission from reference 78. Copyright 2012, American Chemical Society.

Further making hybrids nanocatalysts could bring new properties to the catalyst system. For example, Magnetic nanocomposites can serve as an effective support for the immobilization of active catalysts.[83] The efficient recovery of the catalyst by magnetic separation would further enhance the recovery and reuse of these nanocomposites and their attractiveness as green catalysts.[83] SiO_2/Fe_2O_3 (γ-Fe_2O_3) nanocomposites were used

as a magnetic catalyst support whereby Pd nanoclusters were deposited in high dispersion and stability to synthesize the catalyst for the hydrogenation reaction of nitrobenzene (Figure 19). The excellent reactivity and recyclability of the $Pd/H_2N\text{-}SiO_2/Fe_2O_3$ (99% yield over 6 runs) was due to the amine ligands on SiO_2/Fe_2O_3, which suppressed the agglomeration of Pd nanoclusters during the hydrogenation reaction.

Using semiconducting materials as support for dispersing active metal phase gives rise to catalysts with improved catalytic performance.[78] For these hybrid catalysts, the semiconductor can either withdraw electrons from or donate electrons to the metal nanoparticles.[78] The resulting positively or negatively charged metal nanoparticles can then catalyze different organic transformations.[78] Mitsudome *et al.* have exploited Au and silver (Ag) nanoparticles supported on hydrotalcite (HT, a layered double hydroxide clay) as highly active catalysts for the deoxygenation of epoxides to alkenes using alcohol as a reductant.[84] Excellent selectivities (of >99%) and turnover numbers (up to 20 000) were achieved. Based on their experimental results, the authors proposed that the basic support hydrotalcite promoted the deoxygenation of epoxides by providing the basic sites required for the oxidation of alcohols to produce metal hydride ($[H\text{-}Au]^-$ or $[H\text{-}Ag]^-$) and protonated hydrotalcite ($[H\text{-}HT]^+$) species. Protonation of the epoxide with the $[H\text{-}HT]^+$ species, and subsequent reduction by the metal hydride species, followed by dehydration would provide the desired alkene product. Semiconductor metal oxide based nanomaterials can also serve as a support, providing either basic or acidic sites in close proximity to the active metal nanoparticles. The synergism between the active metal nanoparticles and the basic or acidic support would then catalyze organic reactions. Wang et al. have used a supported Au/MoO_x heterogeneous catalyst for the aerobic oxidation of

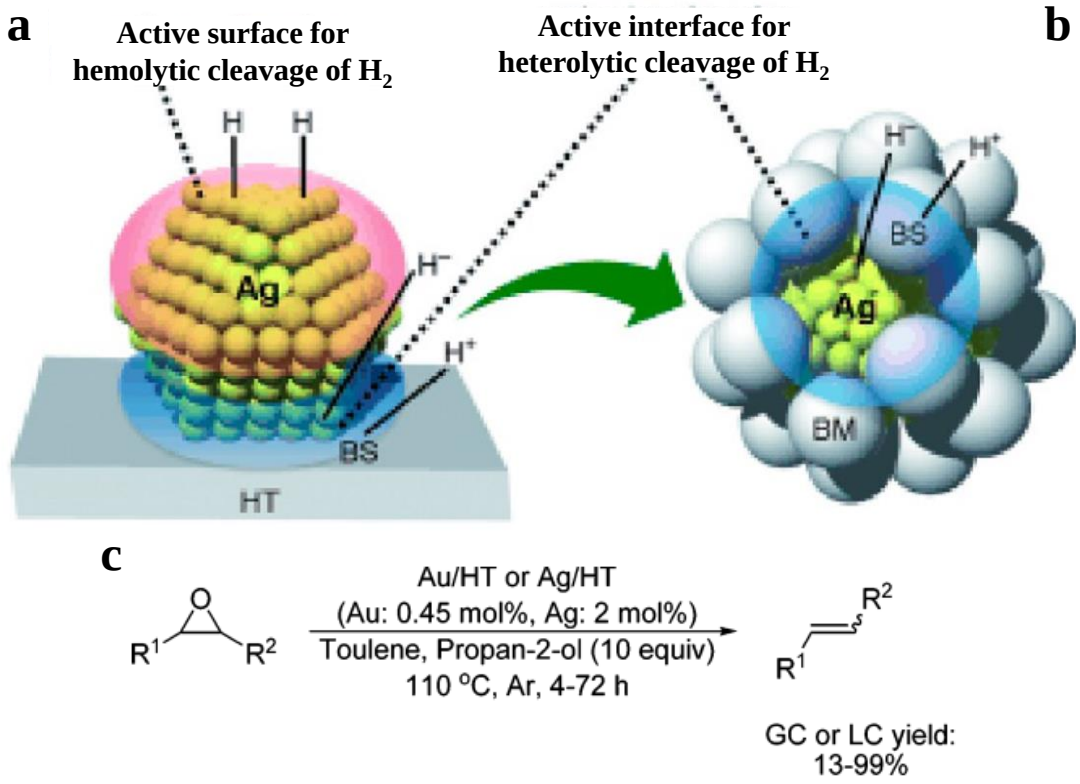

Figure 20: Catalyst design of core-shell nanocomposite for chemoselective reductions with H_2. a) Representation of Ag/HT reacting with H_2; both polar and nonpolar hydrogen species are formed. b) Representation of AgNPs@BM; AgNPs are covered with a basic material (BM), which reacts with H_2 at a basic site (BS) to result in the exclusive formation of polar hydrogen species. c) chemical equation for the reduction. Adapted with permission from reference 78. Copyright 2012, American Chemical Society.

alcohols to aldehydes in high yields. In their study, the authors confirmed that electron transfer from the partially reduced MoO_x support to the Au nanoparticles would result in negatively charged Au cores, yielding highly active catalysts for the selective aerobic oxidation of alcohols.

1.4 Carbonaceous and layered materials in drug delivery and catalysis:

Nanocarbons, or carbon-based nanomaterials including fullerenes, carbon nanoparticles, carbon nanotubes (CNTs), graphene, and nano-diamonds (NDs), have attracted particular interest in biomedicine.[85-87] This is because of their outstanding physicochemical properties.[85-87] For example, many nano-carbons, including CNTs, graphene derivatives, carbon dots, and NDs, show inherent fluorescence, absorption *etc.* making them useful contrast agents in optical imaging and sensing.[88-92] CNTs and graphene derivatives with strong optical absorbance in the near-infrared region are also useful for photothermal ablation of cancer.[89-90] Compared with many other inorganic nanomaterials such as quantum dots (QDs) which usually contain heavy metals, nano-carbons are relatively safe at least in term of elementary composition.[87] On the other hand, due to their easy synthesis, versatility, biodegradability and biocompatibility, the layered clay materials are especially attractive towards biomedical applications such as drug delivery and diagnostics.[93-96] This is because the clay materials can accommodate polar and non-polar (modified clays) organic compounds between their layers and form a variety of intercalated compounds which releases the drugs in potentially controllable manner.[94,95]

Layered materials such as anionic clays, pillared clays, layered perovskite, carbon nitride, graphene, *etc.* have been attractive candidates for applications in catalysis.[97-105] This is due their low cost, larger specific surface areas, and presence of acid/base sites on their surface which could act as catalytic sites or strongly interact and influence the active catalyst phase. For example, clays or clay-modified catalysts (in particular acid treated clays) are commercially used catalysts.[97] Acid-treated montmorillonites are offered from

various companies as catalysts for hydrocarbon cracking.[106] Kaolinites are quite good catalysts for Diels–Alders reactions.[106] They are also excellent supports for Lewis acids ($ZnCl_2$, in particular) or for transition metals (copper and iron, in particular), to be applied in various organic reactions (Friedel–Crafts, acylation and alkylation of aromatics, etc.).[107,108] Depending on the metal, the Brönsted versus Lewis acidity can be tuned, to obtain a family of catalysts. Also, it has been shown that by intercalating, the layered materials show improved stability of the active catalyst phase during the reactions.[97]

Clearly, carbonaceous and layered materials are promising candidates for drug delivery and catalysis due to their intriguing physicochemical properties. In the present thesis, we have fabricated a number of carbonaceous and layered material based hybrids and explored their potential towards drug delivery and catalysis.

1.5 Conclusions:

Functional hybrid organic- (bio-) inorganic materials truly represent a multidisciplinary area of research which stands at the cross-roads of inorganic chemistry, polymer chemistry, organic chemistry, and biology. The high versatility with regard to shaping, and chemical and physical properties, hybrid nanocomposites are very promising class of materials. A multitude of functional hybrid materials spanning over a large set of structures, textures and chemical compositions have be synthesized and their apt applications have been discussed. Functional hybrids are extremely talented candidates for theranostics and efficient and stable catalysis. However, a range of hybrids, for a specific purpose, needs to be synthesized and validated for their utility and success for the precise goal.

1.6 References:

1. Kickelbick G., Hybrid Materials: Synthesis, Characterization and Application. Wiley-VCH: Weinheim, Germany, **2007**.
2. Gómez-Romero P.; Sanchez C., Functional Hybrid Materials. Wiley-VCH: Weinheim, Germany, **2004**.
3. Sanchez, C.; Julian, B.; Belleville, P.; Popall, M., Applications of hybrid organic-inorganic nanocomposites. *J. Mater. Chem.* **2005,** *15*, 3559-3592.
4. Sanchez, C.; Boissiere, C.; Cassaignon, S.; Chaneac, C.; Durupthy, O.; Faustini, M.; Grosso, D.; Laberty-Robert, C.; Nicole, L.; Portehault, D.; Ribot, F.; Rozes, L.; Sassoye, C., Molecular Engineering of Functional Inorganic and Hybrid Materials. *Chem. Mater.* **2014,** *26*, 221-238.
5. Sanchez, C.; Belleville, P.; Popall, M.; Nicole, L., Applications of advanced hybrid organic-inorganic nanomaterials: from laboratory to market. *Chem. Soc. Rev.* **2011,** *40*, 696-753.
6. Drisko, G. L.; Sanchez, C., Hybridization in Materials Science – Evolution, Current State, and Future Aspirations. *Eur. J. Inorg. Chem.* **2012,** 5097-5105.
7. Mehdi, A.; Reye, C.; Corriu, R., From molecular chemistry to hybrid nanomaterials. Design and functionalization. *Chem. Soc. Rev.* **2011,** *40*, 563-574.
8. Mann S., Biomineralization: principles and concepts in bioinorganic materials chemistry, Oxford University Press, New York, **2001**.
9. Allen, T. M.; Cullis, P. R., Drug Delivery Systems: Entering the Mainstream. *Science* **2004,** *303*, 1818-1822.
10. Bourzac, K., Nanotechnology: Carrying drugs. *Nature* **2012,** *491*, S58-S60.

11. Doane, T. L.; Burda, C., The unique role of nanoparticles in nanomedicine: imaging, drug delivery and therapy. *Chem. Soc. Rev.* **2012,** *41*, 2885-2911.
12. Farokhzad, O. C.; Langer, R., Impact of Nanotechnology on Drug Delivery. *ACS Nano* **2009,** *3*, 16-20.
13. Hubbell, J. A.; Chilkoti, A., Nanomaterials for Drug Delivery. *Science* **2012,** *337*, 303-305.
14. Sun, T.; Zhang, Y. S.; Pang, B.; Hyun, D. C.; Yang, M.; Xia, Y., Engineered Nanoparticles for Drug Delivery in Cancer Therapy. *Angew. Chem. Int. Ed.* **2014,** *53*, 12320-12364.
15. Anselmo, A. C.; Mitragotri, S., An overview of clinical and commercial impact of drug delivery systems. *J. Contr. Release* **2014,** *190*, 15-28.
16. Duncan, R.; Gaspar, R., Nanomedicine(s) under the Microscope. *Mol. Phar.* **2011,** *8*, 2101-2141.
17. Fu, A.; Tang, R.; Hardie, J.; Farkas, M. E.; Rotello, V. M., Promises and Pitfalls of Intracellular Delivery of Proteins. *Biocon. Chem.* **2014,** *25*, 1602-1608.
18. Juliano, R., Nanomedicine: is the wave cresting? *Nat. Rev. Drug Discov.* **2013,** *12*, 171-172.
19. Venditto, V. J.; Szoka Jr, F. C., Cancer nanomedicines: So many papers and so few drugs! *Adv. Drug Delivery Rev.* **2013,** *65*, 80-88.
20. Hauert, S.; Bhatia, S. N., Mechanisms of cooperation in cancer nanomedicine: towards systems nanotechnology. *Trends in Biotechnology* **2014,** *32*, 448-455.
21. Nichols, J. W.; Bae, Y. H., Odyssey of a cancer nanoparticle: From injection site to site of action. *Nano Today* **2012,** *7*, 606-618.

22. Babiuch, K.; Gottschaldt, M.; Werz, O.; Schubert, U. S., Particulate transepithelial drug carriers: barriers and functional polymers. *RSC Advances* **2012,** *2*, 10427-10465.
23. Bertrand, N.; Leroux, J.-C., The journey of a drug-carrier in the body: An anatomo-physiological perspective. *J. Contr. Release* **2012,** *161*, 152-163.
24. http://en.wikipedia.org/wiki/Systemic_administration.
25. Mitragotri, S.; Lahann, J., Materials for Drug Delivery: Innovative Solutions to Address Complex Biological Hurdles. *Adv. Mater.* **2012,** *24*, 3717-3723.
26. Barua, S.; Mitragotri, S., Challenges associated with penetration of nanoparticles across cell and tissue barriers: A review of current status and future prospects. *Nano Today* **2014,** *9*, 223-243.
27. Lai, S. K.; O'Hanlon, D. E.; Harrold, S.; Man, S. T.; Wang, Y.-Y.; Cone, R.; Hanes, J., Rapid transport of large polymeric nanoparticles in fresh undiluted human mucus. *Proc. Natl. Acad. Sci. U.S.A* **2007,** *104*, 1482-1487.
28. Xie, X.; Tao, Q.; Zou, Y.; Zhang, F.; Guo, M.; Wang, Y.; Wang, H.; Zhou, Q.; Yu, S., PLGA Nanoparticles Improve the Oral Bioavailability of Curcumin in Rats: Characterizations and Mechanisms. *J. Agricul. Food Chem.* **2011,** *59*, 9280-9289.
29. Osada, K.; Christie, R. J.; Kataoka, K., Polymeric micelles from poly(ethylene glycol)–poly(amino acid) block copolymer for drug and gene delivery. *J. Royal Soc. Inter.* **2009,** *6*, S325–S339.
30. Wang, B.; He, X.; Zhang, Z.; Zhao, Y.; Feng, W., Metabolism of Nanomaterials in Vivo: Blood Circulation and Organ Clearance. *Acc. Chem. Res.* **2013,** *46*, 761-769.

31. Monopoli, M. P.; Aberg, C.; Salvati, A.; Dawson, K. A., Biomolecular coronas provide the biological identity of nanosized materials. *Nat. Nanotech.* **2012,** *7*, 779-786.

32. Nel, A. E.; Madler, L.; Velegol, D.; Xia, T.; Hoek, E. M. V.; Somasundaran, P.; Klaessig, F.; Castranova, V.; Thompson, M., Understanding biophysicochemical interactions at the nano-bio interface. *Nat. Mater.* **2009,** *8*, 543-557.

33. Koo, H.; Huh, M. S.; Sun, I.-C.; Yuk, S. H.; Choi, K.; Kim, K.; Kwon, I. C., In Vivo Targeted Delivery of Nanoparticles for Theranosis. *Acc. Chem. Res.* **2011,** *44*, 1018-1028.

34. Ding, H.; Wu, F.; Nair, M. P., Image-guided drug delivery to the brain using nanotechnology. *Drug Discov. Today* **2013,** *18*, 1074-1080.

35. Goldsmith, M.; Abramovitz, L.; Peer, D., Precision Nanomedicine in Neurodegenerative Diseases. *ACS Nano* **2014,** *8*, 1958-1965.

36. Kozlovskaya, L.; Stepensky, D., Quantitative analysis of the brain-targeted delivery of drugs and model compounds using nano-delivery systems. *J. Contr. Release* **2013,** *171*, 17-23.

37. Krol, S., Challenges in drug delivery to the brain: Nature is against us. *J. Contr. Release* **2012,** *164*, 145-155.

38. Chen, Y.; Liu, L., Modern methods for delivery of drugs across the blood–brain barrier. *Adv. Drug Delivery Rev.* **2012,** *64*, 640-665.

39. Longmire, M.; Choyke, P. L.; Kobayashi, H., Clearance properties of nano-sized particles and molecules as imaging agents: considerations and caveats. *Nanomedicine* **2008,** *3*, 703-717.

40. Petros, R. A.; DeSimone, J. M., Strategies in the design of nanoparticles for therapeutic applications. *Nat. Rev. Drug. Discov.* **2010,** *9*, 615-627.

41. Conner, S. D.; Schmid, S. L., Regulated portals of entry into the cell. *Nature* **2003,** *422*, 37-44.

42. Duan, X.; Li, Y., Physicochemical Characteristics of Nanoparticles Affect Circulation, Biodistribution, Cellular Internalization, and Trafficking. *Small* **2013,** *9*, 1521-1532.

43. Albanese, A.; Tang, P. S.; Chan, W. C. W., The Effect of Nanoparticle Size, Shape, and Surface Chemistry on Biological Systems. *Ann. Rev. Biomed. Eng.* **2012,** *14*, 1-16.

44. Zhu, M.; Nie, G.; Meng, H.; Xia, T.; Nel, A.; Zhao, Y., Physicochemical Properties Determine Nanomaterial Cellular Uptake, Transport, and Fate. *Acc. Chem. Res.* **2013,** *46*, 622-631.

45. Sahay, G.; Alakhova, D. Y.; Kabanov, A. V., Endocytosis of nanomedicines. *J. Contr. Release* **2010,** *145*, 182-195.

46. Gratton, S. E. A.; Ropp, P. A.; Pohlhaus, P. D.; Luft, J. C.; Madden, V. J.; Napier, M. E.; DeSimone, J. M., The effect of particle design on cellular internalization pathways. *Proc. Natl. Acad. Sci. U.S.A* **2008,** *105*, 11613-11618.

47. Alexis, F.; Pridgen, E.; Molnar, L. K.; Farokhzad, O. C., Factors Affecting the Clearance and Biodistribution of Polymeric Nanoparticles. *Mol. Phar.* **2008,** *5*, 505-515.

48. Koo, H.; Huh, M. S.; Sun, I.-C.; Yuk, S. H.; Choi, K.; Kim, K.; Kwon, I. C., In Vivo Targeted Delivery of Nanoparticles for Theranosis. *Acc. Chem. Res.* **2011,** *44*, 1018-1028.

49. Jain, R. K.; Stylianopoulos, T., Delivering nanomedicine to solid tumors. *Nat. Rev. Clin. Oncol.* **2010,** *7*, 653-664.

50. Jain, R. K., Transport of Molecules in the Tumor Interstitium: A Review. *Cancer Res.* **1987,** *47*, 3039-3051.

51. Stylianopoulos, T.; Poh, M.-Z.; Insin, N.; Bawendi, M. G.; Fukumura, D.; Munn, Lance L.; Jain, R. K., Diffusion of Particles in the Extracellular Matrix: The Effect of Repulsive Electrostatic Interactions. *Biophysical Journal* **2010,** *99*, 1342-1349.

52. Pluen, A.; Boucher, Y.; Ramanujan, S.; McKee, T. D.; Gohongi, T.; di Tomaso, E.; Brown, E. B.; Izumi, Y.; Campbell, R. B.; Berk, D. A.; Jain, R. K., Role of tumor–host interactions in interstitial diffusion of macromolecules: Cranial vs. subcutaneous tumors. *Proc. Natl. Acad. Sci. U.S.A* **2001,** *98*, 4628-4633.

53. Chauhan, V. P.; Popović, Z.; Chen, O.; Cui, J.; Fukumura, D.; Bawendi, M. G.; Jain, R. K., Fluorescent Nanorods and Nanospheres for Real-Time In Vivo Probing of Nanoparticle Shape-Dependent Tumor Penetration. *Angew. Chem. Int. Ed.* **2011,** *123*, 11619-11622.

54. Wong, C.; Stylianopoulos, T.; Cui, J.; Martin, J.; Chauhan, V. P.; Jiang, W.; Popović, Z.; Jain, R. K.; Bawendi, M. G.; Fukumura, D., Multistage nanoparticle delivery system for deep penetration into tumor tissue. *Proc. Natl. Acad. Sci. U.S.A* **2011,** *108*, 2426-2431.

55. Barua, S.; Yoo, J.-W.; Kolhar, P.; Wakankar, A.; Gokarn, Y. R.; Mitragotri, S., Particle shape enhances specificity of antibody-displaying nanoparticles. *Proc. Natl. Acad. Sci. U.S.A* **2013,** *110*, 3270-3275.

56. Eskelinen, E.-L.; Tanaka, Y.; Saftig, P., At the acidic edge: emerging functions for lysosomal membrane proteins. *Trends in Cell Biology* **2003,** *13*, 137-145.

57. Panyam, J.; Zhou, W.-Z.; Prabha, S.; Sahoo, S. K.; Labhasetwar, V., Rapid endo-lysosomal escape of poly(dl-lactide-co-glycolide) nanoparticles: implications for drug and gene delivery. *The FASEB Journal* **2002,** *16*, 1217-1226.

58. Akinc, A.; Thomas, M.; Klibanov, A. M.; Langer, R., Exploring polyethylenimine-mediated DNA transfection and the proton sponge hypothesis. *J. Gene Medicine* **2005,** *7*, 657-663.

59. Sakhrani, N. M.; Padh, H., Organelle targeting: third level of drug targeting. *Drug Design, Development and Therapy* **2013,** *7*, 585-599.

60. Rajendran, L.; Knolker, H.-J.; Simons, K., Subcellular targeting strategies for drug design and delivery. *Nat. Rev. Drug. Discov.* **2010,** *9*, 29-42.

61. Perry, J. L.; Herlihy, K. P.; Napier, M. E.; DeSimone, J. M., PRINT: A Novel Platform Toward Shape and Size Specific Nanoparticle Theranostics. *Acc. Chem. Res.* **2011,** *44*, 990-998.

62. Doshi, N.; Mitragotri, S., *Needle-shaped polymeric particles induce transient disruption of cell membranes*. *J. Royal Soc. Inter.* **2010**, 1-8.

63. Kolhar, P.; Doshi, N.; Mitragotri, S., Polymer Nanoneedle-Mediated Intracellular Drug Delivery. *Small* **2011,** *7*, 2094-2100.

64. Herd, H.; Daum, N.; Jones, A. T.; Huwer, H.; Ghandehari, H.; Lehr, C.-M., Nanoparticle Geometry and Surface Orientation Influence Mode of Cellular Uptake. *ACS Nano* **2013,** *7*, 1961-1973.

65. Cheng, Z.; Al Zaki, A.; Hui, J. Z.; Muzykantov, V. R.; Tsourkas, A., Multifunctional Nanoparticles: Cost Versus Benefit of Adding Targeting and Imaging Capabilities. *Science* **2012,** *338*, 903-910.

66. Sailor, M. J.; Park, J.-H., Hybrid Nanoparticles for Detection and Treatment of Cancer. *Adv. Mater.* **2012,** *24*, 3779-3802.

67. Ahmed, N.; Fessi, H.; Elaissari, A., Theranostic applications of nanoparticles in cancer. *Drug Discov. Today* **2012,** *17*, 928-934.

68. Lammers, T.; Aime, S.; Hennink, W. E.; Storm, G.; Kiessling, F., Theranostic Nanomedicine. *Acc. Chem. Res.* **2011,** *44*, 1029-1038.

69. Ma, X.; Zhao, Y.; Liang, X.-J., Theranostic Nanoparticles Engineered for Clinic and Pharmaceutics. *Acc. Chem. Res.* **2011,** *44*, 1114-1122.

70. Rizzo, L. Y.; Theek, B.; Storm, G.; Kiessling, F.; Lammers, T., Recent progress in nanomedicine: therapeutic, diagnostic and theranostic applications. *Curr. Opi. Biotech.* **2013,** *24*, 1159-1166.

71. Weng, K. C.; Noble, C. O.; Papahadjopoulos-Sternberg, B.; Chen, F. F.; Drummond, D. C.; Kirpotin, D. B.; Wang, D.; Hom, Y. K.; Hann, B.; Park, J. W., Targeted Tumor Cell Internalization and Imaging of Multifunctional Quantum Dot-Conjugated Immunoliposomes in Vitro and in Vivo. *Nano Lett.* **2008,** *8*, 2851-2857.

72. Park, J.-H.; von Maltzahn, G.; Ruoslahti, E.; Bhatia, S. N.; Sailor, M. J., Micellar Hybrid Nanoparticles for Simultaneous Magnetofluorescent Imaging and Drug Delivery. *Angew. Chem. Int. Ed.* **2008,** *120*, 7394-7398.

73. Mura, S.; Nicolas, J.; Couvreur, P., Stimuli-responsive nanocarriers for drug delivery. *Nat. Mater.* **2013,** *12*, 991-1003.

74. Xiao, Z.; Ji, C.; Shi, J.; Pridgen, E. M.; Frieder, J.; Wu, J.; Farokhzad, O. C., DNA Self-Assembly of Targeted Near-Infrared-Responsive Gold Nanoparticles for Cancer Thermo-Chemotherapy. *Angew. Chem. Int. Ed.* **2012,** *124*, 12023-12027.

75. Diaz, U.; Brunel, D.; Corma, A., Catalysis using multifunctional organosiliceous hybrid materials. *Chem. Soc. Rev.* **2013,** *42*, 4083-4097.

76. Chng, L. L.; Erathodiyil, N.; Ying, J. Y., Nanostructured Catalysts for Organic Transformations. *Acc. Chem. Res.* **2013,** *46*, 1825-1837.

77. Foo, M. L.; Matsuda, R.; Kitagawa, S., Functional Hybrid Porous Coordination Polymers. *Chem. Mater.* **2014,** *26*, 310-322.

78. Zhang, Q.; Lee, I.; Joo, J. B.; Zaera, F.; Yin, Y., Core–Shell Nanostructured Catalysts. *Acc. Chem. Res.* **2013,** *46*, 1816-1824.

79. Grunes, J.; Zhu, J.; Somorjai, G. A., Catalysis and nanoscience. *Chem. Comm.* **2003,** 2257-2260.

80. Bell, A. T., The Impact of Nanoscience on Heterogeneous Catalysis. *Science* **2003,** *299*, 1688-1691.

81. Lee, I.; Zhang, Q.; Ge, J.; Yin, Y.; Zaera, F., Encapsulation of supported Pt nanoparticles with mesoporous silica for increased catalyst stability. *Nano Res.* **2011,** *4*, 115-123.

82. Zhang, Q.; Zhang, T.; Ge, J.; Yin, Y., Permeable Silica Shell through Surface-Protected Etching. *Nano Lett.* **2008,** *8*, 2867-2871.

83. Yi, D. K.; Lee, S. S.; Ying, J. Y., Synthesis and Applications of Magnetic Nanocomposite Catalysts. *Chem. Mater.* **2006,** *18*, 2459-2461.

84. Mitsudome, T.; Noujima, A.; Mikami, Y.; Mizugaki, T.; Jitsukawa, K.; Kaneda, K., Supported Gold and Silver Nanoparticles for Catalytic Deoxygenation of Epoxides into Alkenes. *Angew. Chem. Int. Ed.* **2010,** *122*, 5677-5680.

85. Liu, Z.; Liang, X.-J., Nano-Carbons as Theranostics. *Theranostics* **2012,** *2*, 235-237.

86. Liu, Z.; Robinson, J. T.; Tabakman, S. M.; Yang, K.; Dai, H., Carbon materials for drug delivery & cancer therapy. *Materials Today* **2011,** *14*, 316-323.

87. Swierczewska, M.; Choi, K. Y.; Mertz, E. L.; Huang, X.; Zhang, F.; Zhu, L.; Yoon, H. Y.; Park, J. H.; Bhirde, A.; Lee, S.; Chen, X., A Facile, One-Step Nanocarbon Functionalization for Biomedical Applications. *Nano Lett.* **2012,** *12*, 3613-3620.

88. Hong, S. Y.; Tobias, G.; Al-Jamal, K. T.; Ballesteros, B.; Ali-Boucetta, H.; Lozano-Perez, S.; Nellist, P. D.; Sim, R. B.; Finucane, C.; Mather, S. J.; Green, M. L. H.; Kostarelos, K.; Davis, B. G., Filled and glycosylated carbon nanotubes for in vivo radioemitter localization and imaging. *Nat. Mater.* **2010,** *9*, 485-490.

89. Moon, H. K.; Lee, S. H.; Choi, H. C., In Vivo Near-Infrared Mediated Tumor Destruction by Photothermal Effect of Carbon Nanotubes. *ACS Nano* **2009,** *3*, 3707-3713.

90. Yang, K.; Feng, L.; Shi, X.; Liu, Z., Nano-graphene in biomedicine: theranostic applications. *Chem. Soc. Rev.* **2013,** *42*, 530-547.

91. Yang, K.; Wan, J.; Zhang, S.; Tian, B.; Zhang, Y.; Liu, Z., The influence of surface chemistry and size of nanoscale graphene oxide on photothermal therapy of cancer using ultra-low laser power. *Biomaterials* **2012,** *33*, 2206-2214.

92. Yang, K.; Zhang, S.; Zhang, G.; Sun, X.; Lee, S.-T.; Liu, Z., Graphene in Mice: Ultrahigh In Vivo Tumor Uptake and Efficient Photothermal Therapy. *Nano Lett.* **2010,** *10*, 3318-3323.

93. Dawson, J. I.; Oreffo, R. O. C., Clay: New Opportunities for Tissue Regeneration and Biomaterial Design. *Adv. Mater.* **2013,** *25*, 4069-4086.

94. Alcantara, A. C. S.; Aranda, P.; Darder, M.; Ruiz-Hitzky, E., Bionanocomposites based on alginate-zein/layered double hydroxide materials as drug delivery systems. *J. Mater. Chem.* **2010,** *20*, 9495-9504.

95. Patel, H.; Somani, R.; Bajaj, H.; Jasra, R., Nanoclays for polymer nanocomposites, paints, inks, greases and cosmetics formulations, drug delivery vehicle and waste water treatment. *Bull. Mater. Sci.* **2006,** *29*, 133-145.

96. Li, B.; He, J.; G. Evans, D.; Duan, X., Inorganic layered double hydroxides as a drug delivery system-intercalation and in vitro release of fenbufen. *App. Clay Sci.* **2004,** *27*, 199-207.

97. Centi, G.; Perathoner, S., Catalysis by layered materials: A review. *Microp. Mesop. Mater.* **2008,** *107*, 3-15.

98. Choudary, B. M.; Madhi, S.; Chowdari, N. S.; Kantam, M. L.; Sreedhar, B., Layered Double Hydroxide Supported Nanopalladium Catalyst for Heck-, Suzuki-, Sonogashira-, and Stille-Type Coupling Reactions of Chloroarenes. *J. Am. Chem. Soc.* **2002,** *124*, 14127-14136.

99. De Stefanis, A.; Tomlinson, A. A. G., Towards designing pillared clays for catalysis. *Catalysis Today* **2006,** *114*, 126-141.

100. Li, Y.; Fan, X.; Qi, J.; Ji, J.; Wang, S.; Zhang, G.; Zhang, F., Gold nanoparticles–graphene hybrids as active catalysts for Suzuki reaction. *Mater. Res. Bull.* **2010,** *45*, 1413-1418.

101. Liang, Y.; Li, Y.; Wang, H.; Zhou, J.; Wang, J.; Regier, T.; Dai, H., Co3O4 nanocrystals on graphene as a synergistic catalyst for oxygen reduction reaction. *Nat. Mater.* **2011,** *10*, 780-786.

102. Thomas, A.; Fischer, A.; Goettmann, F.; Antonietti, M.; Muller, J.-O.; Schlogl, R.; Carlsson, J. M., Graphitic carbon nitride materials: variation of structure and morphology and their use as metal-free catalysts. *J. Mater. Chem.* **2008,** *18*, 4893-4908.

103. Zhang, F.; Xiang, X.; Li, F.; Duan, X., Layered Double Hydroxides as Catalytic Materials: Recent Development. *Catal. Surv. Asia.* **2008,** *12*, 253-265.

104. Zhu, J.; Xiao, P.; Li, H.; Carabineiro, S. A. C., Graphitic Carbon Nitride: Synthesis, Properties, and Applications in Catalysis. *ACS App. Mater. & Inter.* **2014,** *6*, 16449-16465.

105. Su, D. S.; Perathoner, S.; Centi, G., Nanocarbons for the Development of Advanced Catalysts. *Chem. Rev.* **2013,** *113*, 5782-5816.

106. Lee K. Y., Ko K. Y., Envirocat EPZ10: A Recyclable Solid Acid Catalyst for the Synthesis of Biginelli-type 3,4-Dihydropyrimidin-2(1H)-ones. *Bull. Korean Chem. Soc.* **2004**, *25*, 1929-1931.

107. Chitnis, S. R.; Mohan Sharma, M., Industrial applications of acid-treated clays as catalysts. *Reactive and Functional Polymers* **1997,** *32*, 93-115.

108. Bandgar, B. P.; Kasture, S. P., Envirocats, as Novel Solid-Supported Catalysts for Friedel-Crafts Acylation. *J. Chinese Chem. Soc.* **2000,** *47*, 1243-1246.

Chapter 2

Multifunctional Carbon Nanospheres with Magnetic and Luminescent Probes: A Probable Brain Theranostics

Summary:

Multi-functional carbon nanospheres with magnetic Prussian blue nanoparticles and luminescent lanthanide ions have been prepared. The negatively charged surface of the glucose derived carbon sphere facilitates the nucleation of Prussian blue nanoparticles on its surface. The luminescent lanthanide probes were attached on the surface of the carbon sphere through benzene tricarboxylic acid linker. These multifunctional hybrid organic-inorganic composites are superparamagnetic and show enhanced luminescent properties. Their ability to cross blood-brain barrier (enter the brain cell nucleus with no animal toxicity) in mice model indicate that these nanocomposites are promising theranostic agents for the treatment of brain diseases.

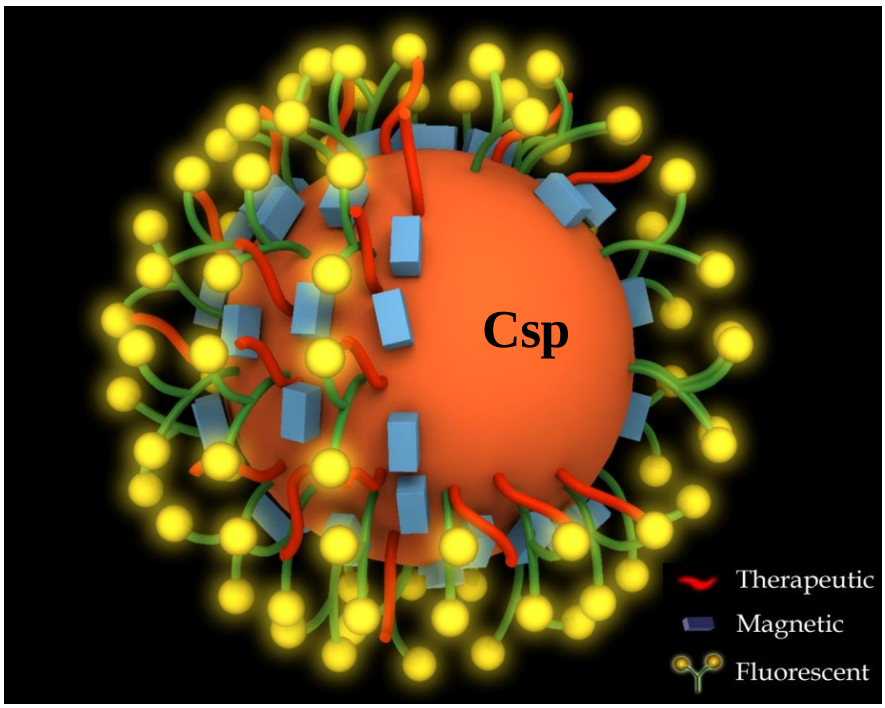

A paper based on this chapter has been published as an article in *J. Mater. Chem. B* 2013, 1, 897.

2.1 Introduction:

Crossing of blood-brain barrier (BBB) is one of the difficult tasks to be surmounted when the delivery of drugs and diagnostics to the brain is considered.[1] BBB is an enzymatic and physical barrier which prevents the entry of toxins from blood to the brain and maintain brain homeostasis.[1] At the same time it also forms a formidable obstacle in the treatment of neurological deceases such as, Alzimer's, Perkinson's, Brain tumor etc, because the effective delivery of drug molecules or diagnostic probes is prohibited.[1] It has been shown that 100% of high molecular weight drugs and more than 98% of low molecular weight drugs cannot traverse through the BBB.[1] Same is the case with most of the imaging contrast agents (ICA).[2] Current methods to overcome BBB includes temporary opening of BBB, administration of very high doses of drug, and direct injection of drug into the spinal cord. These procedures are invasive and involve high risk of infection and toxicity, and demand highly accomplished personnel.[1,2] Very recently, shuttle mediated delivery methods have proven to be promising approach to surmount BBB.[1] A variety of strategies such as, chemical delivery systems, carrier-mediated transport, molecular trojan horses, colloidal carriers *etc.* have been developed under shuttle mediated delivery.[1] Of these methods, nanoparticle mediated targeting of brain has gained tremendous attention by research groups worldwide due to 1) their ability to carry a wide range of drugs to the central nervous system (CNS) and release them in a controlled manner, 2) high loading/encapsulation capacity, 3) tunable circulation lifetime, 4) enhanced permeability and retention (EPR) effect, that up-regulates intratumoral delivery due to high permeability of tumor vasculatures, and 5) multivalent effect increases receptor targeting specificity by labeling multiple ligands on a single

nanoparticle.[1] The futuristic methods of nano-biomedicine relies on the theranostic approaches, in which the therapeutic and imaging components are integrated together, leading towards the concept of personalized medicine.[3-5] Though various nanotheranostic formulations have been developed and demonstrated for their use in the cure of different

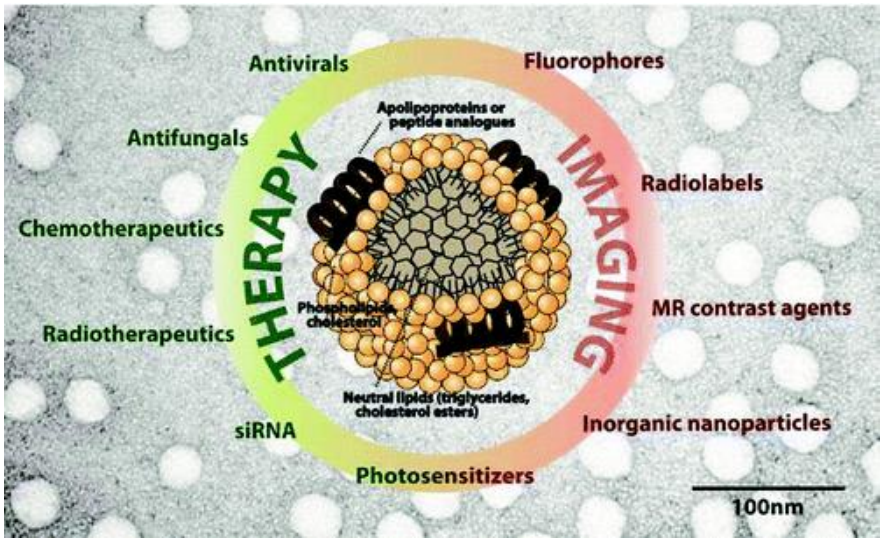

Figure 1: Theranostic Nanomedicine. Adapted with permission from reference 8. Copyright 2011, American Chemical Society.

diseases in diverse body organs,[6-15] only a very few examples are found for brain theranostic.[16,17] Understandably, there is a growing need for developing biocompatible theranostic nanocarriers which can selectively target brain and deliver membrane-impermeable drugs and imaging agents.

2.2 Scope of the Present Study:

Recently, using mice model it was shown, that nanospheres of carbon, synthesized hydrothermally from glucose, have the preferential uptake in the brain.[18] These amorphous carbon nanospheres were biocompatible, biodegradable, and could localize in the nucleus of the brain cells. The rich functional surface and their ability to cross the BBB make these carbon spheres a suitable candidate for brain theranostic applications by incorporating fluorescent and magnetic component in the same nanoparticles.[19,20] In this chapter, we have fabricated a carbon based hybrid material with multiple functionalities by integrating Prussian blue nanoparticles and lanthanide ions as magnetic and luminescent probe respectively. Though the carbon nanospheres are intrinsically fluorescent[18] they suffer from weak photoluminescence intensity. To enhance the luminescence of the spheres, the surface was attached with lanthanide ion through a well known organic linker, benzene tricarboxylic acid (BTC). Lanthanide ions (Sm^{3+}, Tb^{3+}, Eu^{3+}, *etc.*) were selected for fluorescent probe as they are known to show large Stoke shifts, extremely narrow band photoluminescence ranging from visible to near-infrared (NIR), and long lifetimes based on antenna effect when connected to a suitable organic linker.[21-31] On the other hand, conventionally used organic fluorescent molecules[33,34] show rapid photobleaching,[35] whereas inorganic quantum dots[36-38] suffer from fluorescence intermittence[39,40] and toxicity.[41] The high photostability, absence of photoblinking, biocompatibility, monochromaticity, and most importantly, their ultrasensitivity to in vitro and in vivo bioassays make the lanthanide complexes suitable choice for the fluorescence imaging.[28-32,42] For magnetic applications we have chosen Prussian blue (PB) ($Fe_3[Fe(CN)_6]_2$) and its nickel-chromium analogue (NC)

($Ni_3[Cr(CN)_6]_2$) for their ability to couple magnetism with other properties such that transduction, sensing, triggering and porosity.[43-46] These cyno-bridged coordination polymer nanoparticles have also been demonstrated for their uses as MRI contrast agents.[47-50] Prussian blue nanoparticles are known to catalyze the conversion of H_2O_2 (a reactive oxygen species, ROS) into O_2 and this property has been ingeniously used for ultrasound and MR imaging to diagnose ROS changes inside the biological system.[51] The O_2 bubbles generated by the catalytic conversion of H_2O_2 were used as ultrasound contrast agent as they changed the acoustic impedance of the tissue under oxidative stress due to ROS. Also, the longitudinal relaxivity (r_1) of water proton increased due to Prussian blue in the presence of dissolved molecular oxygen (a paramagnetic species) making it a potential nanoparticle T_1 contrast agent. The *in situ* synthesized magnetic nanoparticles are stabilized by the functional groups (-OH, -CHO, -COOH) present on the surface of carbon spheres.

2.3 Materials and Methods:

a. Materials:

α D(+) glucose, iron(II) chloride tetrahydrate, nickel(II) chloride hexahydrate, potassium hexacyano ferrate, potassium hexacyano chromate, benzene trycarboxylic acid (BTC), terbium nitrate, samarium nitrate, MTT ((3-(4,5-Dimethylthiazol-2-yl)-2,5-diphenyltetrazolium bromide) and agarose were purchased from Sigma Aldrich. The 60 ml teflon lined autoclave was constructed. Millipore water and ethanol were used wherever required.

b. Synthesis of spherical amorphous carbon spheres (Csp):

Csp were synthesized by previously reported method.[52] An aqueous solution of α-D-glucose (55 ml of 0.5 M) was placed in a 60 ml teflon lined stainless steel autoclave. The solution was maintained at 180^{o}C for 16 h after which it was allowed to cool down naturally to room temperature. The solid brown product was collected by centrifuging at 6,000 rpm for 5 min. It was thoroughly washed with ethanol and water and dried at 80^{o}C in air for 4 h.

c. Synthesis of Prussian blue nanoparticle modified carbon spheres (Csp@PB):

To a ferrous chloride solution, 0.01 g of ferrous chloride in 8 ml water, 5mg of Csp was added. The resulting solution was sonicated for 5 min. and then stirred vigorously for 25 min. Then the solution was centrifuged, 6,000 rpm for 10 min. and the supernatant was discarded. The precipitate was re-dispersed in 8 ml water followed by dropwise addition of 2 ml of 0.1 mmol $K_3Fe(CN)_6$ soln. with vigorous stirring. This

solution was aged for next two days with continuous stirring. The product was separated by adding 25 ml of acetone to the above mixture with stirring, and then centrifuged at 6,000 rpm for 10 min. The product was then washed 3 times with 15 ml acetone and was dried in a dessicator overnight.

d. Synthesis of nickel-chromium analogue of Prussian blue nanoparticles, modified carbon spheres (Csp@NC):

0.01 g $NiCl_2.6H_2O$ was mixed in 8 ml H_2O and 5 mg carbon spheres was added to it. The solution was sonicated for 5 min. and then stirred vigorously for 25 min. Then it was centrifuged at 6,000 rpm for 10 min and the supernatant was discarded. The solid was dispersed in 8 ml of water and then 0.1 mmol $K_3Cr(CN)_6$ solution (0.033 g in 2 ml water) was added dropwise to this solution with vigorous stirring. The stirring was continued for next two days. For product separation, 25 ml of acetone was added to the above mixture while stirring, and then it was centrifuged at 6,000 rpm for 10 min. The product was washed 3 times with 25 ml acetone and then kept for overnight drying in a dessicator.

e. Benzene tricarboxylic acid (BTC) attachment to the surface of magnetic nanoparticle modified Csp:

To a 3 ml ethanolic solution of Csp@PB or Csp@NC (1 mg/ml), 9 ml solution of benzene tricarboxylic acid (5 mg/ml) prepared in ethanol, was added slowly. The homogeneous mixture was stirred for 2 days continuously and centrifuged at 6,000 rpm for 10 min. The final product was dried in dessicator for overnight.

f. Lanthanide tagging:

3 mg of BTC attached Csp@PB or Csp@NC was soaked in 0.05 M solution of terbium nitrate or samarium nitrate solutions prepared in water for 24 h. The solution was centrifuged at 6,000 rpm for 10 min., and the supernatant was discarded. The final precipitate was dried in a desiccator for overnight.

g. Characterization:

Morphology of the samples was analyzed by a field emmision scanning electron microscope, FESEM (FEI Nova-Nano SEM-600, Netherlands). Transmission electron microscope, TEM images were recorded with a JEOL JEM 3010 instrument (Japan) operated with an accelerating voltage of 300 kV. Powder X-ray diffraction, XRD characterization was done at 25^{o}C with a Bruker-D8 diffractometer employing Cu Kα. Fourier transform infra-red, FTIR Spectra were acquired on Bruker IFS 66v/S instrument in the range of 4000-400 cm^{-1}. Photoluminescence, PL spectra were taken with Perkin-Elmer model LS 55 luminescence spectrometer. Magnetic measurements were carried out with a vibrating sample magnetometer using the physical property measurement system (Quantum Design, US).

h. In vitro Magnetic resonance imaging (MRI) Experiments:

The in vitro MRI studies were carried out using a vertical wide bore (89 mm) 14.1 T magnet interfaced with Avance II Microimager (Bruker Biospin, Germany) equipped with 60 mm actively shielded gradient at 25°C. In a typical measurement, surface modified carbon nanospheres were dispersed in 0.5 % agarose gel in the molten condition

and the dispersion was cooled in a 0.8 ml microfuge tube to form a gel. The longitudinal relaxation time (T_1) and transverse relaxation time (T_2) were measured using saturation recovery and multiecho method respectively, where the axial images of the microfuge tube filled with agarose gel were obtained. The typical parameters used for T_1 measurements are: echo time (TE) = 7 ms; repetition time (TR) = varies from 250 ms to 15000 ms; slice thickness = 0.5 mm; field of view: 15 mm x 15 mm; matrix size = 64 x 64). The T_1 value was determined by fitting the function $S_{TR}= S_{TR(\infty)}(1-\exp(-TR/T_1))$ to the signal intensity versus repetition time graph. The parameters used for the T_2 measurements were: TR = 10000 ms and TE varying between 10 ms to 320 ms. All other parameters used were same as that of the T_1 measurements. The value was obtained by fitting a decreasing mono exponential function to the signal intensity versus echo time plot. The longitudinal (r_1) and transverse relaxivity (r_2) were calculated from the slope of relaxation rate (R_1 ($1/T_1$) / R_2 ($1/T_2$)) versus concentration graph.

i. MTT assay:

HEK293T cells (5000 cells) were seeded in 96 well plate. The cells were treated with different nanoparticles and apoptosis inducing compound plumbagin (RTK1), for the indicated time points. Following the period of treatment, MTT solution was added (as per the manufacturer's instructions). After incubation with the reagent for 3 h at 37^0C and 5% CO_2, the absorbance was recorded at 595 nm in an ELISA reader (VERSA Max microplate reader, Molecular Devices). The values were normalized with the untreated control and plotted.

j. Immunofluorescence:

Cell lines:

To visualize the entry of different nanoparticles in cellular system, HEK293T and HeLa cells were cultured as monolayer on poly L-lysine-coated cover slips in DMEM (Sigma) medium. After 12 h of treatment with different nanoparticles, cells were fixed with 4% paraformaldehyde and the chromosomal DNA was stained with Hoechst 33528 (Sigma). The images were taken by using Zeiss LSM 510 laser scanning confocal microscope.

Animal tissue:

BALB/c mice were injected intra-peritoneally with (20 mg/kg of body weight) of different nanoparticles. Injection volume was kept constant at 250 μL. Mice were sacrificed 3 days, 7 days or 14 days following the injection. Brain, liver and spleen tissues were collected and fixed in 5% formaldehyde solution for 12-24 h. After formalin fixation the tissues were progressively dehydrated in increasing concentration of ethanol followed by xylene or chloroform. The dehydrated tissues were embedded in paraffin wax and kept at 4ºC till further use. The paraffin blocks were sectioned into 5-10 μm thin sections using a microtome (Leica) and after deparaffinization were progressively rehydrated and the chromosomal DNA was stained with Hoechst 33528 (Sigma). The images were taken by using Zeiss LSM 510 laser scanning confocal microscope.

k. Animal toxicity:

BALB/c mice were injected intraperitoneally with (20 mg/kg of body weight) of different nanoparticles. Food intake and body weight of each mice were monitored for 30 days. The mice were also regularly checked for any growth in the body.

2.4 Results and Discussions:

Amorphous carbon nanospheres were synthesized by hydrothermal method reported elsewhere.[52] The FESEM image (Figure 2a) of as synthesized spheres show that the particles are ~500 nm in size and monodispersed. The absorption bands at ~1620,

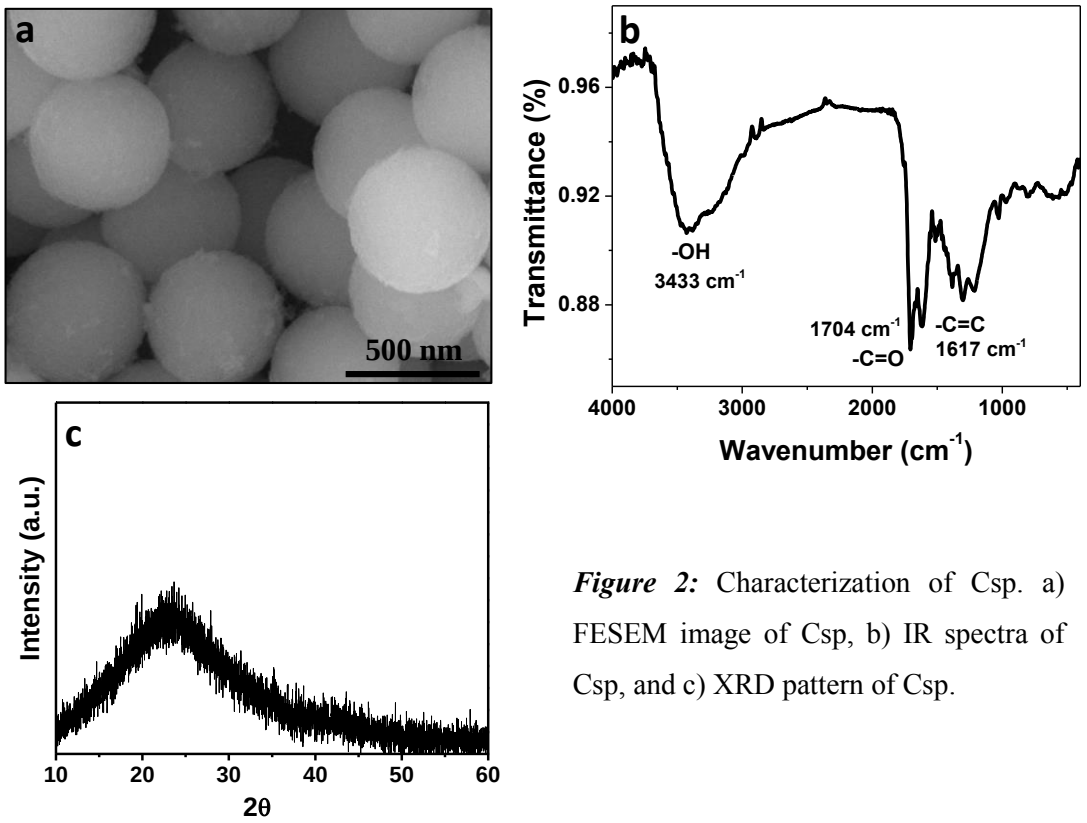

Figure 2: Characterization of Csp. a) FESEM image of Csp, b) IR spectra of Csp, and c) XRD pattern of Csp.

~1707, and 3420 cm^{-1}, in the IR spectra (Figure 2b) indicate the presence of various functional groups like, -C=C-, -CHO, –COOH, -OH, *etc* on its surface.[18] The XRD pattern of Csp does not show any sharp peaks (Figure 2c), which characteristic of a

disordered or amorphous system. At neutral pH, deprotonation of some of the carboxyl functional groups makes the Csp negatively charged with zeta potential value of ~ -25 mV.[53] This renders Csp to adsorb positively charged species on its surface. The synthesis

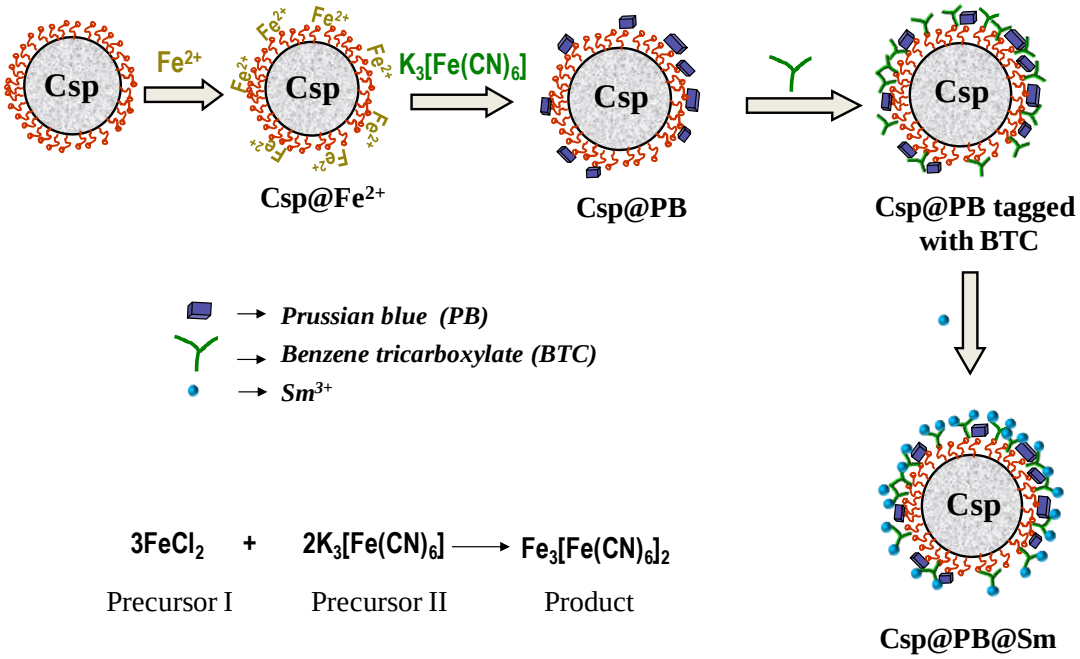

Scheme 1: Schematic showing fabrication of the nanocomposites.

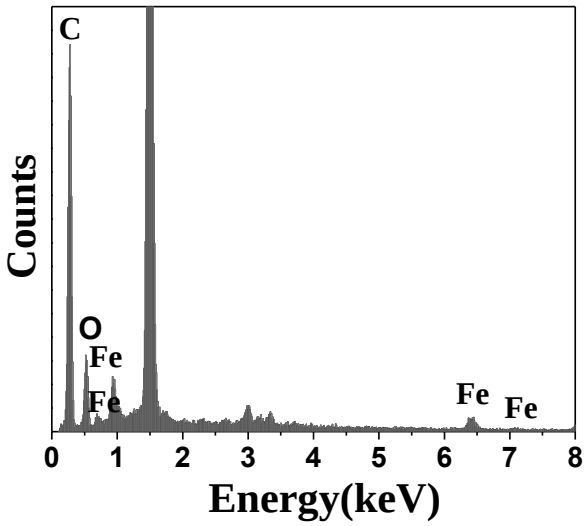

Figure 3: EDX plot of Csp@Fe^{2+}.

of PB and NC nanoparticles was carried by stepwise adsorption of the corresponding metal ions and hexacyanometallates. For example, PB containing carbon spheres, Csp@PB, were synthesized by first adsorbing Fe^{2+} ions on the carbon surface followed by the addition of $[Fe(CN)_6]^{3-}$ (Scheme 1). Energy dispersive X-ray analysis (EDAX) of Fe^{2+} adsorbed carbon sphere shows clearly the presence of iron (Figure 3).

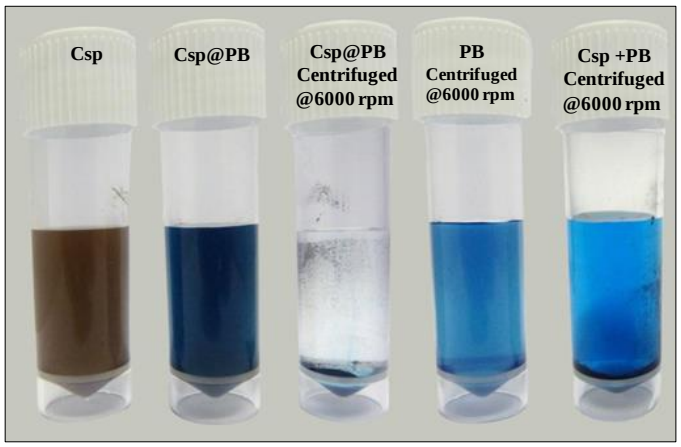

Figure 4: Optical image of various water dispersions.

In a similar way, NC modified Csp (Csp@NC) were also synthesized (see the experimental section). Figure 4 shows that Csp@PB dispersed in water gives blue color while Csp dispersion had brown color. When the dispersion of Csp@PB was centrifuged at 6000 rpm, it gave a clear supernatant. On the other hand, dispersions of ~25 nm Prussian blue particles, as well as physical mixture of Csp and Prussian blue nanoparticles dispersed in water left blue supernatant when centrifuged at 6000 rpm. This is a clear indication that Prussian blue nanoparticles are strongly bound to the Csp surface in Csp@PB. The powder X-ray diffraction (XRD) patterns of Csp@PB (Figure 5a) and Csp@NC (Figure 5b) exhibit peaks corresponding to the crystals of PB and NC and can be indexed as the cubic space group *Fm*3*m*.[54] The peak broadening in the XRD patterns

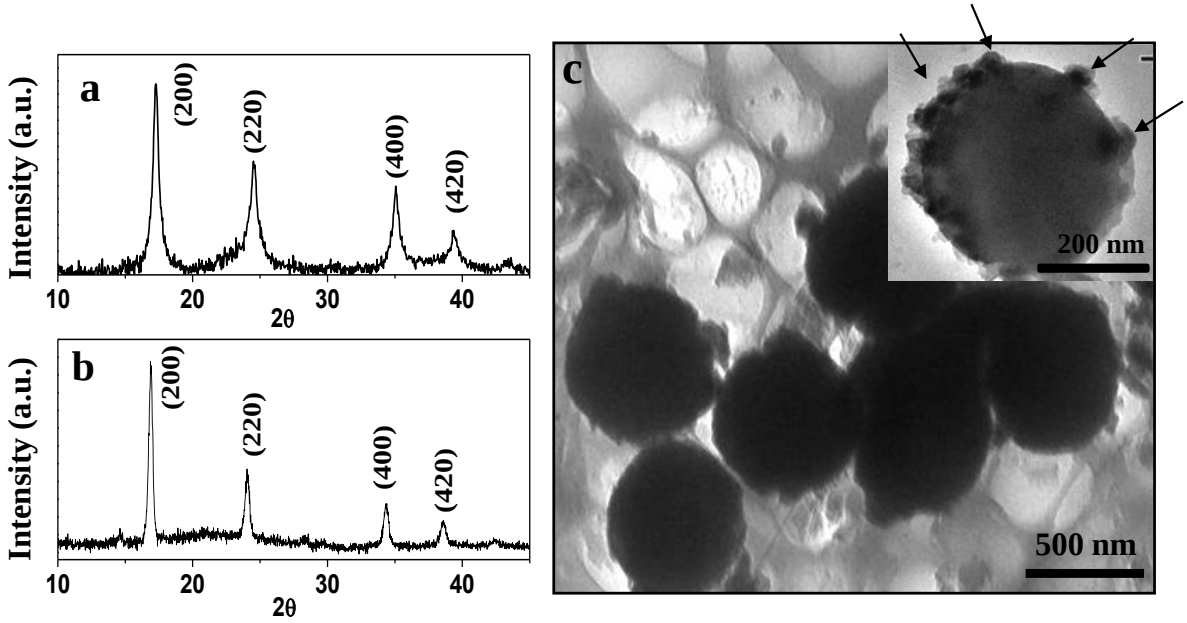

Figure 5: a) XRD of Csp@PB, b) XRD of Csp@NC, c) TEM image of Csp@PB (inset shows presence of nanoparticles on the Csp surface).

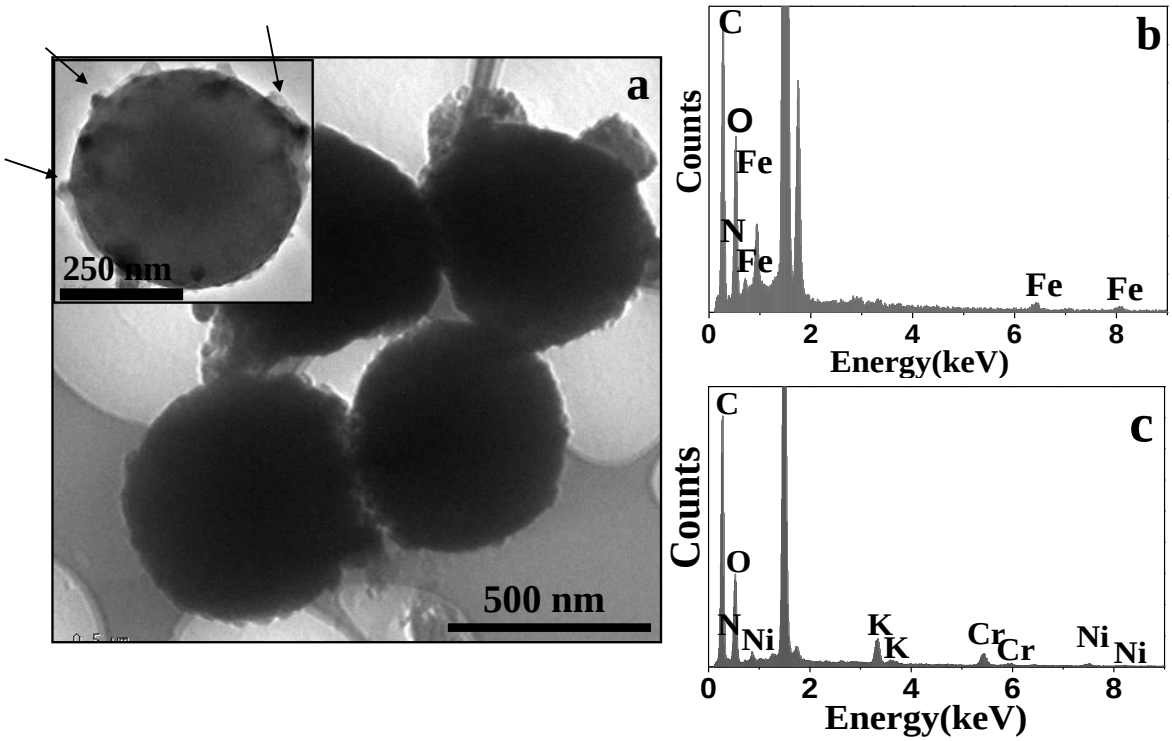

Figure 6: TEM image of Csp@NC (a) and EDX analysis of Csp@PB (b) and Csp@NC (c). Inset of (a) shows nanoparticles (indicated by arrows) on the Csp surface.

is indicative of the presence of nanoparticles on the surface of amorphous Csp. Transmission electron microscopy (TEM) images of Csp@PB (Figure 5c) and Csp@NC (Figure 6a), shows the presence of dark contrast particles (arrows in the inset) of size ~22 nm. This clearly suggests that the carbon spheres are not completely covered with PB or NC layers. The EDX analysis of these samples showed presence of Fe for Csp@PB (Figure 6b) and Ni and Cr for Csp@NC (Figure 6c). The new bands appearing at 2087 cm^{-1} and at 2167 cm^{-1} in the IR spectra of Csp@PB (Figure 7a) and Csp@NC (Figure 7b) as compared to the bare Csp are associated with the cyanide stretching in PB and NC respectively. Presence of broad characteristic band with λ_{max} at 693 nm in UV-Vis spectra for Csp@PB is consistent with the intermetal charge-transfer from Fe^{2+} to Fe^{3+} in Prussian blue nanoparticles[55] while this band was absent for Csp (Figure 8). Furthermore,

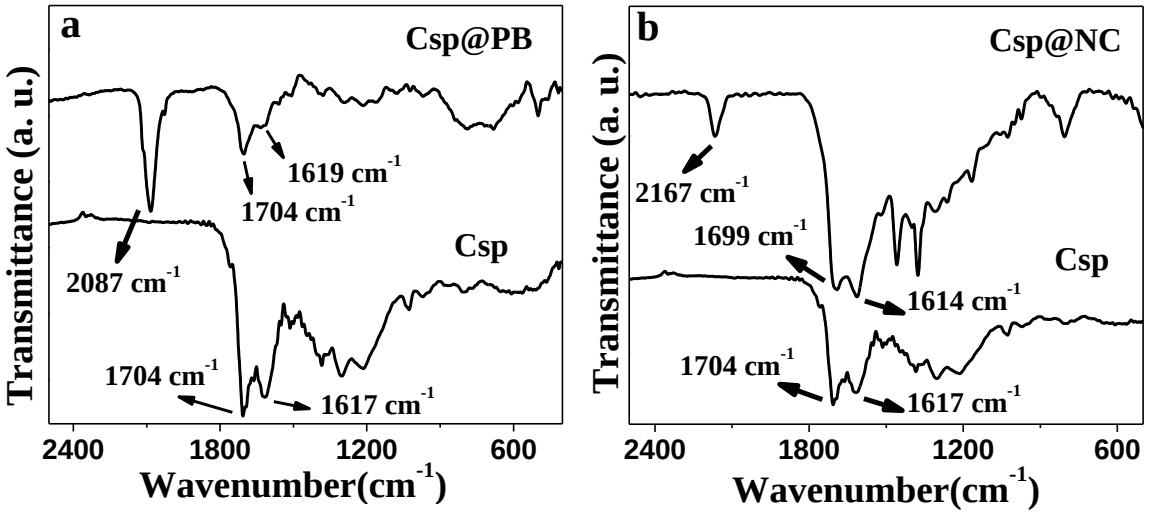

Figure 7: IR spectra of Csp@PB and Csp (a) and Csp@NC and Csp (b).

Csp@PB was tested for its ability to catalyze the H_2O_2 to O_2 at pH 7.4 (PBS buffer) and 25°C. Plenty of gas bubbles were noticed when H_2O_2 was added to dispersion of Csp@PB in PBS buffer (Figure 9). On the other hand, controls PBS buffer and Csp dispersion in

PBS buffer generated no gas bubbles on addition of H_2O_2. The presence of –C=O stretching bands at 1724 cm^{-1} and 1734 cm^{-1} for BTC modified Csp@PB (Figure 10a) and Csp@NC (Figure 10b) respectively, indicates condensation of BTC with Csp via ester

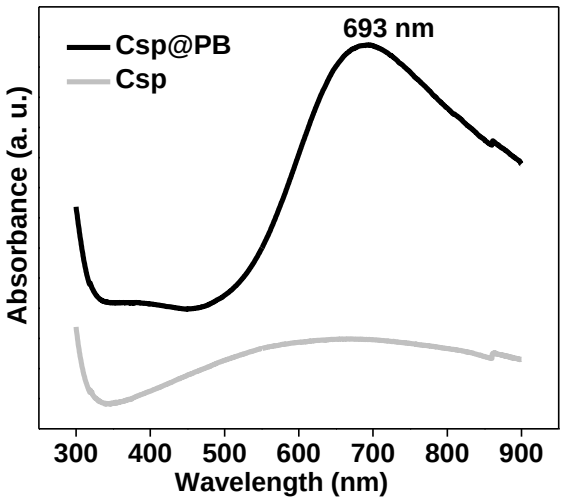

Figure 8: UV-Vis spectra of Csp@PB and Csp.

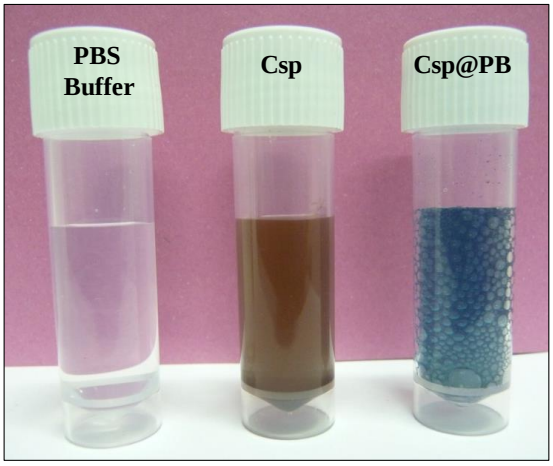

Figure 9: Optical images after 10 minutes of addition of H_2O_2 to the PBS buffer, Csp dispersion in PBS buffer and Csp@PB dispersion in PBS buffer.

formation. The IR bands near 1430 cm^{-1} reveals the presence of -C-O-H in plane bending vibration of carboxylic acid. Finally, the luminescent lanthanide ions, Sm^{3+} and Tb^{3+},

were immobilized on the surface individually through coordinate interactions with the carboxylate groups of the linker. The composites formed with Sm^{3+} were named as Csp@PB@Sm and Csp@NC@Sm and with Tb^{3+} were named as Csp@PB@Tb, and Csp@NC@Tb. The tagging of these ions to the surface was confirmed by EDX analysis of the finally modified composite materials which showed presence of peaks due to Sm(III) or Tb(III) (Figure 11). The luminescent and magnetic properties of these composite materials were studied and the results are following.

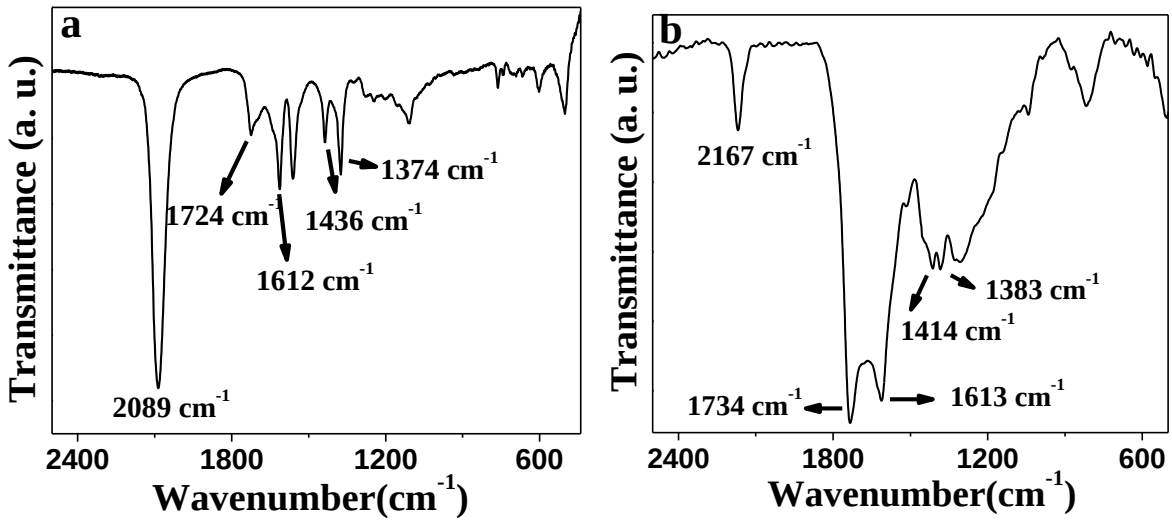

Figure 10: IR spectra of Csp@PB tagged with BTC (a) and Csp@NC tagged with BTC (b).

The emission spectra of the final composites Csp@PB@Sm, Csp@NC@Sm, Csp@PB@Tb, and Csp@NC@Tb are shown in Figure 12. Free Sm(III) ions gives rise to very weak characteristics luminescence intensity in the aqueous solutions, but when attached to BTC linker through hard donors like oxygen, show abrupt enhancement in the luminescence intensity, due to efficient ligand to metal energy transfer through antenna effect.[56-62] The aqueous solutions of $Sm(NO_3)_3$ shows characteristic peaks at 563.5 nm

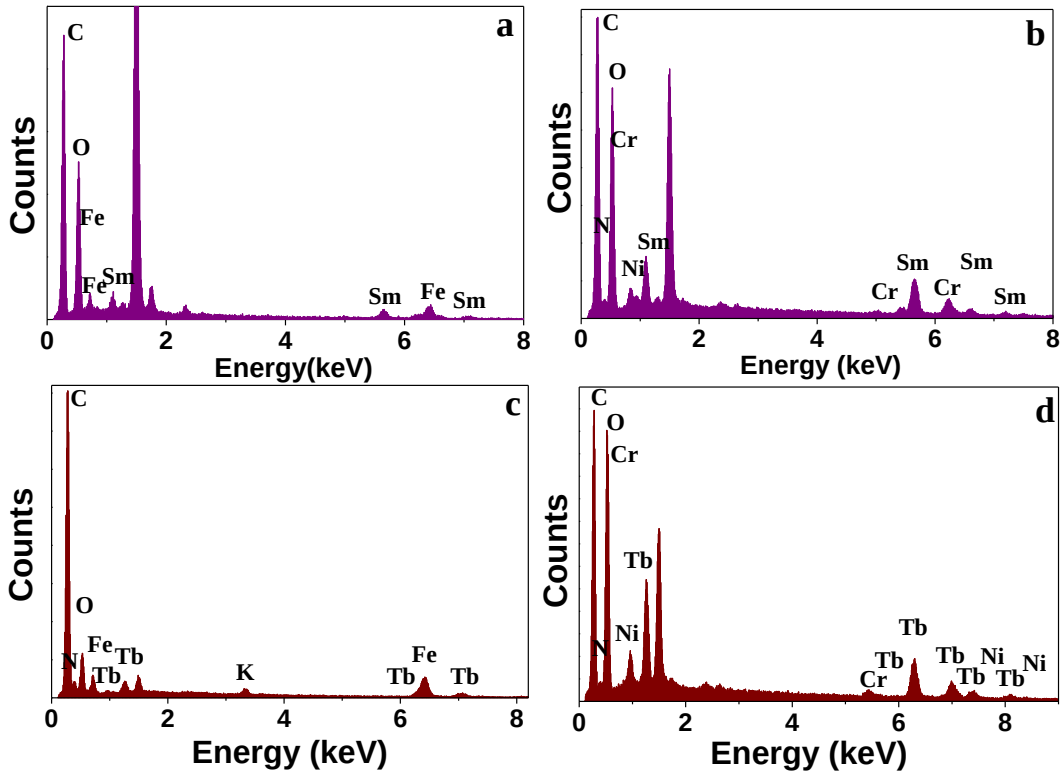

Figure 11: EDX analysis of Csp@PB@Sm (a), Csp@NC@Sm (b), Csp@PB@Tb (c), and Csp@NC@Tb (d).

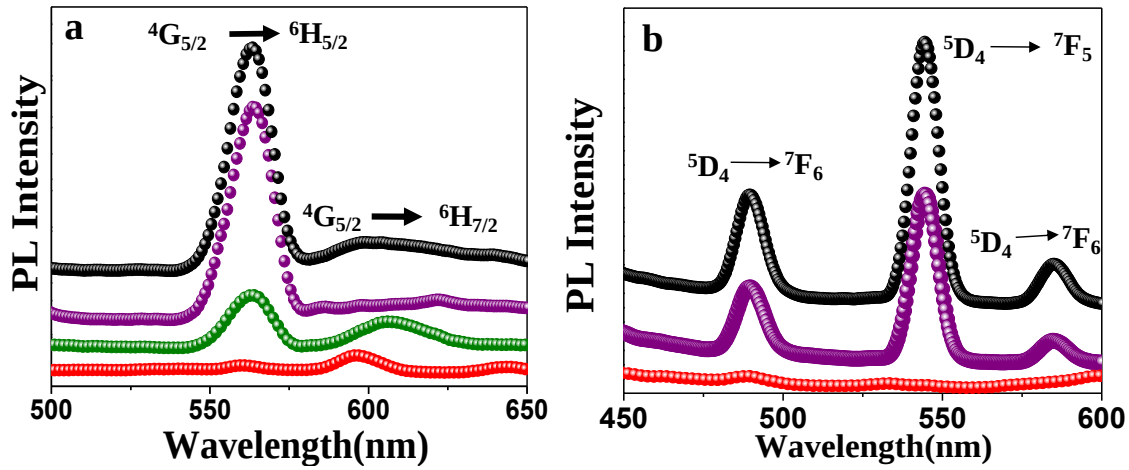

Figure 12: PL spectra. a) Enhancement in the fluorescence intensity of Sm in Csp@PB@Sm (purple spheres) and Csp@NC@Sm (black spheres). The aqueous solution of the Sm^{3+} ions showed very weak luminescence intensity (red spheres). Sm directly attached to Csp@PB without BTC linker showed very less enhancement in the luminescence of Sm (green spheres). The

excitation wavelenth, λ_{ex} was 275 nm. b) Enhancement in the fluorescence intensity of Tb in Csp@PB@Tb (purple spheres) and Csp@NC@Tb (black spheres). The aqueous solution of the Tb^{3+} ions showed very weak luminescence intensity (red spheres). The excitation wavelenth, λ_{ex} was 300 nm.

and 599.5 nm corresponding to $^4G_{5/2}$ to $^6H_{5/2}$ and $^4G_{5/2}$ to $^6H_{7/2}$ transitions, respectively.[63] When Sm(III) in the composites was excited at 275 nm, an abrupt enhancement in their luminescence intensity was observed due to the energy transfer from BTC to Sm(III) ions. As a control experiment, we have looked into the enhancement in the luminescent intensity of Sm(III), directly attached to Csp@PB without using linker. As apparent in Figure 12a the enhancement is very less compared to the samples in which the BTC linker is used to attach Sm(III). So, the Sm(III) ions bonded to Csp@PB linked with BTC has a more effective sensitization of their luminescence through BTC. The emission spectra of Csp@PB@Tb and Csp@NC@Tb (Figure 12b) also showed luminescence enhancement of characteristic peaks of Tb(III) at 489 nm, 544.5 nm and 584.5 nm corresponding to $^5D_4$ to ^7F_J (J = 6, 5, 4) transitions, respectively.

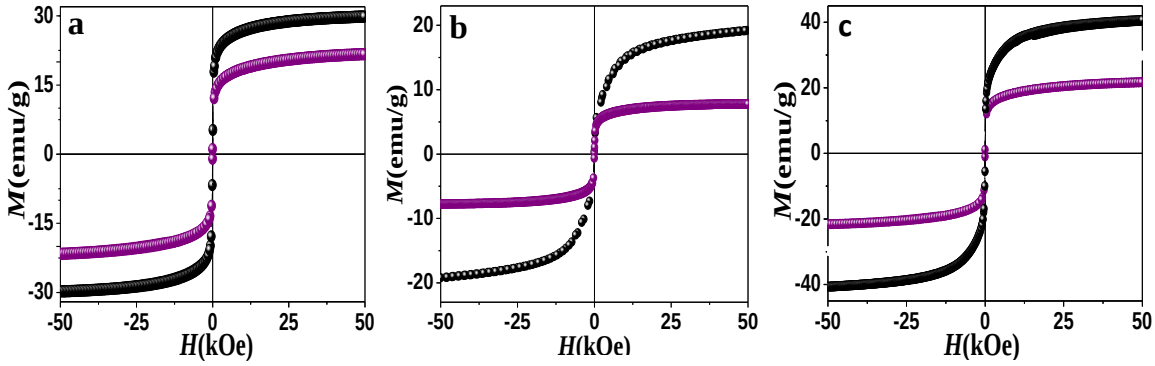

Figure 13: a) M vs H curve for Csp@PB (purple spheres), and Csp@PB@Sm (black spheres), b) M vs H curve for Csp@NC (purple spheres) and Csp@NC@Sm (black spheres) and c) M vs H curve for Csp@PB (purple spheres), Csp@PB@Tb (black spheres).

The isothermal magnetization studies of Csp@PB and Csp@NC as well as the final Sm(III) incorporated nanocomposites were carried out up to a magnetic field of 5T at 2.5 K. At low temperatures, Prussian blue is known to show three-dimensional long-range super-exchange interactions between neighboring Fe(III) ions (S=5/2) through CN–Fe(II)–CN linkages which results in ferromagnetic ordering with T_c = 9.2 K. Similar ferromagnetic behavior also observed with NC having T_c around 52 K.[43,55] Both Csp@PB (Figure 13a) and Csp@NC (Figure 13b) were superparamagnetic at 2.5 K which is similar in line with the earlier reported nanoscale PB analogue.[43] The composites Csp@PB@Sm (Figure 13a) and Csp@NC@Sm (Figure 13b) were also found to be superparamagnetic with increased saturation magnetization values, 30 emu/g and 20

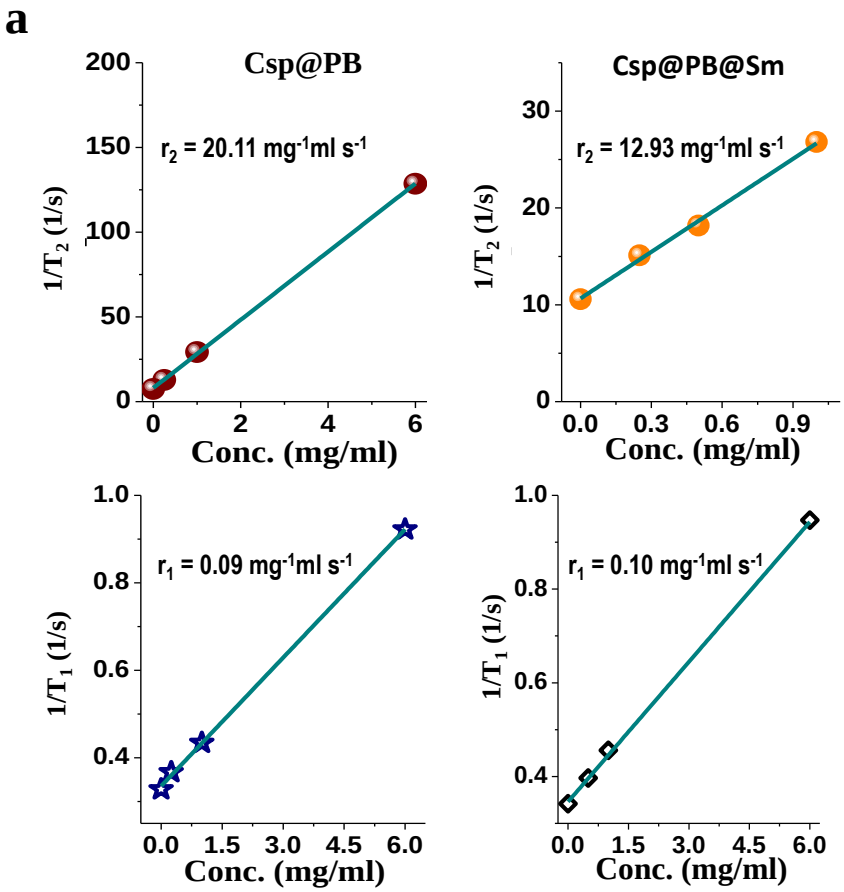

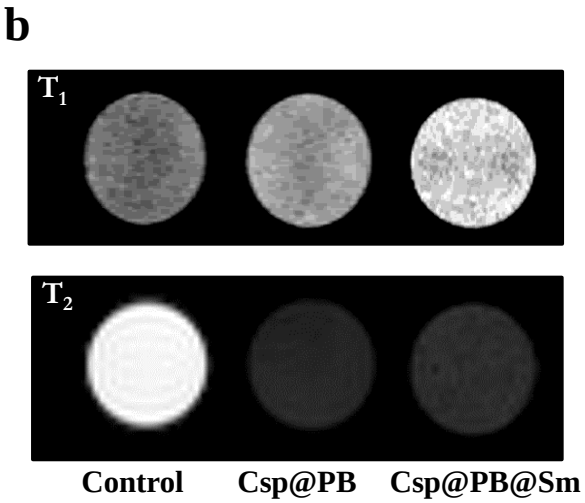

Figure 14: a) The transverse (r_2) and longitudinal (r_1) relaxivity measurement of the Csp@PB and Csp@PB@Sm. The T_1 and T_2 were measured using saturation recovery and multiecho method, respectively, where the axial images of the microfuge tube filled with agarose gel were obtained. The T_1 and T_2 values were determined by fitting an exponential function to signal intensity versus repetition time and signal intensity versus echotime time graph, respectively. The longitudinal (r_1) and transverse relaxivity (r_2) were calculated from the slope of R_1/R_2 versus concentration graph. b) Magnetic resonance (MR) Images of microfuge tube filled with different samples depicting the T_1 and T_2 contrast. The parameters used for the T_1 weighted MR imaging, were: TR = 250 ms and TE = 7 ms and for the T_2 weighted MR imaging, were TR = 10000 ms and TE = 10 ms. The image was acquired with matrix size of 64x64 with spatial resolution of 0.312 mm/pixel.

emu/g respectively, as compared to those of respective Csp@PB (20 emu/g) and Csp@NC (8 emu/g). This increase in the saturation magnetization can be attributed to the presence of paramagnetic Sm(III) ions with S=5/2. Csp@PB@Tb also shows the similar behavior as that of the Csp@PB@Sm (Figure 13c). Furthermore, the saturation magnetization of Tb(III) tagged composite is larger than the Sm(III) tagged composite due to the higher total spin associated with Tb(III) (S=3) in comparisn to Sm(III) (S=5/2).

In order to examine the potential of the composite particles as magnetic resonance imaging (MRI) contrast agent we carried out proton longitudinal relaxation time (T_1) and

transverse relaxation time (T_2) measurements using a 14.1 T NMR Microimager, by dispersing Csp@PB and Csp@PB@Sm into 0.5% agarose gel. The relaxivity values (calculated from the plot of $1/T_1$ and $1/T_2$ Vs concentration, Figure 14a), for both the samples are listed in Table 1. The r_2 of the composite nanoparticles, Csp@PB@Sm (12.93 $mg^{-1}ml\ s^{-1}$) is slightly lower than that of the Csp@PB (20.11 $mg^{-1}\ ml\ s^{-1}$) while the r_1 of Csp@PB@Sm (0.10 $mg^{-1}\ ml\ s^{-1}$) is higher than Csp@PB (0.09 $mg^{-1}\ ml\ s^{-1}$). T_1 and T_2 weighted MR images of the samples (concentration = 1 mg/ml) and of the control,

Sample	Longitudinal Relaxivity r_1 ($mg^{-1}\ ml\ s^{-1}$)	Transverse Relaxivity r_2 ($mg^{-1}\ ml\ s^{-1}$)
Csp@PB	*0.09*	*20.11*
Csp@PB@Sm	*0.10*	*12.93*

Table 1: Relaxivity properties of the composite materials.

0.5% agarose gel, are shown in Figure 14b. The MR images consisting of weighted MR imaging, the brightness (increased intensity) of composite nanoparticles are brighter in T_1 images and darker in T_2 images as compared to the control (agarose gel). In T_1 weighted image the brightness increases with an increase of longitudinal relaxation rate, whereas the darkness in the T_2 weighted image increases with increase of transverse relaxation rate.

The PB and Sm(III) modified carbon spheres were tested for their biocompatibility, ability to enter cells and blood-brain barrier crossing property. The cytotoxicity of the PB and lanthanide ion containing Csp were checked by the standard

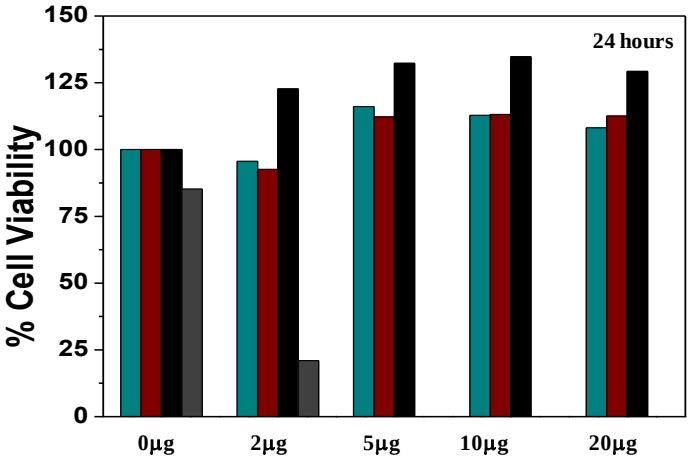

Figure 15: Cytotoxicity for human embryonic kidney Cells (HEK 293T). MTT assay of HEK 293T cells treated with Csp (cyan bar), Csp@PB@Sm (wine bar), Csp@NC@Sm (black bar), and positive control RTK1 (gray bar).

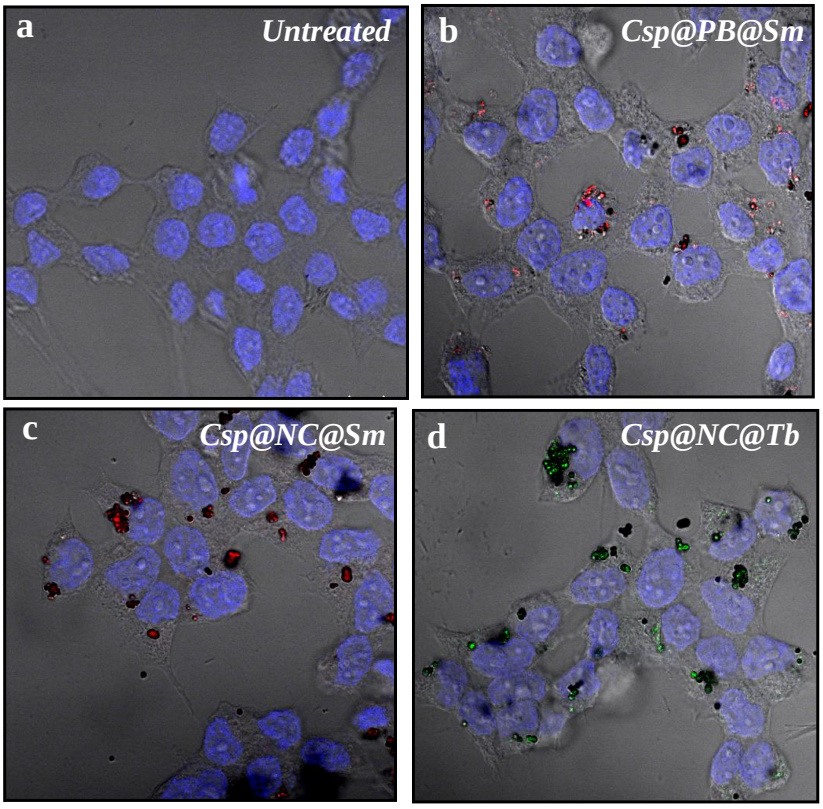

Figure 16: Cell entry studies for human embryonic kidney Cells (HEK 293T). a) Confocal microscope image of untreated HEK 293T cells, b) HEK 293T cells treated with Csp@PB@Sm, c) HEK 293T cells treated with Csp@NC@Sm, and d) HEK 293T cells treated with Csp@NC@Tb.

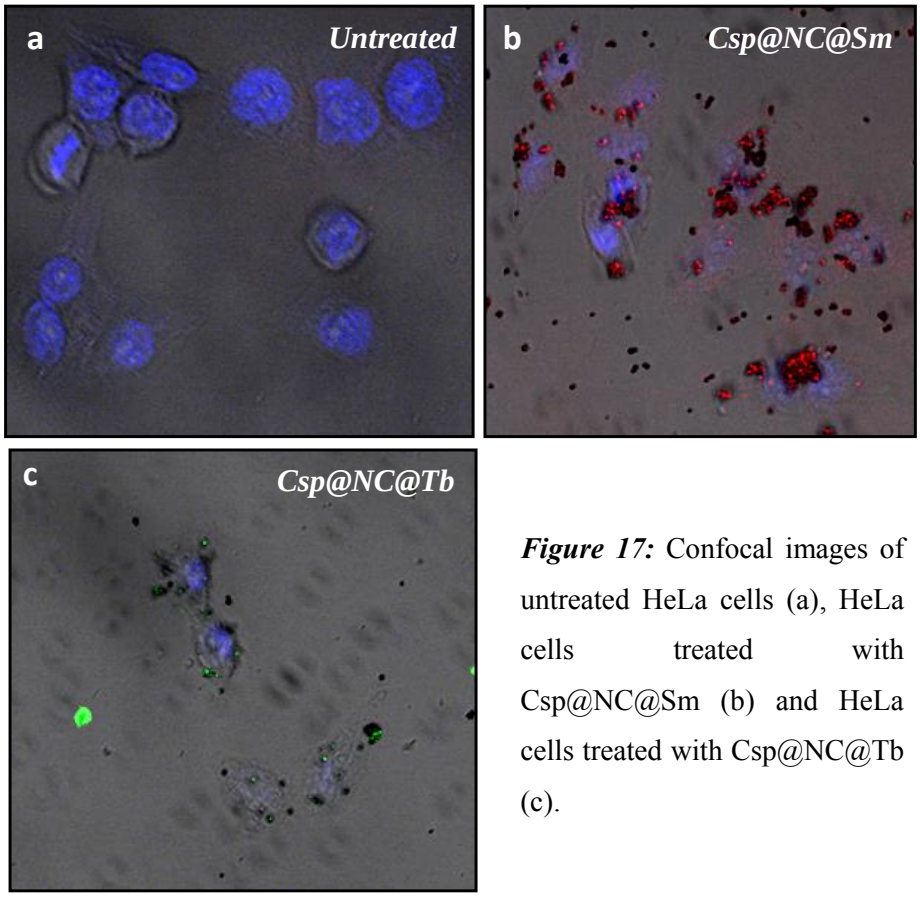

Figure 17: Confocal images of untreated HeLa cells (a), HeLa cells treated with Csp@NC@Sm (b) and HeLa cells treated with Csp@NC@Tb (c).

MTT ((3-(4,5-Dimethylthiazol-2-yl)-2,5-diphenyltetrazolium bromide) based assays. Viable living cells reduce the yellow colored MTT inside the cytoplasm to purple formazan. The measurement of intensity of the purple color gives an estimate for the amount of viable cells in a culture media. The test shows that Csp@PB@Sm did not show any toxicity even upto 20 µg/ml concentration, whereas the positive control RTK1[64] shows severe cytotoxicity with a 2 µg/ml concentration (Figure 15). Entry of these lanthanide containing spheres inside the Human Embryonic Kidney Cells (HEK 293T cells) was investigated by exciting the samples with a two photon laser, λ_{ex} = 680 nm, and observing their emission in the wavelength window of 540-600 nm. HEK 293T cells were treated separately with Csp@PB@Sm and Csp@NC@Sm spheres for 24 hours. The

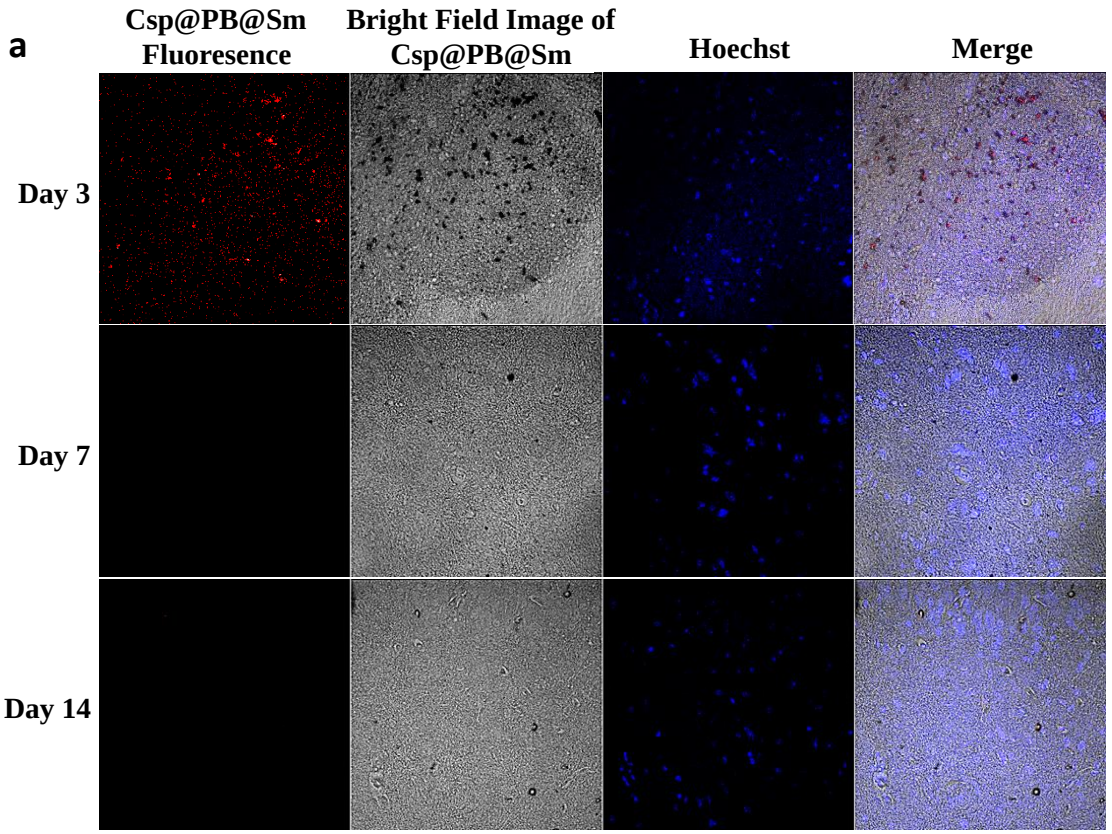
a
Csp@PB@Sm Fluoresence
Bright Field Image of Csp@PB@Sm
Hoechst
Merge
Day 3
Day 7
Day 14

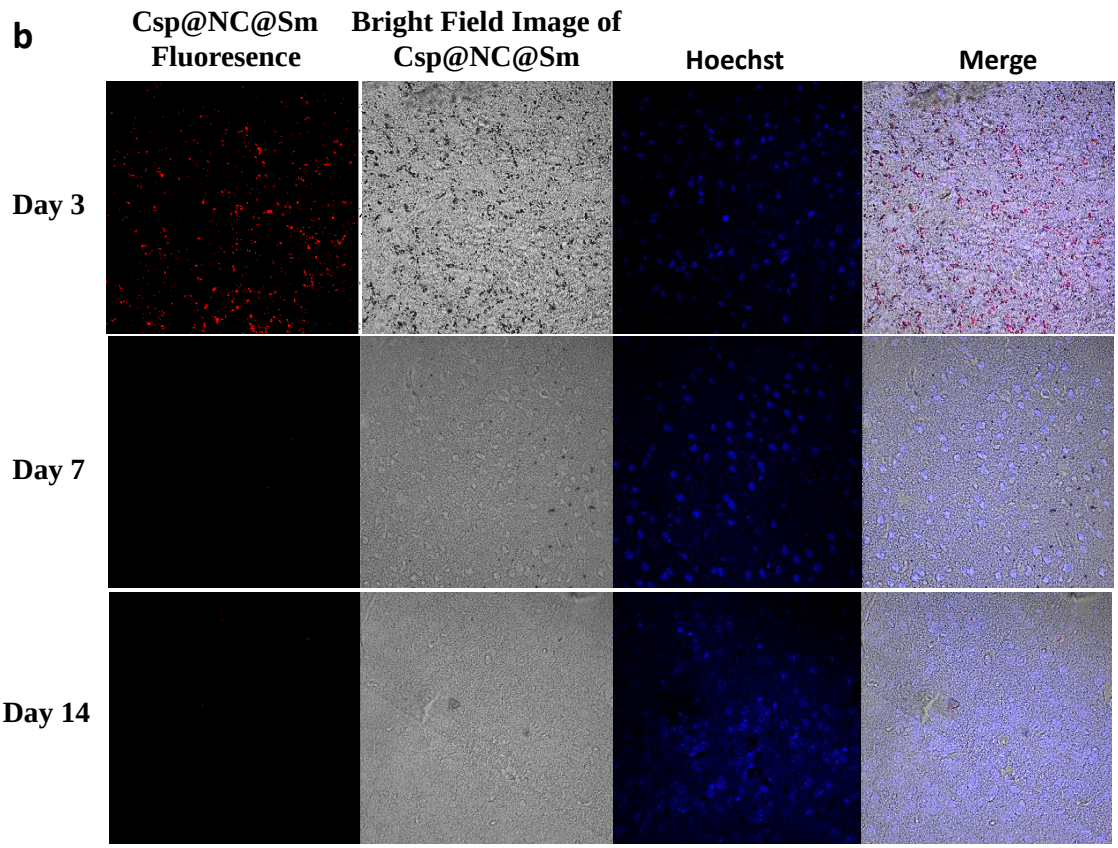
b
Csp@NC@Sm Fluoresence
Bright Field Image of Csp@NC@Sm
Hoechst
Merge
Day 3
Day 7
Day 14

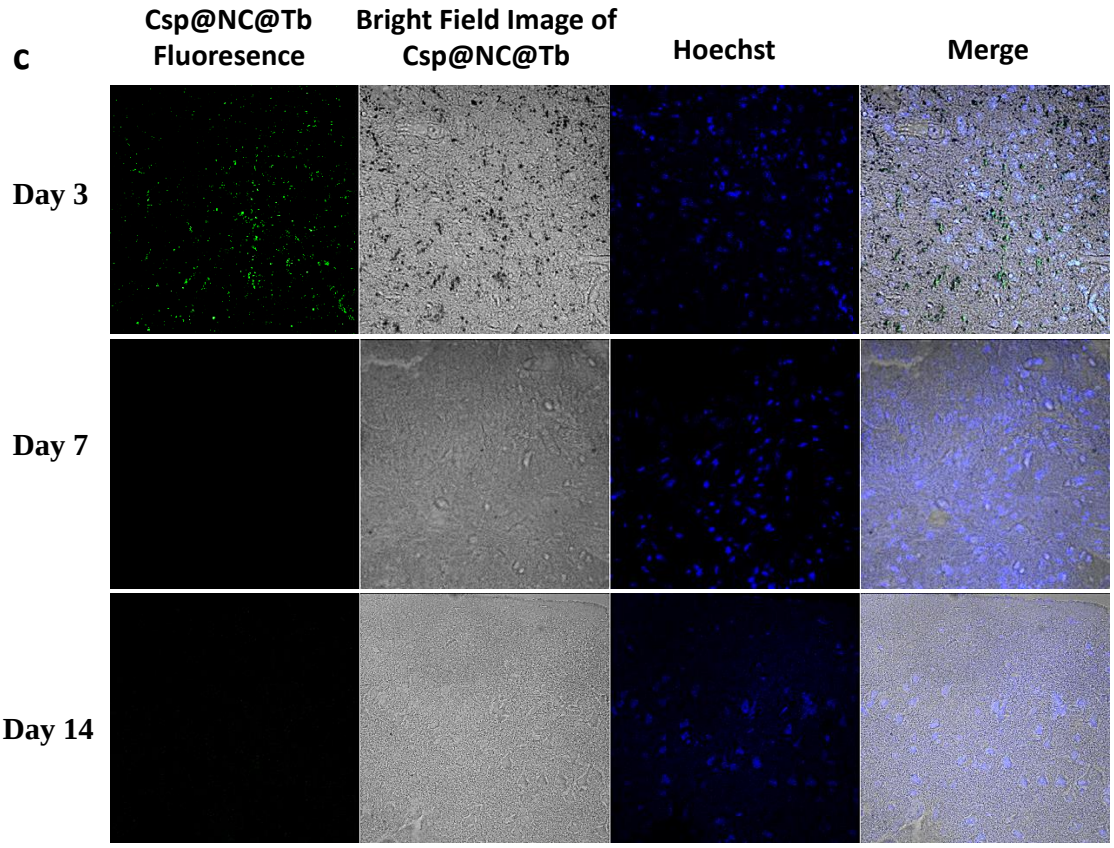

Figure 18: Brain entry. Confocal images of nanoparticles inside the brain tissue of mice sacrificed after 3 days, 7 days and 14 days of injection, Csp@PB@Sm (a), Csp@NC@Sm (b), and Csp@NC@Tb (c).

fluorescence images confirmed the presence of the nanoparticles inside HEK293T cells and some of them entered the nucleus as well (Figure 16). The same results were obtained when human cervical cancer derived HeLa cells were treated with the nanoparticles (Figure 17). This clearly suggests that the modified Csp (by PB and lanthanide ions) still retain their ability to enter the cell nucleus.

Further, the ability of these modified carbon spheres to cross the blood brain barrier (BBB) was monitored in the mice model. BALB/c mice were intraperitoneally injected with the Csp@PB@Sm, and were sacrificed after 3 days, 7 days and 14 days.

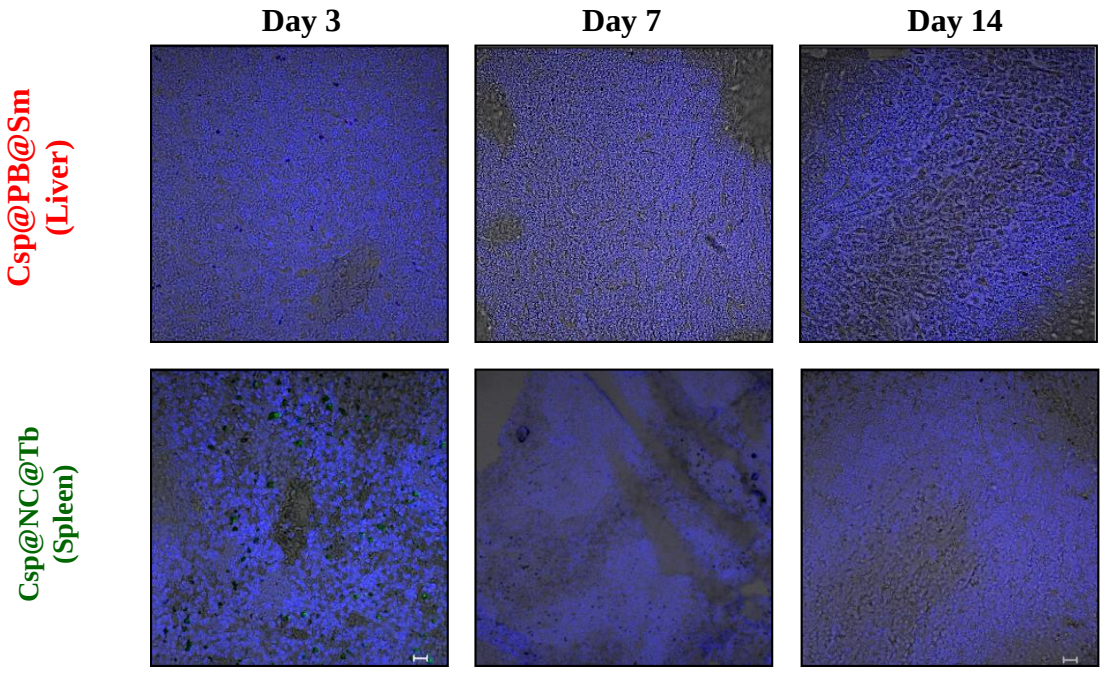

Figure 19: Confocal images of Csp@PB@Sm inside the liver tissue of mice sacrificed after 3 days, 7 days and 14 days of injection and confocal images of Csp@NC@Tb inside the spleen tissue of mice sacrificed after 3 days, 7 days and 14 days of injection.

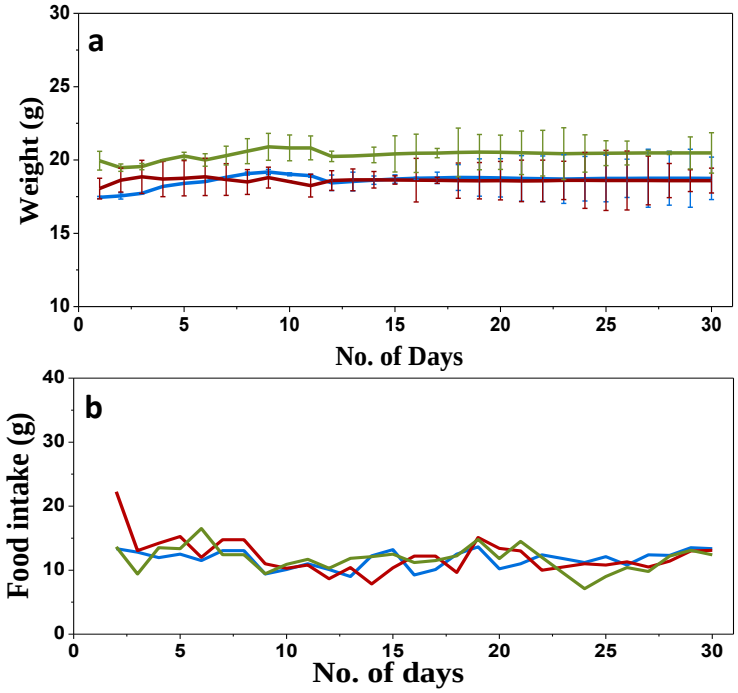

Figure 20: Animal toxicity. Weight (a) and food intake (b) monitored over a period of one month for mice injected with water (blue), Csp@PB@Sm (dark yellow), Csp@NC@Sm (wine).

Localization of nanospheres in different organs (brain, liver and spleen) of mice was examined by confocal microscopy. The presence of large number of colored spots associated with Sm^{3+} emission (linked to the carbon spheres) in the brain cells indicate that Csp@PB@Sm spheres could efficiently cross the BBB and were maximally localized in the brain after 3 days of injection (Figure 18a). A drastic decrease of nanospheres was observed in mice brain sacrificed after 7 days of injection whereas, the nanospheres were completely absent in the brain after 14 days of injection. Similar results were obtained with Csp@NC@Sm/Csp@NC@Tb (Figure 18b/18c respectively). Localization of the nanospheres in other organs like liver and spleen were also studied (Figure 19). As compared to the brain, very less amount of nanospheres are localized in the liver and spleen on the third day after injection. Day 7 and 14 show little or no spheres in liver and spleen. In order to study the animal toxicity of the surface modified spheres BALB/c mice were treated with Csp@PB@Sm, Csp@NC@Sm and water (control). The weight and the food intake of each mice was monitored for 30 days (Figure 20). Mice injected with Csp@PB@Sm (dark yellow) and Csp@NC@Sm (wine) showed similar behavior for its food intake and weight to the mice injected with water (blue) suggesting no animal toxicity.

2.5 Conclusions:

In conclusion, we have successfully modified the surface of the carbon nanospheres with magnetic Prussian blue nanoparticles and luminescent lanthanide ions. The surface modified spheres are superparamagnetic, luminescent, could enter the cell nucleus, and are non-cytotoxic. These nanospheres could traverse through BBB and enter the brain efficiently and show no animal toxicity, proving their potential as brain theranostic agents. The future development of the multifunctional carbon nanospheres as targeted brain theranostic vehicle by modifying its surface with the MOF (a class of co-ordination polymers) which could store and deliver drugs in a controlled manner is under progress in our laboratory.[65-67] Also, these spheres are being explored for their ability to image ROS overproducing tissues inside the brain.

2.6 References:

1. Malakoutikhah M.; Teixid M.; Giralt E. Shuttle-Mediated Drug Delivery to the Brain. *Angew. Chem. Int. Ed.* **2011**, *50*, 2–19.
2. Koffiea R. M.; Farrar C. T.; Saidi L.-J.; Williama C. M.; Hymana B. T.; Spires-Jones T. L. Nanoparticles enhance brain delivery of blood–brain barrier-impermeable probes for in vivo optical and magnetic resonance imaging. *Proc. Natl. Acad. Sci. U.S.A* **2011**, *108*, 18837-18842.
3. Chen X.; Gambhir S. S.; Cheon J. Theranostic Nanomedicine. *Acc. Chem. Res.* **2011**, *44*, 841–841.
4. Sumar B.; Gao J. Theranostic Nanomedicine for Cancer. *Nanomedicine* **2008**, *3*, 137-140.
5. Lammers T.; Aime S. Hennink W. E.; Storm G.; Kiessling F. Theranostic Nanomedicine. *Acc. Chem. Res.* **2011**, *44*, 1029–1038.
6. Xia Y.; Li W.; Cobley C. M.; Chen J.; Xia X.; Zhang Q.; Yang M.; Cho E. C.; Brown P. K. Gold Nanocages: From Synthesis to Theranostic Applications. *Acc. Chem. Res.* **2011**, *44*, 914–924.
7. Tanner P.; Baumann P.; Enea R.; Onaca O.; Palivan C.; Meier W. Polymeric Vesicles: From Drug Carriers to Nanoreactors and Artificial Organelles *Acc. Chem. Res.* **2011**, *44*, 1039–1049..
8. Ng, K. K.; Lovell, J. F.; Zheng, G., Lipoprotein-Inspired Nanoparticles for Cancer Theranostics. *Acc. Chem. Res.* **2011,** *44,* 1105-1113.
9. Rocca J. D.; Liu D.; Lin W. Nanoscale Metal–Organic Frameworks for Biomedical Imaging and Drug Delivery. *Acc. Chem. Res.* **2011**, *44*, 957–968.

10. Lee J. E.; Lee N.; Kim T.; Kim J.; Hyeon T. Multifunctional Mesoporous Silica Nanocomposite Nanoparticles for Theranostic Applications. *Acc. Chem. Res.* **2011**, *44*, 893–902.
11. Yoo D.; Lee J.-H.; Shin T.-H.; Cheon J. Theranostic Magnetic Nanoparticles. *Acc. Chem. Res.* **2011**, *44*, 863–874.
12. Tassa C.; Shaw S. Y.; Weissleder R. Dextran-Coated Iron Oxide Nanoparticles: A Versatile Platform for Targeted Molecular Imaging, Molecular Diagnostics, and Therapy. *Acc. Chem. Res.* **2011**, *44*, 842–852.
13. Ho D.; Sun X.; Sun S. Monodisperse Magnetic Nanoparticles for Theranostic Applications. *Acc. Chem. Res.* **2011**, *44*, 875–882.
14. Kievit F. M.; Zhang M. Surface Engineering of Iron Oxide Nanoparticles for Targeted Cancer Therapy. *Acc. Chem. Res.* **2011**, *44*, 853–862.
15. Xie J.; Liu G.; Eden H. S.; Al H.; Chen X.; Surface-Engineered Magnetic Nanoparticle Platforms for Cancer Imaging and Therapy. *Acc. Chem. Res.* **2011**, *44*, 883–892.
16. Chertok B.; David A. E.; Yang V. C. Magnetically-enabled and MR-monitored selective brain tumor protein delivery in rats via magnetic nanocarriers. *Biomaterials* **2011**, *32*, 6245–6253.
17. Chertok B.; Moffat B. A.; David A. E.; Yu F.; Bergemann C.; Ross B. D.; Yang V. C. PEGylated Poly(amidoamine) dendrimer-based dual-targeting carrier for treating brain tumors. *Biomaterials* **2008**, *29*, 487–496.
18. Ruthrotha Selvi B.; Jagadeesan D.; Nagashankar G.; Suma B. S.; Arif M.; Balasubramanyam K.; Eswaramoorthy M.; Kundu T. K. Intrinsically fluorescent

carbon nanospheres as a nuclear targeting vector: Delivery of membrane impermeable molecule to modulate gene expression in vivo. *Nano Lett.* **2008**, *8*, 3182–3188.

19. Kim J.; Piao Y.; Hyeon T. Multifunctional nanostructured materials for multimodal imaging, and simultaneous imaging and therapy. *Chem. Soc. Rev.* **2009**, *38*, 372–390.
20. Choi J. H.; Nguyen F. T.; Barone P. W.; Heller D. A.; Moll A. E.; Patel D.; Boppart S. A.; Strano M. S. Multimodal Biomedical Imaging with Asymmetric Single-Walled Carbon Nanotube/Iron Oxide Nanoparticle Complexes. *Nano Lett.* **2007**, *7*, 861-867.
21. Heer S.; Kömpe K.; Gudel H. U.; Haase M. Highly Efficient Multicolour Upconversion Emission in Transparent Colloids of Lanthanide-Doped $NaYF_4$ Nanocrystals. *Adv. Mater.* **2004**, *16*, 2102-2105.
22. Lehmann O.; Kömpe K.; Haase M. Synthesis of Eu^{3+}-Doped Core and Core/Shell Nanoparticles and Direct Spectroscopic Identification of Dopant Sites at the Surface and in the Interior of the Particles. *J. Am. Chem. Soc.* **2004**, *126*, 14935-14942.
23. Ferreira R. A. S.; Carlos L. D.; Goncüalves R. R.; Ribeiro S. J. L.; Bermudez V. Z. Energy-Transfer Mechanisms and Emission Quantum Yields In Eu^{3+}-Based Siloxane-Poly(oxyethylene) Nanohybrids. *Chem. Mater.* **2001**, *13*, 2991-2998.
24. Fu L.; Ferreira R. A. S.; Silva N. J. O.; Carlos L. D.; Bermudez V. d. Z.; Rocha J. Photoluminescence and Quantum Yields of Urea and Urethane Cross-Linked Nanohybrids Derived from Carboxylic Acid Solvolysis. *Chem. Mater.* **2004**, *16*, 1507-1516.
25. Nogami M.; Suzuki K. Fast Spectral Hole Burning in Sm^{2+}-Doped Al2O3–SiO2 Glasses. *Adv. Mater.* **2002**, *14*, 923-926.

26. Chengelis D. A.; Yingling A. M.; Badger P. D.; Shade C. M.; Petoud S. Incorporating Lanthanide Cations with Cadmium Selenide Nanocrystals: A Strategy to Sensitize and Protect Tb(III). *J. Am. Chem. Soc*. **2005**, *127*, 16752-16753.
27. Petoud, S.; Muller, G.; Moore, E. G.; Xu, J.; Sokolnicki, J.; Riehl, J. P.; Le, U. N.; Cohen, S. M.; Raymond, K. N. Brilliant Sm, Eu, Tb, and Dy Chiral Lanthanide Complexes with Strong Circularly Polarized Luminescence. *J. Am. Chem. Soc*. **2007**, *129*, 77-83.
28. Bouzigues C.; Gacoin T.; Alexandrou A. Biological Applications of Rare-Earth Based Nanoparticles. *ACS Nano* **2011**, *5*, 8488–8505.
29. Pellegatti L.; Zhang J.; Drahos B.; Villette S.; Suzenet F.; Guillaumet G.; Petoud S.; Tóth É. Pyridine-based lanthanide complexes: towards bimodal agents operating as near infrared luminescent and MRI reporters. *Chem. Commun.* **2008**, 6591–6593.
30. Wolfbeis O. S.; Durkop A.; Wu M.; Lin Z. H. A Europium-Ion-Based Luminescent Sensing Probe for Hydrogen Peroxide. *Angew. Chem., Int. Ed.* **2002**, *41*, 4495-4498.
31. Jin D.; Piper J. A. Time-Gated Luminescence Microscopy Allowing Direct Visual Inspection of Lanthanide-Stained Microorganisms in Background-Free Condition. *Anal. Chem.* **2011**, *83*, 2294-2300.
32. Bünzli J.-C. G.; Piguet C. Taking advantage of luminescent lanthanide ions. *Chem. Soc. Rev.* **2005**, *34*, 1048-1077.
33. Lu Y.; Yin Y. D.; Mayers B. T.; Xia Y. N. Modifying the Surface Properties of Superparamagnetic Iron Oxide Nanoparticles through A Sol−Gel Approach. *Nano Lett.* **2002**, *2*, 183-186.
34. Lee J. E.; Lee N.; Kim H.; Kim J.; Choi S. H.; Kim J. H.; Kim T.; Song I. C.; Park S. P.; Moon W. K.; Hyeon T. Uniform Mesoporous Dye-Doped Silica Nanoparticles

Decorated with Multiple Magnetite Nanocrystals for Simultaneous Enhanced Magnetic Resonance Imaging, Fluorescence Imaging, and Drug Delivery. *J. Am. Chem. Soc.* **2010**, *132*, 552-557.

35. Schrum K. F.; Lancaster J. M.; Johnston S. E.; Gilman S. D. Monitoring Electroosmotic Flow by Periodic Photobleaching of a Dilute, Neutral Fluorophore. *Anal. Chem.* **2000**, *72*, 4317-4321.
36. Yi D. K.; Selvan S. T.; Lee S. S.; Papaefthymiou G. C.; Kundaliya D.; Ying J. Y. Silica-Coated Nanocomposites of Magnetic Nanoparticles and Quantum Dots. *J. Am. Chem. Soc.* **2005**, *127*, 4990-4991.
37. Gu H.; Zheng R.; Zhang X. X.; Xu B. Facile One-Pot Synthesis of Bifunctional Heterodimers of Nanoparticles: A Conjugate of Quantum Dot and Magnetic Nanoparticles. *J. Am. Chem. Soc.* **2004**, *126*, 5664-5665.
38. Cohen B. E. Biological imaging: Beyond fluorescence. *Nature* **2010**, *467*, 407-408.
39. Hohng S.; Ha T. Near-Complete Suppression of Quantum Dot Blinking in Ambient Conditions. *J. Am. Chem. Soc.* **2004**, *126*, 1324-1325.
40. Brokmann X.; Hermier J. P.; Desbiolles P.; Bouchaud J. P.; Dahan M. Statistical Aging and Nonergodicity in the Fluorescence of Single Nanocrystals. *Phys. Rev. Lett.* **2003**, *90*, 120601.
41. Fischer H. C.; Liu L. C.; Pang K. S.; Chan W. C. W. Pharmacokinetics of Nanoscale Quantum Dots: In Vivo Distribution, Sequestration, and Clearance in the Rat. *Adv. Funct. Mater.* **2006**, *16*, 1299-1305.
42. Wang L. Y.; Yan R. X.; Huo Z. Y.; Wang L.; Zeng J. H.; Bao J.; Wang X.; Peng Q.; Li Y. D. Fluorescence Resonant Energy Transfer Biosensor Based on Upconversion-Luminescent Nanoparticles. *Angew. Chem., Int. Ed.* **2005**, *44*, 6054-6057.

43. Tokoro H.; Ohkoshi S.-I. Novel magnetic functionalities of Prussian blue analogs. *Dalton Trans.* **2011**, *40*, 6825-6833.

44. Janiak C. Engineering coordination polymers towards applications. *Dalton Trans.* **2003**, 2781-2804.

45. Verdaguer M.; Bleuzen A.; Marvaud V.; Vaissermann J.; Seuleiman M.; Desplanches C.; Scuiller A.; Train C.; Garde R.; Gelly G.; Lomenech C.; Rosenman I.; Veillet P.; Cartier C.; Villain F. Molecules to Build Solids: High TC Molecule-based Magnets by Design and Recent Revival of Cyano Complexes Chemistry. *Coord. Chem. Rev.* **1999**, *192*, 1023-1047.

46. Vaucher S.; Li M.; Mann S. Synthesis of Prussian Blue Nanoparticles and Nanocrystal Superlattices in Reverse Microemulsions. *Angew. Chem. Int. Ed.* **2000**, *39*, 1793-1796.

47. Chelebaeva E.; Larionova J.; Guari Y.; Ferreira R. A. S.; Carlos L. D.; Trifonov A. A.; Kalaivani T.; Lascialfari A.; Guérin C.; Molvinger K.; Datas L.; Maynadier M.; Gary-Bobo M.; Garcia M. Nanoscale Coordination Polymers Exhibiting Luminescence Properties and NMR Relaxivity. *Nanoscale* **2011**, *3*, 1200-1210.

48. Larionova J.; Guari Y.; Sangregoriob C.; Guérina C. Cyano-bridged Coordination Polymer Nanoparticles. *New J. Chem.*, **2009**, *33*, 1177-1190.

49. Gauri Y.; Larionova J.; Corti M.; Lascialfari A.; Marinone M.; Poletti G.; Molvinger K.; Guerin C. Cyano-bridged Coordination Polymer Nanoparticles with High Nuclear Relaxivity: Toward New Contrast Agents for MRI. *Dalton Trans.* **2008**, 3658-3660.

50. Shokouhimehr M.; Soehnlen E. S.; Hao J.; Griswold M.; Flask C.; Fan X.; Basilion J. P.; Basu S.; Huang S. D. Dual Purpose Prussian Blue Nanoparticles for Cellular

Imaging and Drug Delivery: A New Generation of T_1-weighted MRI Contrast and Small Molecule Delivery Agents. *J. Mater. Chem.* **2010**, *20*, 5251-5259.

51. Yang F.; Hu S.; Zhang Y.; Cai X.; Huang Y.; Wang F.; Wen S.; Teng G.; Gu N. A Hydrogen Peroxide-Responsive O_2 Nanogenerator for Ultrasound and Magnetic-Resonance Dual Modality Imaging. *Adv. Mater.* **2012**, *24*, 5205-5211.
52. Sun X.; Li Y. Colloidal Carbon Spheres and Their Core/Shell Structures with Noble-Metal Nanoparticles. *Angew. Chem. Int. Ed.* **2004**, *43*, 597-601.
53. Jagadeesan D. Diverse Applications of Glucose Derived Functionalized Carbon Nanostructures. PhD thesis JNCASR **2009**.
54. Buser H. J.; Schwarzenbach D.; Petter W.; Ludi A. The crystal structure of Prussian Blue: $Fe_4[Fe(CN)_6]_3.xH_2O$. *Inorg. Chem.* **1977**, *16*, 2704-2710.
55. Uemura T.; Kitagawa S. Prussian Blue Nanoparticles Protected by Poly(vinylpyrrolidone). *J. Am. Chem. Soc.* **2003**, *125*, 7814-7815.
56. Lehn J. M. Perspectives in Supramolecular Chemistry—From Molecular Recognition towards Molecular Information Processing and Self-Organization. *Angew. Chem. Int. Ed.* **1990**, *29*, 1304-1319.
57. Wu J.-Y.; Yeh T.-T.; Wen Y.-S.; Twu J.; Lu K.-L. Unusual Robust Luminescent Porous Frameworks Self-Assembled from Lanthanide Ions and 2,2‘-Bipyridine-4,4‘-dicarboxylate. *Cryst. Growth Des.* **2006**, *6*, 467-473.
58. Calefi P. S.; Ribeiro A. O.; Pires A. M.; Serra O. A. Characterization and spectroscopic studies of Eu^{3+} and Tb^{3+} complexes with 2,2′-bipyridine-4,4′-dicarboxylic acid. *J. Alloys Compd.* **2002**, *344*, 285-288.
59. Bünzli J. C. G. Benefiting from the Unique Properties of Lanthanide Ions. *Acc. Chem. Res.* **2006**, *39*, 53–61.

60. Balzani V.; Juris A.; Venturi M. Luminescent and Redox-Active Polynuclear Transition Metal Complexes. *Chem. Rev.* **1996**, *96*, 759-833.

61. Zhang S.; Trokowski R.; Sherry A. D. A Paramagnetic CEST Agent for Imaging Glucose by MRI. *J. Am. Chem. Soc.* **2003**, *125*, 15288-15289.

62. Zhang S.; Malloy C. R.; Sherry A. D. MRI Thermometry Based on PARACEST Agents. *J. Am. Chem. Soc.* **2005**, *127*, 17572-17573.

63. Xia J.; Zhao B.; Wang H.-S.; Shi W.; Ma Y.; Song H.-B.; Cheng P.; Liao D.-Z.; Yan S.- P. Two- and Three-Dimensional Lanthanide Complexes: Synthesis, Crystal Structures, and Properties. *Inorg. Chem.* **2007**, 46, 3450-3458.

64. Srinivas P.; Gopinath G.; Banerji A.; Dinakar A.; Srinivas G. Plumbagin induces reactive oxygen species, which mediate apoptosis in human cervical cancer cells. *Mol Carcinog.* **2004**, *40*, 201-211.

65. McKinlay A. C.; Morris R. E.; Horcajada P.; Férey G.; Gref R.; Couvreur P.; Serre C. BioMOFs: Metal–Organic Frameworks for Biological and Medical Applications. *Angew. Chem. Int. Ed.* **2010**, *49*, 6260-6266.

66. Xuan W.; Zhu C.; Liu Y.; Cui Y. Mesoporous metal–organic framework materials. *Chem. Soc. Rev.* **2012**, *41*, 1677-1695.

67. Horcajada P.; Chalati T.; Serre C.; Gillet B.; Sebrie C.; Baati T.; Eubank J. F.; Heurtaux D.; Clayette P.; Kreuz C.; Chang J.-S.; Hwang Y. K.; Marsaud V.; Bories P.-N.; Cynober L.; Gil S.; Férey G.; Couvreur P.; Gref R. Porous metal–organic-framework nanoscale carriers as a potential platform for drug delivery and imaging. *Nat. Mater.* **2010**, *9*, 172-178.

Chapter 3

Shape Directed *In Vivo* Compartmentalized Delivery of Drug-Nanoparticle Conjugates in the Brain Cells

Summary:

Delivery of drugs in specific subcellular compartments of brain cells is quite challenging despite their importance in the treatment of several brain related diseases. Herein, we report on the shape directed, intracellular compartmentalization of nanoparticles in the brain cells and their ability to deliver the therapeutic molecules in specific organelle. Iron oxide (Fe_3O_4) nanoparticles of different morphologies (spheres, spindles, biconcaves, and nanotubes) were synthesized and coated with fluorescent carbon layer derived from glucose (Fe_3O_4@C). *In vivo* studies showed that the Fe_3O_4@C nanoparticles of biconcave geometry preferably localized in the nucleus of the brain cells, while the nanotube geometry were contained mostly in the cytoplasm. Remarkably, a small molecule activator of histone acetyltransferases delivered into the nucleus of the brain cells using the nanoparticles of biconcave geometry showed three times enhancement in the enzymatic activity and thereby specific gene expression (transcription) as compared to the molecule delivered in the cytoplasm using nanotube geometry.

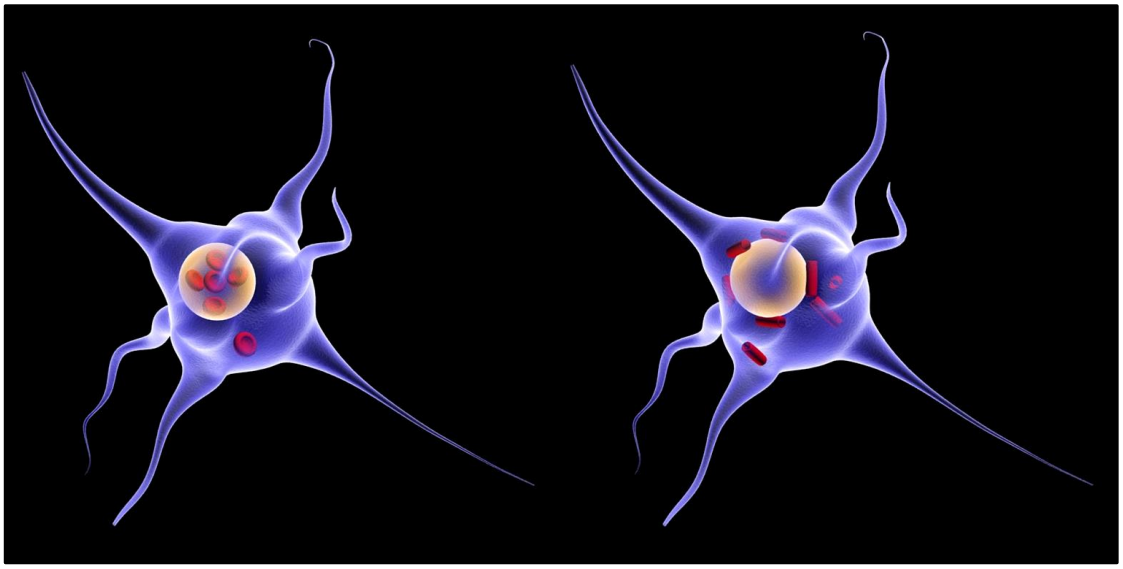

Manuscript based on this chapter has been submitted for publication.

3.1 Introduction:

Biocompatible nanoparticles showing blood brain barrier (BBB) permeation have tremendous applications in nanomedicine as they have the potential to be used as brain theranostics (therapeutic & diagnostics) for the treatment of many dreadful diseases like, brain tumors, HIV, Alzheimer's, Parkinson's *etc*.[1-8] However, the success of nanoparticles in the delivery of drugs in the brain depends not only on their ability to cross the BBB, but also their competence to transport the therapeutic molecules to the specific site within the brain cells.[9-16] For example, it is important to deliver several anticancer drugs and DNAs inside the nucleus as their actions are based on their interactions within the nucleus in the treatment of brain tumors, Parkinson's disease *etc*.[3,12,17] On the other hand, HIV drugs, siRNA, proteins *etc* elicit their therapeutic outcomes efficiently when present in the cytoplasmic region.[2,14,18] Nuclear delivery often demands the carrier nanoparticles to be tagged with nuclear localization signals, TAT peptides, or cationic polymers, in addition to their drug load.[19-28] For instance, the anti-cancer drug doxorubicin (DOX), having its therapeutic action in the nucleus, mostly localized in the cytoplasm of the HeLa cells with a little diffusion into the nucleus (Figure 1a).[9] Doxorubicin encapsulated in the mesoporous silica nanoparticles of size 20 nm (MSNs-20 nm) also failed to enter the nucleus (Figure 1a).[9] However, when the surface of the mesoporous silica nanoparticles loaded with doxorubicin was modified with the TAT peptide, the drug was effectively delivered in the nucleus of the cell (Figure 1a).[9] This clearly demonstrates the necessity of the nuclear targeting agents (Figure 1b).[9] On the other hand, cytoplasmic delivery for which endosomal escape is critical, the nanoparticles need to be modified with cationic polymers/lipids, cell-penetrating peptides (CPP),

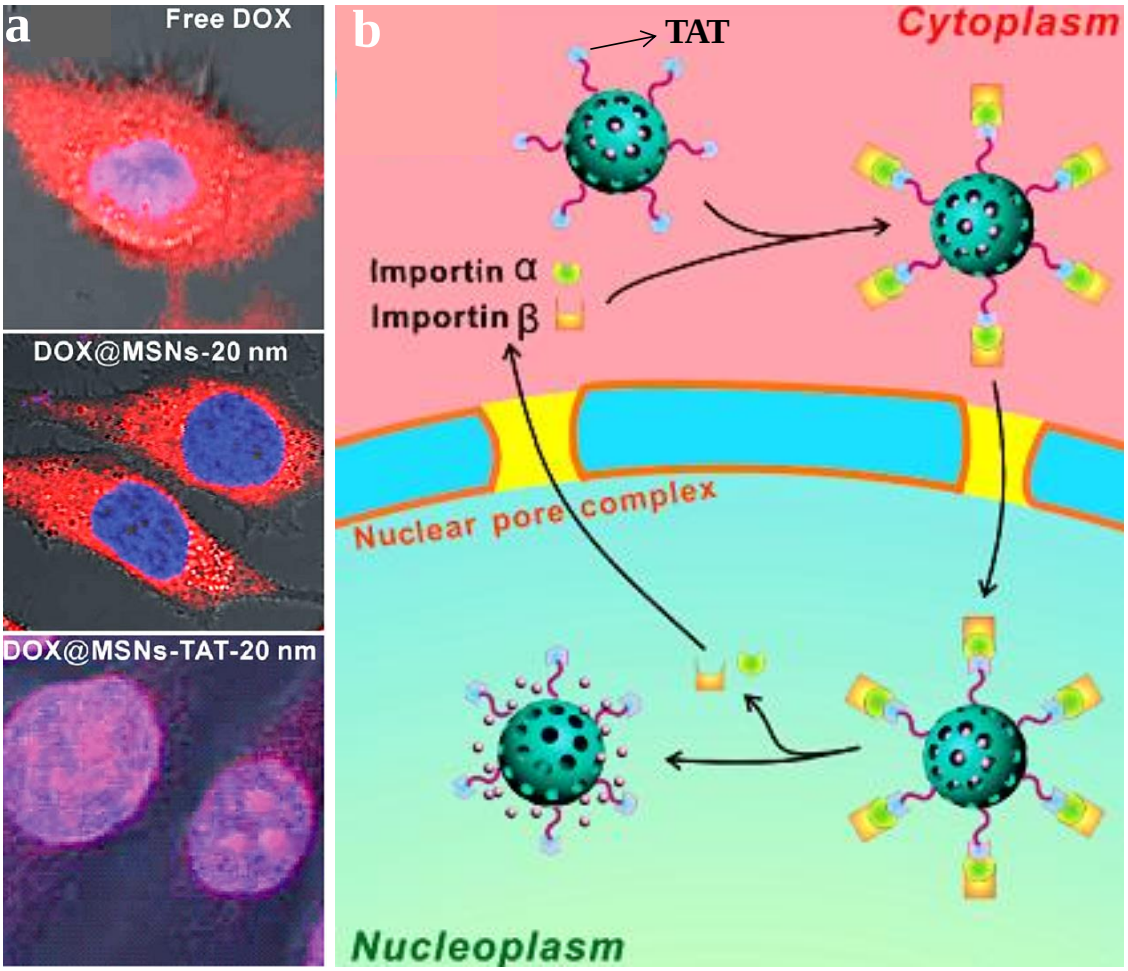

Figure 1: Nuclear delivery using TAT peptide. a) Intracellular distribution of free doxorubicin, DOX (top), doxorubicin loaded in mesoporous silica nanoparticles, DOX@MSNs-20 nm (centre), and doxorubicin loaded in MSNs-20 nm tagged with TAT, DOS@MSNs-TAT-20 nm (bottom). The red fluorescence is from DOX, and the blue fluorescence is from 4,6-diamidino-2-phenylindole (DAPI) used to stain the nuclei. b) Schematic showing mechanism of TAT mediated nuclear transport of drug loaded nanoparticles. Adapted with permission from reference 9. Copyright 2014, John Wiley and Sons.

pH-responsive carriers or endosome-disrupting agents.[29-37] Brinker *et. al.* showed that nanoporous silica nanoparticles (~100 nm) coated with a lipid bilayer and surface functionalized with polyethylene glycol and cell targeting peptide SP94 for human hepatocellular carcinoma, Hep3B cells (Figure 2a) could not escape the endosome (Figure

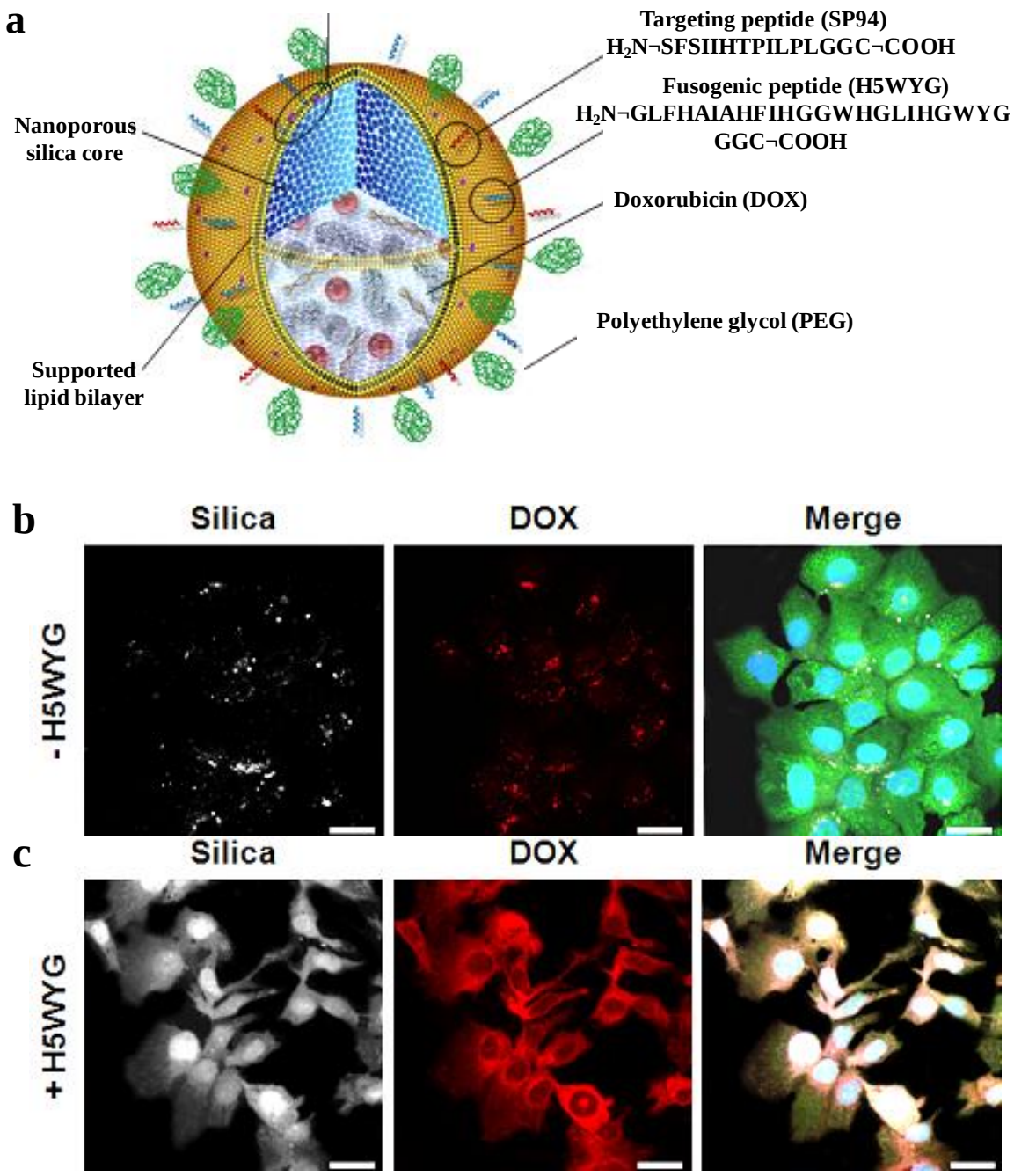

Figure 2: Cytoplasmic delivery following endosomal escape using fusogenic peptide (H5WYG). a) Schematic showing nanoparticle (~ 100 nm) of nanoporous silica coated with a lipid bilayer shell. The surface of the nanoparticles was modified with polyethylene glycol, a cell (human hepatocellular carcinoma, Hep3B cells) targeting peptide SP94, and a fusogenic peptide H5WYG. Doxorubicin was loaded in the nanoporous silica core. b) Nanoparticles without fusogenic peptide tagging were found to have punctate appearance inside the Hep3B cells, indicating endosomal

entrapment of the nanoparticles. c) H5WYG tagged nanoparticles were found to spread, following endosomal escape, throughout the cell. In (b) and (c) silica core was labeled with Alexa Fluor® 647 (white), Hep3B cells are stained with CellTracker™ (Green) CMFDA and DAPI (blue), and the red fluorescence is for doxorubicin. Adapted with permission from reference 22. Copyright 2011, Nature Publishing Group.

2b).[22] Model drug doxorubicin was loaded in the nanoporous silica core of these nanoparticles. However, when the surface of these particles was further modified with a fusogenic peptide H5WYG, the particles escaped endosomal compartment and distributed throughout the cell (Figure 2c).[22] Although, these surface modifications are essential for the cargo loaded nanoparticles to deliver the drugs at the site of its action within the cell, such complex alterations are often laborious and could alter the biological behaviour of the nanodrug.[38] Nanoparticles which could compartmentalize inside the brain cells by virtue of their size or shape could overcome many of these intricate functional modifications and would be of significant interest in brain theranostics. However, there are no reports on size or shape dependent, sub-cellular compartmentalisation of nanoparticles inside the brain cells, although size and shape dependent uptake of nanoparticles inside the cells are known.[39-43]

3.2 Scope of the present study:

In the present chapter, we have shown for the first time the shape-dependent compartmentalisation of carbon coated, iron oxide (Fe_3O_4@C) core-shell nanoparticles in the brain cells. The iron-oxide nanoparticles, Fe_3O_4, coated with carbon (Fe_3O_4@C) were used as core-shell particles in this study. Iron oxide was selected here for two reasons. Firstly, it is biocompatible and can be used as contrast agent for MRI[44,45] and secondly, it can be synthesized in different shapes.[46-49] The carbon shell over iron oxide nanoparticles was derived from glucose using hydrothermal carbonization method.[50] The glucose derived carbon spheres were earlier shown to cross the BBB and preferably enter cell membranes rich with glucose receptors (such as glial and cancerous cells) and further into their nucleus.[51-53] These biocompatible, fluorescent carbon spheres were utilized to deliver the membrane impermeable molecule, CTPB inside the cell in order to modulate the gene expression.[54] Amalgamating glucose derived carbonaceous materials with magnetic iron oxide would enable them to be used as brain theranostics by coupling MRI imaging, magnetic based targeting and drug delivery, hyperthermia, etc.[55-59] Moreover, the increasing use of carbon nanomaterials of different morphologies (nanotubes, nanospheres, nanosheets etc.,) as well as iron oxide in biomedicine stresses the need for understanding the shape-dependent behavior within the brain cell so as to utilize them for better theranostic effect.[60-65] To our knowledge this is the first *in vivo* report on shape induced sub-cellular compartmentalisation of nanoparticles within the mice brain. Furthermore, using this shape-dependent, sub-cellular localization property of nanoparticle carrier we have demonstrated the importance of delivering small molecule

HAT activator, TTK21[51], inside the mice brain cell nucleus to get better efficacy in comparison to cytoplasmic delivery.

3.3 Materials and Methods:

a. Materials:

Iron (III) chloride hexahydrate, ammonium hydrogen phosphate, sodium sulphate, sodium acetate, polyethylene glycol 2000, ethylene glycol were purchased from SDFine chemicals (India). α-D(+)-Glucose, Poly(sodium 4-styrenesulfonate) (PSS), Poly(diallyldimethylammonium chloride) (PDADMAC), α-tubulin, DAPI, and HEPES buffer were purchased from Sigma Aldrich. All the chemicals were used as received from the company. 21.5 ml Teflon lined autoclave was constructed. MilliQ water and ethanol was used where ever needed.

b. Synthesis of Fe_2O_3 nanoparticles:

Biconcave: Synthesis of Fe_2O_3 nanoparticles of biconcave morphology was optimized in our laboratory. In a typical procedure 16.8 ml aqueous solution of 0.02 M $FeCl_3.6H_2O$, 1.8 x 10^{-4} M $NH_4H_2PO_4$, and 5.5 x 10^{-4} M Na_2SO_4 was taken in the 21.5 ml Teflon lined autoclave and heated at 220°C for 48 hours. The autoclave was cooled to room temperature. Product was centrifuged at 7000 rpm for 10 minutes. Washing was done using water (4 times) and ethanol (1 time) followed by overnight drying at 60°C.

Spindle: Synthesis of Fe_2O_3 nanoparticles of spindle morphology was carried out using a reported procedure[53]. To obtain the desired size of the spindles the synthesis process was optimized. In a typical procedure 16.8 ml aqueous solution of 0.05 M

$FeCl_3.6H_2O$, 0.01 M $NH_4H_2PO_4$ was taken in the 21.5 ml Teflon lined autoclave and heated at 220°C for 2 hours. The autoclave was cooled to room temperature. Product was centrifuged at 7000 rpm for 10 minutes. Washing was done using water (4 times) and ethanol (1 time) followed by overnight drying at 60°C.

Nanotube: Synthesis of Fe_2O_3 nanoparticles of nanotube morphology was carried out using a reported procedure[54]. To obtain the desired size of the nanotubes the synthesis process was optimized. In a typical procedure 16.8 ml aqueous solution of 0.02 M $FeCl_3.6H_2O$, 5.0 x 10^{-4} M $NH_4H_2PO_4$, and 5.5 x 10^{-4} M Na_2SO_4 was taken in the 21.5 ml Teflon lined autoclave and heated at 220°C for 48 hours. The autoclave was cooled to room temperature. Product was centrifuged at 7000 rpm for 10 minutes. Washing was done using water (4 times) and ethanol (1 time) followed by overnight drying at 60°C.

c. Synthesis of Fe_3O_4 nanoparticles:

The Fe_2O_3 spindles, biconcaves, and nanotubes were converted to Fe_3O_4 by heating them in quartz boat at 275°C, 275°C, and 300°C respectively in the flow of dilute H_2 (5% H_2 in N_2) for 7 hours with a heating rate of 2.5°C/min.

d. *Synthesis of Fe_3O_4 spheres:*

The spheres of Fe_3O_4 were synthesized by dissolving 0.567 g $FeCl_3.6H_2O$, 5.024 g of sodium acetate, and 0.42 g of polyethylene glycol 2000 in 16.8 of ethylene glycol and heating the solution in a 21.5 ml Teflon lined autoclave at 200°C for 6 hours. Resulting product was isolated magnetically followed by 6 washing and magnetic isolation step with ethanol. Further, the product was dried at 60°C in a hot air oven for overnight.

e. Carbon coating on the Fe_3O_4 nanoparticles:

The magnetic nanoparticles of different shapes were first coated with polyelectrolytes poly(sodium 4-styrenesulfonate) (PSS) and poly**(**diallyldimethylammonium chloride**)** **(**PDADMAC). 25 mg of the nanoparticles were dispersed in 30 ml aqueous solution of PSS (2 mg/ml) having 0.5 M NaCl followed by constant vortexing for 30 minutes. The nanoparticles were isolated magnetically and were washed with water 3 times. The PSS coated nanoparticles were then redispersed in 30 ml aqueous solution of PDADMAC (2 mg/ml) having 0.5 M NaCl and were constantly vortexed for 30 minutes. This was followed by magnetic separation and three times washing with water. The polyelectrolyte coated nanoparticles were then dispersed in aqueous solution of α-D(+)-Glucose (1.5 g glucose in 16.8 ml water) which was then transferred to a 21.5 ml Teflon lined autoclave and heated at 180^{o}C for 5, 5, 4, and 7 hours for sphere, spindle, biconcave, and nanotube respectively. Further the autoclaves were cooled to the room temperature and products were isolated magnetically. Washing with water (3 times) and ethanol (4 times) were carried out and product was dried for 2 hours at 60^{o}C in a hot air oven.

f. Characterization:

Morphology of the samples was analysed by FESEM (FEI NovaNano SEM-600, Netherlands). TEM images were acquired with a JEOL JEM 3010 instrument (Japan) operated with an accelerating voltage of 300 kV. XRD characterization was done at room temperature with a Bruker-D8 diffractometer employing Cu Ka. Zeta potential and hydrodynamic size were measured at 25^{o}C using Zetasizer Nano ZS (Malvern

Instruments). FTIR Spectra were acquired on Bruker IFS 66v/S instrument in the range of 4000–400 cm^{-1}. PL spectra were taken with Perkin-Elmer model LS 55 luminescence spectrometer. Magnetic measurements were carried out with a vibrating sample magnetometer using the physical properties measurement system (Quantum Design, US). Confocal laser scanning fluorescence microscope imaging was carried out on a Zeiss LSM 510 Meta (Carl Zeiss). Inductively coupled plasma optical emission spectroscopy (ICP-OES) was carried out with Perkin-Elmer Optima 7000 DV instrument.

g. Zeta potential and hydrodynamic size measurement:

Zeta potential and hydrodynamic diameter were measured at pH 7.4 in 10 mM HEPES buffer. For zeta potential measurement the nanoparticles concentration was 100 μg/ml while for size measurement it was 25 μg/ml.

h. Cell culture:

U87 MG (ATCC® HTB-14™) glial cells and NCI-H1299 (ATCC® CRL-5803™) lung carcinoma cells were cultured as monolayer on poly(L-lysine)-coated cover slips in DMEM (Sigma) medium and were treated with 2.5 μg/ml of different shaped nanoparticles for 12 hours. Cells were fixed with 4% paraformaldehyde after the treatment. Then primary antibody (α-tubulin) staining (1:1K) for cytoplasm was carried out for 1 hour followed by addition of A488 dye tagged secondary antibodies for 45 minutes. Hoechst 33258 (10 μg/ml) was used for nuclear counter staining. Then the cover slips were mounted with 70% glycerol after washing twice with PBS having 0.1% Triton

X-100. Images were acquired on a Carl Zeiss Laser Scanning Microscope (LSM510 META).

i. MTT assay:

5,000 of U87 cells were seeded in 96-well plate and cultured for 12 h. For dose-dependent experiments, cells were treated with 5 and 10 µg/ml of nanoparticles (Sph, SP, BC, and NT), for 24 hours, in duplicates. Water was used as a control. This was followed by incubation with 20 µl of MTT (5 mg/ml) for 3 h. Then 100 µl of DMSO was added to solubilise formazan obtained from the reduction of MTT by the mitochondrial reductase of the viable cells. Absorbance was recorded at 570 nm in ELISA reader (VERSA Max micro plate reader, Molecular Devices). The data was normalized with control and plotted with mean and standard error.

j. Animal Experiments:

BALB/c female mice were intra-peritoneally injected with 1 mg of BC (for 1, 3, 6 and 14 days) and NT (for 3 and 6 days) for different periods. After that the mice were sacrificed and the brain tissue was fixed in 10% formalin. Then paraffin blocks were prepared and 15 µm paraffin sections were made for nanoparticle localization study. Hoechst 33258 was used for nuclear staining and the imaging was carried out on a Zeiss Laser Scanning Microscope (LSM510 META).

k. Conjugation of TTK21 on the surface of Fe_3O_4@C:

The covalent tagging of TTK21, through the reaction between -NH group of TTK21 and –COOH groups of nanoparticles, was carried out with nanoparticles of

biconcave and nanotube morphology. However, the possibility of physical adsorption of TTK21 on the nanoparticle surface is not ruled out. To a dilute solution (5 mg in 70 ml) of BC & NT nanoparticles in dichloromethane (DCM) 7 µl of $SOCl_2$ and 2-5 drops of dimethylformamide (DMF) were added. This chlorination process of the surface of carbon coating was carried out for two hours at 50^oC under constant sonication. Excess $SOCl_2$ was removed by washing twice with DCM and evaporating the solvent. The chlorinated nanoparticles were re-dispersed in 70 ml DCM and 5 mg of TTK21 was added to this dispersion. This was followed by the addition of 2-4 drops of triethylamine base. The reaction was carried out for 4 hours at 50^oC under constant sonication. The final product was separated magnetically, washed with DCM 7-10 times and dried in a hot air oven at 60^oC for 1 hour.

l. HAT activation experiment:

BALB/c female mice were treated with 1 mg/ml of BC and NT in triplicates. Mice were sacrificed after 3 days and brain tissue was collected and fixed in 10% formalin. 5µm sections of the paraffin block of brain tissue were made for immunohistochemistry (IHC). The slides made for tissue slices were deparaffinised and rehydrated in graded alcohol. Antigen retrieval was done in citrate buffer for 10 min and kept in 3% H_2O_2 (made in methanol) for 15 min. To avoid non-specific binding, blocking was done with 5% non-fat milk and then incubated with rabbit polyclonal anti-H3K9ac primary antibody for overnight at room temperature in humid chamber. After washing twice with PBS, slides were incubated with biotin labelled secondary antibody and then peroxidase streptavidin was added for 40 minutes. The antigen signal was developed using DAB

solution and then counter stained with diluted haematoxylin. Slides were mounted with DPX and observed under Zeiss bright field microscope. Immunohistochemistry (IHC) was evaluated by counting 300-400 cells from 4 different regions in each tissue sections and percentage of positive cells (brown colour which was indicative of antibody staining) was plotted between the groups for analysis.

m. Real-time qRT-PCR:

Paraffin sections of the brain of BALB/c mice treated with different nanoparticles were made. After de-paraffinizion in xylene the tissues were homogenized with a Dounce in TRIzol reagent (Invitrogen). RNAs were extracted using chloroform followed by two times precipitation with ethanol. RNA samples were denatured for 10 min at 70°C. The cDNA synthesis was performed on 500 ng of total RNA using M-MLV reverse transcriptase enzyme (sigma). The qRT-PCR conditions were 3 minutes at 94°C, followed by 40 cycles of 45 seconds at 94°C and 30 seconds at 65°C in BIORAD CFX96 Real Time thermo-cycler using specific primer of BDNF and actin. ΔCt value were calculated and plotted with fold change taking mean ± SEM.

3.4 Results and Discussions:

Iron oxide, Fe_2O_3 nanoparticles with various shapes like spindles ($Fe_2O_{3\text{-}SP}$), and nanotubes ($Fe_2O_{3\text{-}NT}$) were prepared using hydrothermal method reported elsewhere.[49] Fe_2O_3 nanoparticles of biconcave ($Fe_2O_{3\text{-}BC}$) morphology were synthesized in our lab by modifying the reported synthetic procedure for nanotubes (see methods and materials section). Field emission scanning electron microscope (FESEM) images (Figure 3) of as synthesized α-Fe_2O_3 nanoparticles of all the three morphologies show that they are uniform in size and shape (their dimensions given in figure 4). The peaks in their X-ray diffraction (XRD) pattern (Figure 5a) can be indexed for pure corundum structure of hematite (JCPDS no. 33-0664). The hematite particles of different geometry were then converted to magnetic Fe_3O_4 by heating them in hydrogen flow at around 270^{o}C temperatures (see methods and materials section) without affecting their shape and size

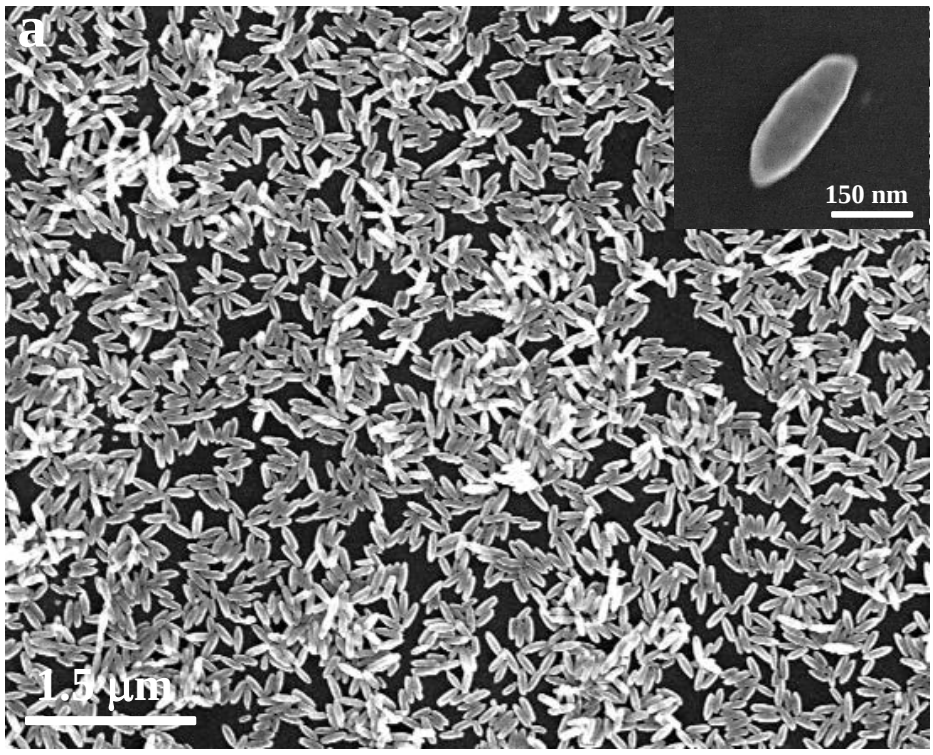

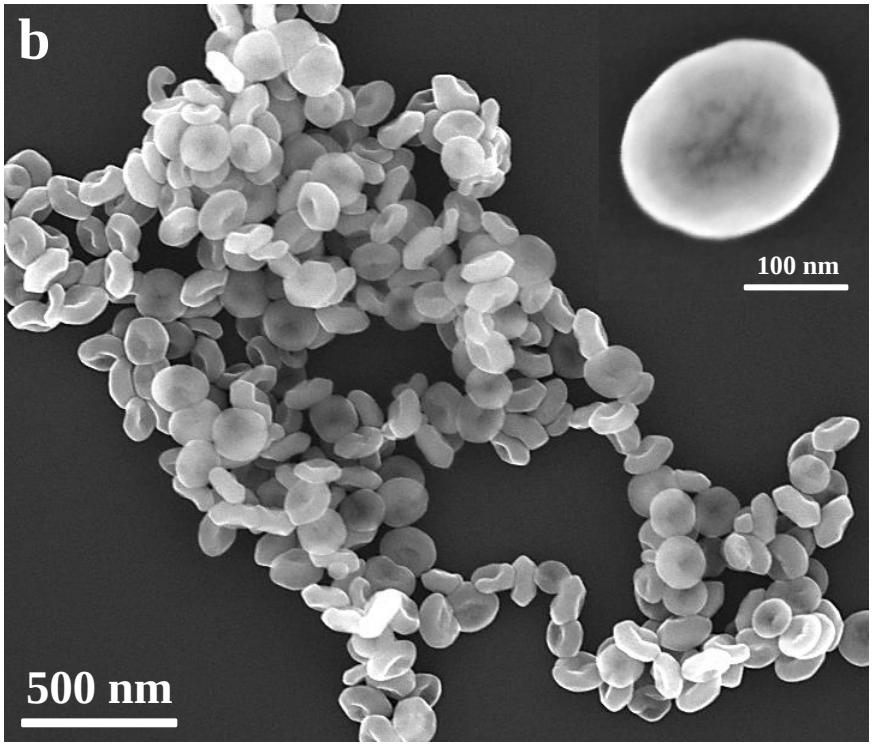

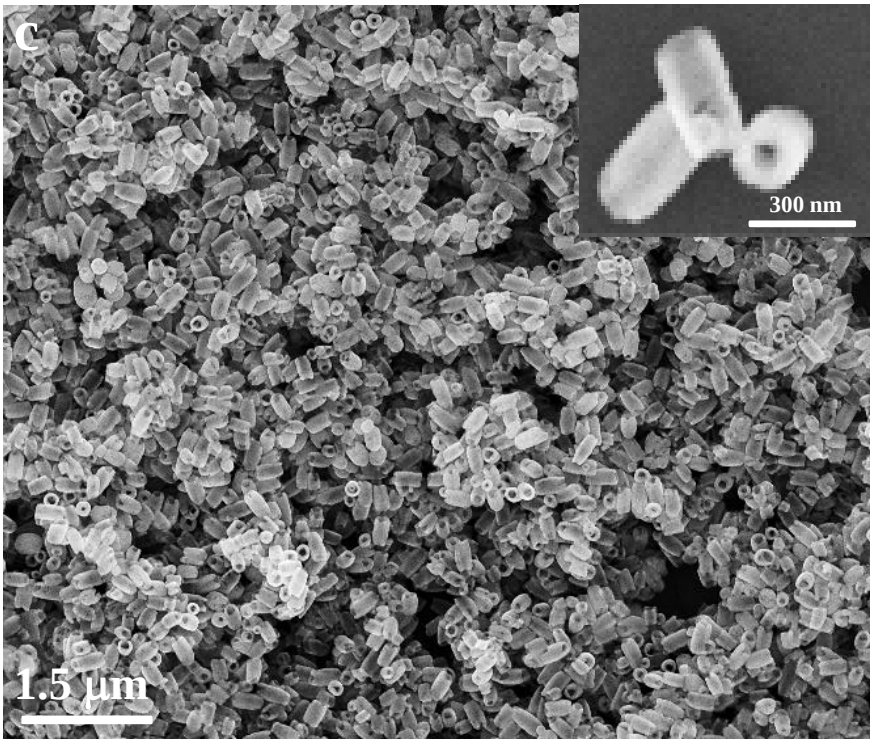

Figure 3: Field emission scanning electron microscope (FESEM) images of different shapes of Fe_2O_3. a) Spindle, b) biconcave, and c) nanotube. Insets show magnified images of the respective nanoparticles.

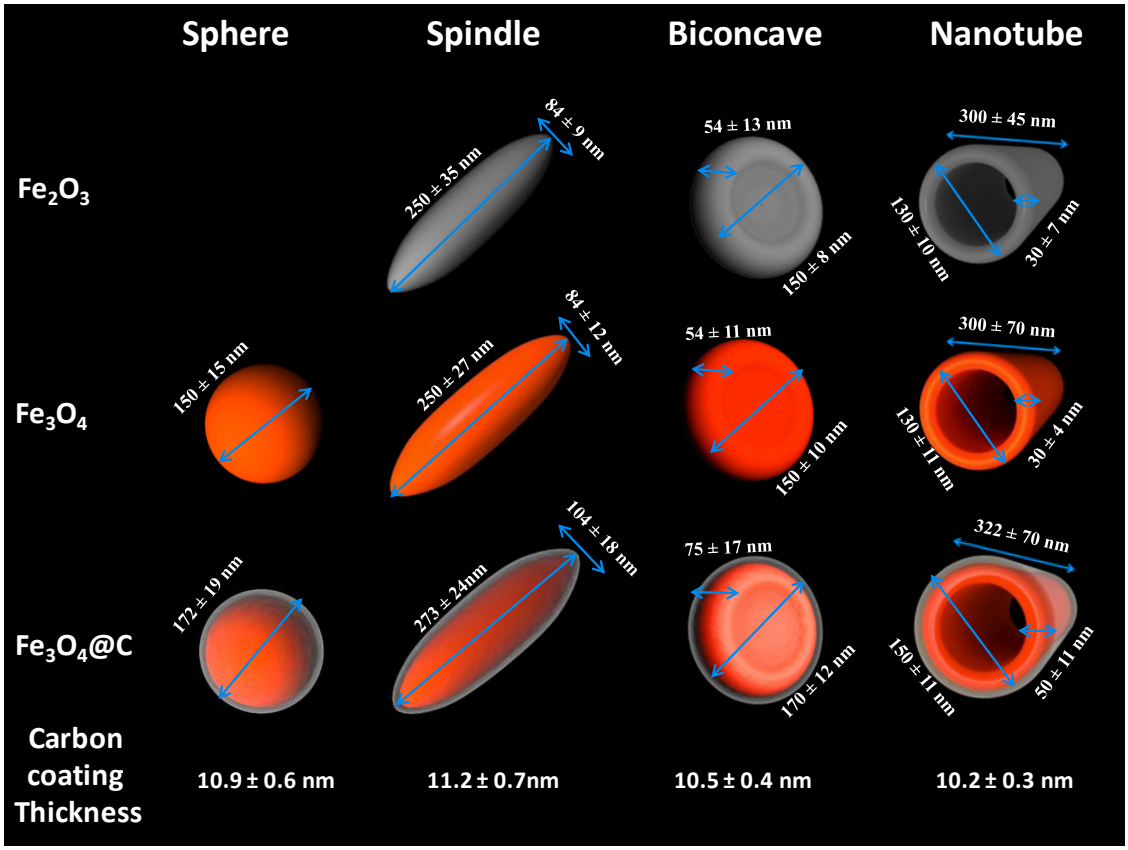

Figure 4: Dimensions of various nanoparticles. Measurements were carried out over a minimum of 250 nanoparticles using FESEM images. The carbon coating thickness was measured (over ~120 particles) using transmission electron microscope (TEM) images for Fe_3O_4@C nanoparticles.

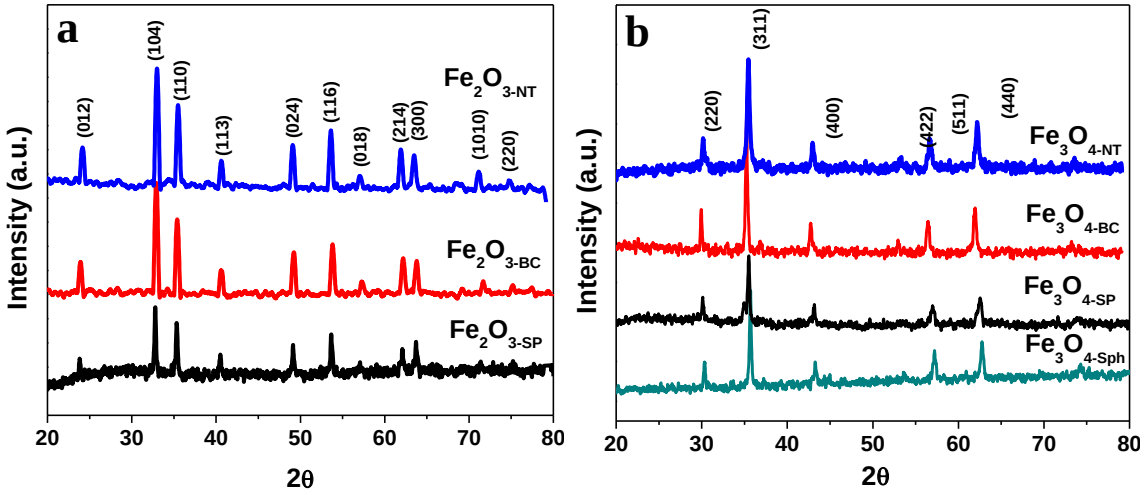

Figure 5: Powder X-ray Diffraction pattern of a) Fe_2O_3, and b) Fe_3O_4 nanoparticles.

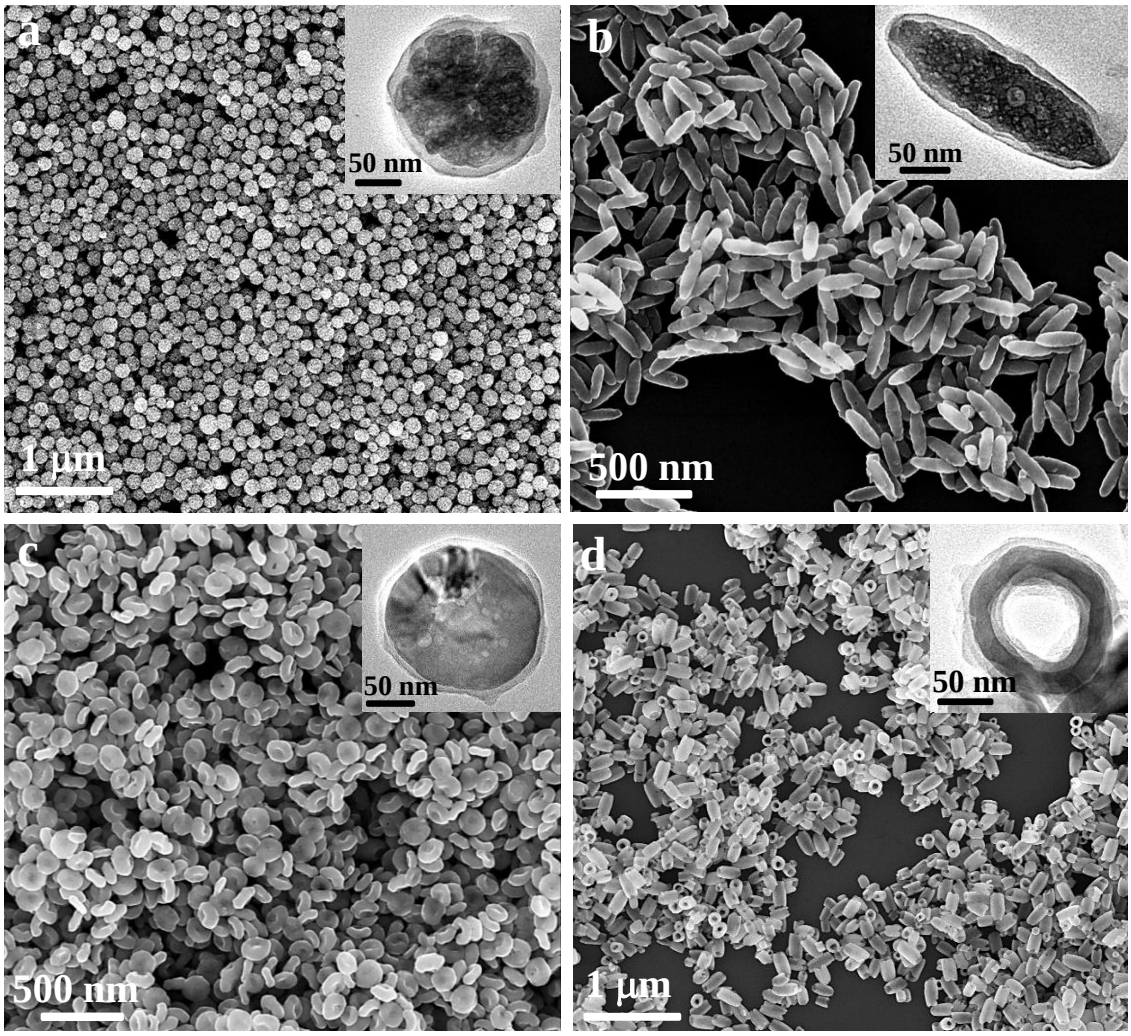

Figure 6: FESEM images of different shapes of Fe_3O_4. a) Sphere, b) Spindle, c) Biconcave, d) Nanotube. The insets show transmission electron microscope (TEM) images of carbon coated nanoparticles of the respective shape.

(Figure 6b,c,d). Fe_3O_4 of spherical ($Fe_3O_{4\text{-Sph}}$) morphology (Figure 6a) were directly synthesized using a reported method.[46] The XRD patterns (Figure 5b) of all the nanoparticles ($Fe_3O_{4\text{-Sph}}$, $Fe_3O_{4\text{-SP}}$, $Fe_3O_{4\text{-BC}}$, & $Fe_3O_{4\text{-NT}}$) were indexed as phase pure inverse spinel structure of magnetite (JPCDS no. 11-0614). The nanoparticles of four different geometries were having similar size at least in one of their dimensions (Figure 4).

The magnetic nanoparticles of different shapes, were then coated with glucose derived carbon. Since, the nuclei formed in the process of glucose-carbonization process are negatively charged,[66] the nucleation of carbon on the surface of Fe_3O_4 nanoparticles would be favored, only if the surface charge of nanoparticles is positive. However, the zeta potential values (pH 7) for all the Fe_3O_4 nanoparticles were found to be considerably negative (Figure 7).

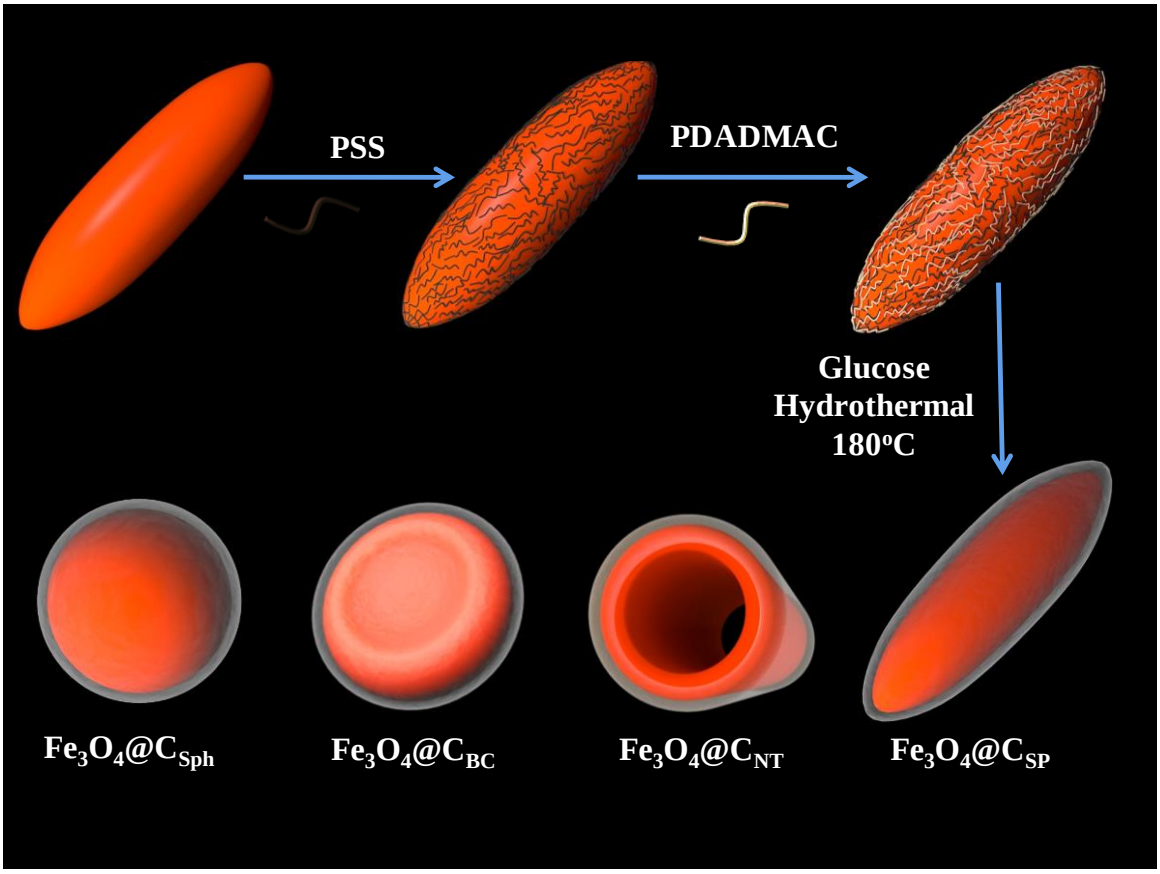

Scheme 1: Schematic showing the process of carbon coating on Fe_3O_4 spindles. The Fe_3O_4 particles are shown in orange colour and the gray coating is carbon. The Fe_3O_4 nanoparticles of sphere, biconcave, and nanotube morphology coated with carbon (using similar procedure) are shown for comparison.

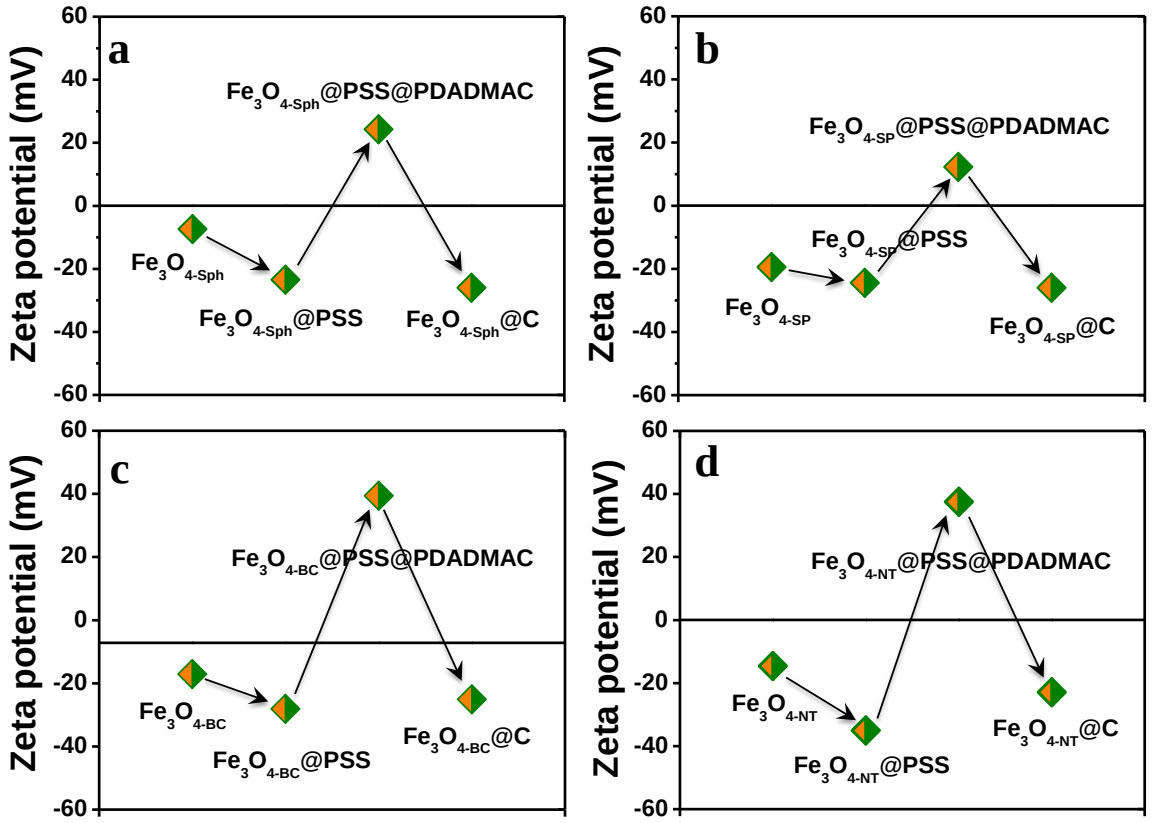

Figure 7: Zeta potential measurements at various steps of carbon coating. (a) Sphere, (b) spindle, (c) biconcave, and (d) nanotube. These measurements were carried out in 10 mM HEPES buffer, pH 7.4.

To achieve a positive surface charge for the nanoparticles, we carried out layer-by-layer assembly of polyelectrolyte's, a) Poly(sodium 4-styrenesulfonate) (PSS) and b) Poly**(**diallyldimethylammoniumchloride**)** (PDADMAC) on the surface of the nanoparticles (Scheme 1). PSS is known to coat on neutral or slightly negative surfaces,[67] and coating PSS shifts the surface charge towards more negative side (Figure 7). Then PDADMAC coating was carried out to make the zeta potential positive (Figure 7). Finally, the carbon coating was carried out hydrothermally on the positively charged nanoparticles, by dispersing the Fe_3O_4 nanoparticles of desired shape in an aqueous glucose solution of known concentration, followed by heating the mixture at 180^{o}C. The

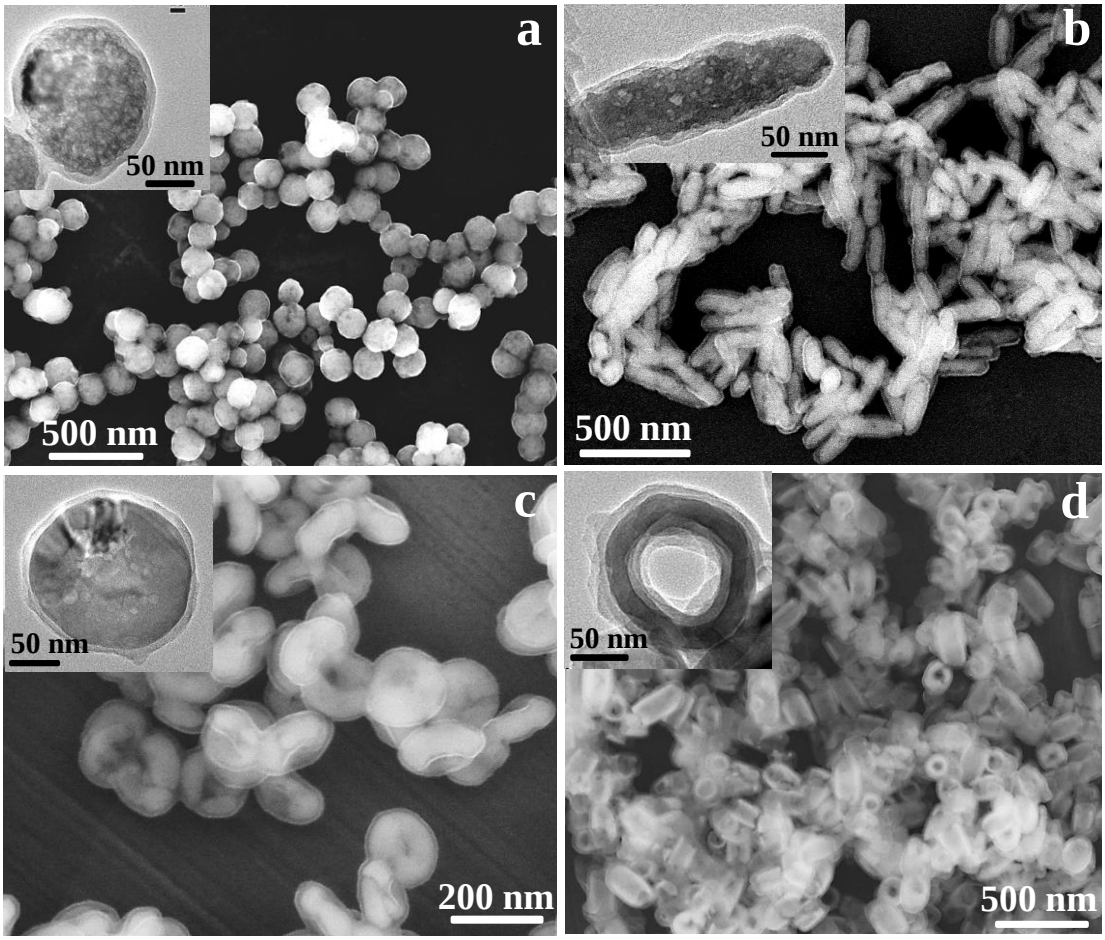

Figure 8: Imaging Fe_3O_4@C nanoparticles. FESEM images of (a) $Fe_3O_4@C_{Sph}$, (b) $Fe_3O_4@C_{SP}$, (c) $Fe_3O_4@C_{BC}$, (d) $Fe_3O_4@C_{NT}$. The insets show transmission electron microscope (TEM) images of carbon coated nanoparticles of the respective shape.

coating thickness of the glucose derived fluorescent carbon layer on different shape nanoparticles was optimized to be around 10 nm (Figure 8) by varying the time duration of coating (see methods and materials section). The crystal structure of all the Fe_3O_4 nanoparticles remained intact as confirmed by their XRD patterns (Figure 9a). The energy dispersive X-ray (EDX) analysis (Figure 9b) shows the presence of carbon in addition to Fe and O from Fe_3O_4 nanoparticles, resulting from the carbon coating. The existence of phosphorous in the EDX spectra of $Fe_3O_4@C_{SP}$, $Fe_3O_4@C_{BC}$, $Fe_3O_4@C_{NT}$ is again due to Fe_3O_4 nanoparticles, as phosphate ions were used as stabilizing agents in their synthesis.

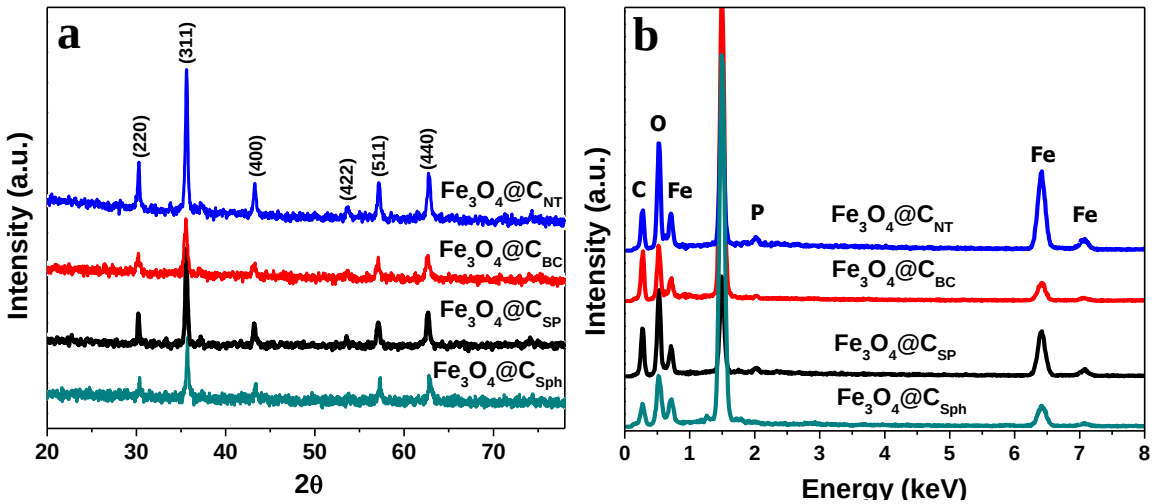

Figure 9: Structure and elemental analysis of carbon coated magnetite nanoparticles. a) Powder X-ray Diffraction pattern. b) The energy dispersive X-ray (EDX) analysis.

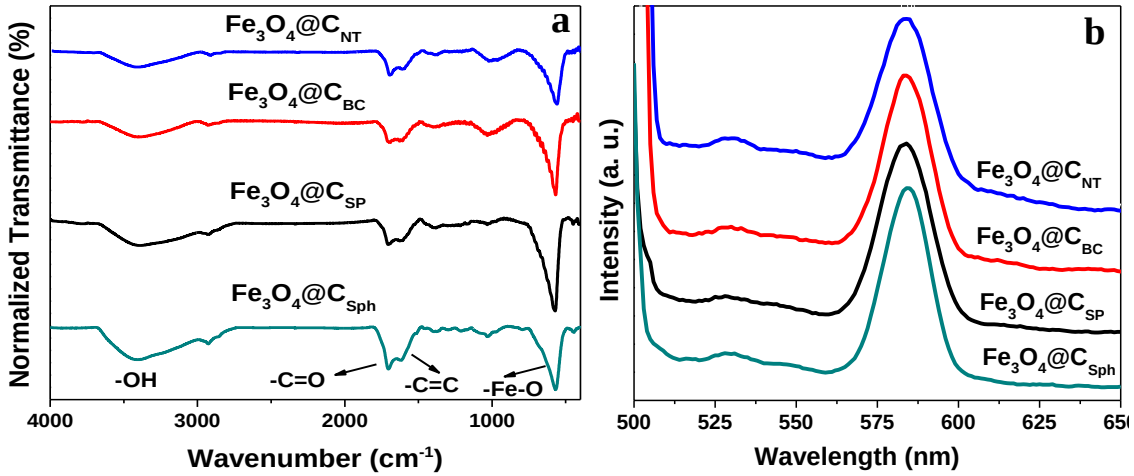

Figure 10: Spectroscopic characterization of Fe_3O_4@C nanoparticles. a) Infrared spectra. b) Photoluminescence spectra with excitation wavelength being 488 nm.

The presence of O-H, C=O, and C=C stretching vibrations for the Fe_3O_4@C in FTIR spectra (Figure 10a) suggests that the surface chemistry of carbon shell is similar to that of carbon spheres prepared from glucose.[54] The emission at ~590 nm associated with carbon coating can be seen in all the shapes on exciting the Fe_3O_4@C nanoparticles at 488 nm (Figure 10b). The Fe_3O_4@C particles were found to be ferromagnetic and have

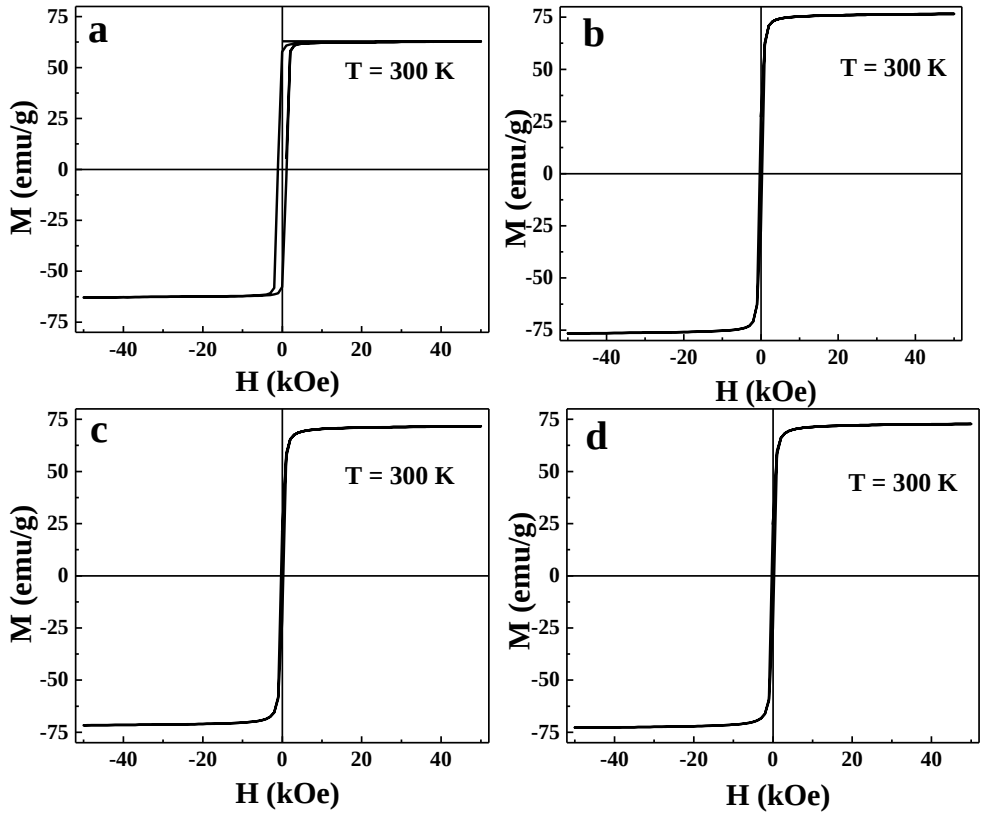

Figure 11: Isothermal magnetization Vs applied field curve for Fe_3O_4@C nanoparticles. a) $Fe_3O_4@C_{Sph}$, b) $Fe_3O_4@C_{SP}$, c) $Fe_3O_4@C_{BC}$, and d) $Fe_3O_4@C_{NT}$. The measurements were carried out at 300 K.

similar saturation magnetization values (70 ± 8 emu/g) (Figure 11), at room temperature, due to the presence of magnetite core. The zeta potential measurements of all the carbon coated Fe_3O_4 nanoparticles of different shapes shows similar values about -44.0 ± 4.0 mV (Figure 12a) at pH 7.4. To study the effect of serum protein adsorption on the surface charge of the nanoparticles, we carried out soaking of all different shape nanoparticles with 10% fetal bovine serum for two hours and measured their zeta potentials. The adsorption of serum proteins makes the surface charge of nanoparticles less negative, from -44.0 ± 4.0 mV to -19.0 ± 2.0 mV, and the extent of change is more or less equal for

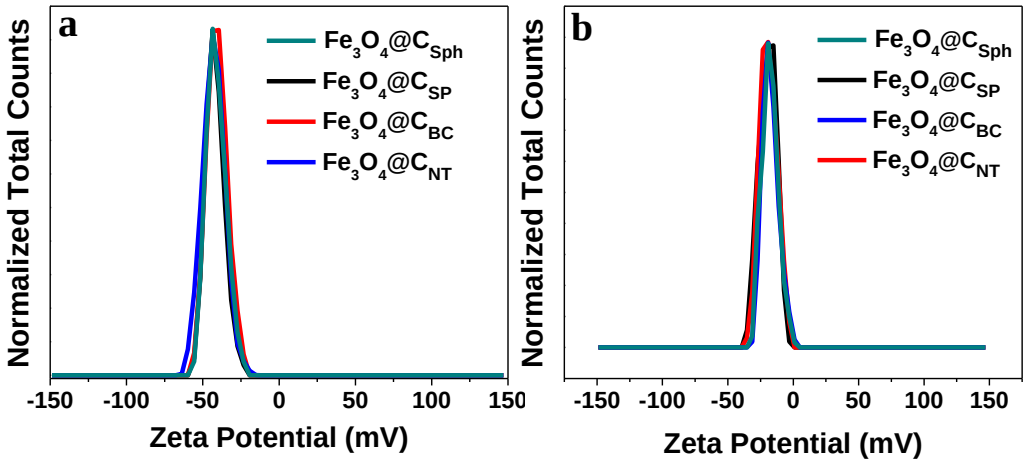

Figure 12: Surface charge and Serum protein adsorption. a) Zeta potential of Fe_3O_4@C nanoparticles. b) Zeta potential of Fe_3O_4@C nanoparticles soaked with 10% fetal bovine serum for 2 hours in PBS buffer of pH 7.4 at 37°C. Particles were separated magnetically, washed twice with PBS and were re-suspended in HEPES buffer, pH 7.4 for the zeta potential measurements. All zeta potential measurements were carried out in 10 mM HEPES buffer, pH 7.4.

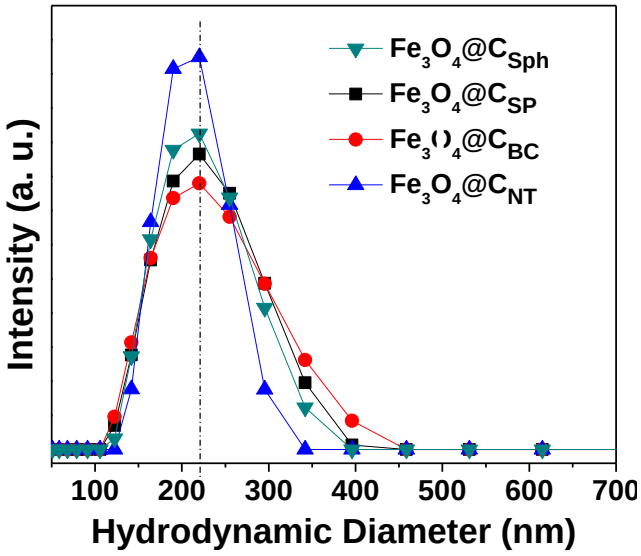

Figure 13: Hydrodynamic size of Fe_3O_4@C nanoparticles using dynamic light scattering. Measurement was carried out in 10 mM HEPES buffer, pH 7.4.

all the nanoparticles (Figure 12b). Figure 13 shows particle size distribution measured using dynamic light scattering (DLS). The hydrodynamic diameter of Fe_3O_4@C for all the geometries are around same, 220 ± 35 nm, which ensures similar diffusive transport for all the nanoparticles irrespective of their geometry.

The cellular uptake of Fe_3O_4@C nanoparticles of different morphologies was carried out with U87 MG (ATCC® HTB-14™) glial cells as it was shown earlier that the glucose derived carbon spheres have strong specificity for the GLUT1 receptor containing glial cells.[53] The MTT assay (Figure 14) with U87 glial cells indicated that all the Fe_3O_4 nanoparticles did not show any significant cytotoxicity. Glial cells incubated with biocompatible Fe_3O_4@C nanoparticles of different shapes for 12 hours shows

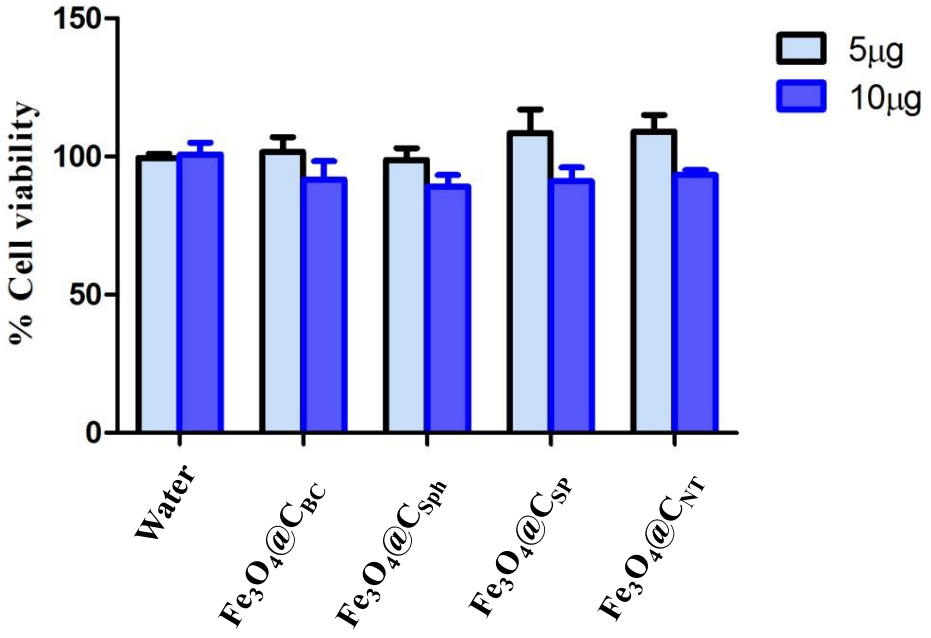

Figure 14: Toxicity of Fe_3O_4@C nanoparticle as measured by MTT-assay. The U87 cells were treated with 5 µg and 10 µg of different nanoparticle (as indicated) for 24 hours and subjected to MTT assay. Water was taken as control for the experiment.

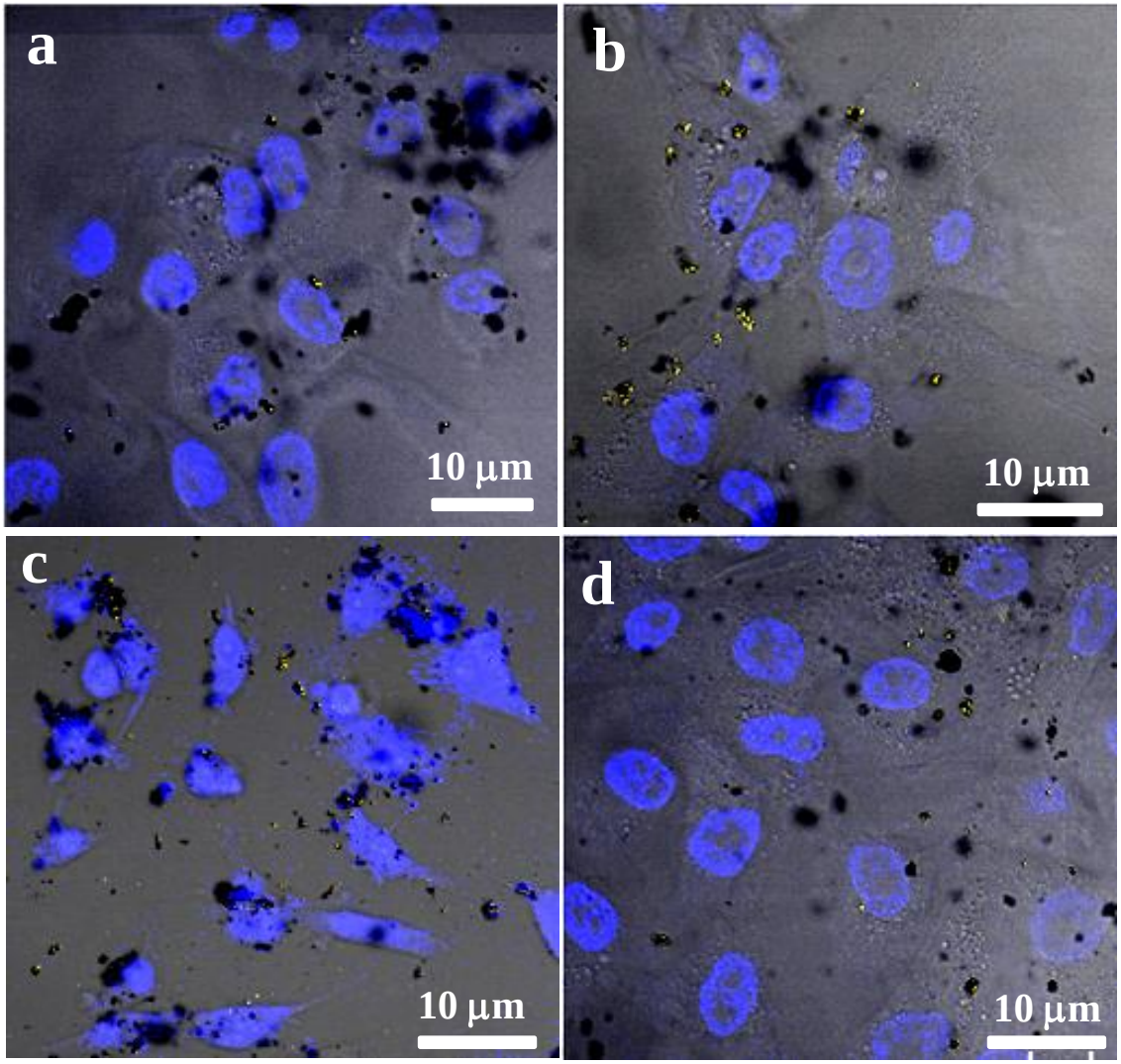

Figure 15: Cellular Entry in U87 glial cells. Confocal microscope images of cells treated with a) $Fe_3O_4@C_{Sph}$, b) $Fe_3O_4@C_{SP}$, c) $Fe_3O_4@C_{BC}$, and d) $Fe_3O_4@C_{NT}$. Yellow – nanoparticle fluorescence, Blue – DAPI staining for nucleus.

significant uptake for all the morphologies (Figure 15). However, the subcellular localization of $Fe_3O_4@C$ nanoparticles varied remarkably with shape. While, the biconcave particles ($Fe_3O_4@C_{BC}$) preferably localized in the nucleus, the spindle ($Fe_3O_4@C_{SP}$) and nanotube ($Fe_3O_4@C_{NT}$) geometries are seen mostly in the cytoplasm (Figure 16). Spheres ($Fe_3O_4@C_{Sph}$) were distributed in both cytoplasm and nucleus

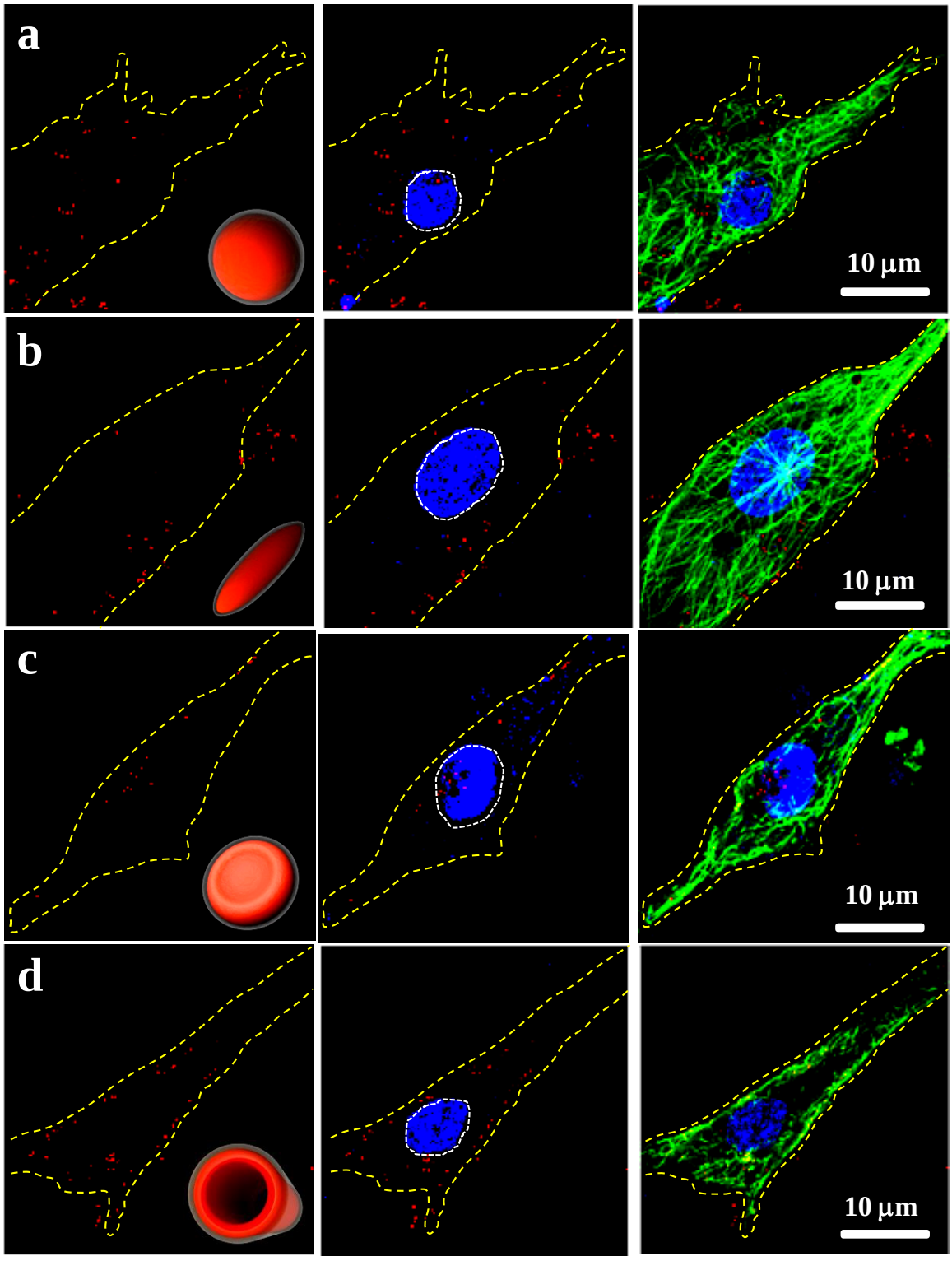

Figure 16: Differential Cellular uptake of nanoparticles in U87 glial cells. Confocal microscope images showing nanoparticle localization in the different cellular compartments, panel a) $Fe_3O_4@C_{Sph}$, panel b) $Fe_3O_4@C_{SP}$, panel c) $Fe_3O_4@C_{BC}$, and panel d) $Fe_3O_4@C_{NT}$. The yellow

and white dotted lines define the boundaries of the cell and the cell nucleus respectively. In every panel the first image shows nanoparticles (red), the middle images show nanoparticles (red) and nucleus (blue, DAPI staining), and the right most images show nanoparticles (red), nucleus (blue), and cytoplasm (green, β-tubulin staining). The inset in the first image of every panel shows the respective nanoparticle morphology.

(Figure 16). Quantitative estimation of number of cells having the nanoparticles of particular shape inside the nucleus clearly indicates the strong preference of biconcave particles to the nuclear internalization. More than 95% of the total cells (250) show the

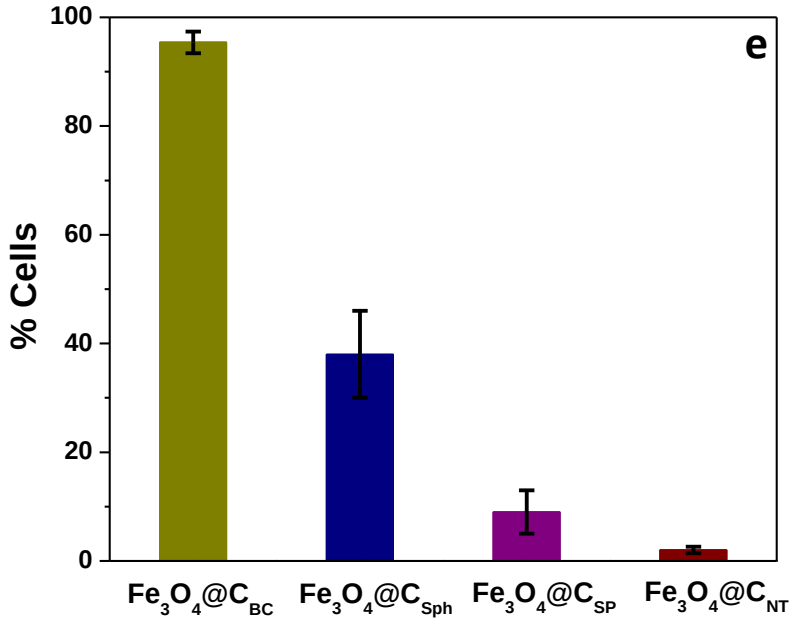

Figure 17: Percentage of nanoparticles populated cells having their nucleus positive with the particles for different shape nanoparticles. Counting was done over 250 cells.

nucleus positive for $Fe_3O_4@C_{BC}$ and less than 2% of the total cells show nucleus positive for the $Fe_3O_4@C_{NT}$ (Figure 17). No nuclear entry for nanotubes (Figure 18), even after 36 h of incubation with U87 MG glial cells strongly suggests that the nanotube morphology has the difficulty in crossing the nuclear membrane in spite of its presence in the cytoplasm. We also carried out similar experiments with the H1299 lung carcinoma

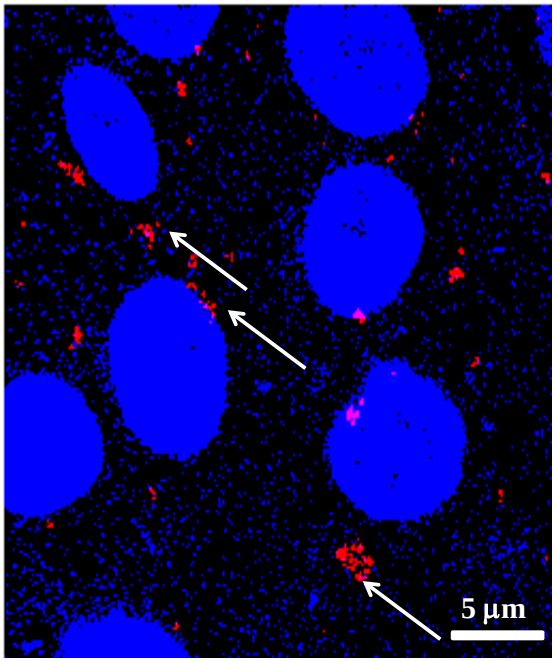

Figure 18: Prolonged treatment of U87 glial cells with $Fe_3O_4@C_{NT}$ nanoparticles. Confocal microscope image of $Fe_3O_4@C_{NT}$ treated cells for the duration of 36 hours. Red – nanoparticle fluorescence, Blue – DAPI staining for nucleus. Arrows point out the red coloured nanoparticles lying outside the nucleus.

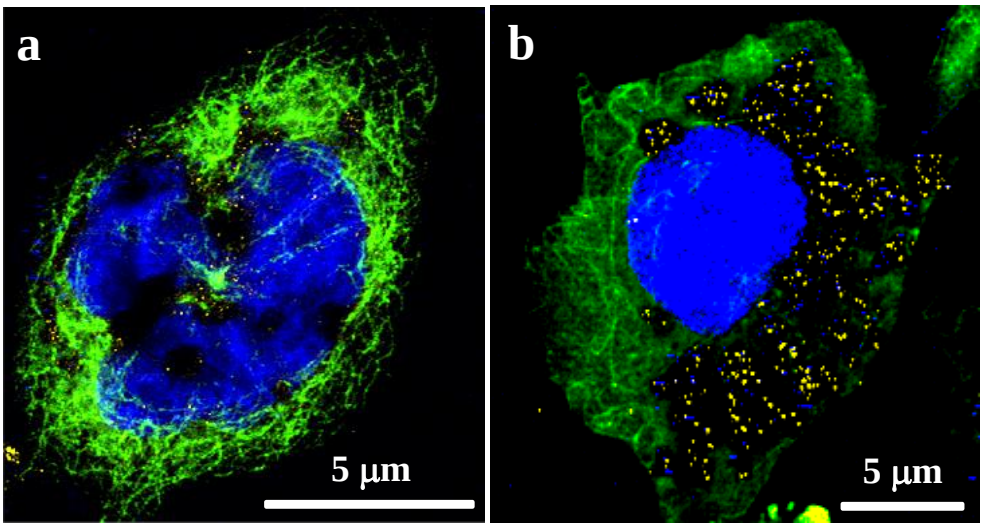

Figure 19: Cellular Entry in H1299 lung carcinoma cells. Confocal microscope images of H1299 lung cancer cells treated with a) $Fe_3O_4@C_{BC}$, and b) $Fe_3O_4@C_{NT}$. Yellow – nanoparticle fluorescence, Blue – DAPI staining for nucleus and Green-β–tubulin staining for cytoplasm.

cancerous cell line using nanoparticles with biconcave and nanotube morphologies, and these cells showed trends similar to those observed with the U87 MG glial cells (Figure 19). Considering that nanoparticles injected into blood vessels would adsorb various serum proteins and biomolecules[68-70] and would additionally encounter a variety of cells (such as endothelial, epithelial, and immune cells)[71,72] before entering the brain, it is all the more important to understand their behavior under *in vivo* conditions.

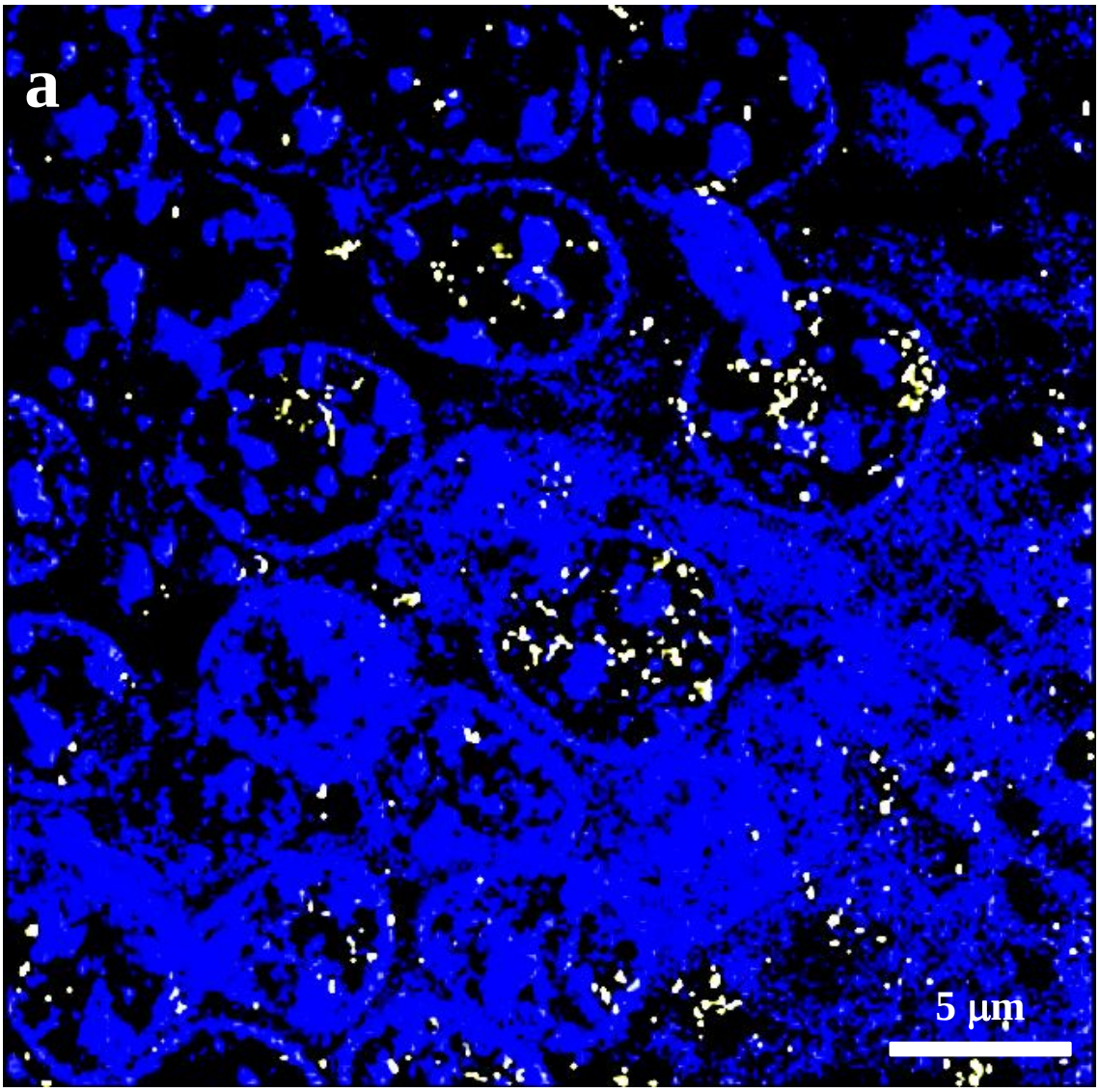

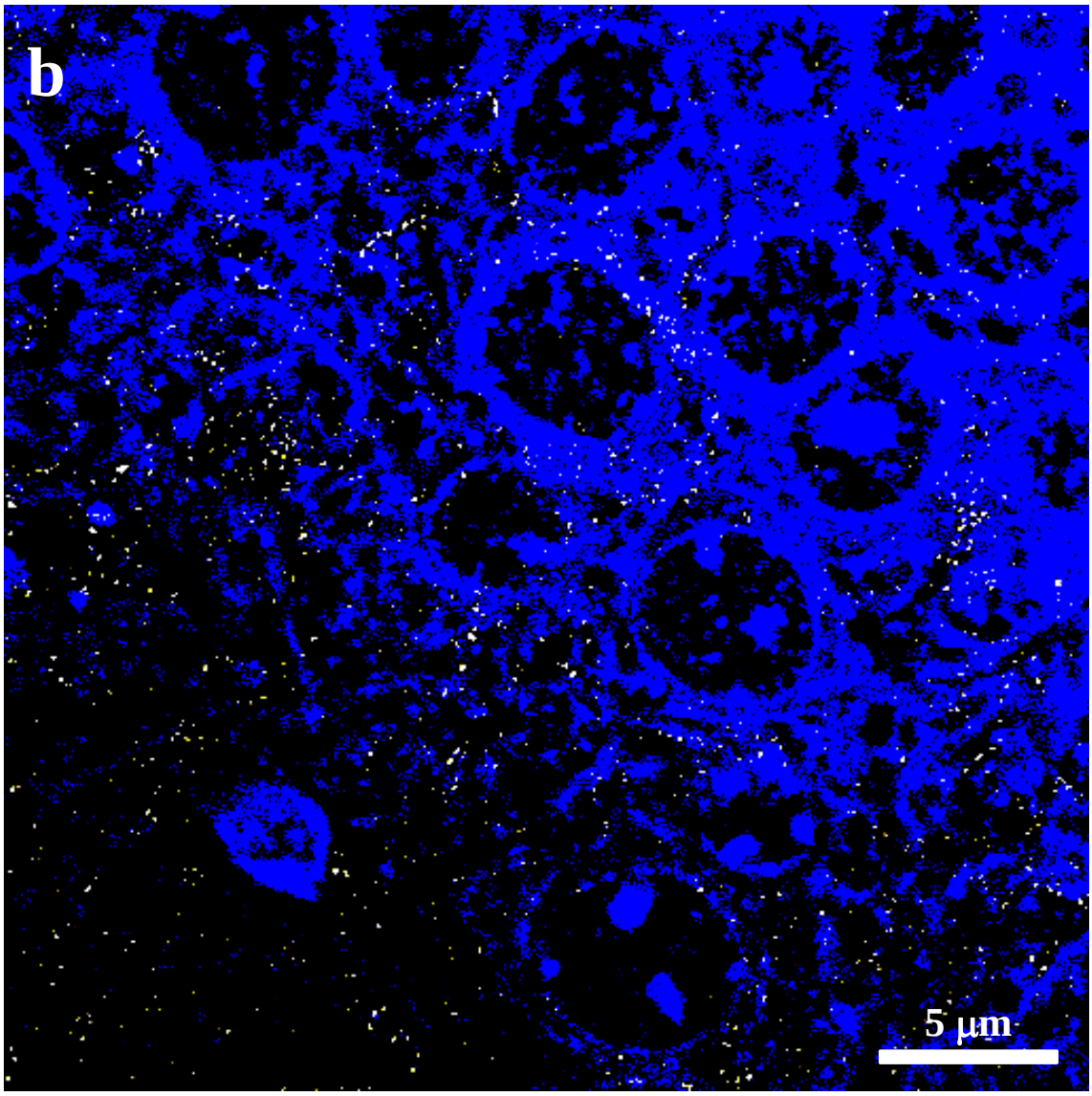

Figure 20: Differential entry of nanoparticle in the brain cell nucleus. After 3 days of intra-peritoneal injection with $Fe_3O_4@C_{BC}$ (a) and $Fe_3O_4@C_{NT}$ (b) the BALB/c mice was sacrificed and its brain was processed for confocal microscopy. Blue - nuclear staining with Hoechst and Yellow – nanoparticle fluorescence. Note: a and b images were taken at 100x magnification from hippocampal region.

To know whether such shape dependent, subcellular localization of $Fe_3O_4@C$ nanoparticles occurs inside the animal brain in the complex physiological conditions, we have carried out *in vivo* experiments with BABL/c mice by intra-peritoneally injecting the

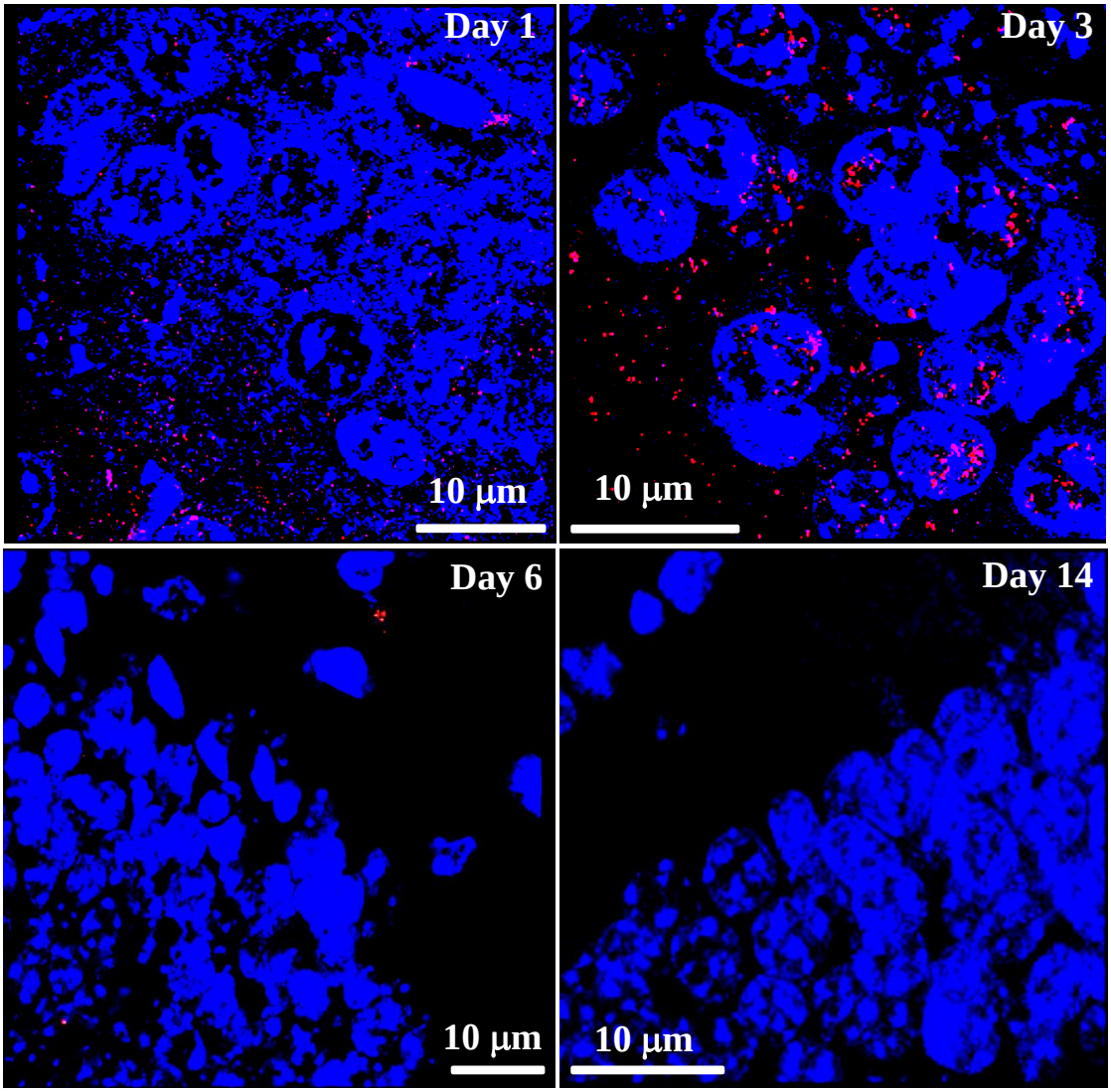

Figure 21: Processing of $Fe_3O_4@C_{BC}$ nanoparticles in the mice brain. Confocal microscope images of the brain section of BALB/c mice treated with $Fe_3O_4@C_{BC}$ for different time durations. Blue – nuclear staining with DAPI and Red – nanoparticle fluorescence.

aqueous dispersions of nanoparticles of two different shapes (biconcave & nanotube). BALB/c mice separately injected with $Fe_3O_4@C_{BC}$ and $Fe_3O_4@C_{NT}$ were sacrificed at different time durations (3 & 6 days), and their brain sections were processed for the confocal microscope imaging (materials and methods section). Nanoparticles of both the morphologies entered the mice brain by crossing the BBB and were accumulated in the

cerebral cortex region. This is possibly due to higher preference of glucose derived carbon shell (over Fe_3O_4) for the glial cells.[53] After 3 days of injection, nanoparticles of

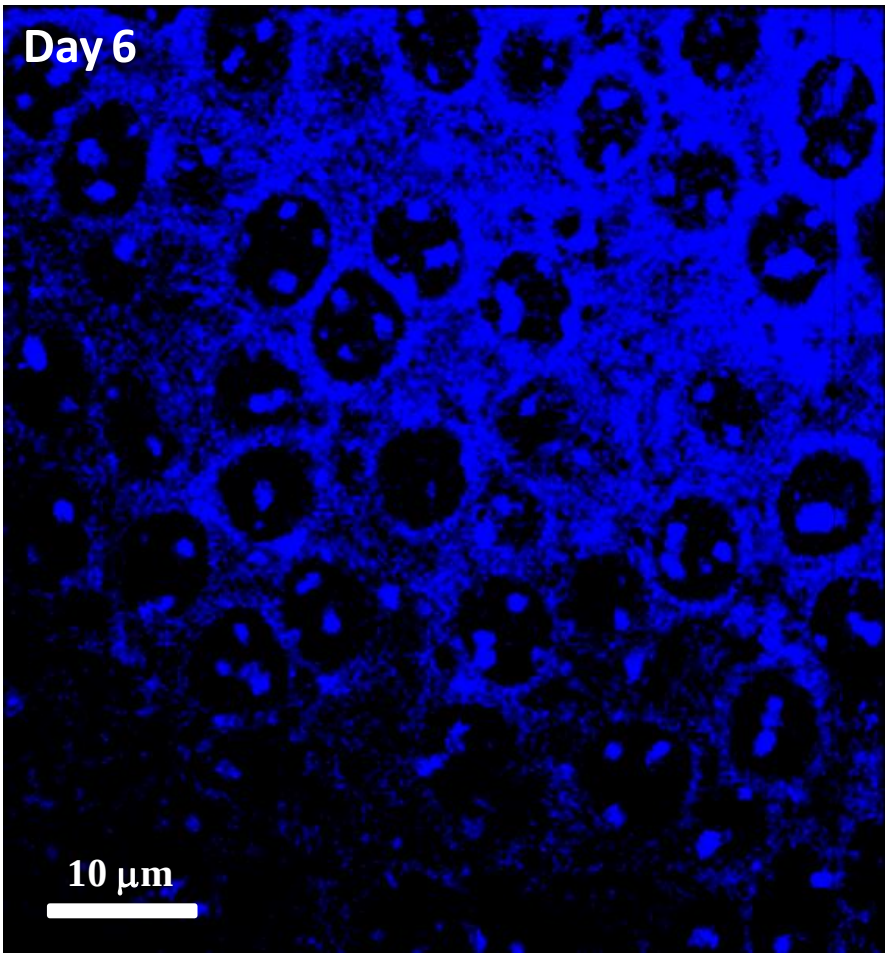

Figure 22: Processing of $Fe_3O_4@C_{NT}$ nanoparticles in the mice brain. Confocal microscope images of the brain sections of BALB/c mice treated with $Fe_3O_4@C_{NT}$ for 6 days. Blue – nuclear staining with DAPI and Red – nanoparticle fluorescence.

biconcave geometry were found mostly in the nucleus of the brain cells (Figure 20c). This is in sharp contrast to nanotube particles which were present only in the extra nuclear region and on the periphery of the nucleus (Figure 20d). Very few $Fe_3O_4@C_{BC}$ nanoparticles were present in the brain on day 6, while day 14 shows complete absence of nanoparticle fluorescence (Figure 21). In the case of nanotube morphology, the particles

were cleared within 6 days (Figure 22). The quantitative estimation of iron present in the brain of the mice treated with $Fe_3O_4@C_{BC}$ and $Fe_3O_4@C_{NT}$ for 3 days was carried out by digesting the brain in concentrated nitric acid followed by inductively coupled plasma mass spectroscopy (ICPMS) analysis. The amount of iron present in brain of $Fe_3O_4@C_{BC}$ & $Fe_3O_4@C_{NT}$ treated mice were 0.24 ± 0.03 μg and 0.282 ± 0.003 μg respectively per mg of the brain tissue, indicating slightly higher uptake for nanoparticles with nanotube morphology in the brain (Figure 23).

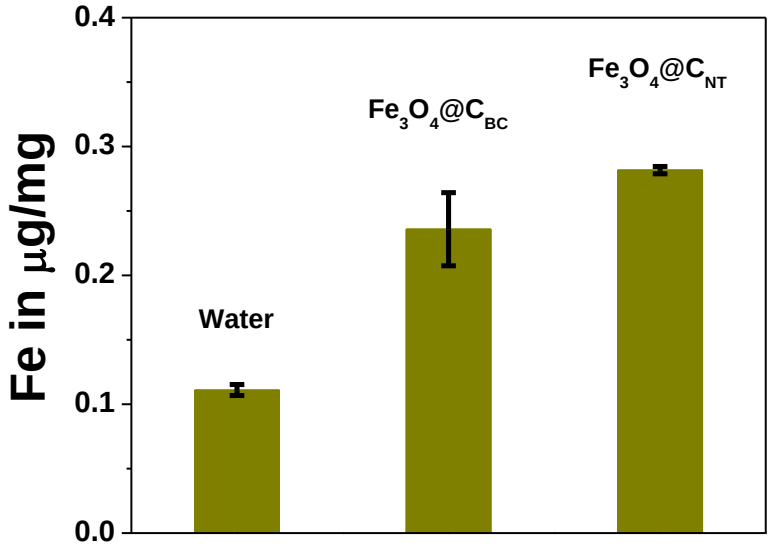

Figure 23: Quantitative estimation of nanoparticle entry level in the mice brain using ICPMS. Amount of iron present in the mice brain (μg of iron per mg of the brain tissue) treated with water, $Fe_3O_4@C_{BC}$, and $Fe_3O_4@C_{NT}$ for 3 days. For ICPMS measurements, brains of the mice treated with nanoparticles were first digested in 4 ml of 67-70 % HNO_3 (Alfa Aesar) at 80°C, till the solution became completely clear, followed by complete drying at 120°C. The sample was then diluted with 2 % HNO_3 and ICP mass spectra was recorded followed by calculations of the iron content from the standard curve. The standard intensity vs Fe concentration curve was plotted from serial dilutions made from the iron standard (Alfa Aesar) in 2% HNO_3.

Further, we tested the *in vivo* subcellular compartmentalizing ability of the $Fe_3O_4@C$ nanoparticles of biconcave and nanotube geometry for the compartment

specific drug delivery. We selected specific activator of p300, a nuclear lysine acetyltransferases (KAT) enzyme, TTK21 (N-(4-chloro-3-trifluoromethylphenyl)-2-N-propoxy-benzamide)[54] as a model compound. Acetyltransferases are known to carry out acetylation of histone proteins of the chromatin, which is a highly compact and dynamic nucleoprotein structure composed of DNA, RNA, and different proteins (histones and nonhistones).[73] Controlled acetylation of histones plays a significant role in the dynamics of chromatin, and regulates transcription.[74] However, the imbalance in the enzymatic activity of acetyltransferases leads to diseases such as cancer, diabetes, cardiovascular diseases, and asthma.[74] Thus activators or deactivators of the enzymatic activity of acetyltransferases are potential drugs.[75] TTK21 was loaded on the surface of Fe_3O_4@C

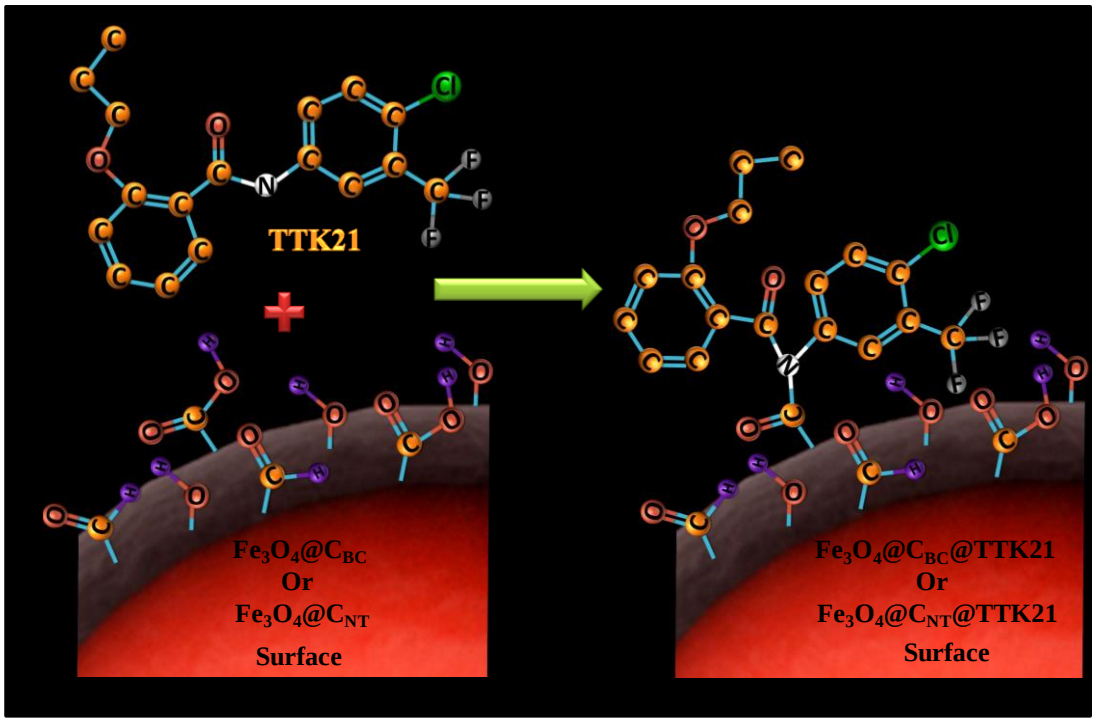

Scheme 2: Schematic for conjugation of small molecule TTK21 to the nanoparticles surface. The -NH group of TTK21 reacts with –COOH group on the nanoparticles surface. The possibility of physical adsorption of TTK21 on the nanoparticle surface is not ruled out.

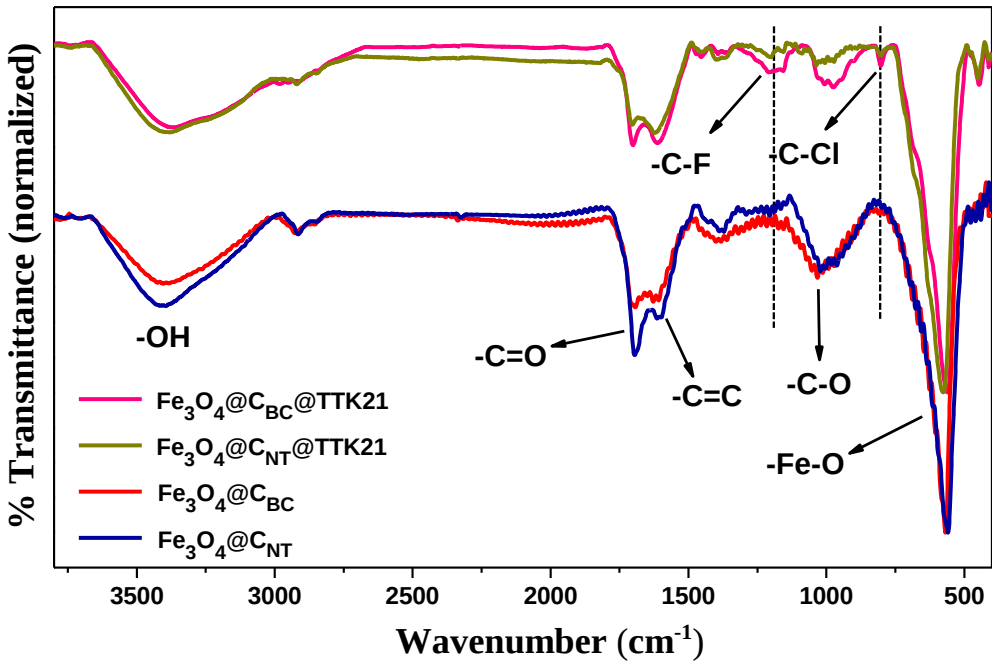

Figure 24: Infrared spectra of Fe_3O_4@C nanoparticles attached with drug molecule TTK21.

nanoparticles of both geometries biconcave and nanotube ($Fe_3O_4@C_{BC}$@TTK21 and $Fe_3O_4@C_{NT}$@TTK21 respectively) through an amide bond formation (Scheme 2 and materials and methods section). The physical adsorption of the TTK21 was also observed. The presence of TTK21 on the nanoparticles surface was confirmed by FTIR spectra and EDX mapping. The bands near 1200 cm^{-1} and 800 cm^{-1}, in the IR spectra of TTK21 attached nanoparticles, corresponds to the C-F and C-Cl stretching vibrations respectively (Figure 24). While the respective particles without TTK21 showed no such IR bands confirming the presence of TTK21. Additionally, EDX elemental mapping (Figure 25) showed presence of Fe, C, O, F, N, and Cl, in which F, N, and Cl are from the TTK21. The TTK21 conjugated and un-conjugated Fe_3O_4@C nanoparticles of biconcave and nanotube morphologies were then injected intra-peritoneally to BABL/c mice. All the four treated mice were sacrificed after 72 hours of injection, their brain was collected and

brain slices were prepared for the immunohistochemistry (IHC). The state of H3K9 acetylation in two different regions of the mice brain *viz.* hippocampus and cerebellum was examined under the microscope. As shown in the figure 26 I (c & d) and figure 26 II,

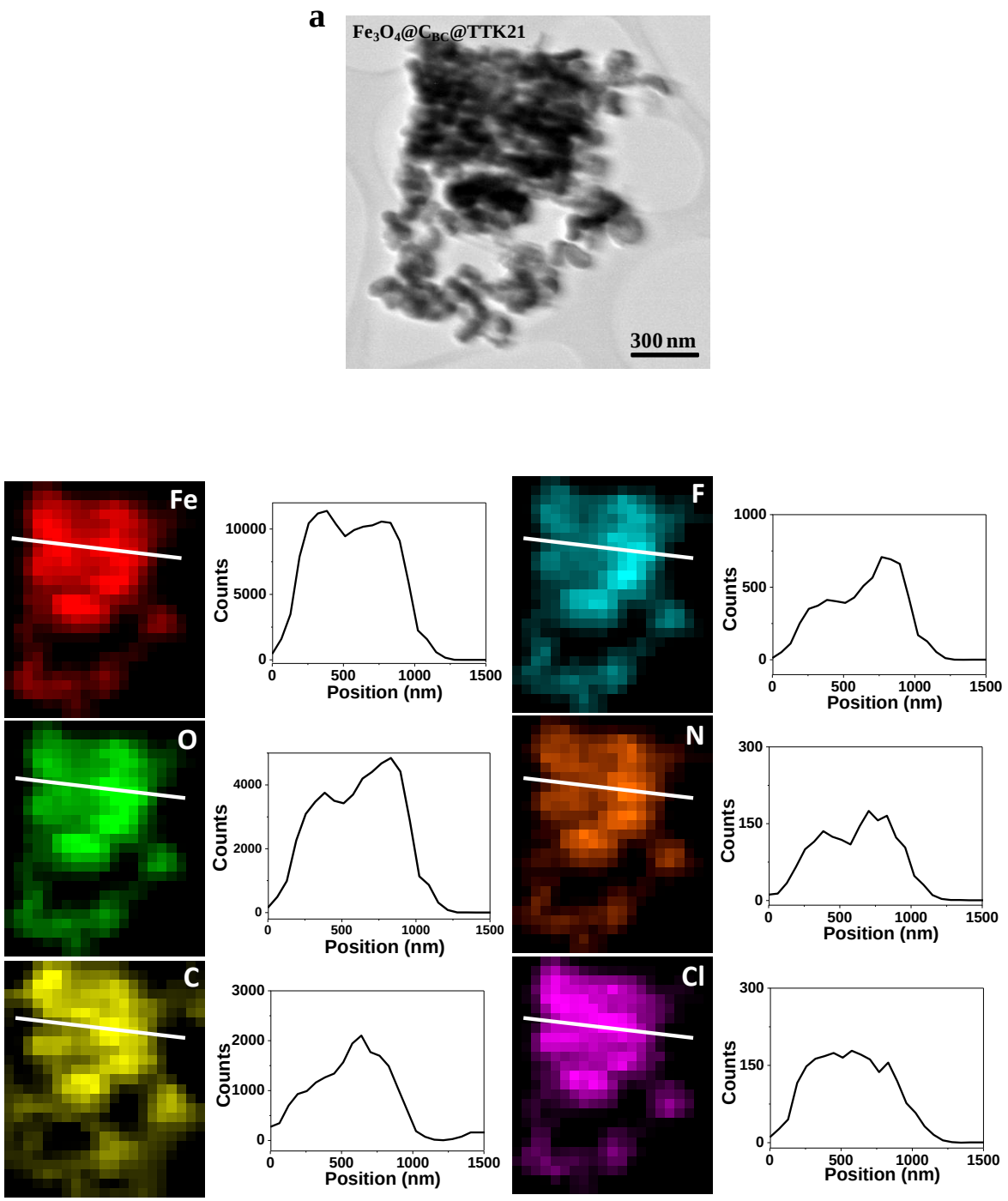

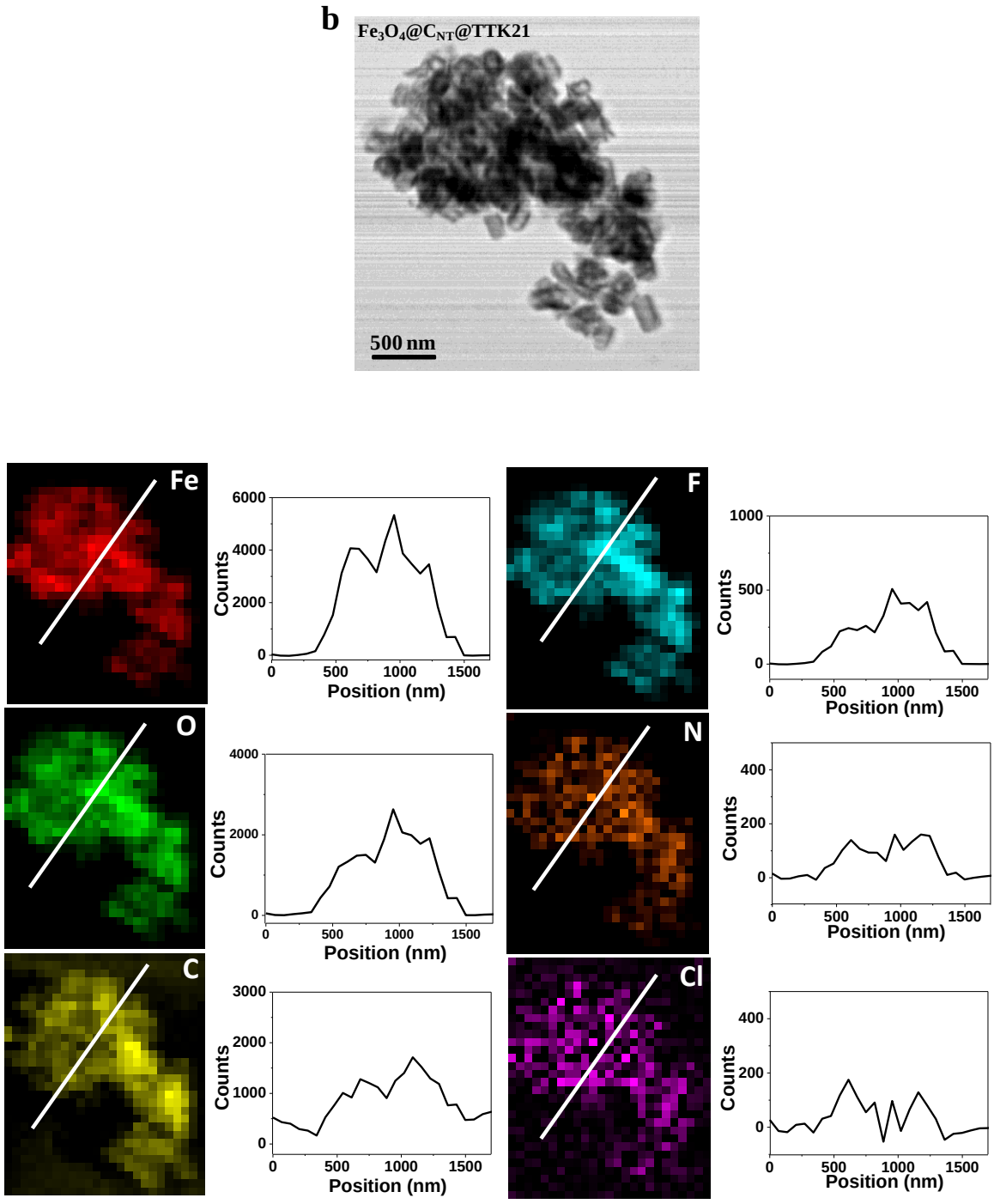

Figure 25: Elemental mapping for a) $Fe_3O_4@C_{BC}$@TTK21 and b) $Fe_3O_4@C_{NT}$@TTK21. Energy dispersive X-ray mapping (elemental mapping) was carried out using TEM. The top black and while pictures are TEM images of different samples and down colored images are the elemental maps for different elements. Beside every colored elemental map are given the intensity profile, along the line drown in the map, indicating relative presence of various elements in the sample.

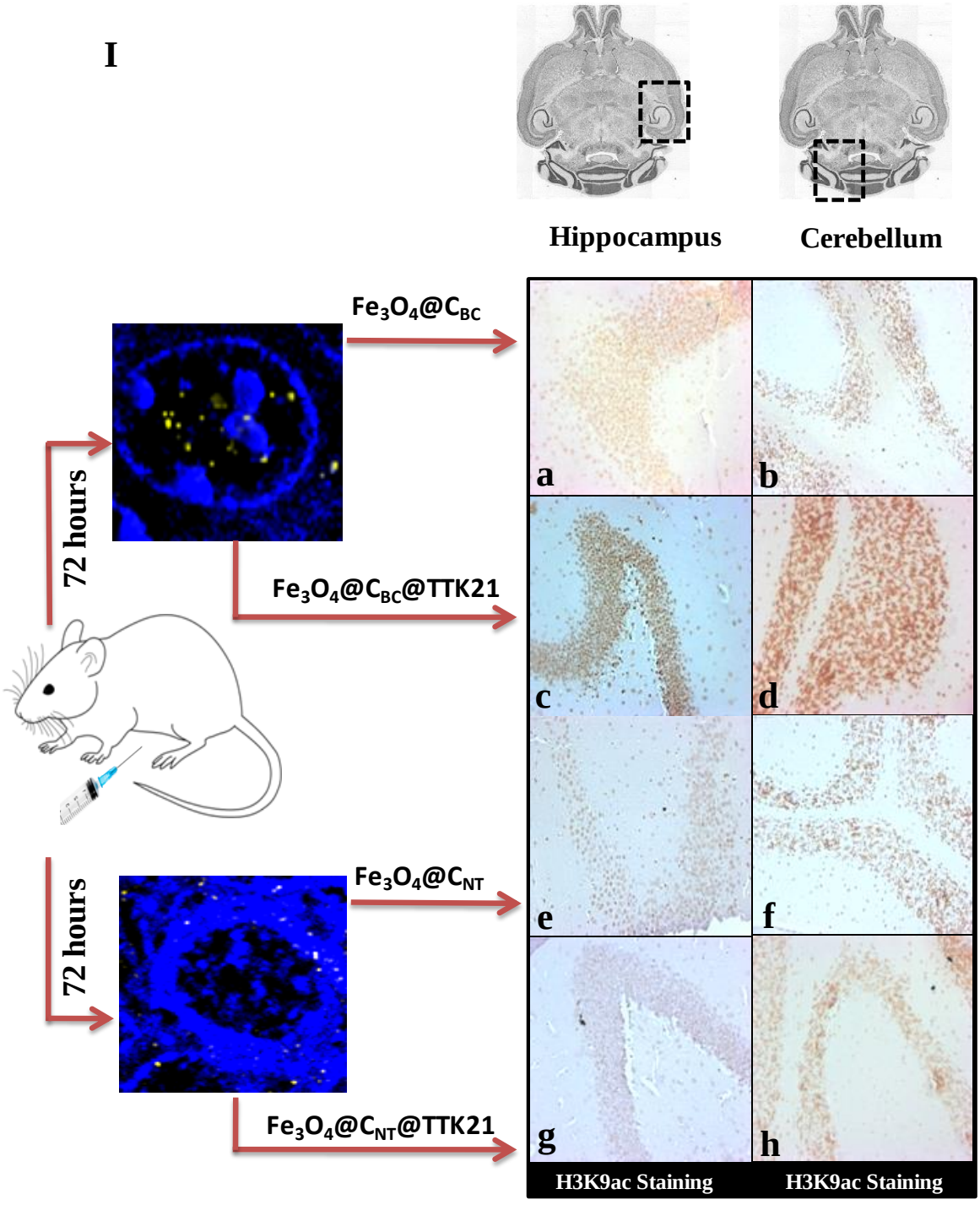
I
Hippocampus
Cerebellum
$Fe_3O_4@C_{BC}$
72 hours
$Fe_3O_4@C_{BC}@TTK21$
$Fe_3O_4@C_{NT}$
72 hours
$Fe_3O_4@C_{NT}@TTK21$
a
b
c
d
e
f
g
h
H3K9ac Staining
H3K9ac Staining

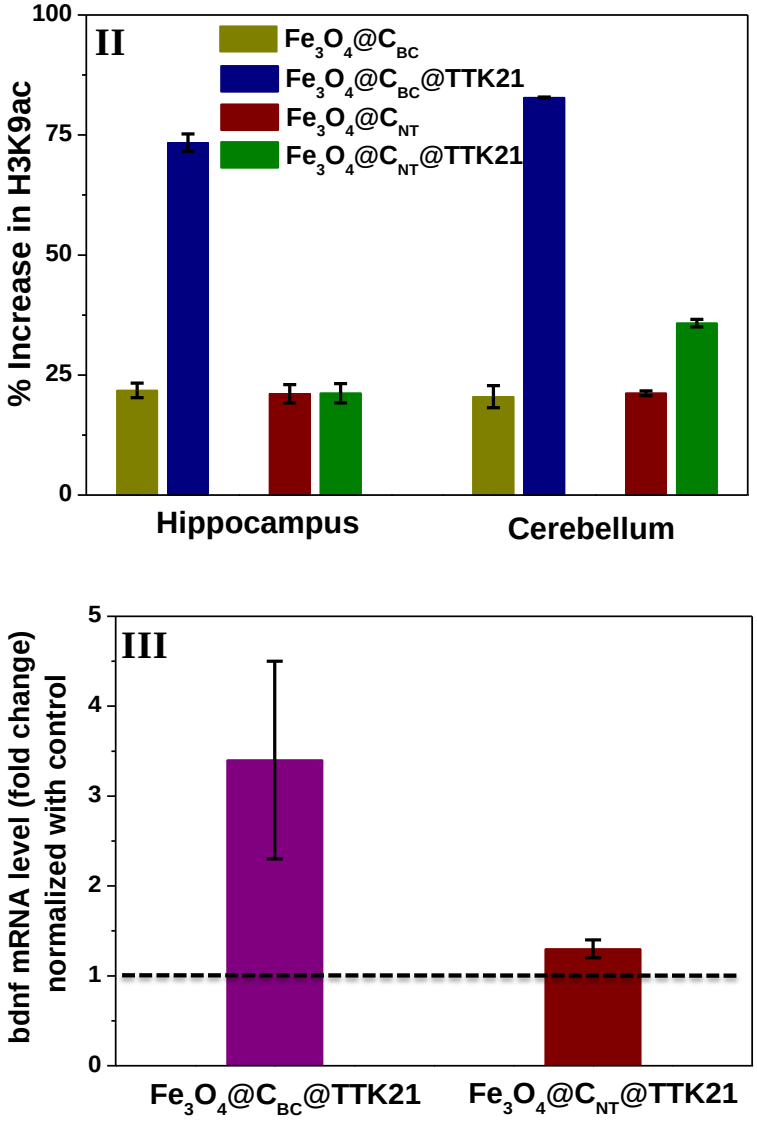

Figure 26: Activation of nuclear CBP/p300 KAT acetyltransferases in the hippocampus and cerebellum. (I) Microscope images (20X). The immunohistochemistry images of mice brain (hippocampus and cerebellum): upon sub peritoneal injection of $Fe_3O_4@C_{BC}$ (a and b), $Fe_3O_4@C_{BC}$@TTK21 (c and d), $Fe_3O_4@C_{NT}$ (e and f) and $Fe_3O_4@C_{NT}$@TTK21 (g and h) for 72hrs, mice were sacrificed and subjected to IHC analysis by indicated antibody. (II) Quantification of immunohistochemistry. (III) Activation of p300/CBP KAT activity induces expression of several genes related to neurogenesis and memory. *bdnf* is one such marker gene. qRT-PCR of *bdnf* mRNA level (fold change) was investigated upon injecting $Fe_3O_4@C_{BC}$@TTK21 and $Fe_3O_4@C_{NT}$@TTK21 normalized with control ($Fe_3O_4@C_{BC}$ & $Fe_3O_4@C_{NT}$) using specific primer for *bdnf* and *actin*.

acetylated H3K9 level is significantly induced in the brain of the mice treated with $Fe_3O_4@C_{BC}$@TTK21 suggesting activation of p300 acetyltransferases activity in the nucleus. The quantification of the acetylation level showed that the H3K9ac signal is nearly threefold higher as compared to the control $Fe_3O_4@C_{BC}$ particles (Figure 26 I (a & b) and Figure 26 II). On the other hand, $Fe_3O_4@C_{NT}$@TTK21 treated mice showed nearly similar H3K9ac level (Figure 26 I g & h and Figure 26 II) as that of control particles $Fe_3O_4@C_{NT}$ treatment (Figure 26 I e& f and Figure 26 II). Collectively, these data confirms that nuclear delivery of the KAT activator by the $Fe_3O_4@C_{BC}$@TTK21. Activation of acetyltransferase p300, should lead to over expression of several genes, related to neurogenesis and memory such as bdnf, neuroD1, Egr-1, Arc, cFos , and CREB1 *etc*.[76-79] To confirm the functional delivery of the KAT activator in the nucleus, further we analyzed the bdnf gene expression upon $Fe_3O_4@C_{BC}$@TTK21 treatment by real time PCR (qRT-PCR). It was found that the mRNA levels of bdnf genes was nearly threefold higher in the brain of the mice treated with $Fe_3O_4@C_{BC}$@TTK21 as compared to the mice treated with $Fe_3O_4@C_{NT}$@TTK21 (Figure 26 III). Taken together, these results established the role of Fe_3O_4@C particles of biconcave shape as a functional nuclear delivery vehicle of the brain. On the other hand nanotube morphology, being cytoplasm specific, could not enhance the enzymatic activity and thereby gene expression (transcription).

3.5 Conclusions:

In conclusion, here we have presented the first *in vivo* report on shape directed subcellular compartmentalization of nanoparticles in the animal brain. The core-shell biocompatible Fe_3O_4@C nanoparticles (with similar size and surface properties) of biconcave and nanotube morphology specifically localized in the nucleus and cytoplasm, respectively, of the brain cells. Fe_3O_4@C nanoparticles of biconcave and nanotube geometries, tagged with a small molecule lysine acetyltransferases activator TTK21 were demonstrated with their ability to effectively deliver the drug in the specific subcellular compartment. Biconcave nanoparticles, being nuclear specific, could deliver the drug in the nucleus of the brain cells hence enhancing the enzymatic activity and corresponding gene expression. The nanotube morphology of Fe_3O_4@C could be exploited for the specific delivery of molecules in the cytoplasm. Furthermore, the functionally rich carbon surface would facilitate the loading of many therapeutic molecules like HIV drugs, siRNA, proteins, DNA, etc on Fe_3O_4 @C nanoparticles and hence their spatial delivery inside the brain cells.

3.6 References:

1. Bhaskar, S.; Tian, F.; Stoeger, T.; Kreyling, W.; de la Fuente, J. M.; Grazu, V.; Borm, P.; Estrada, G.; Ntziachristos, V.; Razansky, D. Multifunctional Nanocarriers for diagnostics, drug delivery and targeted treatment across blood-brain barrier: perspectives on tracking and neuroimaging. *Part Fibre Toxicol.* **2010,** *7*, 3.
2. Bozdağ Pehlivan, S. Nanotechnology-Based Drug Delivery Systems for Targeting, Imaging and Diagnosis of Neurodegenerative Diseases. *Pharm. Res.* **2013,** *30*, 2499-2511.
3. Cheng, Y.; Morshed, R. A.; Auffinger, B.; Tobias, A. L.; Lesniak, M. S. Multifunctional nanoparticles for brain tumor imaging and therapy. *Adv. Drug Delivery Rev.* **2014,** *66*, 42-57.
4. Gao, H.; Pang, Z.; Jiang, X. Targeted Delivery of Nano-Therapeutics for Major Disorders of the Central Nervous System. *Pharm. Res.* **2013,** *30*, 2485-2498.
5. Krol, S. Challenges in drug delivery to the brain: Nature is against us. *J. Contr. Release* **2012,** *164*, 145-155.
6. Krol, S.; Macrez, R.; Docagne, F.; Defer, G.; Laurent, S.; Rahman, M.; Hajipour, M. J.; Kehoe, P. G.; Mahmoudi, M. Therapeutic Benefits from Nanoparticles: The Potential Significance of Nanoscience in Diseases with Compromise to the Blood Brain Barrier. *Chem. Rev.* **2012,** *113*, 1877-1903.
7. Meyers, J. D.; Doane, T.; Burda, C.; Basilion, J. P. Nanoparticles for imaging and treating brain cancer. *Nanomedicine* **2012,** *8*, 123-143.
8. Wong, H. L.; Wu, X. Y.; Bendayan, R. Nanotechnological advances for the delivery of CNS therapeutics. *Adv. Drug Delivery Rev.* **2012,** *64*, 686-700.

9. He, Q.; Shi, J. MSN Anti-Cancer Nanomedicines: Chemotherapy Enhancement, Overcoming of Drug Resistance, and Metastasis Inhibition. *Adv. Mater*. **2014,** *26*, 391-411.
10. Huang, J. G.; Leshuk, T.; Gu, F. X. Emerging nanomaterials for targeting subcellular organelles. *Nano Today* **2011,** *6*, 478-492.
11. Li, S.; Huang, L. Nonviral gene therapy: promises and challenges. *Gene. Ther*. **2000,** *7*, 31-34.
12. Meng, F.; Cheng, R.; Deng, C.; Zhong, Z. Intracellular drug release nanosystems. *Materials Today* **2012,** *15*, 436-442.
13. Pérez-Martínez, F.; Guerra, J.; Posadas, I.; Ceña, V. Barriers to Non-Viral Vector-Mediated Gene Delivery in the Nervous System. *Pharm. Res.* **2011,** *28*, 1843-1858.
14. Rajendran, L.; Knolker, H.-J.; Simons, K. Subcellular targeting strategies for drug design and delivery. *Nat. Rev. Drug Discovery* **2010,** *9*, 29-42.
15. Sakhrani, N. M.; Padh, H. Organelle targeting: third level of drug targeting. *Drug Des. Devel. Ther*. **2013,** *7*, 585-99.
16. Sui, M.; Liu, W.; Shen, Y. Nuclear drug delivery for cancer chemotherapy. *J. Contr. Release* **2011,** *155*, 227-236.
17. You, J.; Hu, F. Q.; Du, Y. Z.; Yuan, H. Improved cytotoxicity of doxorubicin by enhancing its nuclear delivery mediated via nanosized micelles. *Nanotechnology* **2008,** *19*, 255103.
18. Kuo, Y. C.; Ko, H. F. Targeting delivery of saquinavir to the brain using 83-14 monoclonal antibody-grafted solid lipid nanoparticles. *Biomaterials* **2013,** *34*, 4818-4830.

19. Wei, W.; Ma, G.-H.; Hu, G.; Yu, D.; McLeish, T.; Su, Z.-G.; Shen, Z.-Y. Preparation of Hierarchical Hollow $CaCO_3$ Particles and the Application as Anticancer Drug Carrier. *J. Am. Chem. Soc.* **2008,** *130*, 15808-15810.
20. Xu, P.; Van Kirk, E. A.; Zhan, Y.; Murdoch, W. J.; Radosz, M.; Shen, Y. Targeted Charge-Reversal Nanoparticles for Nuclear Drug Delivery. *Angew. Chem. Int. Ed.* **2007,** *46*, 4999-5002.
21. Zhou, Z.; Shen, Y.; Tang, J.; Fan, M.; Van Kirk, E. A.; Murdoch, W. J.; Radosz, M. Charge-Reversal Drug Conjugate for Targeted Cancer Cell Nuclear Drug Delivery. *Adv. Funct. Mater.* **2009,** *19*, 3580-3589.
22. Ashley, C. E.; Carnes, E. C.; Phillips, G. K.; Padilla, D.; Durfee, P. N.; Brown, P. A.; Hanna, T. N.; Liu, J.; Phillips, B.; Carter, M. B.; Carroll, N. J.; Jiang, X.; Dunphy, D. R.; Willman, C. L.; Petsev, D. N.; Evans, D. G.; Parikh, A. N.; Chackerian, B.; Wharton, W.; Peabody, D. S.; Brinker, C. J. The targeted delivery of multicomponent cargos to cancer cells by nanoporous particle-supported lipid bilayers. *Nat. Mater.* **2011,** *10*, 389-397.
23. Austin, L. A.; Kang, B.; Yen, C.-W.; El-Sayed, M. A. Nuclear Targeted Silver Nanospheres Perturb the Cancer Cell Cycle Differently than Those of Nanogold. *Bioconj. Chem.* **2011,** *22*, 2324-2331.
24. Austin, L. A.; Kang, B.; Yen, C.-W.; El-Sayed, M. A. Plasmonic Imaging of Human Oral Cancer Cell Communities during Programmed Cell Death by Nuclear-Targeting Silver Nanoparticles. *J. Am. Chem. Soc.* **2011,** *133*, 17594-17597.
25. de la Fuente, J. M.; Berry, C. C. Tat Peptide as an Efficient Molecule To Translocate Gold Nanoparticles into the Cell Nucleus. *Bioconj. Chem.* **2005,** *16*, 1176-1180.

26. Kang, B.; Mackey, M. A.; El-Sayed, M. A. Nuclear Targeting of Gold Nanoparticles in Cancer Cells Induces DNA Damage, Causing Cytokinesis Arrest and Apoptosis. *J. Am. Chem. Soc.* **2010,** *132*, 1517-1519.

27. Qian, Y.; Zha, Y.; Feng, B.; Pang, Z.; Zhang, B.; Sun, X.; Ren, J.; Zhang, C.; Shao, X.; Zhang, Q.; Jiang, X. PEGylated poly(2-(dimethylamino) ethyl methacrylate)/DNA polyplex micelles decorated with phage-displayed TGN peptide for brain-targeted gene delivery. *Biomaterials* **2013,** *34*, 2117-2129.

28. Xu, C.; Xie, J.; Kohler, N.; Walsh, E. G.; Chin, Y. E.; Sun, S. Monodisperse Magnetite Nanoparticles Coupled with Nuclear Localization Signal Peptide for Cell-Nucleus Targeting. *Chemistry – An Asian J.* **2008,** *3*, 548-552.

29. Boussif, O.; Lezoualc'h, F.; Zanta, M. A.; Mergny, M. D.; Scherman, D.; Demeneix, B.; Behr, J. P. A versatile vector for gene and oligonucleotide transfer into cells in culture and in vivo: polyethylenimine. *Proc. Natl. Acad. Sci. U.S.A* **1995,** *92*, 7297-7301.

30. Li, W.; Nicol, F.; Szoka Jr, F. C. GALA: a designed synthetic pH-responsive amphipathic peptide with applications in drug and gene delivery. *Adv. Drug Delivery Rev.* **2004,** *56*, 967-985.

31. Gupta, B.; Levchenko, T. S.; Torchilin, V. P. Intracellular delivery of large molecules and small particles by cell-penetrating proteins and peptides. *Adv. Drug Delivery Rev.* **2005,** *57*, 637-651.

32. Khalil, I. A.; Kogure, K.; Akita, H.; Harashima, H. Uptake pathways and subsequent intracellular trafficking in nonviral gene delivery. *Pharmacol. Rev.* **2006,** *58*, 32-45.

33. Duncan, R. Designing polymer conjugates as lysosomotropic nanomedicines. *Biochem. Soc. Trans.* **2007,** *35*, 56-60.

34. Vasir, J. K.; Labhasetwar, V. Biodegradable nanoparticles for cytosolic delivery of therapeutics. *Adv. Drug Delivery Rev.* **2007,** *59*, 718-728.

35. Ke, C.-J.; Su, T.-Y.; Chen, H.-L.; Liu, H.-L.; Chiang, W.-L.; Chu, P.-C.; Xia, Y.; Sung, H.-W. Smart Multifunctional Hollow Microspheres for the Quick Release of Drugs in Intracellular Lysosomal Compartments. *Angew. Chem. Int. Ed.* **2011,** *123*, 8236-8239.

36. Chen, K.-J.; Liang, H.-F.; Chen, H.-L.; Wang, Y.; Cheng, P.-Y.; Liu, H.-L.; Xia, Y.; Sung, H.-W. A Thermoresponsive Bubble-Generating Liposomal System for Triggering Localized Extracellular Drug Delivery. *ACS Nano* **2012,** *7*, 438-446.

37. Chung, M.-F.; Chen, K.-J.; Liang, H.-F.; Liao, Z.-X.; Chia, W.-T.; Xia, Y.; Sung, H.-W. A Liposomal System Capable of Generating CO_2 Bubbles to Induce Transient Cavitation, Lysosomal Rupturing, and Cell Necrosis. *Angew. Chem. Int. Ed.* **2012,** *124*, 10236-10240.

38. Bottini, M.; Sacchetti, C.; Pietroiusti, A.; Bellucci, S.; Magrini, A.; Rosato, N.; Bottini, N. Targeted Nanodrugs for Cancer Therapy: Prospects and Challenges. *J. Nanosc. Nanotechnol.* **2014,** *14*, 98-114.

39. Albanese, A.; Tang, P. S.; Chan, W. C. W. The Effect of Nanoparticle Size, Shape, and Surface Chemistry on Biological Systems. *Ann. Rev. Biomed. Eng.* **2012,** *14*, 1-16.

40. Duan, X.; Li, Y. Physicochemical Characteristics of Nanoparticles Affect Circulation, Biodistribution, Cellular Internalization, and Trafficking. *Small* **2013,** *9*, 1521-1532.

41. Ma, N.; Ma, C.; Li, C.; Wang, T.; Tang, Y.; Wang, H.; Mou, X.; Chen, Z.; He, N. Influence of Nanoparticle Shape, Size, and Surface Functionalization on Cellular Uptake. *J. Nanosci. Nanotechnol.* **2013,** *13*, 6485-6498.
42. Shang, L.; Nienhaus, K.; Nienhaus, G. U. Engineered nanoparticles interacting with cells: size matters. *J. Nanobiotechnol.* **2014,** *12*, 5.
43. Zhu, M.; Nie, G.; Meng, H.; Xia, T.; Nel, A.; Zhao, Y. Physicochemical Properties Determine Nanomaterial Cellular Uptake, Transport, and Fate. *Acc. Chem. Res.* **2012,** *46*, 622-631.
44. Boyer, C.; Whittaker, M. R.; Bulmus, V.; Liu, J.; Davis, T. P. The design and utility of polymer-stabilized iron-oxide nanoparticles for nanomedicine applications. *NPG Asia Mater.* **2010,** *2*, 23-30.
45. Ling, D.; Hyeon, T. Chemical Design of Biocompatible Iron Oxide Nanoparticles for Medical Applications. *Small* **2013,** *9*, 1450-1466.
46. Deng, H.; Li, X.; Peng, Q.; Wang, X.; Chen, J.; Li, Y. Monodisperse Magnetic Single-Crystal Ferrite Microspheres. *Angew. Chem. Int. Ed.* **2005,** *44*, 2782-2785.
47. Guardia, P.; Di Corato, R.; Lartigue, L.; Wilhelm, C.; Espinosa, A.; Garcia-Hernandez, M.; Gazeau, F.; Manna, L.; Pellegrino, T. Water-Soluble Iron Oxide Nanocubes with High Values of Specific Absorption Rate for Cancer Cell Hyperthermia Treatment. *ACS Nano* **2012,** *6*, 3080-3091.
48. Hu, X.; Yu, J. C.; Gong, J.; Li, Q.; Li, G. α-Fe2O3 Nanorings Prepared by a Microwave-Assisted Hydrothermal Process and Their Sensing Properties. *Adv. Mater.* **2007,** *19*, 2324-2329.

49. Jia, C.-J.; Sun, L.-D.; Luo, F.; Han, X.-D.; Heyderman, L. J.; Yan, Z.-G.; Yan, C.-H.; Zheng, K.; Zhang, Z.; Takano, M.; Hayashi, N.; Eltschka, M.; Kläui, M.; Rüdiger, U.; Kasama, T.; Cervera-Gontard, L.; Dunin-Borkowski, R. E.; Tzvetkov, G.; Raabe, J. Large-Scale Synthesis of Single-Crystalline Iron Oxide Magnetic Nanorings. *J. Am. Chem. Soc.* **2008,** *130*, 16968-16977.
50. Sun, X.; Li, Y. Colloidal Carbon Spheres and Their Core/Shell Structures with Noble-Metal Nanoparticles. *Angew. Chem. Int. Ed.* **2004,** *43*, 597-601.
51. Chatterjee, S.; Mizar, P.; Cassel, R.; Neidl, R.; Selvi, B. R.; Mohankrishna, D. V.; Vedamurthy, B. M.; Schneider, A.; Bousiges, O.; Mathis, C.; Cassel, J. C.; Eswaramoorthy, M.; Kundu, T. K.; Boutillier, A. L. A novel activator of CBP/p300 acetyltransferases promotes neurogenesis and extends memory duration in adult mice. *J. Neurosci.* **2013,** *33*, 10698-10712.
52. Chaturbedy, P.; Chatterjee, S.; Selvi, R. B.; Bhat, A.; Kavitha, M. K.; Tiwari, V.; Patel, A. B.; Kundu, T. K.; Maji, T. K.; Eswaramoothy, M. Multifunctional carbon nanospheres with magnetic and luminescent probes: probable brain theranostic agents. *J. Mater. Chem. B* **2013,** *1*, 939-945.
53. Selvi, R. B.; Chatterjee, S.; Jagadeesan, D.; Chaturbedy, P.; Suma, B. S.; Eswaramoorthy, M.; Kundu, T. K. ATP driven clathrin dependent entry of carbon nanospheres prefer cells with glucose receptors. *J. Nanobiotechnol.* **2012,** *10*, 35.
54. Selvi, B. R.; Jagadeesan, D.; Suma, B. S.; Nagashankar, G.; Arif, M.; Balasubramanyam, K.; Eswaramoorthy, M.; Kundu, T. K. Intrinsically Fluorescent Carbon Nanospheres as a Nuclear Targeting Vector: Delivery of Membrane-

Impermeable Molecule to Modulate Gene Expression *In Vivo*. *Nano Lett.* **2008,** *8*, 3182-3188.

55. Cohen, Y.; Shoushan, S. Y. Magnetic nanoparticles-based diagnostics and theranostics. *Curr. Opin. Biotechnol.* **2013,** *24*, 672-681.
56. Ho, D.; Sun, X.; Sun, S. Monodisperse Magnetic Nanoparticles for Theranostic Applications. *Acc. Chem. Res.* **2011,** *44*, 875-882.
57. Mornet, S.; Vasseur, S.; Grasset, F.; Duguet, E. Magnetic nanoparticle design for medical diagnosis and therapy. *J. Mater. Chem.* **2004,** *14*, 2161-2175.
58. Singh, A.; Sahoo, S. K. Magnetic nanoparticles: a novel platform for cancer theranostics. *Drug Discovery Today* **2014,** *19*, 474-481.
59. Xie, J.; Liu, G.; Eden, H. S.; Ai, H.; Chen, X. Surface-Engineered Magnetic Nanoparticle Platforms for Cancer Imaging and Therapy. *Acc. Chem. Res.* **2011,** *44*, 883-892.
60. Ding, C.; Zhu, A.; Tian, Y. Functional Surface Engineering of C-Dots for Fluorescent Biosensing and *in vivo* Bioimaging. *Acc. Chem. Res.* **2013,** *47*, 20-30.
61. Liu, Z.; Liang, X. J. Nano-carbons as theranostics. *Theranostics* **2012,** *2*, 235-237.
62. Liu, Z.; Robinson, J. T.; Tabakman, S. M.; Yang, K.; Dai, H. Carbon materials for drug delivery & cancer therapy. *Mater. Today* **2011,** *14*, 316-323.
63. Wang, J.; Hu, Z.; Xu, J.; Zhao, Y. Therapeutic applications of low-toxicity spherical nanocarbon materials. *NPG Asia Mater.* **2014,** *6*, e84.
64. Yang, K.; Feng, L.; Shi, X.; Liu, Z. Nano-graphene in biomedicine: theranostic applications. *Chem. Soc. Rev.* **2013,** *42*, 530-547.

65. Zhu, J.; Liao, L.; Bian, X.; Kong, J.; Yang, P.; Liu, B. pH-controlled delivery of doxorubicin to cancer cells, based on small mesoporous carbon nanospheres. *Small* **2012,** *8*, 2715-2720.

66. Ikeda, S.; Tachi, K.; Ng, Y. H.; Ikoma, Y.; Sakata, T.; Mori, H.; Harada, T.; Matsumura, M., Selective Adsorption of Glucose-Derived Carbon Precursor on Amino-Functionalized Porous Silica for Fabrication of Hollow Carbon Spheres with Porous Walls. *Chem. Mater*. **2007,** *19*, 4335-4340.

67. Peyratout, C. S.; Dahne, L., Tailor-made polyelectrolyte microcapsules: from multilayers to smart containers. *Angew. Chem. Int. Ed.* **2004,** *43*, 3762-83.

68. Cedervall, T.; Lynch, I.; Lindman, S.; Berggård, T.; Thulin, E.; Nilsson, H.; Dawson, K. A.; Linse, S. Understanding the nanoparticle–protein corona using methods to quantify exchange rates and affinities of proteins for nanoparticles. *Proc. Natl. Acad. Sci. U.S.A* **2007,** *104*, 2050-2055.

69. Monopoli, M. P.; Aberg, C.; Salvati, A.; Dawson, K. A. Biomolecular coronas provide the biological identity of nanosized materials. *Nat. Nanotechnol.* **2012,** *7*, 779-786.

70. Tenzer, S.; Docter, D.; Kuharev, J.; Musyanovych, A.; Fetz, V.; Hecht, R.; Schlenk, F.; Fischer, D.; Kiouptsi, K.; Reinhardt, C.; Landfester, K.; Schild, H.; Maskos, M.; Knauer, S. K.; Stauber, R. H. Rapid formation of plasma protein corona critically affects nanoparticle pathophysiology. *Nat. Nanotechnol.* **2013,** *8*, 772-781.

71. Agarwal, R.; Singh, V.; Jurney, P.; Shi, L.; Sreenivasan, S. V.; Roy, K. Mammalian cells preferentially internalize hydrogel nanodiscs over nanorods and use shape-specific uptake mechanisms. *Proc. Natl. Acad. Sci. U.S.A* **2013,** *110*, 17247-17252.

72. Shimoni, O.; Yan, Y.; Wang, Y.; Caruso, F. Shape-Dependent Cellular Processing of Polyelectrolyte Capsules. *ACS Nano* **2012,** *7*, 522-530.
73. Berger, S. L. The complex language of chromatin regulation during transcription. *Nature* **2007**, 447, 407-412.
74. Swaminathan, V.; Reddy, B. A.; Selvi, B. R.; Sukanya, M. S.; Kundu, T. K. Chromatin and Disease, Springer press. **2007**, 41, 397.
75. Mai, A. The therapeutic uses of chromatin-modifying agents. *Expert. Opin. Ther. Targets* **2007**, 11, 835-851.
76. Chan, J. P.; Cordeira, J.; Calderon, G. A.; Iyer, L. K.; Rios, M., Depletion of central BDNF in mice impedes terminal differentiation of new granule neurons in the adult hippocampus. *Mol. Cell. Neurosci.* **2008,** *39*, 372-383.
77. Gao, Z.; Ure, K.; Ables, J. L.; Lagace, D. C.; Nave, K. A.; Goebbels, S.; Eisch, A. J.; Hsieh, J., Neurod1 is essential for the survival and maturation of adult-born neurons. *Nat. Neurosci.* **2009,** *12*, 1090-1092.
78. Guzowski, J. F.; Setlow, B.; Wagner, E. K.; McGaugh, J. L., Experience-dependent gene expression in the rat hippocampus after spatial learning: a comparison of the immediate-early genes Arc, c-fos, and zif268. *J. Neurosci.* **2001,** *21*, 5089-5098.
79. Lopez de Armentia, M.; Jancic, D.; Olivares, R.; Alarcon, J. M.; Kandel, E. R.; Barco, A., cAMP response element-binding protein-mediated gene expression increases the intrinsic excitability of CA1 pyramidal neurons. *J. Neurosci.* **2007,** *27*, 13909-13918.

Chapter 4

pH Sensitive Breathing of Clay Within the Polyelectrolyte Matrix

Summary:

Stimuli responsive organic-inorganic hybrid spheres were synthesized by coating the colloidal polystyrene spheres with polyelectrolyte protected aminoclay, Mg phyllo(organo)silicate layers in a layer-by-layer (LBL) method. The clay layers are sandwiched between the polyelectrolyte layers. The aminoclay swells in water due to protonation of amino groups and the degree of swelling depends on the pH of the medium. As a result, the hybrid spheres undergo a size increase up to 60 % as the pH is changed from 9 to 4. The stimuli responsive property of the hybrid spheres was used for the release of ibuprofen and eosin at different pH.

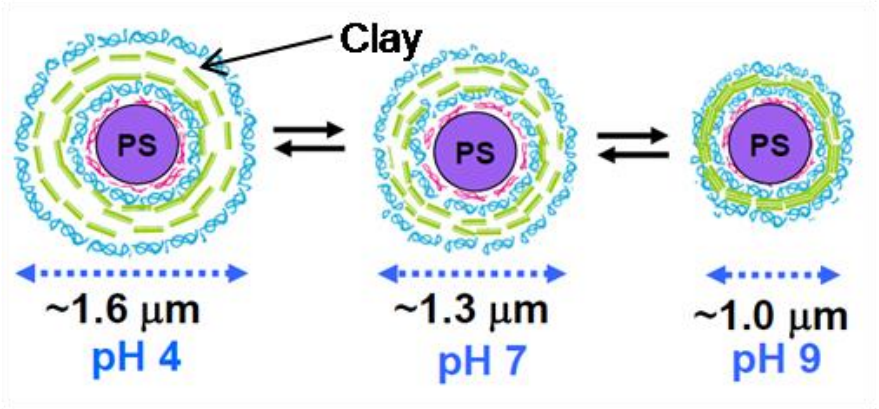

A paper based on this chapter has been published as an article in *ACS Nano* 2010, 4, 5921.

4.1 Introduction:

Advanced futuristic technologies are expected to encompass devices that can operate and even make logical decisions on their own. A successful design of such a technology must certainly involve individual components that are not only capable of sensing small changes in their environment, but also can respond to such changes. Materials with such abilities are broadly termed as smart materials or stimuli responsive materials.[1-4] Materials that can respond to various types of stimulus such as mechanical stress,[5] temperature,[6,7] pH,[8-12] electric field,[13] magnetic field,[14] redox potentials,[15] light,[16,17] and certain chemicals[18,19] have been synthesized in the past.[18,19] Organic materials like polyelectrolyte multilayers,[20] block copolymers,[21] phospholipids[22] and gels[23] possess functional components that can respond to an external stimulus by significantly altering their own physical or chemical properties. For example, the block-copolymer photonic gels, made of Polystyrene-*b*-quaternized poly(2-vinyl pyridine) (PS-*b*-QP2VP), were shown to reversibly change their stop-band position from the ultraviolet-visible region to the near-infrared region in response to aqueous solvents.[23] The hydrophilic layer of these one-dimensional periodic lamellar structures swelled by absorbing aqueous solvents, resulting in an increase in both the polyelectrolyte block domain spacing and the refractive-index contrast (Figure 1), accompanied by strong reflectivity and a shift of the stop band position to longer wavelengths.

On the other hand, inorganic shape-memory alloys,[24] piezoelectric and pyroelectric materials,[25-27] smart window materials[28] achieve their smartness by virtue of their ability to reversibly alter the crystal structure or lattice volume in response to an external stimulus. For example, WO_3, an electrochromic (EC) material,[29] when present in

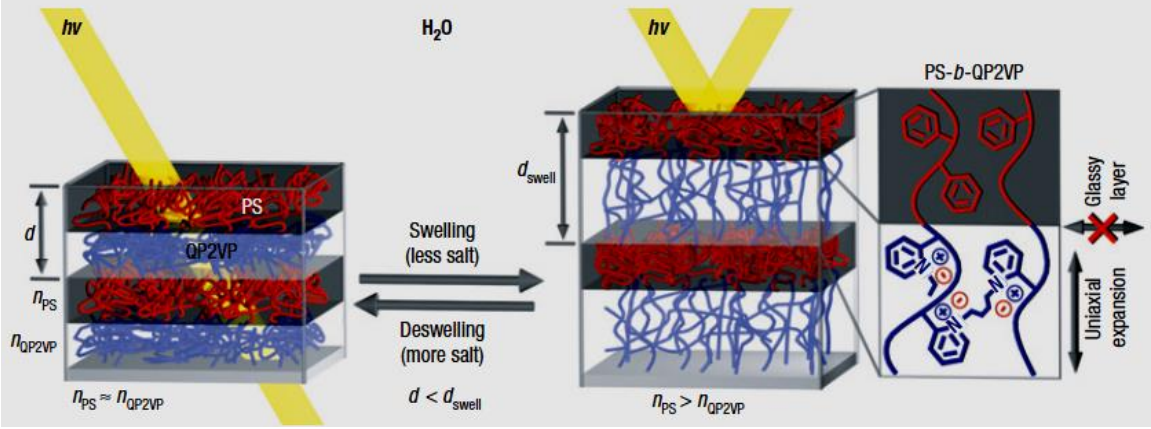

Figure 1: Schematic diagram of the structure of photonic gel film and the tuning mechanism. The photonic gel film was prepared by self-assembly of a diblock copolymer (PS-b-QP2VP). Swelling/de-swelling of the QP2VP gel layers (blue) by aqueous solvents modulates both the domain spacing and the refractive-index contrast, and accordingly shifts the wavelengths of light (hν) reflected by the stop band. The hydrophobic and glassy polystyrene layers (red) limit expansion of the gel layers to the direction normal to the layers. Adapted with permission from reference 23. Copyright 2007, Nature Publishing Group.

an electrochromic device, changes its color in response to an applied electric voltage, which is associated with an electrochemically induced oxidation–reduction reaction within the WO_3 crystals.[30] Tungsten trioxide has a cubic crystal structure with large number of interstitial sites. With the help of cathodic polarization, metal atoms gets inserted, as metal ions, into these interstitial sites with expansion of the crystal lattice, and the injected electron reduces some of W^{VI} sites to W^{V} sites (WO_3 (transparent) + $x(Li^+ + e^-) \rightarrow Li_xW_{(1-x)}{}^{VI}W_xVO_3$ (blue)) . The charge transfer between W^{VI} and W^{V} sites imparts blue color to the WO_3 crystals. The electrochromic materials could be used for smart windows, information displays, ski goggles and motorcycle helmet visors. Figure 2 shows a visor with variable transmittance that gives a biker the comfort provided by a dark visor in sunlight and the safety provided by a clear visor in the dark. The colour change takes place in a few seconds.[29]

Figure 2: Motorcycle helmet with visor based on electrochromic foil, in dark and transparent state. The clear-state transmittance was deliberately set to 50%, although new EC materials can give more than 80% transmittance. Adapted with permission from reference 29. Copyright 2006, Nature Publishing Group.

Recently, there have been interests in the synthesis of stimuli responsive composites materials that are made up of organic and inorganic hybrids.[31-38] The composites, besides offering a wider range of options to tune the functionality at the molecular scale (organic component), also provides remarkable robustness (inorganic component).[31] When such systems are tuned to respond to changes in a window of physiologically relevant conditions, many applications in biodiagnosis and controlled drug delivery can be achieved.[2,3] For example, mesoporous silica nanoparticles when loaded with iron oxide superparamagnetic nanocrystals with the help of DNA, was able to perform on-demand stimuli-responsive dosing of therapeutic molecules (Figure 3).[39,40] Single-stranded DNA was immobilized onto the silica nanoparticle (loaded with fluorescein, model drug) surface. The complementary DNA sequence was then attached to magnetic nanoparticles. The DNA/magnetic nanoparticle conjugates are able to cap the pores of the magnetic silica particles upon hybridization of both DNA strands. When subjected to alternating magnetic field, progressive double-stranded DNA melting as a result of temperature increase gave rise to uncapping and the subsequent release of

fluorescein. Further, this system could reach hyperthermic temperatures (42-47ºC) under an alternating magnetic field, generating an advanced drug delivery systems for thermochemotherapy against cancer.

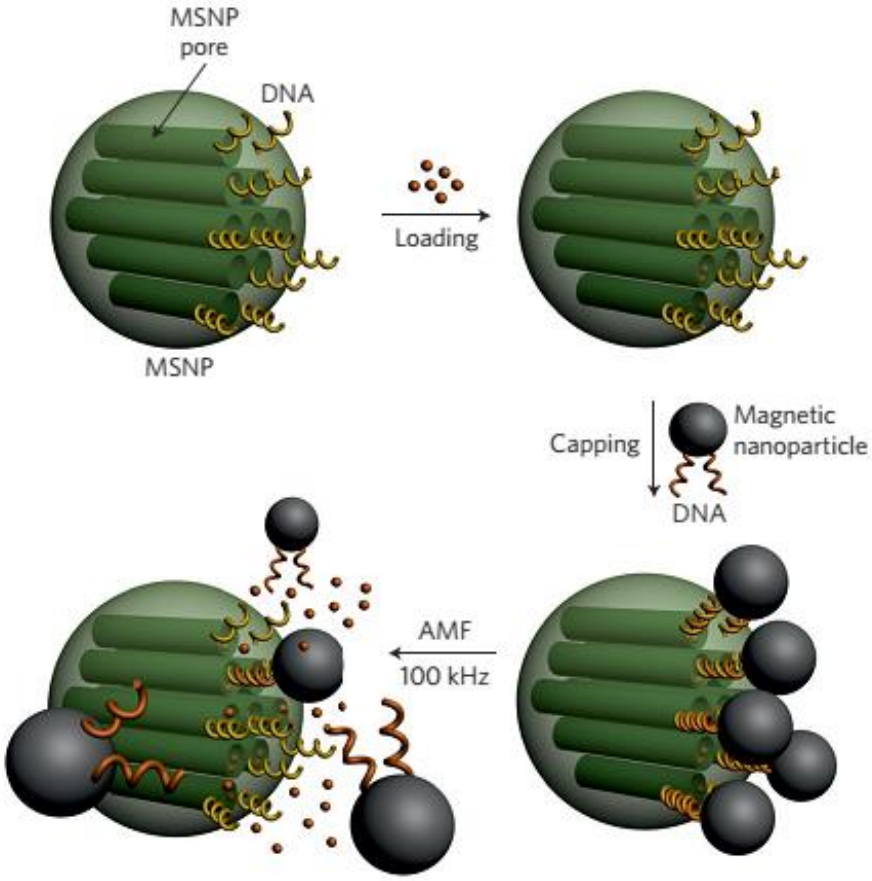

Figure 3: Actuation mechanisms based on the heat generated by an alternating magnetic field (AMF) leading to on-demand pulsatile drug release from mesoporous silica nanoparticles. Capping system based on complementary DNA sequences. Adapted with permission from reference 38. Copyright 2013, Nature Publishing Group.

4.2 Scope of the present study:

In this chapter, we describe the synthesis of stimuli responsive composite spheres composed of organoclay layers protected within the polyelectrolyte matrix. There have been examples in the literature where layered inorganic materials have been used as one of the components of stimuli responsive material. Brinker *et al.* reported a reversible change in the interlayer spacing of hybrid layered silicate derived from an azobenzene-bridged silsesquioxane,[41] in response to photophysical stimuli. Nevertheless, the change in the interlayer spacing is restricted by the dimensions allowed by *cis-trans* isomerism of azobenzene moiety. Mann *et. al*. reported the transformation of perforated microspheres of Mg phyllo(hexadecyl)silicates to apple-shaped structures by prolonged swelling in n-octane.[42] However, the hydrophobic nature of these materials limits their use in the controlled delivery of hydrophilic drugs/molecules in the physiological environment. Therefore, making hydrophilic layered materials in the form of spheres/capsules which could respond to external stimuli will have an added advantage as they can be used to encapsulate and control the release of drug molecules within the layers as well as from the core. Though there are very few reports on the synthesis of clay hollow spheres, to our knowledge they were not shown any stimuli responsive behavior with respect to chemical or physical environment.[43-45] Here, we have shown a clay, having the ability to swell at different pH, wrapped in a polyelectrolyte matrix could reversibly change the size of the spheres with pH which has been used in a controlled release of small molecules.

4.3 Materials and Methods:

a. Materials:

Styrene monomers (Aldrich), potassium persulfate-$K_2S_2O_8$ (Merck, India), poly(diallyldimethylammonium) chloride-PDADMAC (Aldrich, *M*w < 200 000) and poly(styrenesulfonate)-PSS (Aldrich, *M*w 70 000), magnesium chloride-$MgCl_2$ (Merck, India), 3-aminopropyltriethoxysilane (Aldrich), ethanol (HPLC grade), tetrahydrofuran, ethylenediaminetetraacetic acid, calcium chloride-$CaCl_2.2H_2O$ (Merck, India), sodium carbonate-Na_2CO_3 (Ranbaxy, India).

b. Synthesis of polystyrene spheres (PS):

Monodisperse polystyrene spheres (PS) were synthesized as described elsewhere.[46] 3.92 ml of styrene monomer was added to 50 ml water, maintained at 70^oC, followed by slow addition of aqueous solution of $K_2S_2O_8$ (0.082 g in 3.57 ml water), with continuous stirring in nitrogen atmosphere. The resulting solution was stirred for 24 h. Finally, the emulsion was naturally cooled to ambient temperature and filtered to get PS spheres.

c. Synthesis of clay:

An aminopropyl-functionalized magnesium (organo)phyllosilicate clay was synthesized[47] at room temperature by drop-wise addition of 3-aminopropyltriethoxysilane (1.3 ml, 5.85 mmol) to an ethanol solution of magnesium chloride (0.84 g, 3.62 mmol in 20 g ethanol). The white slurry obtained after 5 min was stirred overnight and the precipitate was isolated by centrifugation, washed with ethanol (50 ml) and dried at 40^oC.

d. Fabrication of composite PSL4 and PSL13:

Polyelectrolytes and clay were coated on polystyrene colloids (~680 nm) using layer by layer method. For PSL4 the four layers were coated in the order PDADMAC (+ve), PSS (-ve), Clay (-ve) and PSS (-ve) and for PSL13 the 13 layer coating in the order $(PDADMAC/PSS)_3$-clay-$(PSS/PDADMAC)_3$. The concentration of the polyelectrolytes and clay solutions used was 2 mg/ml. The adsorption of polyelectrolytes was carried out in 0.5 M NaCl solution for 20 min followed by centrifugation at 13500 rpm for 15 min. This was followed by three cycles of centrifugation/washing in water. The clay coating was done in 0.5 M NaCl solution for 1 h followed by washing with water.

e. DLS size and Zeta potential measurements:

The hydrodynamic diameter and the zeta potential measurements at different pH were carried out using Zetasizer Nano ZS (Malvern Instruments). The temperature for the measurement was kept at 25^{o}C. The concentration of the samples was 0.03% w/v. The pH of the solutions was adjusted using 0.5 M aq. HCl/NaOH solutions.

f. Confocal Imaging:

Confocal laser scanning fluorescence microcopy of PSL4 was done on a Zeiss LSM 510 Meta (Carl Zeiss). The instrument was equipped with 100X oil immersion objective with numerical aperture of 1.3. Dilute solutions of PSL4 were maintained at the desired pH using 0.5 M aq. HCl/NaOH solutions. To 100 μL of these solutions, 2μl of 0.1% w/v rhodamine 6G solution was added. Samples were excited using a He-Ne laser, wavelength 543 nm. For precise size measurements of spheres at different pH, fluorescence profiling was done along a diametric line. Size of the sphere was calculated

by taking difference between the intensity minima positions at the two ends of the diametric line.

g. Adsorption and Release of Ibuprofen/Eosin:

The ibuprofen (or eosin) adsorption and release studies were done by monitoring photoluminescence (PL) intensity at emission wavelength of 303 nm (or 538 nm) (λ_{ex}=219 nm for ibuprofen and 515 nm for eosin). To load ibuprofen drug, 1.7 mg of PSL4 was dispersed in 1 ml of aqueous solution containing 63 μg of the drug. This was allowed to equilibrate for 10 h at pH 6.3 followed by syringe filtration (Puradisc 4, Whatman). The amount of drug adsorbed at pH 9 was calculated using a calibration plot (PL intensity Vs drug concentration). This pH was chosen to avoid the experimental error likely to occur in the measurement of PL intensity due to large fluctuations in dissociation near the pKa value of the drug/dye. Finally the drug or dye loaded PSL4 (1.7 mg) was dispersed in MilliQ water (1 ml) at different pH (4, 7, 9) for 1 h and was filtered. Based on the PL intensity of the filtrate measured at pH 9 the amount of released drug or dye was calculated.

h. Capsule preparation:

The capsules were prepared from the polyelectrolyte and clay coated $CaCO_3$ spheres by dissolving the template. The $CaCO_3$ spheres, 3-4 μm in size, were synthesized as described elsewhere.[77] These spheres were coated with multiple layers of polyelectrolytes keeping the clay layer in the middle in the following order, $(PSS/PDADMAC)_3$-PSS-clay- $(PSS/PDADMAC)_2$-PSS. To dissolve the $CaCO_3$ core of this polyelectrolyte/clay coated spheres, 10 mg of the sample was added to 1 ml of 0.2 M

EDTA solution. The solution was stirred for 30 min and then centrifuged at 2000 rpm for 5 min. The solid precipitate was dispersed in MilliQ water and centrifuged. Washing with water was done thrice.

4.4 Results and Discussion:

Polystyrene spheres (PS) used in this study were synthesized by standard emulsion polymerization technique.[46] The polyelectrolytes used were poly(diallyldimethylammonium) chloride (PDADMAC) and poly(styrenesulfonate) (PSS) (Figures 4a and 4b). The aminoclay used in this study is Mg phyllo(organo)silicates having a structure analogous to 2:1 trioctahedral smectites and was synthesized by a chemical method.[47,48] Its structure consists of a central brucite sheet of octahedrally coordinated MgO/OH chains sandwiched between tetrahedral organosilicate network containing covalently linked propylamine pendant groups with an approximate unit cell composition of $R_8Si_8Mg_6O_{16}(OH)_4$, where R = $-CH_2CH_2CH_2NH_2$ (Figure 4c).[48] In water, the clay layers are positively charged over a wide range of pH due to protonation of amine groups (Figure 5) (alkylamine $pK_b \sim 3.4$).[49] As a result, the electrostatic repulsion between the protonated clay layers exfoliates the clay and form a transparent dispersion in water. The extent of protonation of amine groups (and hence the exfoliation) increases with decrease in pH which, in turn, increases the charge density on the individual clay layers. The decrease in clay particles size observed in dynamic light scattering (DLS) with decrease in pH further supports the exfoliation of clay layers due to increased level of protonation at low pH (Figure 5).

The composite spheres were synthesized by a well established electrostatic layer-by-layer technique (LbL)[50-54] (Scheme 1). This technique usually involves the sequential

adsorption of polyelectrolytes of opposite charges on a charged planar surface or around the colloidal spheres. The method has been successfully applied to generate composite

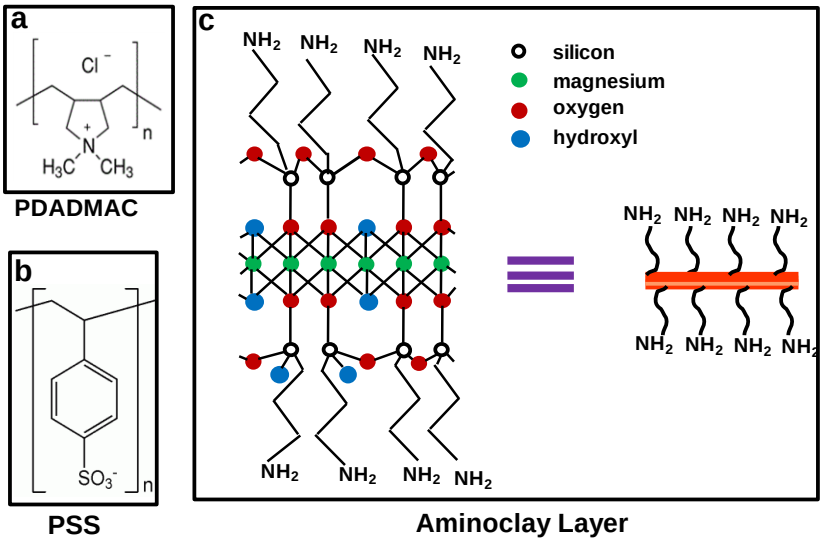

Figure 4: Molecular structure of a) PDADMAC b) PSS c) Aminoclay.

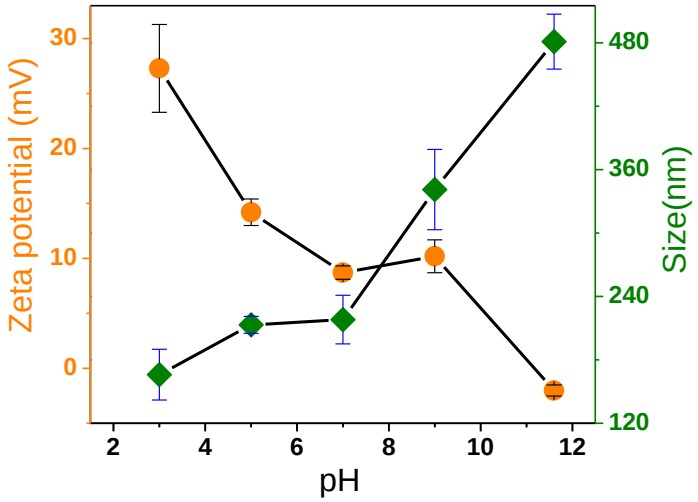

Figure 5: Basic information about Aminoclay. Plot of zeta potential of clay vs. pH (orange circles) and hydrodynamic diameter of clay particles vs. pH (olive diamonds).

films from nanoparticles,[55] nanotubes and nanowires,[56,57] nanoplates,[58,59] DNA,[60] proteins,[61,62] viruses,[63] lipids[64] *etc*. This method was further extended to make nano- and micro-capsules using sacrificial colloidal spheres as templates.[65-67] In Scheme 1, we

describe the experimental protocol to synthesize the stimuli responsive composite of clay and polyelectrolytes. The as prepared PS spheres were used as cores around which the polyelectrolytes and clay were sequentially coated. Initially, colloidal PS spheres were coated with PDADMAC as layer 1 followed by the adsorption of PSS as layer 2. The first two coatings of charged polyelectrolytes over PS are essential to facilitate the subsequent adsorption of clay as the third layer. Finally, the clay layer was wrapped with a layer of negatively charged PSS. The as prepared samples were designated as PSL1, PSL2, PSL3 and PSL4 respectively, depending on the number of layers coated on the PS core. A control sample, PSL4-NC (PSL4–No Clay), was also synthesized where in, the third layer of clay was replaced with a layer of PDADMAC.

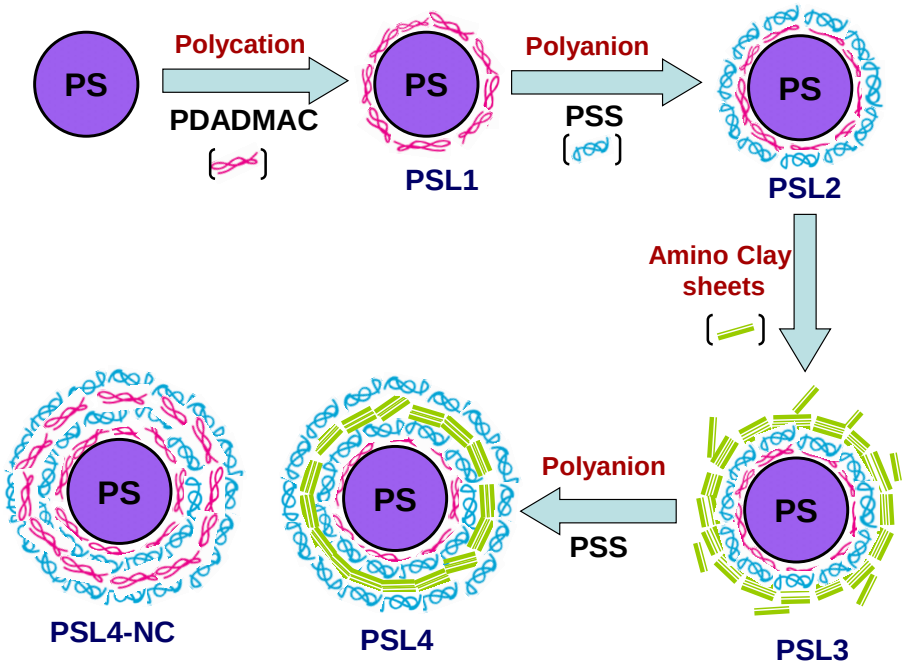

Scheme 1: Scheme to show the making of PSL4 spheres.

The as synthesized PS colloids were in the range of 680 ± 40 nm in diameter as measured by DLS and field emission scanning electron microscopy (FESEM). The success of the coating of each layer of polyelectrolyte and clay was verified by

monitoring the changes in the surface charge using zeta potential measurements at pH 7 (Figure 6a). As expected, the zeta potential for PSL1, PSL2, PSL3 and PSL4 varied between positive and negative values (+40mV to -60 mV at pH 7) depending on the charge on the polyelectrolyte or the clay on the outer layer. However, in case of PSL3, increase in the positive charge on the surface was minimal (+10 mV), probably due to the less charge density on the clay layers compared to the polyelectrolytes at pH 7.

As a next step, we followed the size changes of the spheres brought about by the coating of polyelectrolytes and clay (Figure 6b). From the DLS data, it is evident that each layer of coating of polyelectrolyte increased the thickness of the sphere by 100 nm

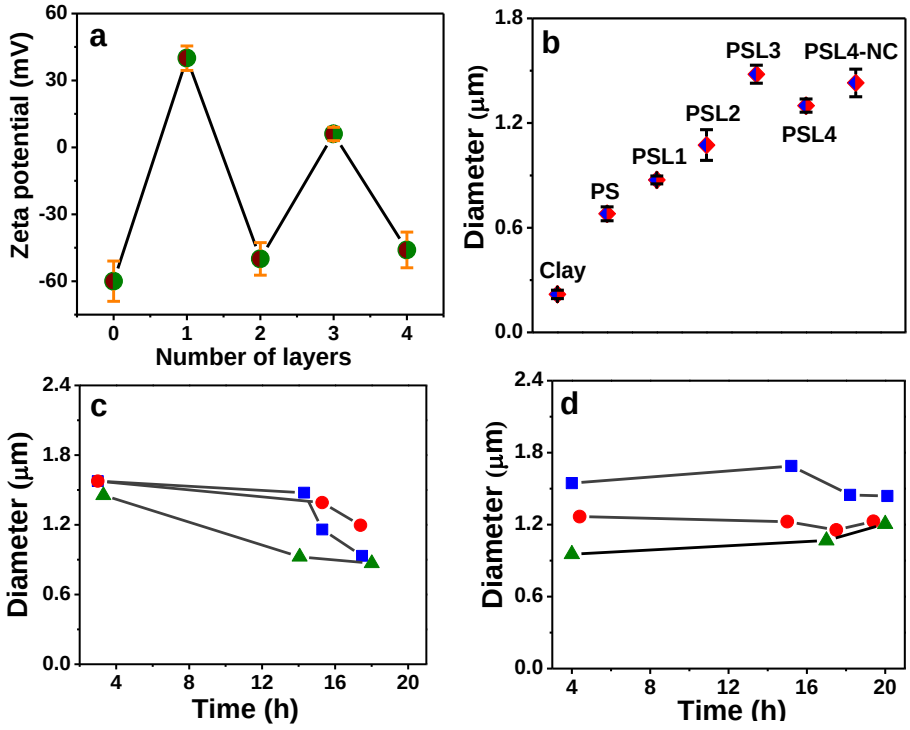

Figure 6: Monitoring coatings. a) Zeta potential variation with number of layers on PS. b) Hydrodynamic diameter of aminoclay, PS, PSL1, PSL2, PSL3, PSL4 and PSL4-NC. c) Variation of hydrodynamic diameter of PSL3 with time. d) Variation of hydrodynamic diameter of PSL4 with time. For c), and d) diameter measured at pH 4 (blue squares), pH 7 (red circles), and pH 9 (olive triangles).

(for PSL1 and PSL2). The size of PSL3 from DLS suggested an increase in the layer thickness corresponding to the clay coating is around 250 nm. However, the size of PSL3 was found to be unstable over a period of time due to dissociation of clay layers from the surface of the spheres (Figure 6c). In order to stabilize the size of PSL3, it was necessary to protect the clay layers from getting stripped away completely. Therefore, an additional layer of negatively charged PSS over the positively charged clay layers was essential to reduce the stripping of clay. The significant increase in the size-stability of PSL4 is

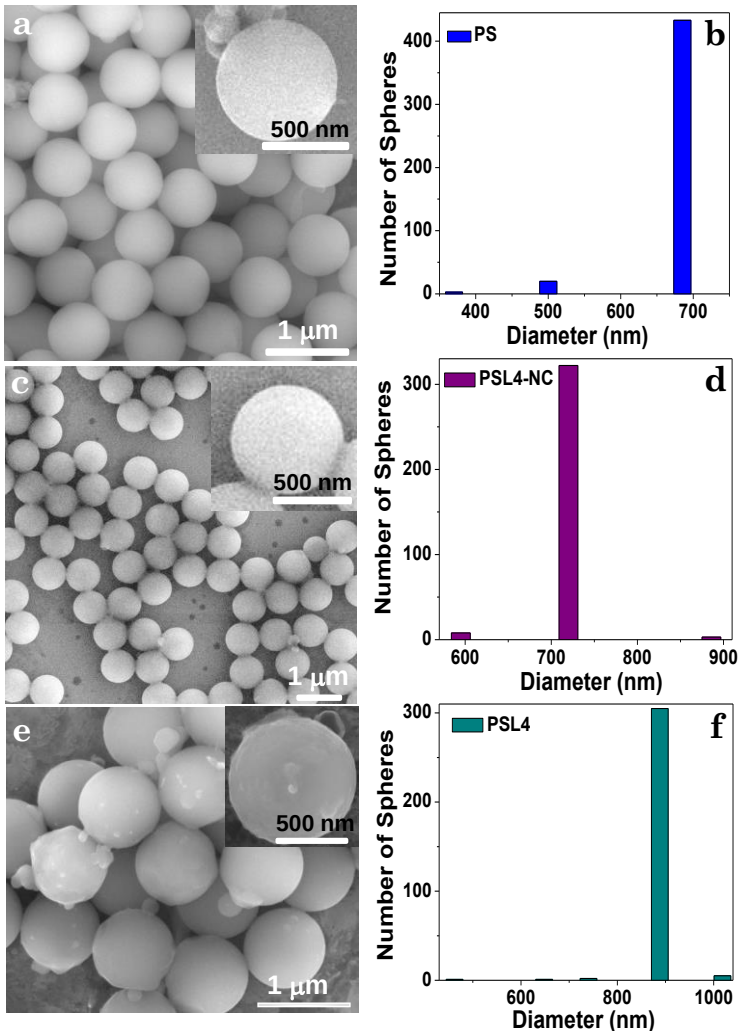

Figure 7: FESEM image and statistical sizing using these images. FESEM images of a) PS, c) PSL4-NC, e) PSL4. Inset in each image shows a magnified single sphere. Statistical sizing of b) PS, d) PSL4-NC, f) PSL4.

shown in Figure 6d. Moreover, it is to be mentioned that the thickness of layers obtained from DLS is from the change in hydrodynamic radius of the PS spheres on coating with polyelectrolytes and clay layers and can be influenced by the density of charges on the surface. We have also calculated the size increase due to polyelectrolytes and the clay layers coating from the FESEM images of the spheres in a dried state.

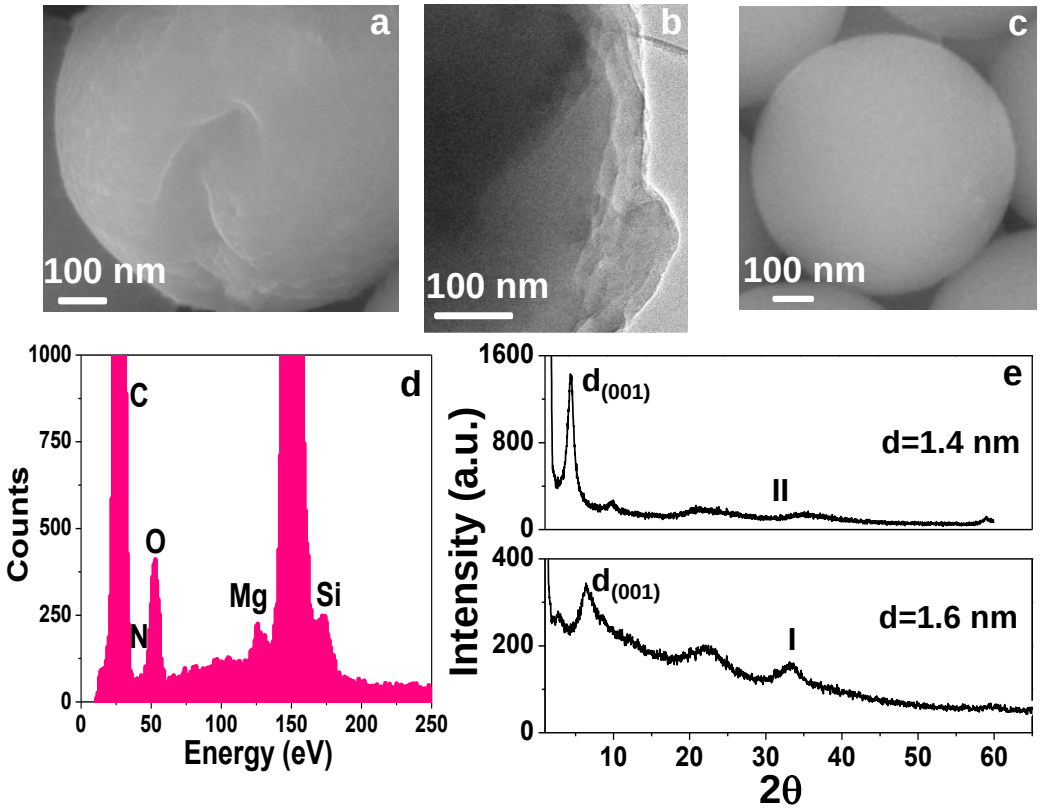

Figure 8: Characterization of PSL4. a) High resolution FESEM image of PSL4, b) High resolution TEM image of PSL4. c) High resolution FESEM image of PS. d) EDAX plot of PSL4. e) XRD pattern of PSL4 (i) and native clay (ii).

The average sizes calculated from FESEM for PS, PSL4 and PSL4-NC spheres (Figure 7) were found to be 685 nm, 890 nm and 720 nm respectively. From the size differences between PS and PSL4-NC, it is estimated that the thickness of 4 layers of polyelectrolyte coating is around 18 nm which is nearly same as the thickness reported

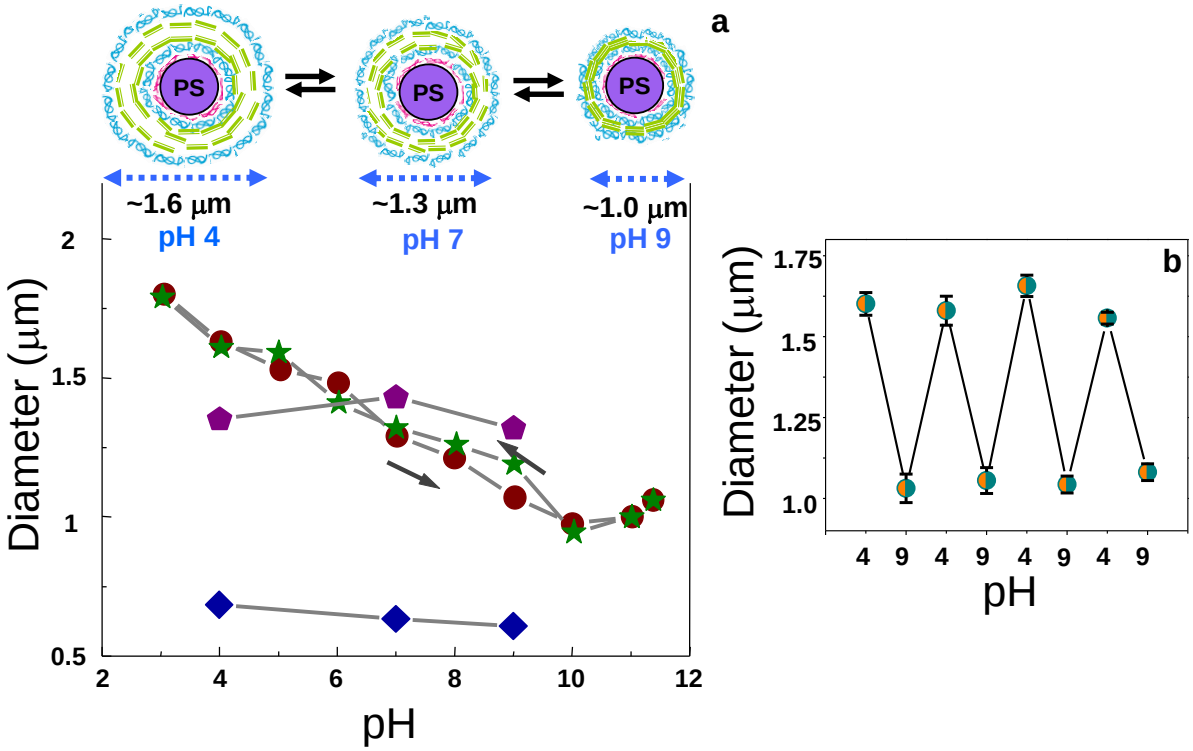

Figure 9: Breathing behavior of PSL4. a) Size variation, of PSL4 with increasing pH (olive stars) and with decreasing pH (wine circles), of PSL4-NC (violet pentagons), of PS (blue diamonds). Cartoon in inset shows the size variation of PSL4, due to swelling/deswelling of clay in the 3rd layer, with respect to pH. b) Reversible size change, for four cycles.

(~4 nm per layer) in the literature.[20,52] The thickness due to clay coating comes around 89 nm (measured from the size difference between PS and PSL4 spheres giving the room for the three polyelectrolyte layer thickness ~14 nm). It suggests that the thickness associated with the clay coating is roughly equivalent to 64 layers of clay considering the d_{001} spacing of 1.4 nm for the aminoclay in the XRD pattern (Figure 8e). The higher magnification FESEM (Figure 8a) and TEM image of PSL4 (Figure 8b) further shows increased surface roughness as compared to PS (Figures 8c) due to the presence of the inorganic clay structure. Energy dispersive X-ray analysis on PSL4 showed the presence of Mg and Si originating from the clay sheets (Figure 8d). The broad, low-angle peak

appeared in the powder XRD pattern of PSL4 (Figure 8e) was due to the reflection from (001) planes of clay resulting from the turbostatic stacking of the layers. The dynamic role played by clay layers in PSL4 spheres was studied in its colloidal state using DLS technique. The high dispersibility (zeta potential -40 mV at pH 7) and the monodispersity of PSL4 allowed the study of volume changes easier using DLS. DLS technique has been

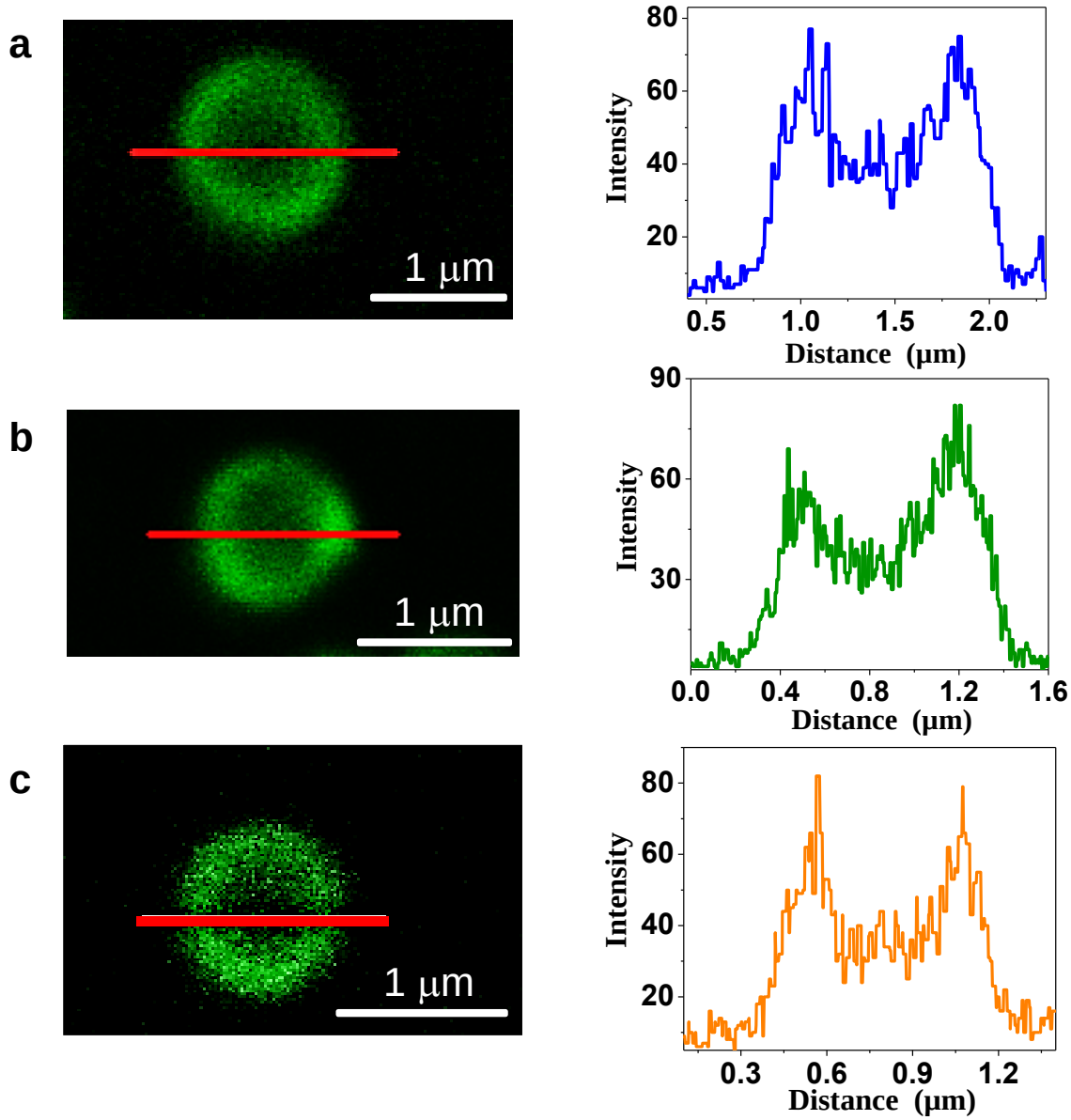

Figure 10: Confocal images and fluorescence profiling of PSL4 for size measurement at different pH. a) pH 4, b) pH 7, c) pH9.

commonly used in the past to study colloidal systems of size less than 5µm.[68-71] The hydrodynamic radius of PSL4 was monitored over a wide range of pH from 3 to 12 and the data is presented in Figure 9a. It can be observed that the size of PSL4 increased steadily from 1 µm to 1.62 µm as the pH was decreased from 9 to 4. The size change was reversible over the pH range from 4 to 9. A slight increase in size at pH values beyond 10 was also observed probably due to the repulsive interactions of the alternate PSS layers. The absence of pH-dependent size oscillation in case of PS and PSL4-NC spheres highlights the importance of clay in the breathing of PSL4. The oscillation of size of PSL4 was repeatable for several cycles of pH changes between 4 and 9 (Figure 9b) and is significant that it occurs in a physiologically relevant pH range. The size change was also observed directly under a confocal microscope with the aid of rhodamine 6G labeled PSL4 (Figure 10). The sizes of a number of PSL4 spheres were measured (from the

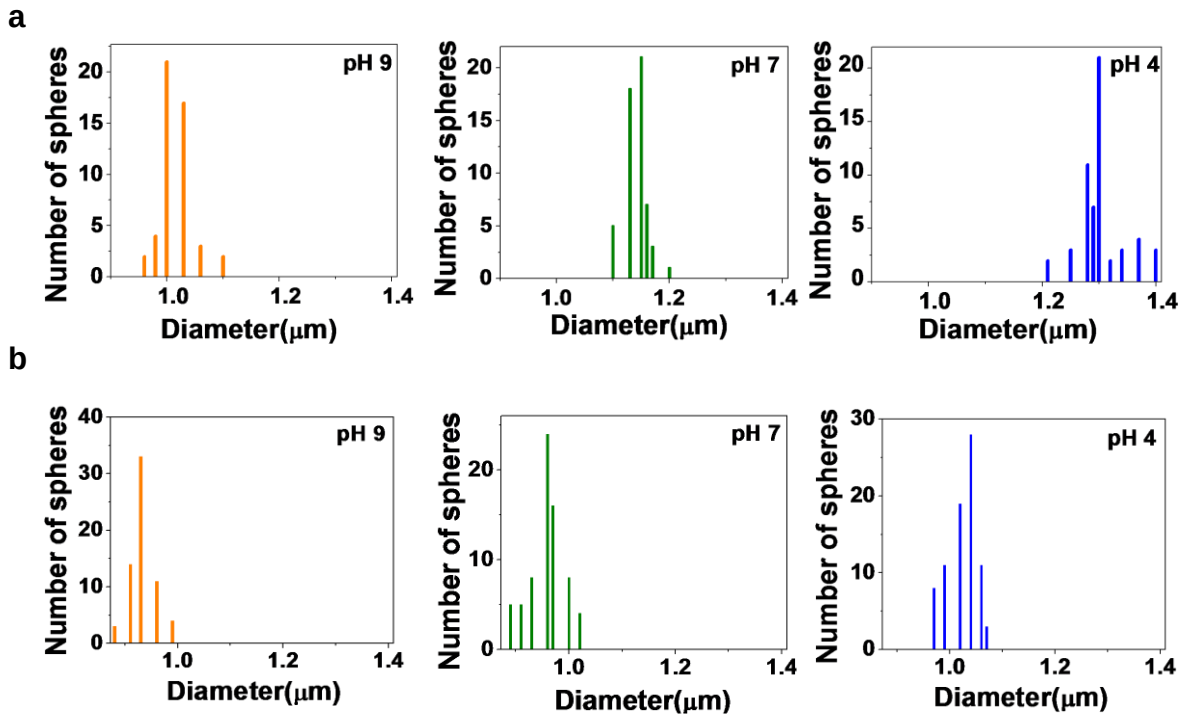

Figure 11: Statistical sizing at different pH using confocal images. a) PSL4, b) PSL4-NC.

confocal images of spheres) at pH values 4, 7 and 9 and a plot of histogram is shown in Figure 11a. The sizes of the PSL4-NC spheres at different pH were also measured for comparison (Figures 11b). The histogram clearly shows a shift, in the size distribution maxima for PSL4 (compared to PSL4-NC) towards larger sizes with decreasing pH. Further, the shift was reversible between pH 4 and 9 (Figure 12), a trend which was similar to the one observed in DLS measurement.

The unique property of size oscillation of PSL4 is a phenomenon arising out of the confinement of clay layers (or bundle of layers) in the polyelectrolyte matrix. It is important to note that the free aminoclay in water is getting exfoliated more and more if the pH is getting reduced. However, when the clay is confined in a smaller volume the

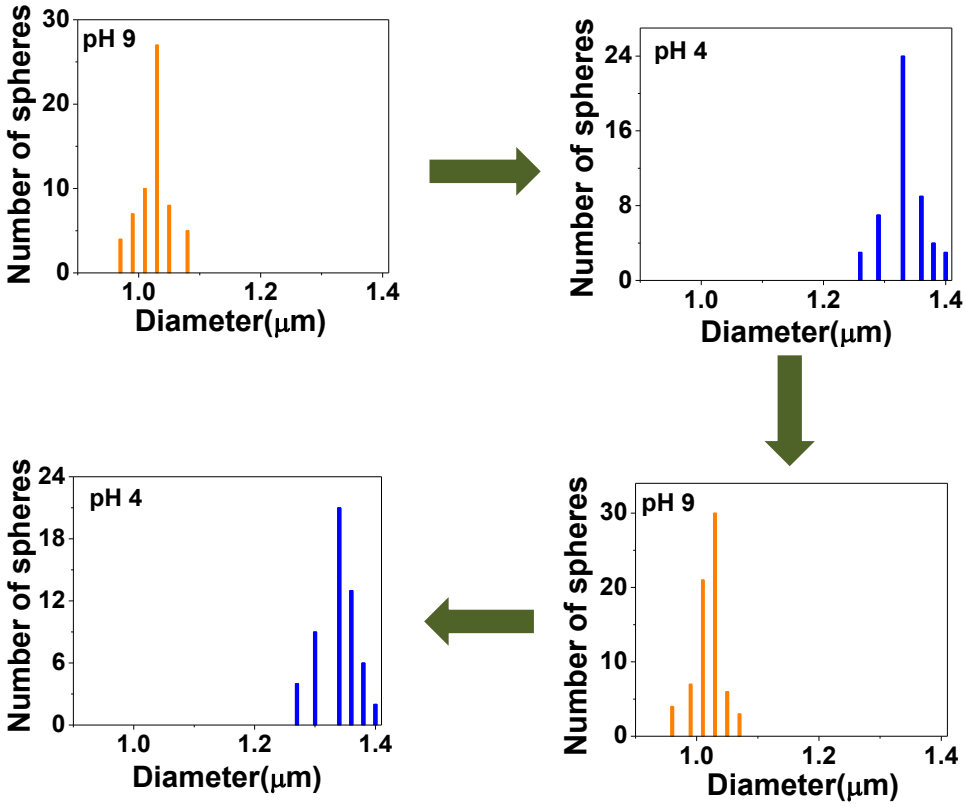

Figure 12: Statistical sizing of PSL4 at different pH using confocal images for two cycles of pH change.

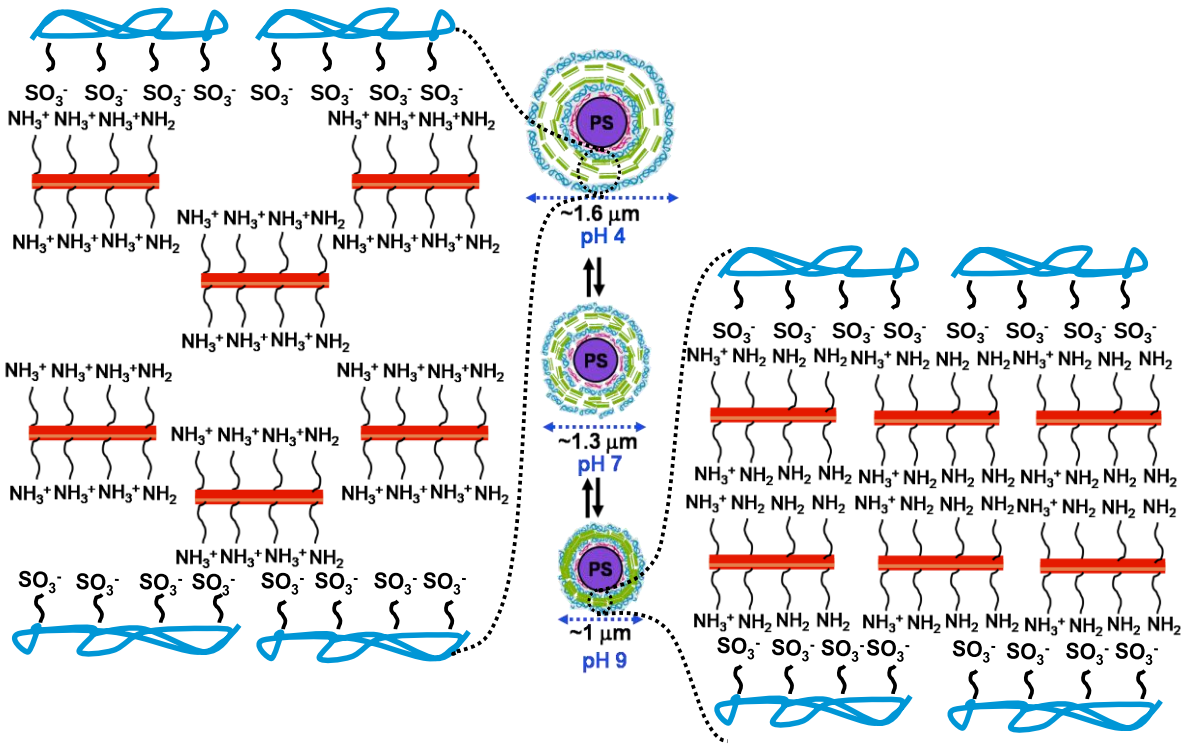

Scheme 2: Schematic, showing swelling and de-swelling of aminoclay layers inside the polyelectrolyte matrix, which results in size changes of PSL4 with pH.

extent of exfoliation is greatly reduced. Unlike free aminoclay, the clay in PSL4 is sandwiched between polyelectrolyte layers which physically entrap the clay layers and prevents their free exfoliation. Rather, it swells with decrease in pH by the inclusion of water molecules around the protonated amine groups (Scheme 2). Such swelling effects are observed in the polyelectrolytes only at a very low pH (<2.5) or at a very high pH (>11.5) and are not stable for a longer period.[72,73]

The size-oscillation resulting from the degree of protonation of amino groups present in the clay is effectively used to demonstrate a pH dependent release of oppositely charged molecules. In an acidic pH, the clay sheets inside the PSL4 would be positively charged and can intercalate negatively charged molecules.[48] To demonstrate the application of PSL4 for small molecule delivery, a model drug Ibuprofen (pKa = 4.4)

which is commonly used in the treatment of arthritis, primary dysmenorrhea, fever *etc* was chosen. After an equilibration time of 10 h, at pH 6.3, the amount of ibuprofen adsorbed per gram of PSL4 was around 3 mg (Figure 13). The release properties of the drug over PSL4 was monitored for 1h at different pH 4, 7 and 9.8 and the results are given in the bar diagram in Figure 14c. The release behavior of the drug over PSL4-NC was also studied for comparison. From the Figure 14c, it is clear that nearly 40 % of the drug was released at pH 7, a slightly higher pH than the drug loading pH, 6.3. As the pH was increased to 9.8, the release was about 90%. However, at pH 4, the release of the drug was around 55%, significantly lower than the release at pH 9.8, but still higher than the release at pH 7. On the other hand, the sample without the clay layer (PSL4-NC) did not show any appreciable variation over the entire pH range studied. At high pH, the extent of protonation in aminoclay is low and therefore, the electrostatic interaction between the negatively charged ibuprofen molecules and the clay layers in PSL4 will be very much reduced. The repulsion between the negatively charged ibuprofen molecules combined with the shrinking of spheres contributes to the higher release at pH 9.8. At

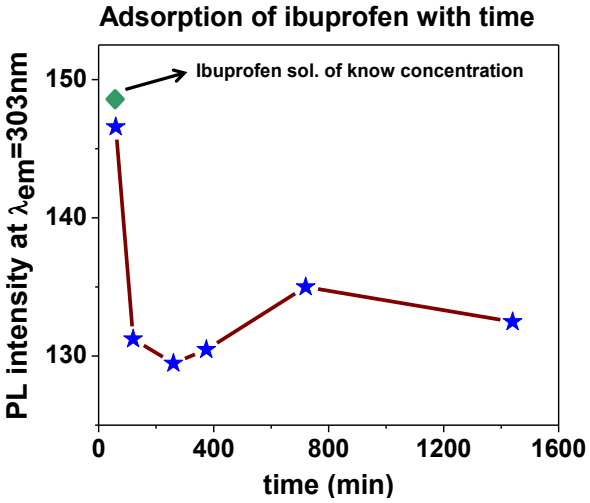

Figure 13: EDAX analysis of hollow spheres/capsules.

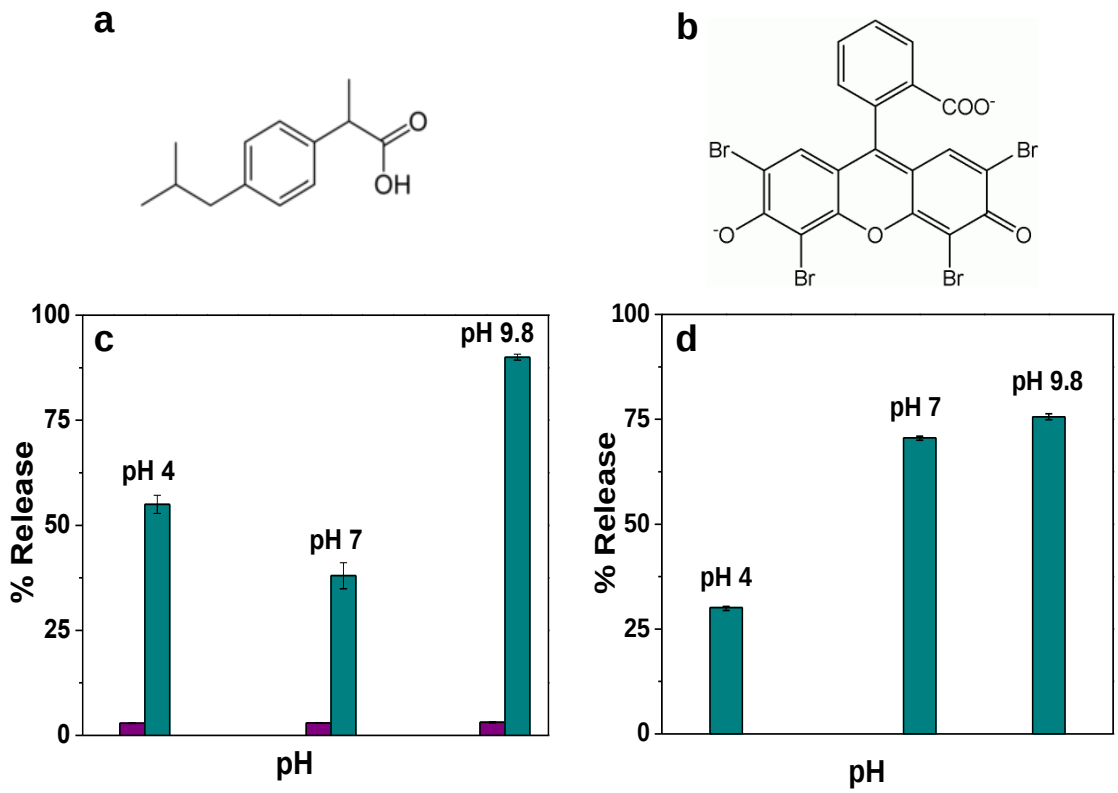

Figure 14: Release behavior of PSL4 at different pH observed for 1h. a) Molecular structure of ibuprofen, b) molecular structure of eosin, c) release of loaded drug, ibuprofen, and d) release of dye, eosin. Cyan bar for PSL4 and purple bar is for PSL4-NC.

neutral pH, the strong electrostatic interaction between the protonated aminoclay and the negatively charged ibuprofen reduces the release level. As the pH goes below 4.4, the pKa value of the ibuprofen, the drug molecules are becoming neutral while more number of amino groups in the clay layers are getting protonated whereas. This again reduces the electrostatic interaction between the clay layers and the drug molecules and hence enhances the drug release.[74] This release behavior is different from the release of ibuprofen from the mesoporous materials, where the rate of release was increased with increase in pH in the first one hour due to increased solubility of the drug molecule.[75] However, when the dye, eosin ($pKa_1 = 3.25$) [76] was used to study the release properties of PSL4 spheres, it shows a different behavior (Figure 14d). About 70 % of the dye was

released even at pH 7 which was more or less equal to the amount released at higher pH, 9.8 (~75 %). Reducing the pH of the medium to 4 markedly reduces the release of the eosin molecules to 27 %, a distinct deviation from the ibuprofen behavior. At pH 4, the dye molecules are still negatively charged[76] which will have strong binding to the highly protonated clay layer and therefore, reduces the dye release to the observed lower level.

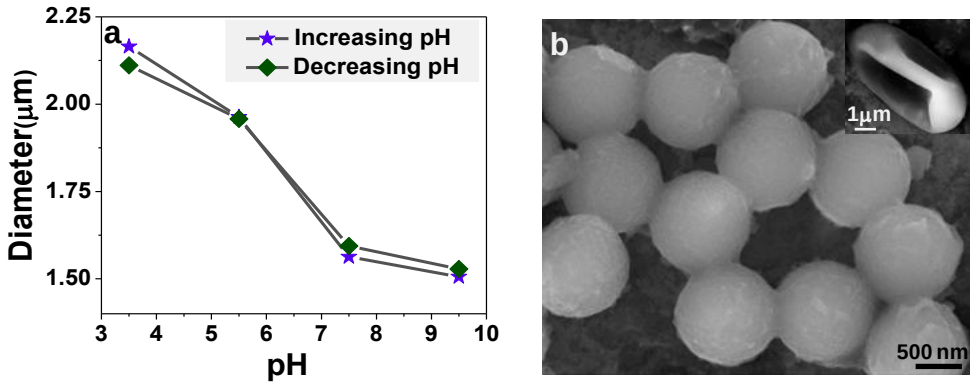

Figure 15: Capsule preparation. a) Size variation of PSL13 spheres with respect to pH, b) Capsules prepared from CaL13 (inset shows a single buckled capsule).

Our efforts to get hollow capsules by dissolving the PS core of PSL4 in tetrahydrofuran failed due to the disruption of fragile walls of the spheres. Fortification of the walls by increasing the number of layers to 13 (PSL13) with the clay layer in the middle (7^{th} layer), still show the reversible volume oscillation with respect to pH (Figure 15a). However, dissolution of polystyrene spheres once again leads to their collapse, probably due to osmotic swelling as the dissolved PS leaves large polymer fragments which cannot permeate out through the polyelectrolyte layers.[20] We therefore made composite spheres similar to PSL13 using $CaCO_3$ spheres as cores. It was possible to successfully produce hollow capsules of polyelectrolyte-clay composite by dissolving the

$CaCO_3$ core using ethylenediaminetetraacetic acid (EDTA)[77] (see Experimental section) (Figure 15b). The absence of Ca in the EDX analysis (Figure 16) confirms the complete

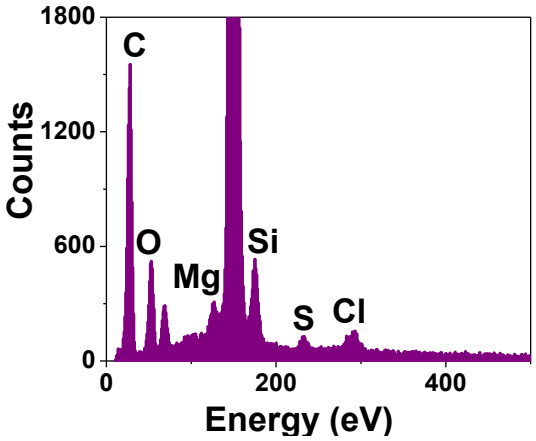

Figure 16: EDAX analysis of hollow spheres/capsules.

removal of $CaCO_3$ leaving the hollow spheres intact due to the presence of inorganic clay component. This is in contrast to the collapsed spheres usually obtained for polyelectrolyte capsules. The buckled morphology (shown in the inset of Figure 15b) templated from a very large calcium carbonate sphere reveals the hollow nature of the spheres after removal of the template.

4.5 Conclusions:

In conclusion, we have demonstrated for the first time the utility of organoclays to form pH responsive spheres. The composites were shown to reversibly expand and shrink in size by 1.6 times over a wide range of pH (4 to 9) due to the protonation of amino groups in the clay layers. This unique behavior of composite spheres was used to demonstrate pH dependent release of negatively charged drug molecule like ibuprofen in the physiologically relevant pH range *i.e.* 4.5 to 7.5. It was also shown that the composite sphere could be successfully used to adsorb eosin quite effectively. The future development of this material could involve changing the hydrophilicity of the clay layers. By increasing the length of the alkylamino pendent groups, one can load both hydrophobic and hydrophilic drug. Furthermore, the hollow capsules prepared after core dissolution can have special advantage over the existing microcapsules as it can be loaded with two different kinds of guest molecules, reactants, or drugs for dual delivery applications.

4.6 References:

1. Stuart, M. A. C.; Huck, W. T. S.; Genzer, J.; Müller, M.; Ober, C.; Stamm, M.; Sukhorukov, G. B.; Szleifer, I.; Tsukruk, V. V.; Urban, M.; Winnik, F.; Zauscher, S.; Luzinov, I.; Minko, S. Emerging Applications of Stumuli-Responsive Polymeric Materials. *Nat. Mater.* **2010**, *9*, 101-113.
2. Xia, F.; Jiang, L. Bio-Inspired, Smart, Multiscale Interfacial Materials. *Adv. Mater*. **2008**, *20*, 2842-2858.
3. Lu, Y.; Liu, J. Smart Nanomaterials Inspired by Biology: Dynamic Assembly of Error-Free Nanomaterials in Response to Multiple Chemical and Biological Stimuli. *Acc. Chem. Res.* **2007**, *40*, 315-323.
4. Luzinova, I.; Minko, S.; Tsukruk, V. V. Adaptive and Responsive Surfaces through Controlled Reorganization of Interfacial Polymer Layers. *Prog. Polym. Sci*. **2004**, *29*, 635–698.
5. Dai, C. D.; Eakins, D. E.; Thadhani, N. N. Dynamic Densification Behavior of Nanoiron Powders Under Shock Compression. *J. Appl. Phy*. **2008**, *103*, 093503.
6. Soppimath, K. S.; Liu, L. H.; Seow, W. Y.; Liu, S. Q.; Powell, R.; Chan, P.; Yang, Y. Multifunctional Core/Shell Nanoparticles Self-Assembled from pH-Induced Thermosensitive Polymers for Targeted Intracellular Anticancer Drug Delivery. *Adv. Funct. Mater.* **2007**, *17*, 355-362.
7. Tan, W. S.; Cohen, R. E.; Rubner, M. F.; Sukhishvili, S. A. Temperature-Induced, Reversible Swelling Transitions in Multilayers of a Cationic Triblock Copolymer and a Polyacid. *Macromolecules* **2010**, *43*, 1950–1957.

8. Yameen, B.; Ali, M.; Neumann, R.; Ensinger, W.; Knoll, W.; Azzaroni, O. Single Conical Nanopores Displaying pH-Tunable Rectifying Characteristics. Manipulating Ionic Transport with Zwitterionic Polymer Brushes. *J. Am. Chem. Soc.* **2009**, *131*, 2070-2071.
9. Sukhorukov, G. B.; Antipov, A. A.; Voigt, A.; Donath, E.; Möhwald, H. pH-Controlled Macromolecule Encapsulation in and Release from Polyelectrolyte Multilayer Nanocapsules. *Macromol. Rapid Commun.* **2001**, *22*, 44–46.
10. Garnweitner, G.; Smarsly, B.; Assink, R.; Ruland, W., Bond, E.; Brinker, C. J. Self-Assembly of an Environmentally Responsive Polymer/Silica Nanocomposite. *J. Am. Chem. Soc.* **2003**, *125*, 5626-5627.
11. Mauser, T.; Déjugnat, C.; Sukhorukov, G. B. Balance of Hydrophobic and Electrostatic Forces in the pH Response of Weak Polyelectrolyte Capsules. *J. Phys. Chem. B* **2006**, *110*, 20246-20253.
12. Mauser, T.; Déjugnat, C.; Sukhorukov, G. B. Reversible pH-Dependent Properties of Multilayer Microcapsules Made of Weak Polyelectrolytes. *Macromol. Rapid Commun.* **2004**, *25*, 1781–1785.
13. Kwon, I. C.; Bae, Y. H.; Kim, S. W. Electrically Erodable Polymer Gel for Controlled Release of Drugs. *Nature* **1991**, *354*, 291-293.
14. Cai, K.; Luo, Z.; Hu, Y.; Chen, X.; Liao, Y.; Yang, L.; Linhong Magnetically Triggered Reversible Controlled Drug Delivery from Microfabricated Polymeric Multireservoir Devices. *Adv. Mater*. **2009**, *21*, 4045-4049.
15. Mai, Y.; Dong, W.; Hempenius, M. A.; Möhwald, H.; Vancso, G. J. Redox-Controlled Molecular Permeability of Composite-Wall Microcapsules. *Nat. Mater.* **2006**, *5*, 724-729.

16. Park, J. M.; Aoyama, S.; Zhang, W.; Nakatsuji, Y.; Ikeda, I. Photodimerisation of a Styrylpyrazine Amphiphile Suppresses the Release of Glucose Entrapped in its Mixed Vesicle with DPPC. *Chem. Commun*. **2000**, 231-232.

17. Liu, N.; Chen, Z.; Dunphy, D. R.; Jiang, Y.B.; Assink, R. A.; Brinker, C. J. Photoresponsive Nanocomposite Formed by Self-Asssembly of an Azobenzene-Modified Silane. *Angew. Chem. Int. Ed.* **2003**, *42*, 1731 – 1734.

18. Ishihara, K.; Muramoto, N.; Shinohara, I. Controlled Release of Organic Substances Using Polymer Membranes with Responsive Function for Amino Compounds. *J. Appl. Polym. Sci*. **1984**, *29*, 211-217.

19. Ibarz, G.; Dähne, L.; Donath, E.; Möhwald, H. Smart Micro- and Nanocontainers for Storage, Transport, and Release. *Adv. Mater.* **2001**, *13*, 1324-1327.

20. Peyratout, C. S.; Dähne, L. Tailor-Made Polyelectrolyte Microcapsules: From Multilayers to Smart Containers. *Angew. Chem. Int. Ed*. **2004**, *43*, 3762-3783.

21. Yu, S.; Azzam, T.; Rouiller, I.; Eisenberg, A. "Breathing" Vesicles. *J. Am. Chem. Soc.* **2009**, *131*, 10557–10566.

22. Sandström, M. C.; Ickenstein, L. M.; Mayer, L. D.; Edwards, K. Effects of Lipid Segregation and Lysolipid Dissociation on Drug Release from Thermosensitive Liposomes. *J. Controlled Release* **2005**, *107*, 131-148.

23. Kang, Y.; Walish, J. J.; Gorishnyy, T.; Thomas, E. L. Broad-Wavelength-Range Chemically Tunable Block-Copolymer Photonic Gels. *Nat. Mater.* **2007**, *6*, 957-960.

24. Feuchtwanger, J.; Asua, E.; García-Arribas, A.; Etxebarria, V.; Barandiaran, J. M. Ferromagnetic Shape Memory Alloys for Positioning with Nanometric Resolution. *Appl. Phys. Lett.* **2009**, *95*, 054102.

25. Cohen, R. E. Origin of Ferroelectricity in Perovskite Oxides. *Nature* **1992**, *358*, 136-138.
26. Jaffe, B.; Cook, W. R.; Jaffe, H. Piezoelectric Ceramics (Academic, New York, **1971**).
27. Ehre, D.; Lyahovitskaya, V.; Tagantsev, A.; Lubomirsky, I. Amorphous Piezo and Pyroelectric Phases of $BaZrO_3$ and $SrTiO_3$. *Adv. Mater.* **2007**, *19*, 1515-1517.
28. Nunes, S. C.; Bermudez, V. D. Z.; Silva, M. M.; Smith, M. J.; Ostrovskii, D.; Ferreira, R. A. S.; Carlos, L. D.; Rocha, J.; Gonçalves, A.; Fortunato E. Sol–Gel-Derived Potassium-Based di-Ureasils for ‘‘Smart Windows’’. *J. Mater. Chem.* **2007**, *17*, 4239-4248.
29. *Granqvist C.-G.;* Electrochromic materials: Out of a niche, *Nat. Mater.* **2006**, *5*, 89-90.
30. *Somani P. R;, Radhakrishnan S.;* Electrochromic materials and devices: present and future. *Materials Chemistry and Physics* **2002**, *77*, 117–133.
31. Kickelbick, G. Hybrid Materials: Synthesis, Characterization and Application; Wiley-VCH: Weinheim, Germany, 2007; pp 7-9.
32. Capadona, J. R.; Shanmuganathan, K.; Tyler, D. J.; Rowan, S. J.; Weder, C. Stimuli-Responsive Polymer Nanocomposites Inspired by the Sea Cucumber Dermis. *Science* **2008,** *319*, 1370-1374.
33. Katagiri, K.; Nakamura, M.; Koumoto, K. Magnetoresponsive Smart Capsules Formed with Polyelectrolytes, Lipid Bilayers and Magnetic Nanoparticles *ACS Applied Materials & Interfaces* **2010**, *2*, 768–773.

34. Schmidt, D. J.; Cebeci, F. C.; Kalcioglu, Z. I.; Wyman, S. G.; Ortiz, C.; Vliet, K. J. V.; Hammond, P. T. Electrochemically Controlled Swelling and Mechanical Properties of a Polymer Nanocomposite. *ACS Nano* **2009**, *3*, 2207–2216.
35. Motornov, M.; Zhou, J.; Pita, M.; Gopishetty, V.; Tokarev, I.; Katz, E.; Minko, S. "Chemical Transformers" from Nanoparticle Ensembles Operated with Logic. *Nano Lett.* **2008**, *8*, 2993-2997.
36. Riskin, M.; Basnar, B.; Huang, Y.; Willner, I. Magnetoswitchable Charge Transport and Bioelectrocatalysis Using Maghemite-Au Core-Shell Nanoparticle/Polyaniline Composites. *Adv. Mater.* **2007**, *19*, 2691–2695.
37. Bédard, M.; Skirtach, A. G.; Sukhorukov, G. B. Optically Driven Encapsulation Using Novel Polymeric Hollow Shells Containing an Azobenzene Polymer. *Macromol. Rapid Commun.* **2007**, *28*, 1517–1521.
38. Mura S.; Nicolas J.; Couvreur P.; Stimuli-responsive nanocarriers for drug delivery. *Nat. Mater.* **2013**, *12*, 991-1003.
39. Ruiz-Hernández E.; Baeza A.; Vallet-Regí M.; Smart Drug Delivery through DNA/Magnetic Nanoparticle Gates. *ACS Nano*, **2011**, *5*, 1259-1266.
40. Geest, B. G. D.; Skirtach, A. G.; Mamedov, A. A.; Antipov, A. A.; Kotov, N. A.; Smedt, S. C. D.; Sukhorukov, G. B. Ultrasound-Triggered Release from Multilayered Capsules *Small* **2007**, *3*, 804 – 808.
41. Liu, N.; Yu, K.; Smarsly, B.; Dunphy, D. R.; Jiang, Ying-Bing; Brinker, C. J. Self-Directed Assembly of Photoactive Hybrid Silicates Derived from an Azobenzene-Bridged Silsesquioxane. *J. Am. Chem. Soc.* **2002**, *124*, 14540-14541.
42. Muthusamy, E.; Walsh, D.; Mann, S. Morphosynthesis of Organoclay Microspheres with Sponge-Like or Hollow Interiors. *Adv. Mater*. **2002**, 14, 969-972.

43. Putlitz, B. Z.; Landfester, K.; Fischer, H.; Antonietti, M. The Generation of ªArmored Latexesº and Hollow Inorganic Shells Made of Clay Sheets by Templating Cationic Miniemulsions and Latexes. *Adv. Mater*. **2001**, *13*, 500-503.

44. Bourlinos, A. B.; Karakassides, M. A.; Petridis, D. Synthesis and Characterization of Hollow Clay Microspheres through a Resin Template Approach. *Chem. Commun.* **2001**, 1518–1519.

45. Caruso, R. A.; Susha, A.; Caruso, F. Multilayered Titania, Silica, and Laponite Nanoparticle Coatings on Polystyrene Colloidal Templates and Resulting Inorganic Hollow Spheres. *Chem. Mater.* **2001,** *13*, 400-409.

46. Furusawa, K.; Norde, W.; Lyklema, A Method for Preparing Surfactant-Free Polystyrene Latices of High Surface Charge. J. *Kolloid-ZZ Polym*. **1972**, 250, 908-909.

47. Patil, A. J.; Muthusamy, E.; Mann, S. Synthesis and Self-Assembly of Organoclay-Wrapped Biomolecules. *Angew. Chem. Int. Ed.* **2004**, *43*, 4928 –4933.

48. Datta, K. K. R.; Eswaramoorthy, M.; Rao, C. N. R. Water-Solubilized Aminoclay–Metal Nanoparticle Composites and their Novel Properties. *J. Mater. Chem*. **2007**, 17, 613-615.

49. Che, S.; Garcia-Bennett, A. E.; Yokoi, T.; Sakamoto, K.; Kunieda, H.; Terasaki, O.; Tatsumi, T. A Novel Anionic Surfactant Templating Route for Synthesizing Mesoporous Silica with Unique Structure. *Nat. Mater.* **2003**, *2*|, 801-805.

50. Decher, G. Fuzzy Nanoassemblies: Toward Layered Polymeric Multicomposites. *Science* **1997**, *277*, 1232–1237.

51. Kleinfeld, E. R.; Ferguson, G. S. Stepwise Formation of Multilayered Nanostructural Films from Macromolecular Precursors. *Science* **1994**, *265*, 370-373.

52. Kozlovskaya, V.; Kharlampieva, E.; Erelb, I.; Sukhishvili, S. A. Multilayer-Derived, Ultrathin, Stimuli-Responsive Hydrogels. *Soft Matter* **2009**, *5*, 4077–4087.
53. Srivastava, S.; Kotov, N. A. Composite Layer-by-Layer (LBL) Assembly with Inorganic Nanoparticles and Nanowires. *Acc. Chem. Res.* **2008**, *41*, 1831-1841.
54. Hammond, P. T. Form and Function in Multilayer Assembly: New Applications at Nanoscale. *Adv. Mater.* **2004**, *16*, 1271-1293.
55. Kotov, N. A.; Dekany, I.; Fendler, J. H. Layer-by-Layer Self-Assembly of Polyelectrolyte-Semiconductor Nanoparticle Composite Films. *J. Phys. Chem.* **1995**, *99*, 13065-13069.
56. Mamedov, A. A.; Kotov, N. A.; Prato, M.; Guldi, D. M.; Wicksted, J. P.; Hirsch, A. Molecular Design of Strong Single-Wall Carbon Nanotube/Polyelectrolyte Multilayer Composites. *Nat. Mater.* **2002**, *1*, 190-194.
57. Jiang, C.; Ko, H.; Tsukruk, V. V. Strain-Sensitive Raman Modes of Carbon Nanotubes in Deflecting Freely Suspended Nanomembranes. *Adv. Mater.* **2005**, *17*, 2127-2131.
58. Kleinfeld, E. R.; Ferguson, G. S. Healing of Defects in the Stepwise Formation of Polymer/Silicate Multilayer Films. *Chem. Mater.* **1996,** *8*, 1575-1578.
59. Kleinfeld, E. R.; Ferguson, G. S. Rapid, Reversible Sorption of Water from the Vapor by a Multilayered Composite Film: A Nanostructured Humidity Sensor. *Chem. Mater.* **1995,** *7*, 2327-2331.
60. Lvov, Y.; Decher, G.; Sukhorukov, G. Assembly of Thin Films by Means of Successive Deposition of Alternate Layers of DNA and poly(allylamine). *Macromolecules* **1993**, *26*, 5396-5399.

61. Hong, J. D.; Lowack, K.; Schmitt, J.; Decher, G. Layer-by-Layer Deposited Multilayer Assemblies of Polyelectrolytes and Proteins: from Ultrathin Films to Protein Arrays. *Prog. Coll. Pol. Sci.* **1993**, *93*, 98-102.

62. Lvov, Y.; Ariga, K.; Kunitake, T. Layer-by-Layer Assembly of Alternate Protein/Polyion Ultrathin Films. *Chem. Lett.* **1994**, *12*, 2323-2326.

63. Yoo, P. J.; Nam, K. T.; Qi, J.; Lee, S. K.; Park, J.; Belcher, A. M.; Hammond, P. T. Spontaneous Assembly of Viruses on Multilayered Polymer Surfaces. *Nat. Mater.* **2006**, *5*, 234 - 240.

64. Cassier, T.; Sinner, A.; Offenhauser, A.; Mohwald, H. Homogeneity, Electrical Resistivity and Lateral Diffusion of Lipid Bilayers Coupled to Polyelectrolyte Multilayers. *Colloids Surf. B* **1999**, *15*, 215-225.

65. Geest, B. G. D.; Sanders, N. N.; Sukhorukov, G. B.; Demeestera, J.; Smedt, S. C. D. Release Mechanisms for Polyelectrolyte Capsules. *Chem. Soc. Rev.* **2007**, *36*, 636–649.

66. Geest, B. G. D.; Koker, S. D.; Sukhorukov, G. B.; Kreft, O.; Parak, W. J.; Skirtach, A. G.; Demeester, J.; Smedt, S. C. D.; Hennink, W. E. Polyelectrolyte Microcapsules for Biomedical Applications. *Soft Matter* **2009**, *5*, 282–291.

67. Angelatos, A. S.; Katagiri, K.; Caruso, F. Bioinspired Colloidal Systems *via* Layer-by-Layer Assembly. *Soft Matter* **2006**, *2*, 18–23.

68. Nalluri, S. K. M.; Ravoo, B. J. Light-Responsive Molecular Recognition and Adhesion of Vesicles. *Angew. Chem. Int. Ed.* **2010**, *49*, DOI: 10.1002/anie.201001442.

69. Yin, J.; Dupin, D.; Li, J.; Armes, S. P.; Liu, S. pH-Induced Deswelling Kinetics of Sterically Stabilized Poly(2-vinylpyridine) Microgels Probed by Stopped-Flow Light Scattering. *Langmuir* **2008**, *24*, 9334–9340.

70. Dupin, D.; Rosselgong, J.; Armes, S. P.; Routh, A. Swelling Kinetics for a pH-Induced Latex-to-Microgel Transition. *Langmuir* **2007**, *23*, 4035–4041.

71. Dupin, D.; Fujii, S.; Armes, S. P.; Reeve, P.; Baxter, S. M. Efficient Synthesis of Sterically Stabilized pH-Responsive Microgels of Controllable Particle Diameter by Emulsion Polymerization. *Langmuir* **2006**, *22*, 3381–3387.

72. Dubas, S. T.; Schlenoff, J. B. Polyelectrolyte Multilayers Containing a Weak Polyacid: Construction and Deconstruction. *Macromolecules* **2001**, *34*, 3736-3740.

73. Déjugnat, C.; Sukhorukov, G. B. pH-Responsive Properties of Hollow Polyelectrolyte Microcapsules Templated on Various Cores. *Langmuir* **2004**, *20*, 7265- 7269.

74. Holmström, S. C.; Patil, A. J.; Butler, M.; Mann, S. Influence of Polymer Co-intercalation on Guest Release from Aminopropylfunctionalized Magnesium Phyllosilicate Mesolamellar Nanocomposites. *J. Mater. Chem*. **2007**, *17*, 3894–3900.

75. Lee, K.; Lee, D.; Lee, H.; Kim, Chang-Koo; Wu, Z.; Lee, K. Comparison of Amine-Functionalized Mesoporous Silica Particles for Ibuprofen Delivery. *Korean J. Chem. Eng*. **2010**, *27*, 1333-1337.

76. Ledlain, P.; Fompeydie, D. Determination of Equilibrium Constants by Derivative Spectrophotometry. Application to the pKas of Eosin. *Anal. Chem.* **1985**, *57*, 2561-2563.

77. Volodkin, D. V.; Petrov, A. I.; Prevot, M.; Sukhorukov, G. B. Matrix Polyelectrolyte Microcapsules: New System for Macromolecule Encapsulation. *Langmuir* **2004**, *20*, 3398-3406.

Chapter 5

Oxidative Dehydrogenation of Propane over Boron Nitride and Boron Nitride Supported Metal Catalysts

Summary:

Metal free catalysts are highly sought after as the metal based catalysts suffer from severe disadvantages such as high cost, poor durability, and detrimental environmental effects of their residues. Here, we report, for the first time, on the catalytic activity of, so called inert, boron nitride materials. Hexagonal boron nitride having high specific surface areas were synthesized using different methods and characterized. Their catalytic activity towards propane oxidative dehydrogenation (ODH) reaction was found to improve with the surface area. The catalytic activity of high surface area BN was found to be stable up to five hours and could be regenerated by heating in dilute ammonia flow. Oxidation of surface B-N bonds in oxygen leads to the diminishing catalytic activity, which on heating in ammonia reduced back to their native form regaining the indigenous catalytic activity. Metal nanoparticles (Au and Pt) supported boron nitride however, did not show better performance for propane ODH in comparison to the BN materials.

Manuscript based on this chapter is under preparation.

5.1 Introduction:

Propene is one of the key commodity chemicals, as it forms a versatile building block and is the feed stock for a wide range of important monomers, polymers, intermediates, and chemicals.[1] This versatility stems from the chemical structure of propene (Figure 1a).[1,2] Propene contains a carbon-carbon double bond which could undergo addition reactions and an allylic methyl group which could undergo substitution

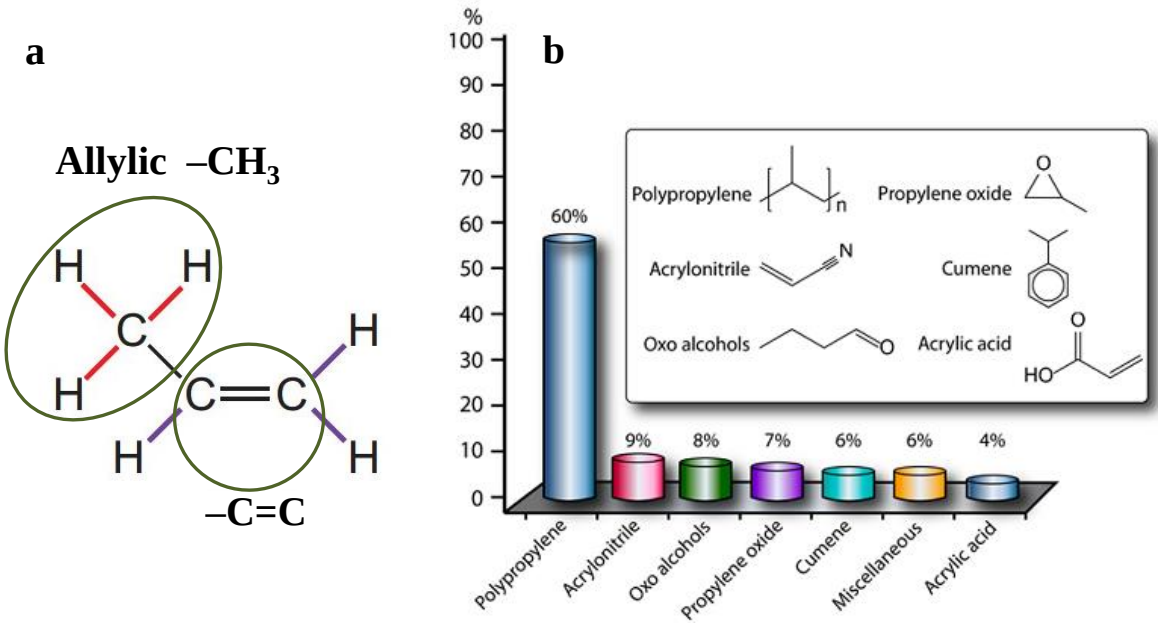

Figure 1: Propene. a) Structure and b) various industrial propene derivatives. Adapted with permission from reference 3. Copyright 2014, American Chemical Society.

reactions resulting in a variety of important industrial derivatives (Figure 1b).[2,3] Consequently, the global propene demand has increased at an average annual growth rate above 6% and is projected to increase significantly in the future (50 million tons in 2011 to 132 million tons in 2025) (Figure 2a).[4] At present, the main sources of propene are: steam cracking (of propane, butane, and naphtha), fluid-catalytic-cracking (of gas oil and

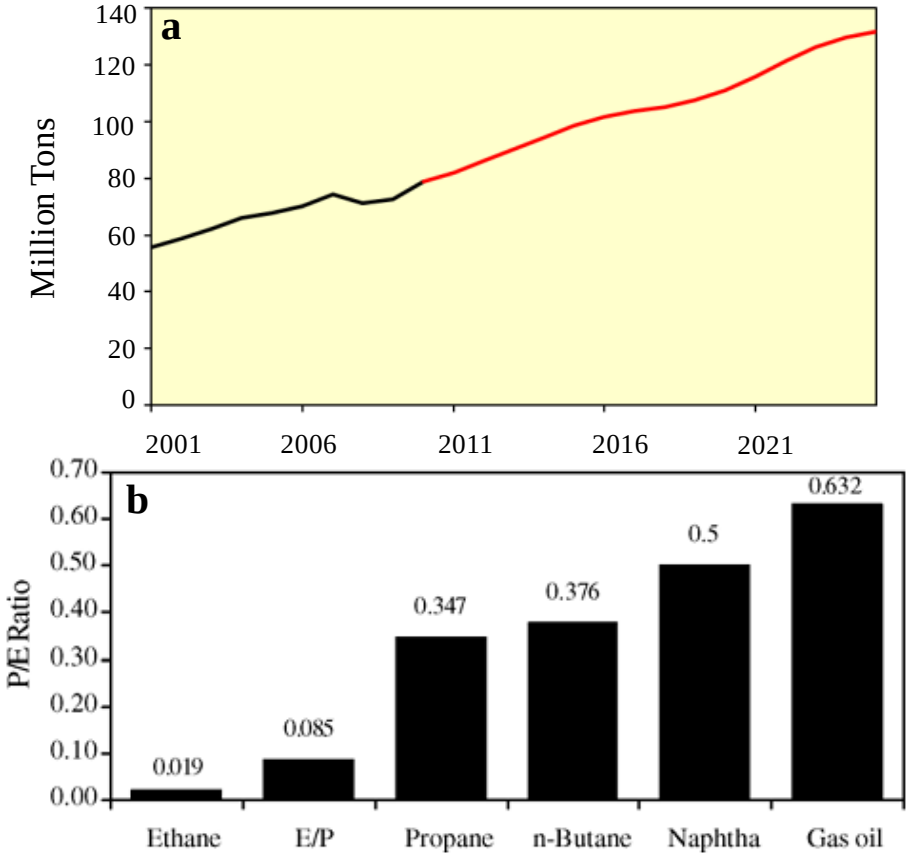

Figure 2: Propene demand and supply. a) Increasing global propene demand (the red line is the projection for future propene demand) with time, and b) ton of propene per ton of ethene for various steam cracker feeds. P/E in the ordinate stands for propene/ethene and E/P in the abscissa stands for ethane/propane. Adapted with permission from reference 1. Copyright 2014, American Chemical Society.

propane), and catalytic dehydrogenation (of propane).[5] In the first two methods, the main product is ethylene, while propene forms as a byproduct in smaller quantities.[5,6] The fraction of propene in the product increases with increasing molecular weight of the paraffin (Figure 2b).[1] However, the advent of shale gas, which mainly consists of methane and natural gas fadliquids (ethane, propane, and butane), is driving the ethene industry away from heavier feedstock (like naphtha) towards low cost ethane feedstock which essentially is putting pressure on the propene market thus making producing

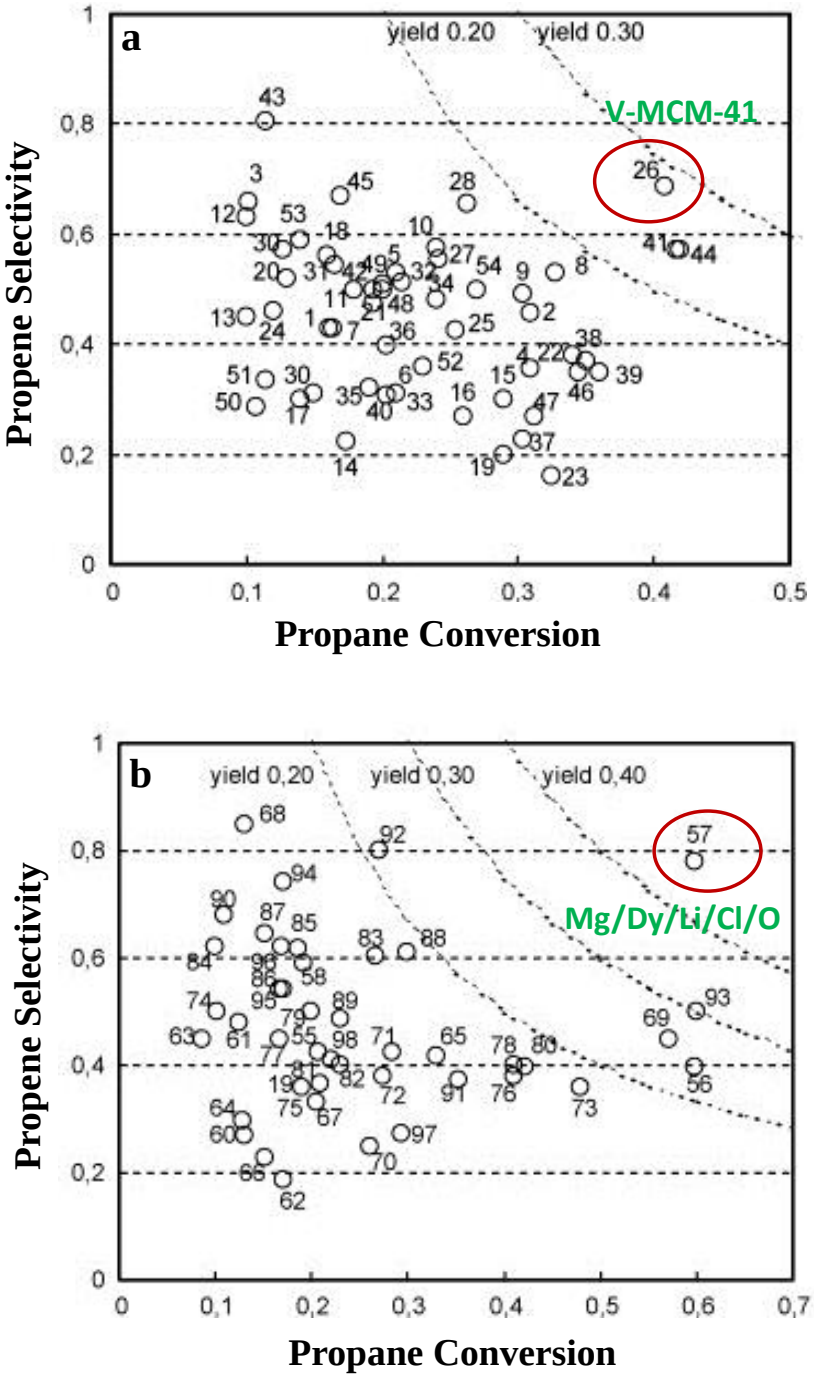

Figure 3: A molar selectivity vs. conversion chart for ODH of propane (catalysts reported over a period of 2000-2006). a) Catalysts containing V as the main active element, and b) other catalysts. Marked with red circle are catalysts (name given in green font) with the highest propene yield. Adapted with permission from reference 5. Copyright 2007, Elsevier.

propene from propane, highly competitive.[4,6] The catalytic dehydrogenation (DH) of propane[7] is the premier technology in use for on purpose propene production.[3,5] But, this reaction is highly endothermic ($C_3H_8 \longrightarrow C_3H_6 + H_2$; ΔH_{298K} = +124 kJ/mol) and operates at high temperatures.[3,5] Also, the rapid catalyst deactivation due to coke deposition is a major concern as it requires frequent catalyst regeneration which significantly adds to the cost of the process.[3,5] Therefore, the present methods of the propene production are not expected to fulfill its increasing demand in the future.

The catalytic oxidative dehydrogenation (ODH) of propane is a promising alternative process, for on-purpose propene production, to close the growing gap between the demand and production of propene.[3,5] The advantages of the propane ODH reaction are that the reaction is (i) exothermic ($C_3H_8 + 1/2O_2 \longrightarrow C_3H_6 + H_2O$; ΔH_{298K} = -117 kJ/mol), (ii) thermodynamically unrestricted, (iii) operates at much lower temperatures, and (iv) minimizes coke deposition (due to presence of oxygen in the feed) ensuring long-term stability of the catalyst.[3] There are number of catalysts reported for the propane ODH reaction, (Figure 3) among them supported vanadium oxides and molybdenum oxides being the most efficient and selective catalysts.[5] In spite of extensive scientific efforts, the maximum propene yields obtained till date are around 30%, which is insufficient to justify the economic feasibility of the propane ODH method.[5] This is mainly due to undesirable parallel (complete oxidation, burning, of propane in oxygen to give carbon oxides) and consecutive (being more reactive propene burns relatively easily in oxygen) side reactions which limit the olefin selectivity. Thus, clearly there is an inherent need to develop catalysts which could minimize unwanted side reactions and improve the yield and selectivity of propene at higher propane conversions.

5.2 Scope of the present study:

In this chapter, we have studied the catalytic activity of high surface area layered hexagonal boron nitride (BN) materials for propane ODH reaction. BN is iso-structural to graphite with in-plane covalent bonds and a weak van der Waals attractions between the planes (Figure 4).[8-11] BN materials exhibit unique features such as high thermal conductivity, excellent mechanical strength, remarkable chemical stability, magnetism, and electrical conductivity due to which they are frequently used as refractory, electronic, and lubricant materials.[8-11] Also, BN materials have been demonstrated for their applications as, multifunctional fillers, ultrathin dielectric separation layers, dielectric and sensing substrates, highly durable field emission devices, superhydrophobic surfaces for self-cleaning, drug delivery, *etc*.[8,12-18] Importantly, these commonly accepted 'inert' materials with high chemical and thermal stability and high thermal conductivity, are being extensively explored as catalyst support, under relatively harsh conditions, as it could avoid the sintering of the supported catalyst on hot spots.[19-28] However, to our knowledge, the application of high surface area BN materials as a catalyst has not been reported till date.

Recently, there have been growing interests towards the development of metal (supported metal/metal oxides-most widely used ones) free catalysts of high performance.[29-31] This is because, the metal-based catalysts often suffer from multiple competitive disadvantages, including their high cost, low selectivity, poor durability, and detrimental environmental effects caused by catalyst residues and/or undesirable side-products.[29-31] Carbon nanomaterials such as carbon nanotubes, nanofibers, nanodiamonds,

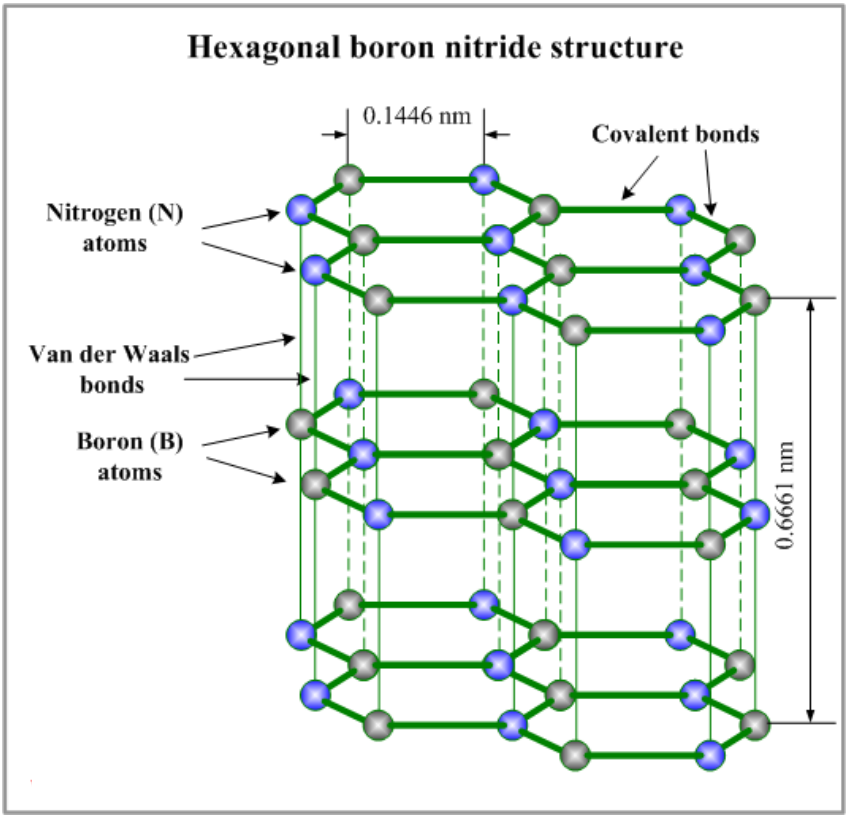

Figure 4: Structure of hexagonal boron nitride. Adapted from www.substech.com.

graphene, etc. are studied as ideal candidates for metal-free catalysts.[32-33] These nanomaterials were shown to catalyze the ODH reaction of ethylbenzene, butane, propane, ethane, etc. with their performances nearly comparable to the traditional catalysts.[34-38] However, the poor stability at higher temperature in presence of oxygen limits their applications in ODH reactions.[39-44] To this end, catalytically active, high surface area BN is an efficient alternative for ODH reactions. This is the first report establishing the catalytic behavior of BN at the nanoscale, which is otherwise well known as an inert material for all the purposes. Further, BN supported metal (Au and Pt) catalysts were also synthesized and tested for their catalytic activity towards propane ODH.

5.3 Materials and Methods:

a. Materials:

Boric acid (H_3BO_3), urea (NH_2CONH_2), melamine ($C_3H_6N_6$), dicyanamide ($C_2H_4N_4$), chloroauric acid ($HAuCl_4$), chloroplatinic acid ($H_2PtCl_6.6H_2O$), sodium borohydride ($NaBH_4$) were purchased from Sigma Aldrich. Propane (2%, He balance), propene (2%, He balance), ethane (2%, He balance), ethene (2%, He balance), butane (2%, He balance), methane (2%, He balance), oxygen (99.99%), hydrogen (99.99%), helium (99.99%), nitrogen (99.99%), air (zero grade), ammonia (99.99%), carbon dioxide (10.1%) gasses were purchased from Chemix, India. All the chemicals and gasses were used as received from the company. Water and methanol were used as solvents wherever required.

b. Synthesis of BN:

Hexagonal boron nitride materials with high specific surface area were synthesized using reported methods.[45-47] The detailed procedures are given below:

BN from boric acid and urea[45]: 0.3 g of boric acid and 7.2 g of urea were dissolved in 50 ml hot water (~85^oC) under constant stirring (Figure 5b). The stirring was continued till all the solvent got evaporated and the samples were completely dry. This resulted in a molecular mixture of the precursors which was thoroughly grinded using mortar and pestle. The dry powder was heated in a tubular furnace (Elite Thermal Systems Limited, TSH15/50/180-2416$_{CG}$) at 900^oC for 5 hours in the nitrogen flow (~ 20 sccm) (Figure 5a,b). The rate of heating and cooling was maintained at 10^oC/min. The

white boron nitride powder obtained was characterized further. This sample was designated as BN-u.

BN from boric acid and melamine[46]: 5 g of boric acid and 2.5 g of melamine were dissolved in 100 ml hot water (~85^{o}C) under constant stirring (Figure 5b). The stirring was continued till all the solvent got evaporated and the samples were completely dry. This resulted in a molecular level mixing of the precursors which was thoroughly grinded using mortar and pestle. The dry powder was heated in a tubular furnace (Elite Thermal Systems Limited, TSH15/50/180-2416$_{CG}$) at 1000^{o}C for 3 hours in the ammonia flow (~ 20 sccm) (Figure 5a,b). The rate of heating and cooling was maintained at 10^{o}C/min. The white boron nitride powder obtained was characterized further. This sample was designated as BN-m.

BN from boric acid and dicyanamide[47]: 1 g of boric acid and 3 g of dicyanamide were dissolved in 100 ml hot water (~85^{o}C) under constant stirring (Figure 5b). The stirring was continued until all the solvent got evaporated and the resulting mixture was thoroughly grinded using mortar and pestle. The dry powder was heated in a tubular furnace (Elite Thermal Systems Limited, TSH15/50/180-2416$_{CG}$) at 1000^{o}C for 3 hours in the ammonia flow (~ 20 sccm) (Figure 5a,b). The rate of heating and cooling was maintained at 10^{o}C/min. The white boron nitride powder obtained was characterized further. This sample was designated as BN-d.

c. Synthesis of BN supported gold and platinum nanoparticles:

BN supported metal nanoparticles were synthesized using wetness incipient impregnation method.[48-49] In a typical procedure, 300 μl of methanol solution of the metal

a

H_3BO_3 + Urea (Weight ratio 1:24) —900°C, 5 hours, N_2→ Non-porous BN sheets (BN-u)

H_3BO_3 + Melamine (Weight ratio 2:1) —1000°C, 3 hours, NH_3→ Porous BN microbelts (BN-m)

H_3BO_3 + Dicyanamide (Weight ratio 1:3) —1000°C, 3 hours, NH_3→ Porous BN microsponges (BN-d)

b

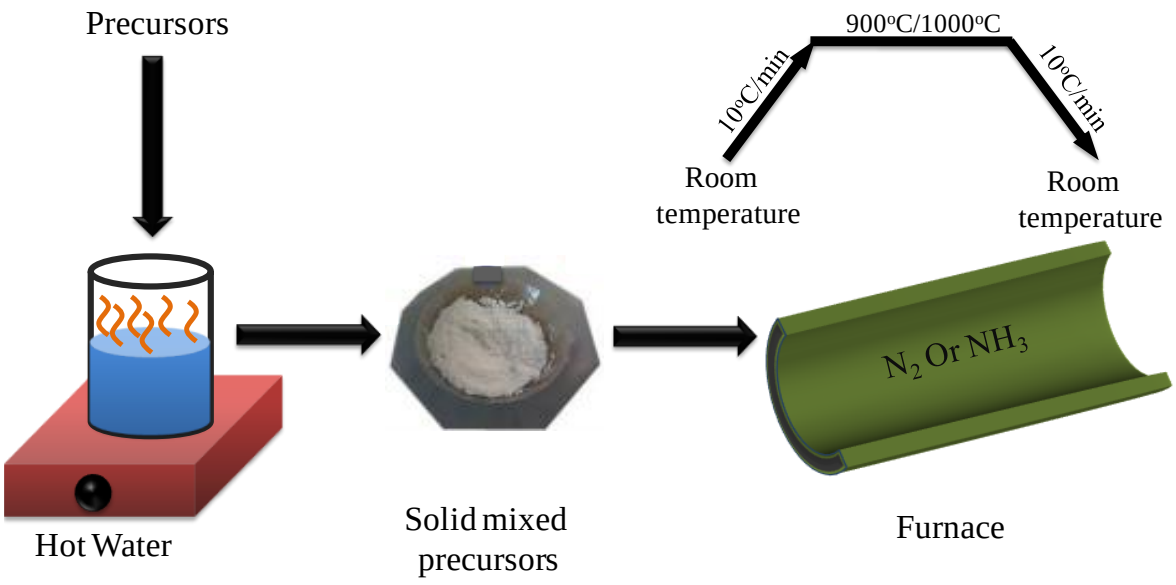

Figure 5: Synthesis of boron nitride. a) Chemical equations for the synthesis and b) schematic representing a typical synthesis procedure.

precursor ($HAuCl_4$, or $H_2PtCl_6.6H_2O$) was added to 200 mg of BN-d (highest surface area (1380 m^2/g) sample, synthesized from boric acid and dicyanamide) sample. The amount of metal in the methanol solution of the metal precursors was fixed at 3 wt% and 1 wt% for gold and platinum respectively. The resulting mixture was dried overnight in a

desiccator under vacuum. The yellow colored dry powder was reduced in hydrogen (99.99%) flow for 2 hours at 400^{o}C (heating rate 2^{o}C/min, cooling rate 5^{o}C/min). The final gold (violet color) and platinum (dark brown color) loaded BN samples were characterized and tested for their catalytic activity towards propane ODH reaction.

d. Characterization:

Morphologies of the samples were analysed by field emission scanning electron microscopy, FESEM (FEI NovaNano SEM-600, Netherlands). Transmission electron microscope, TEM images were acquired with a JEOL JEM 3010 instrument (Japan) operated with an accelerating voltage of 300 kV. Powder X-ray diffraction (XRD) pattern were acquired at room temperature with a Bruker-D8 diffractometer employing Cu Ka. Fourier transform infrared (FTIR) Spectra were acquired on Bruker IFS 66v/S instrument in the range of 4000–400 cm^{-1}. Specific surface area of the samples was measured using N_2 sorption analysis performed at 77K on Autosorb iQ_2. BN samples were out gassed at 150^{o}C under vacuum for 24 hours before the N_2 sorption study. The thermo gravimetric analysis (TGA) was carried out on PerkinElmer Pyris 1 TGA.

e. Catalyst testing:

Catalytic activity of all the samples for propane ODH reaction was tested by fixing 100 mg of the catalyst at the center of a steel tube reactor (of 30 cm length and 6.35 mm inner diameter) with the help of quartz wool on both the sides (Figure 6a). A mixture of 10 sccm of 2% propane in He and 10 sccm oxygen (99.99%) (C_3H_8:O_2 = 1:50, total flow rate 20 sccm) was passed, with the help of mass flow controllers (MFC, MKS systems Singapore), through the reactor at 1 atm (Figure 6b,c). The temperature of the

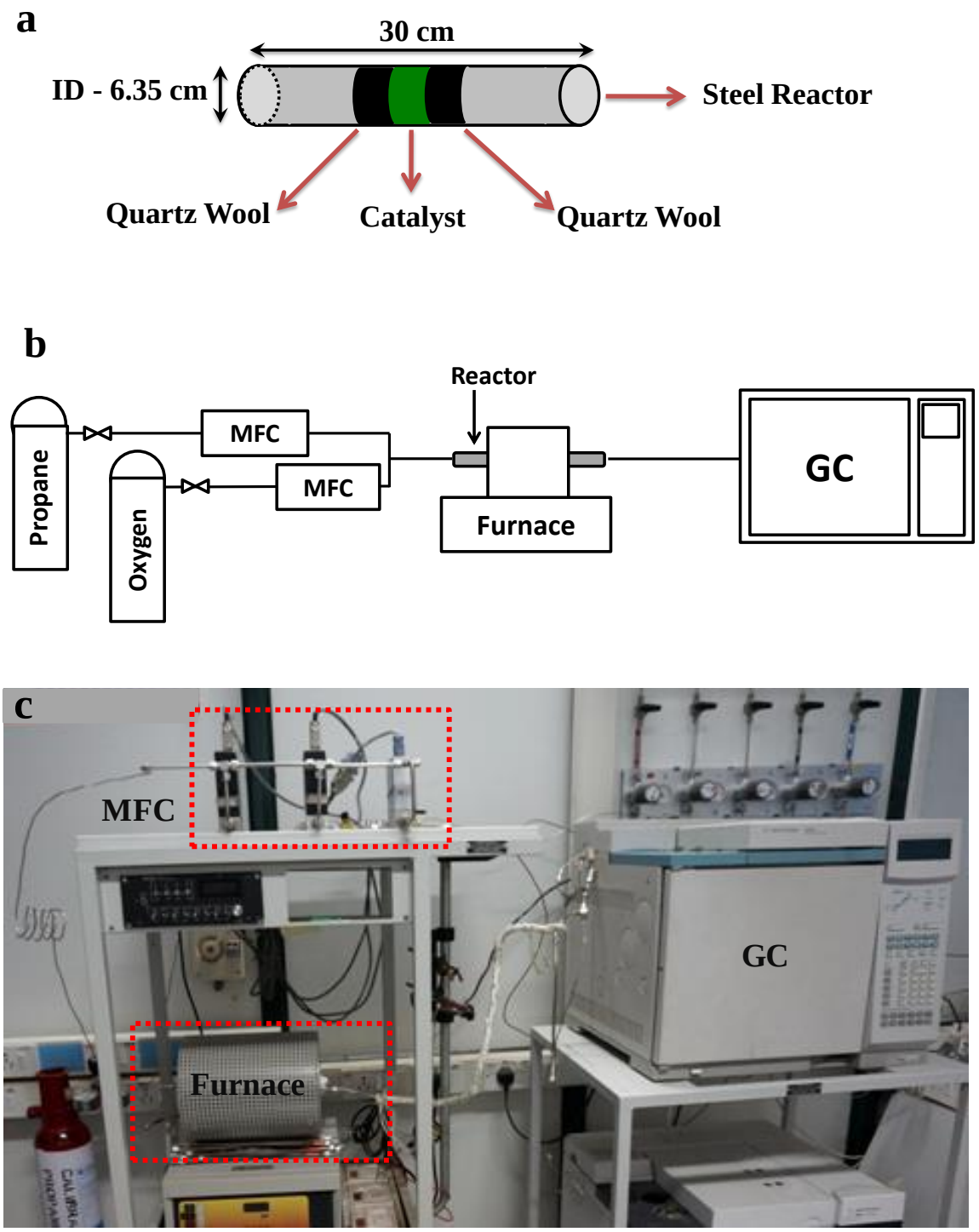

Figure 6: Catalyst testing. a) Packing of the catalyst in the reactor, b) schematic showing typical propane ODH reaction setup used in this study, and c) photograph of the reaction setup. MFC stands for mass flow controller, GC stands for gas chromatogram, and ID is inner diameter.

reactor was controlled by heating it inside a tubular furnace (Carbolite, MTF 12/38/250). The products were analyzed using online gas chromatograms (GC, Agilent 6890N and 7890A) systems fitted with alumina (Rt®-Alumina BOND/Na2SO4, 30m x 0.32mm x 5μm) and molecular sieve (HP MOLESIEVE, 30m x 0.32mm x 12μm) columns. Figure 6c shows the entire reaction system. The performance of the catalyst in the propane ODH reaction was examined on the basis of propane conversion and product selectivities which are defined in the equations given below.[50]

$$\text{\% Conversion (at temperature T)} = \left[1 - \frac{\text{Moles of propane remaining at temperature T}}{\text{Total moles of propane}}\right] \times 100$$

$$\text{\% Selectivity (of a product } i\text{)} = \left[\frac{\text{Moles of propane converted to product } i}{\text{Total moles of propane converted}}\right] \times 100$$

$$\text{\% Yield (of a product } i\text{)} = \left[\frac{(\text{\% Conversion}) \times (\text{\% Selectivity of product } i)}{100}\right]$$

5.4 Results and Discussion:

The as synthesized BN samples were named as BN-u, BN-m, and BN-d, based on the nitrogen source used for their synthesis *viz.* urea, melamine, and dicyanamide respectively (Figure 5a). The field emission scanning electron microscopy (FESEM) and transmission electron microscopy (TEM) images reveal the morphology

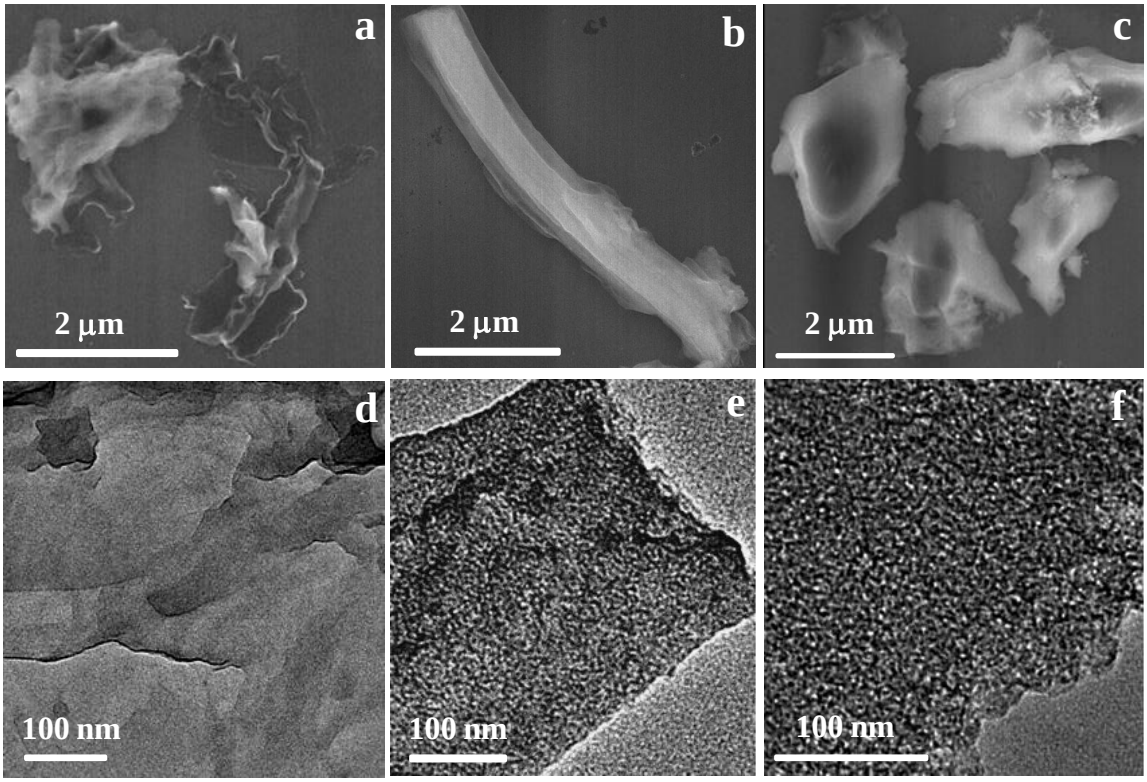

Figure 6: FESEM and TEM images of BN-u (a and d), BN-m (b and e), and BN-d (c and f).

and porosity of the BN samples (Figure 7). FESEM image shows that BN-u forms sheet like nanostructures which are non-porous in nature as revealed by TEM (Figure 7a,d). BN-m have belt like morphology (FESEM in figure 7b) which are porous (TEM in figure 7e). BN-d showed irregular polygon structures in the FESEM image (Figure 7c) and were porous (TEM image, Figure 7f). The crystal structures of the BN samples were deduced

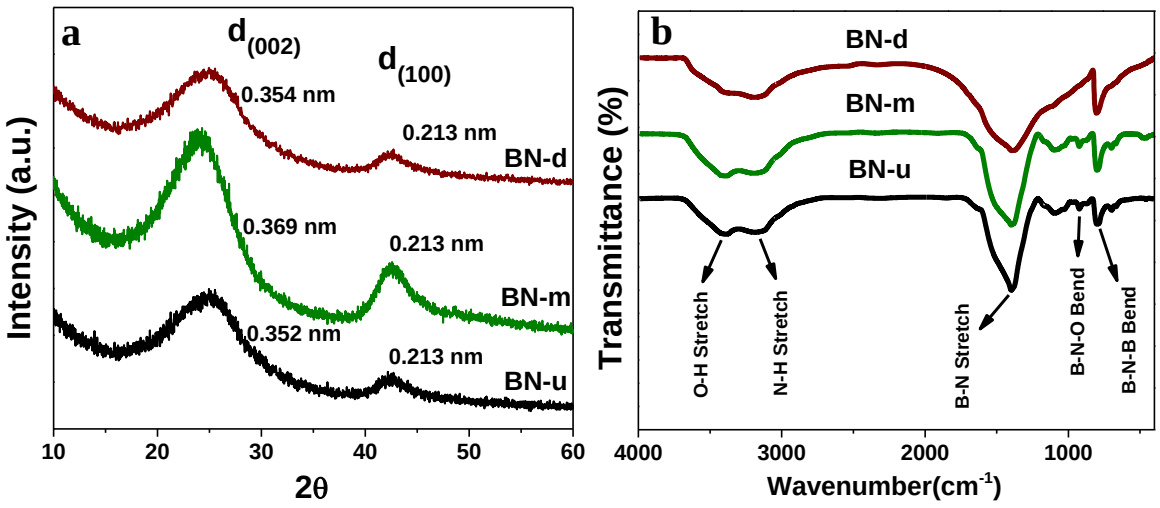

Figure 8: XRD pattern (a) and FTIR spectra (b) of the BN samples.

from the powder X-ray diffraction pattern (XRD) (Figure 8a). The two broad diffraction peaks corresponding to (002) and (100) planes confirms the hexagonal structure for all the BN samples. The interplanar d-spacing values are close to that of the turbostatic BN materials (0.356 nm)[51] and are in good agreement with the reported values.[45-47] The Fourier transform infrared (FTIR) spectra (Figure 8b) of all the as-synthesized samples showed presence of prominent bands at around 1385 cm^{-1} and 800 cm^{-1} corresponding to stretching and bending modes of B-N vibrations respectively, characteristic of hexagonal BN materials.[52-53] The broad absorption bands near 3405 cm^{-1} and 3180 cm^{-1} can be attributed to the stretching vibrations of O–H (from adsorbed water) and N-H (from surface NH_2 groups) bonds respectively.[52-53] The very weak band around 925 cm^{-1} for BN-u and BN-m samples corresponds to B-N-O bending mode.[52]

The specific surface area (SSA) of the various BN samples was determined by measuring N_2 adsorption-desorption isotherms at 77K (Figure 9). Commercially available

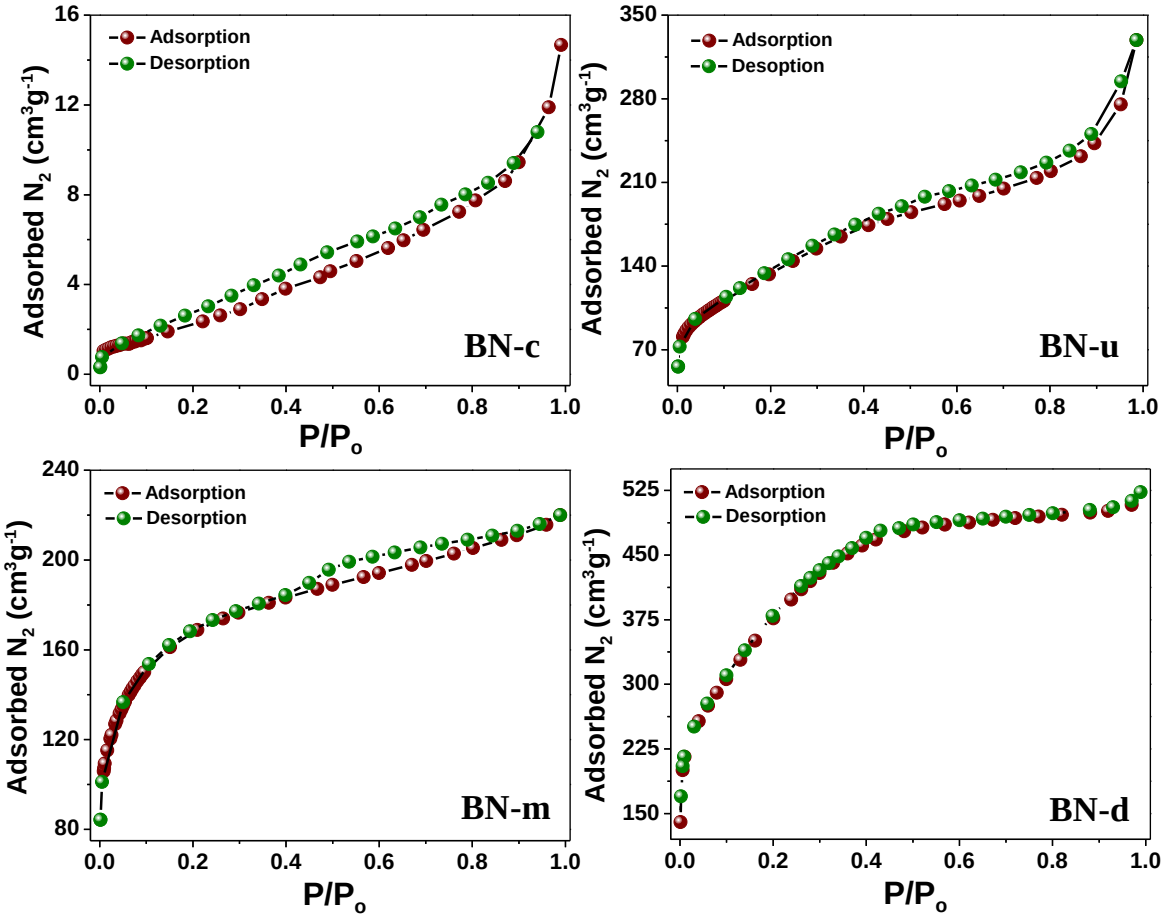

Figure 9: Nitrogen adsorption-desorption isotherms, at 77K, for different BN samples.

Sample	SSA (m^2/g)
BN-c	48
BN-u	590
BN-m	930
BN-d	1380

Table 1: Specific surface area for various BN samples calculated using multipoint BET analysis of the N_2 adsorption-desorption isotherms of the respective samples.

bulk hexagonal boron nitride (Sigma-Aldrich) was used for comparison and was designated as BN-c. Both BN-c and BN-u showed type II isotherm and H3 hysteresis

loop, typically observed for non-porous/macroporous layered boron nitride materials.[54] For BN-m the isotherm could be classified as type I with H4 hysteresis loop, indicating microporosity and slit-shaped mesopores. The BN-d sample was microporous as the adsorption-desorption isotherm was type I with no apparent hysteresis. The SSA for all the BN materials were calculated by carrying out multipoint Brunauer-Emmett-Teller (BET) analysis in the relevant pressure range[45] and are listed in table I. The SSA values increased in the following order BN-c (48 m^2/g) < BN-u (590 m^2/g) < BN-m (930 m^2/g) < BN-d (1380 m^2/g). In the propane ODH reaction one of the reactants is oxygen, so in

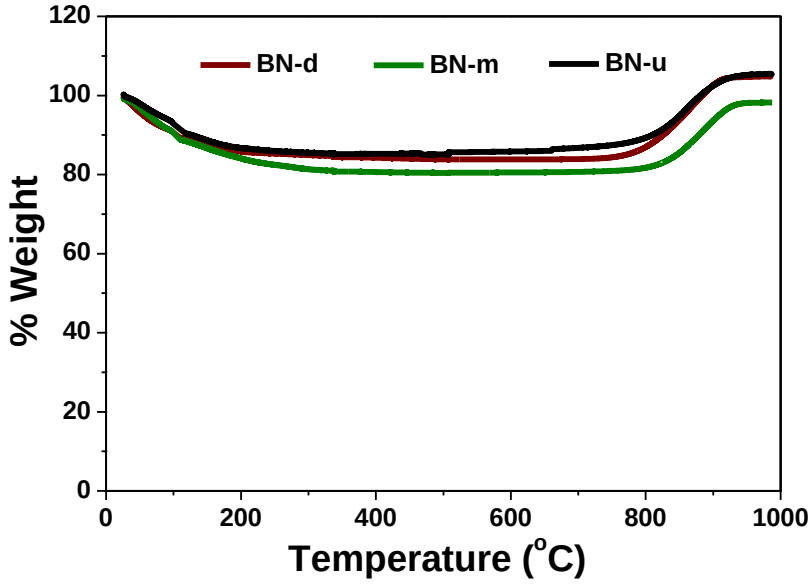

Figure 10: TGA plots for different synthesized boron nitride samples in the oxygen (99.99% pure) environment.

order to test their thermal stability, the thermogravimetric analysis (TGA) for all the synthesized BN samples was carried out in the oxygen environment up to 1000°C. As can be seen in figure 10, all the samples showed similar patterns in TGA. Up to 200°C BN materials showed weight loss of around 14-17% which could be attributed to desorption of adsorbed water molecules from the samples.[24] Between 200°C to 800°C no change in

sample weight was observed confirming stability of the samples in this temperature range in presence of oxygen. From 800°C to 1000°C, however, the weight of the samples increased by nearly 25-28% probably due to oxidation.

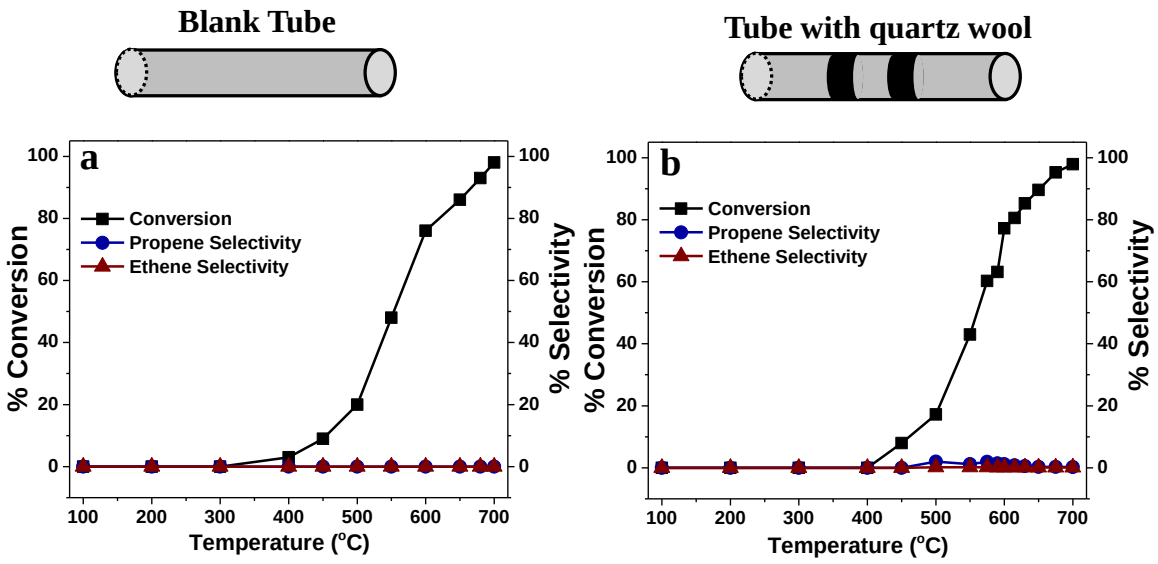

Figure 11: Control reactions. a) Blank tube and b) tube with packing material *i.e.* quartz wool. The total gas flow rate for these reactions was 20 sccm and the ratio of propane and oxygen was 0.02

The catalytic activity of the BN samples towards propane ODH reaction was tested by passing a mixture of propane and oxygen (in a ratio of 1:50 *i.e.* 0.02) through a steel reactor loaded with the catalyst, at different temperatures and analyzing the products on an online GC system. At first, the control reactions with blank reactor tube and tube loaded with the packing material (quartz wool) were carried out. As can be seen in figure 11, propane conversion started above 400°C and reached its maximum value (100%) around 700°C. However, no selectivity for olefins (propene or ethene) was observed and

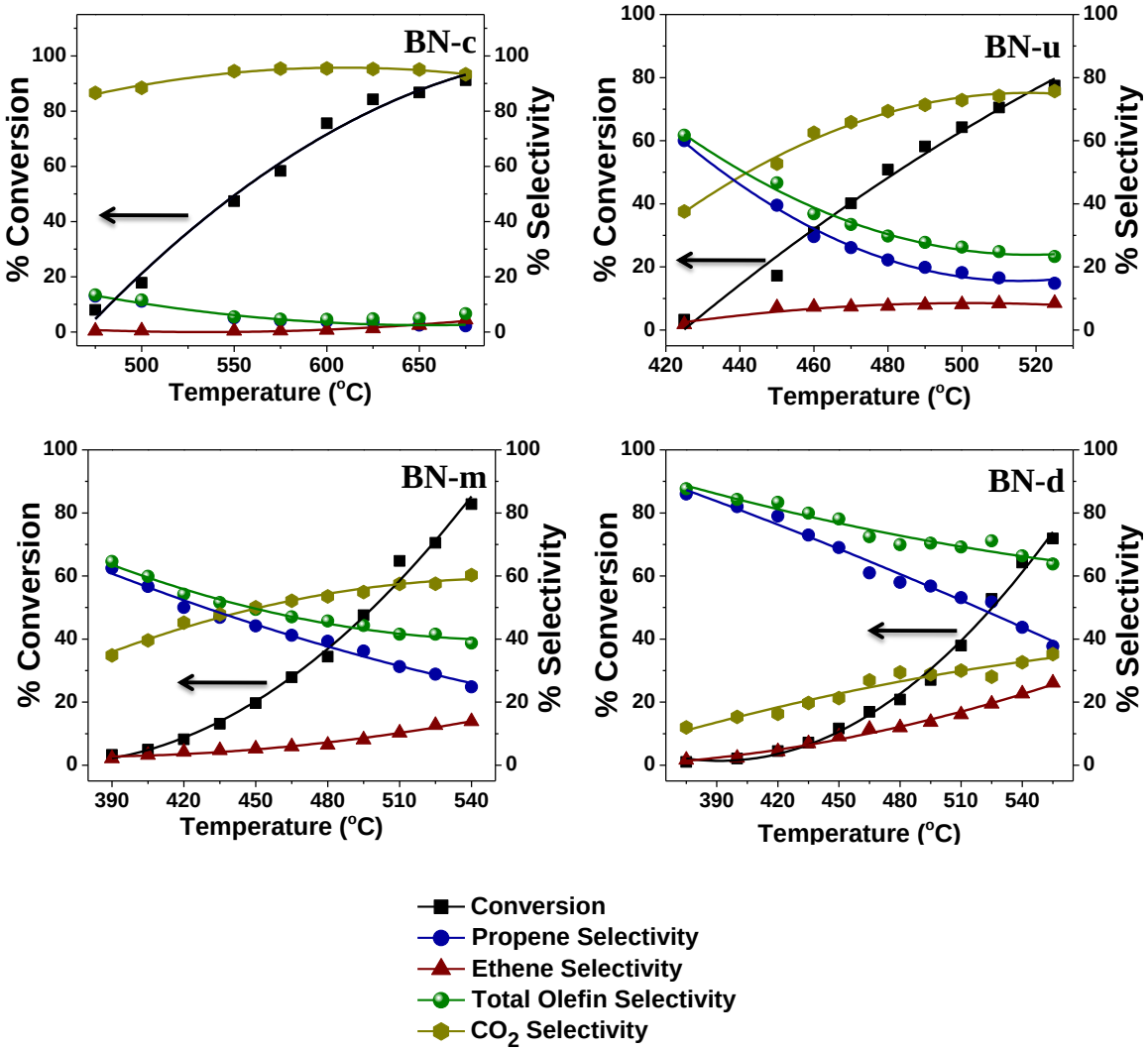

Figure 12: Propane oxidative dehydrogenation reactions over various BN catalysts. For every reaction 100 mg of the catalyst was used, the total gas flow rate was 20 sccm, and the ratio of propane and oxygen was 0.02.

the only product was carbon dioxide due to complete burning of propane in both the cases. In the case of BN-c (commercially obtained BN material, with SSA = 48 m^2/g) also, more or less complete conversion of propane to CO_2 occurred above 500°C (Figure 12). On the other hand, the BN-u, BN-m, and BN-d showed propane conversion starting from 400°C and the products observed were propene, ethene, methane, and carbon dioxide (Figure 12). With increasing temperature, the conversion of propane increases

and at 525°C all the samples shows above 50% conversion (Figure 12). However the selectivity to propene decreases with increasing conversion for all the catalyst probably due to increase in side reactions (cracking, burning of propane and propene, *etc.*) at high temperature as supported by the increase in selectivity for both ethene and CO_2 at higher temperature (Figure 12). The total olefin selectivity *i.e.* summation of the propene and ethene selectivities was found to decrease with increase in temperature for all the BN materials (Figure 12). Methane was formed only in trace amounts (less than 1%) in all the BN catalysts. The carbon balance (calculated using the calibration plots for propane, propene, ethene, methane, and carbon dioxide) for all the reactions in this study was found to be around 98.8 ± 0.8%.

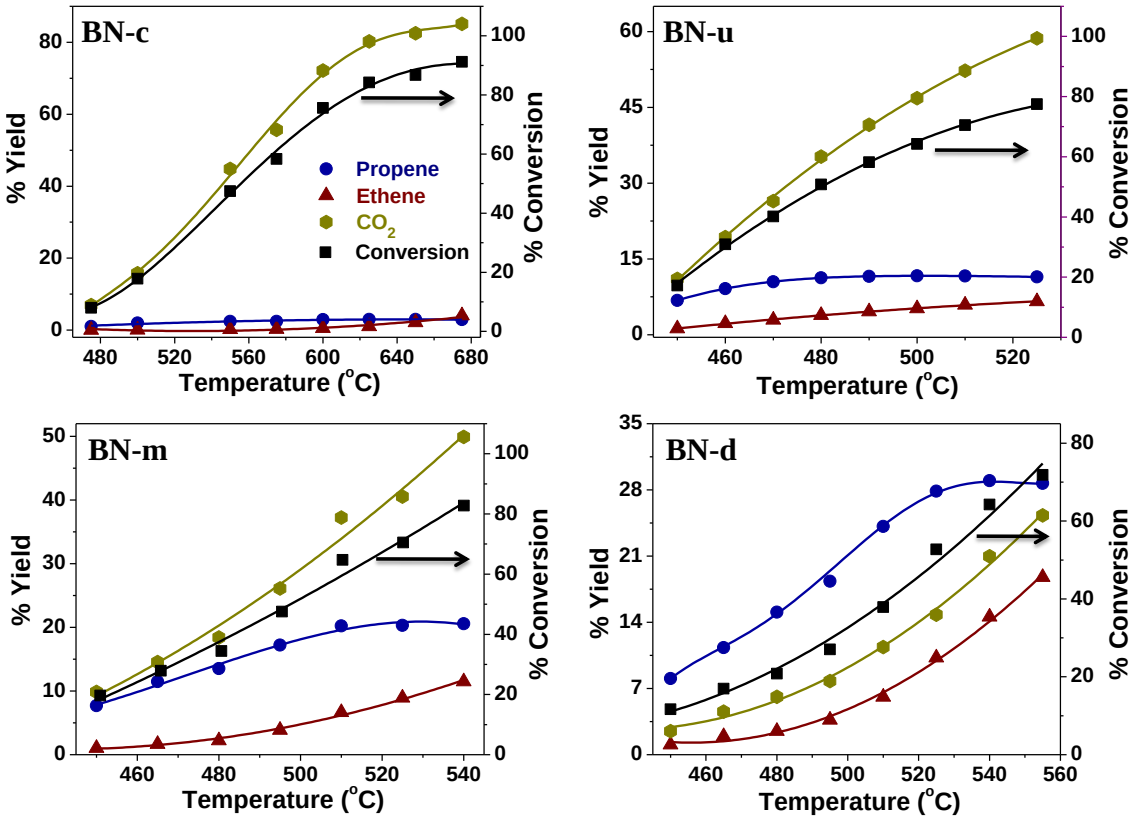

Figure 13: Conversion of propane and the product (various olefins) yield with respect to temperature over BN-c, BN-u, BN-m, and BN-d.

In figure 13, we plot % yield of the olefins (propene, ethene) and carbon dioxide against temperature for each BN sample. The propene yield increased with increasing temperature and reached a saturation level above certain temperature in all the catalysts (600°C, 480°C, 510°C, and 525°C for BN-c, BN-u, BN-m, and BN-d respectively). However, the ethene yield constantly increased with increasing temperature, so did the CO_2 yield. The increase in ethene formation with increase in CO_2 yield at higher temperatures suggests that the cracking reactions dominates over dehydrogenation reactions at high temperatures. In figure 14 we plot propane conversion and the selectivity for various products with respect to surface area of BN samples. At 525°C BN-c shows

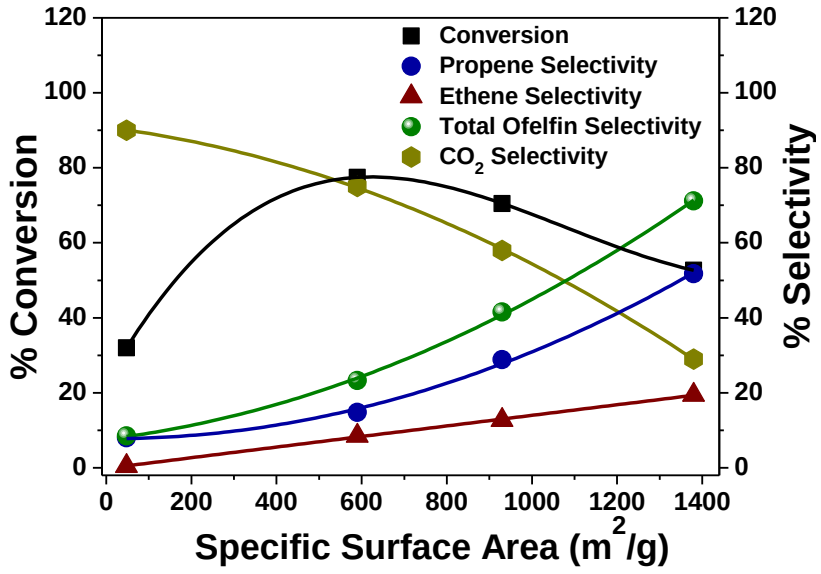

Figure 14: Conversion and selectivity *vs* specific surface area of the BN samples at 525°C. The total olefin selectivity was calculated by adding the selectivity for propene and ethene.

conversion around 30%, which was similar to the value observed for the control reactions (Figure 11) i.e. blank tube and tube with packing material. On the other hand BN-u, BN-m, and BN-d show propane conversion above 50% at 525°C indicating the superior activation of propane by these samples (Figure 14). The propene and ethene selectivity,

show increasing trend with respect to surface area, whereas the CO_2 selectivity decreased with increasing surface area. For BN-d, the highest SSA (1380 m^2/g) BN material used in this study, the propene selectivity observed was around 52% and the total olefin selectivity was ~71% at a conversion of ~53% at 525°C (Figure 14).

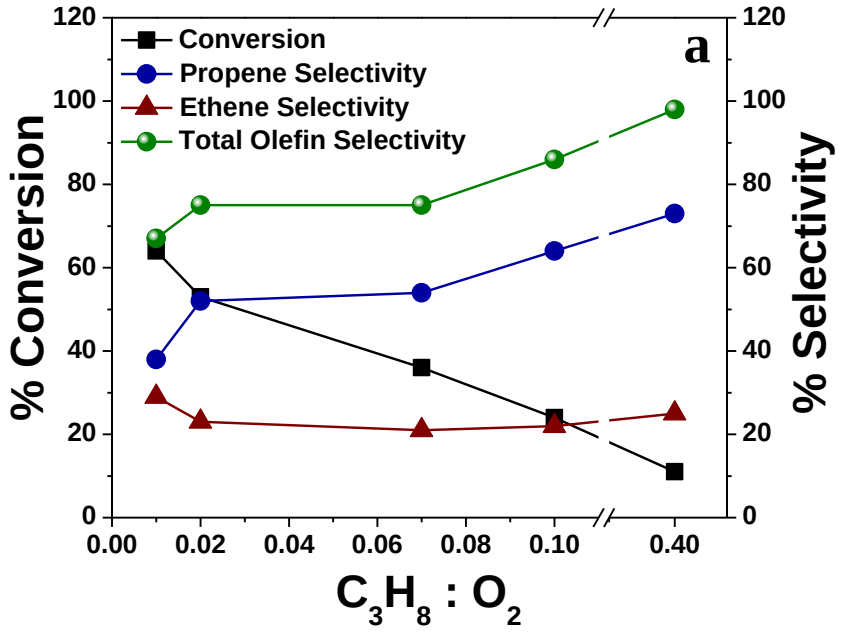

Figure 15: Effect of propane to oxygen ratio on, a) propane conversion and olefin selectivity, and b) olefin yield for BN-d catalyst. The amount of catalyst used was 100 mg and the reaction was carried out at 525°C with a total gas flow rate of 20 sccm.

Figure 15, plot the conversion of propane and the selectivity of products obtained at 525°C over BN-d sample for different propane to oxygen ratio. With increasing C_3H_8:O_2 ratio beyond 0.02, propane conversion sharply decreased, from ~52% to ~10% for C_3H_8:O_2 ratio of 0.4 (Figure 15). The propene selectivity increased from ~53% (for 0.02 ratio) to ~73% for C_3H_8:O_2 ratio of 0.4 (Figure 15). On the other hand, when C_3H_8:O_2 ratio was reduced to 0.01, the conversion increased from ~52% to ~62% with a decrease in selectivity from ~53% to ~36%, Hence, C_3H_8:O_2 ratio of 0.02 appears to be

optimal for propane ODH reaction over boron nitride catalysts. Though this high amount of oxygen in the reaction feed is expected to result in less olefin selectivity due to its burning, evidently it was necessary for the reaction to occur.

We further carried out propane ODH reaction over BN-d catalyst using air as oxidant (C_3H_8:O_2 = 0.1). At 525°C, the propane conversion was around ~20%, with a total olefin selectivity of ~85% (Figure 16a). The conversion of propane and selectivity for olefins varied with temperature, and at around 660°C, it shows ~43% conversion with total olefin selectivity of ~72% (propene 42% and ethene ~30%). The yield of olefins increased with temperature, with propene yield being around 20%, ethene yield around 10%, and total olefin yield reaching around 30% at 660°C (Figure 16b).

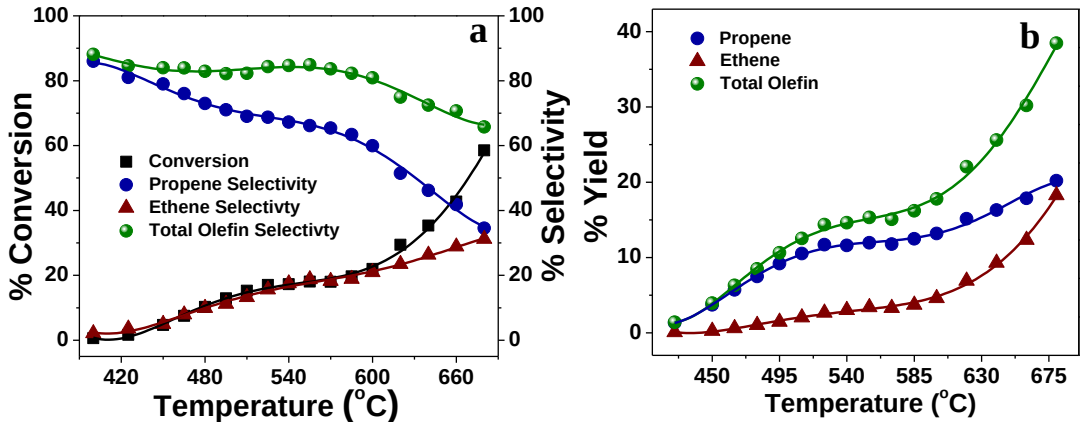

Figure 16: Propane oxidative dehydrogenation reaction over BN-d catalyst using air instead of oxygen. For this reaction 100 mg of the catalyst was used, the total gas flow rate was 20 sccm, and the ratio of propane and oxygen was 0.1.

We studied the stability of the catalytic activity by carrying out time-on-stream (TOS) reaction with BN-d sample at 525°C. As it is evident in figure 17 the catalytic activity was preserved upto 5 hours. After 5 hours, the propane conversion gradually decreased, while propene selectivity increased at first and then reached a saturation level.

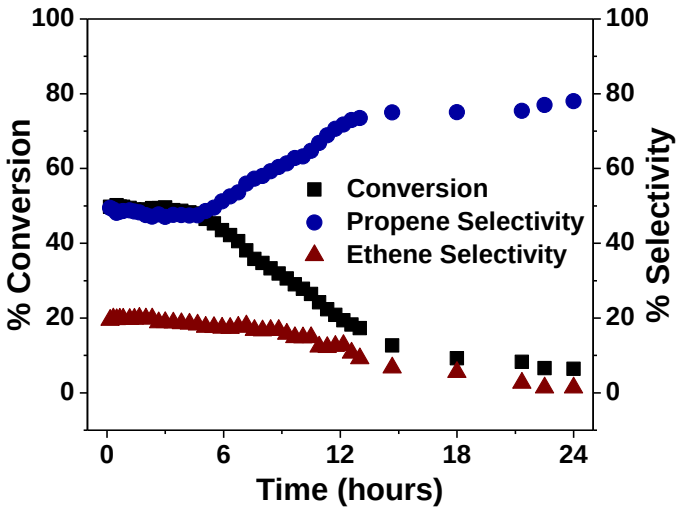

Figure 17: Time on stream reaction over BN-d catalyst. Conversion/selectivity *vs* time. For this reaction 100 mg of the catalyst was used, the total gas flow rate was 20 sccm, and the ratio of propane and oxygen was 0.02.

The ethene selectivity decreased constantly (Figure 17) and at lower conversion there is no formation of ethene. After 24 h of TOS reaction the less active BN-d (TOS) catalyst was characterized thoroughly. At first we carried out the thermogravimetric analysis of the BN-d (TOS) sample to understand any carbon deposition. The TGA of BN-d (TOS) was similar to that of BN-d, with nearly 12% weight loss upto 200^{o}C after which the sample was stable upto 800^{o}C, suggestive of no carbon deposition (Figure 18a). This observation is in agreement with the high carbon balance (98.8 ±0.8%) for the propane ODH reaction. The XRD pattern of BN-d (TOS) sample showed pure hexagonal phase of the BN materials (Figure 18b). The TEM image in figure 18c shows that BN-d (TOS) sample was highly porous. However, the FTIR spectra of BN-d (TOS) showed weak but significant IR bands corresponding to the B-O and B-N-O stretching/bending modes (Figure 18d), in addition to the characteristic IR bands of BN-d (Figure 8b), suggesting oxidation of B-N bonds. The BN-d (TOS) sample was regenerated by heating it in the

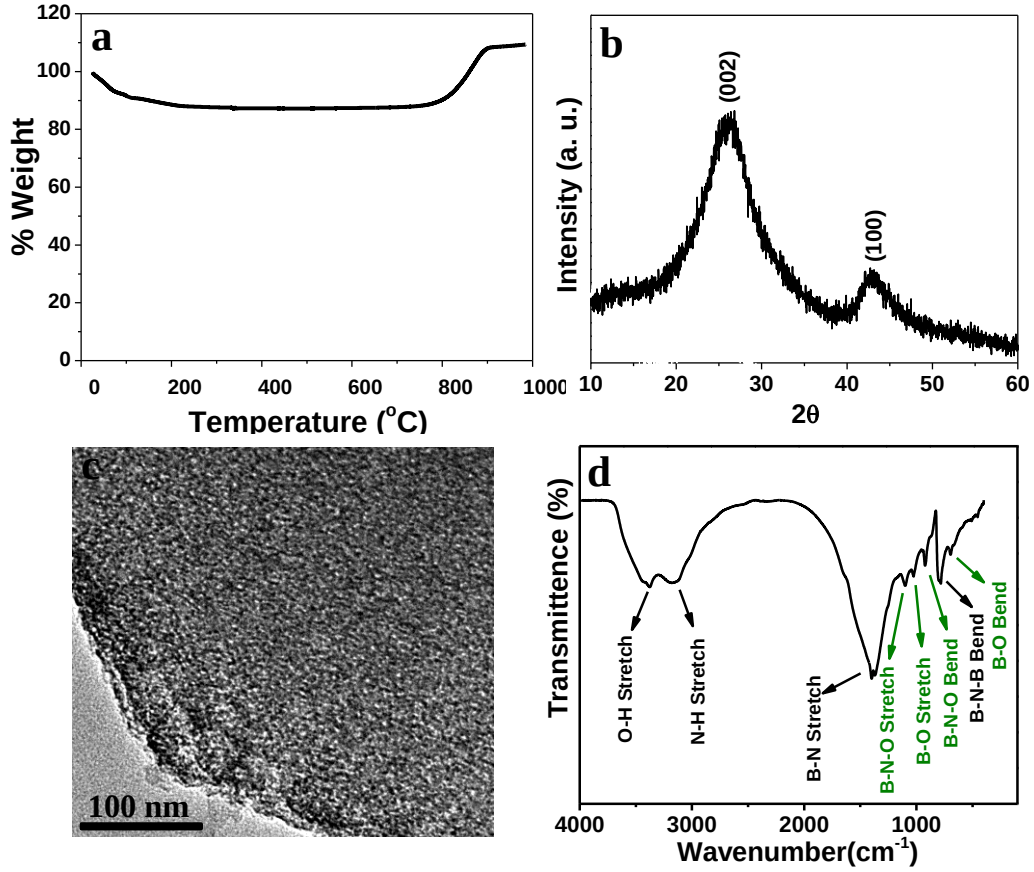

Figure 18: Characterization of BN-d (TOS) sample. a) TGA plot, b) XRD pattern, c) TEM image, and d) FTIR spectra.

ammonia flow at 900°C for 2 hours. Very interestingly, the regenerated boron nitride sample, BN-d (Reg), showed similar catalytic behavior, in terms of the propane conversion, olefin selectivity/yield, and stability of the catalytic activity, as the original BN-d materials (Figure 19). This clearly confirms the complete regeneration of the catalyst. The FTIR spectrum of BN-d (Reg) was very similar to that of the BN-d sample, without any B-O and B-N-O stretching/bending modes (Figure 20). This indicates that the oxidized B-N bonds are reduced back to their native form by heating in ammonia. Increasing catalytic activity of BN samples with increasing surface area, along with oxidation of B-N bonds resulting in diminished catalytic activity which returns back after

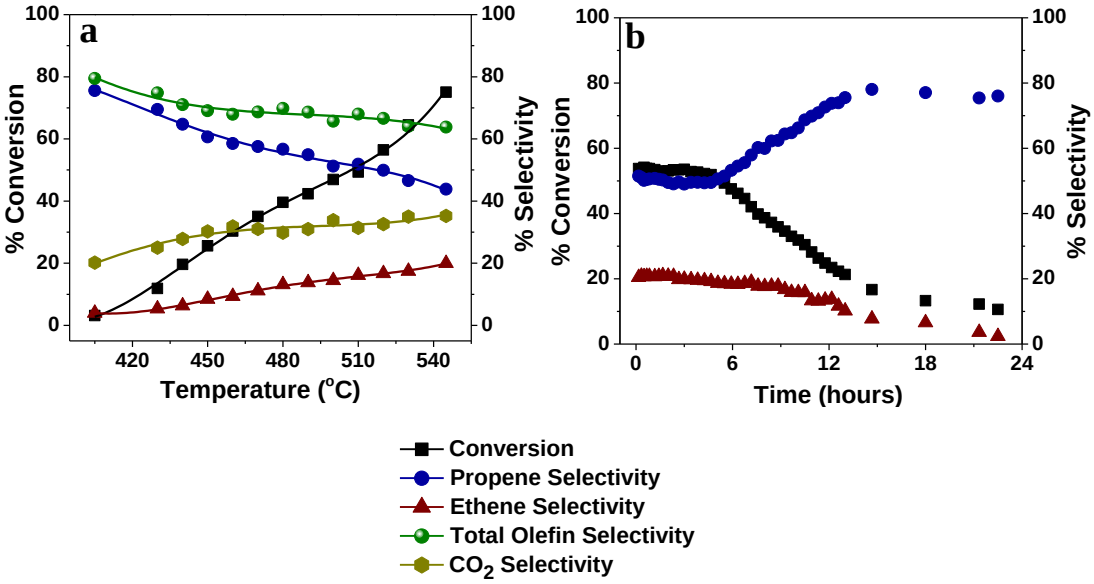

Figure 19: Propane oxidative dehydrogenation reaction (a) and time on stream reaction (b) over BN-d (Reg) catalyst. For these reactions 100 mg of the catalyst was used, the total gas flow rate was 20 sccm, the ratio of propane and oxygen was 0.02, and the TOS reaction was carried out at 525°C.

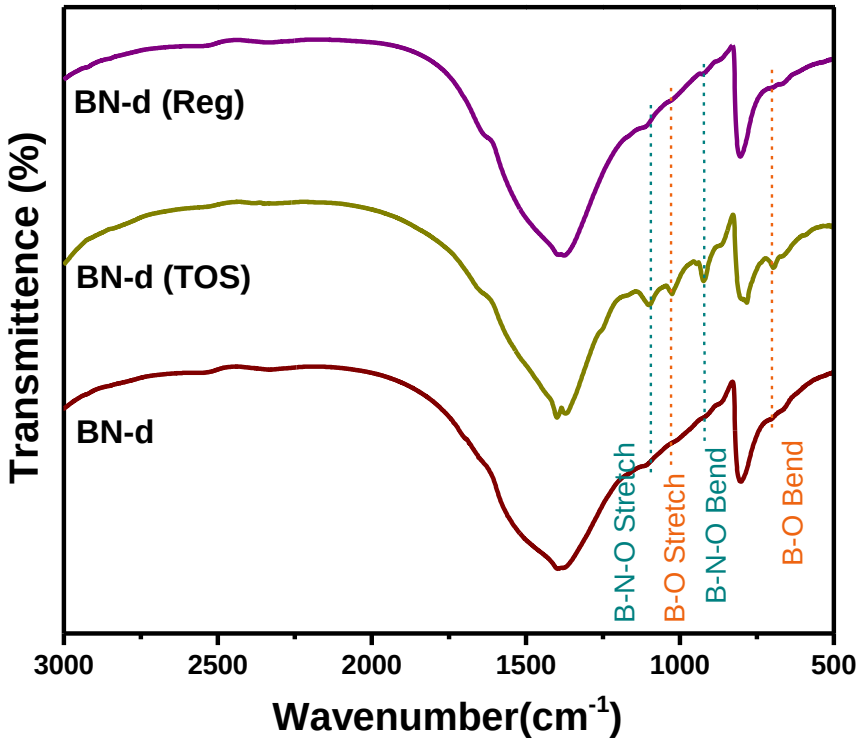

Figure 20: FTIR spectra of BN-d, BN-d (TOS), and BN-d (Reg) samples.

reducing them, strongly suggests that surface B-N bonds are the active catalytic sites for propane ODH reaction. However, a thorough experimental and theoretical study is needed in order to completely understand the mechanism of this reaction.

We also synthesized BN-d supported metal (Au and Pt) nanoparticles and tested their catalytic performance towards propane ODH reaction. Gold nanoparticles (<5 nm) were selected as they are well known oxidation catalysts for reactions like carbon

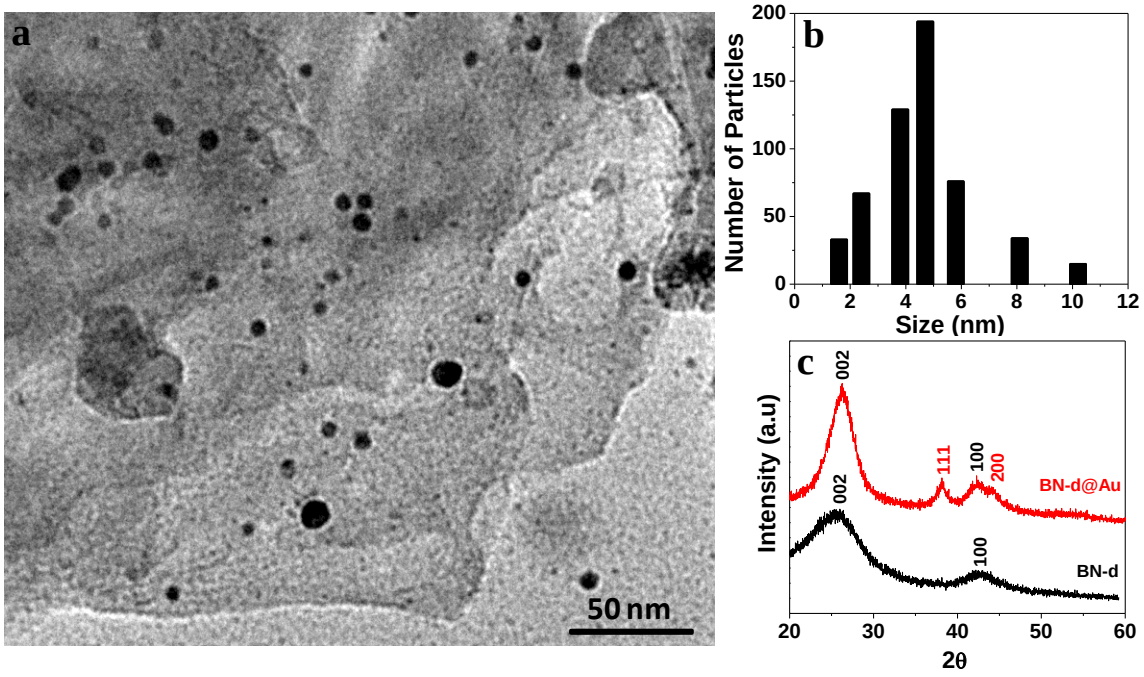

Figure 21: Characterization of BN-d@Au sample. a) TEM image, b) histogram showing particles size distribution for gold nanoparticles (measured from TEM images), and c) XRD pattern.

monoxide oxidation, epoxidation, direct hydrogen peroxide synthesis, *etc*.[56-58] The platinum nanoparticles on the other hand were selected as they are industrial catalyst for the propane dehydrogenation reaction.[59-63] The BN-d supported Au and Pt nanoparticles (BN-d@Au and BN-d@Pt) were synthesized using wetness incipient impregnation

method.[48-49] Figure 21a shows TEM image of Au nanoparticles supported over BN. The nanoparticles of gold were mostly below 5 nm in size (Figure 21b). The XRD pattern of BN-d@Au showed broad peaks corresponding to the (111) and (200) planes of cubic structure of gold in addition to (002) and (100) reflections of the hexagonal BN material (Figure 21c). The particle size of the BN-d supported platinum nanoparticles was around 1.5 nm (Figure 22a,b). The XRD pattern of BN-d@Pt showed peaks corresponding to FCC crystal structure of the platinum (Figure 22c). The BN-d@Au catalyst showed similar catalytic behavior, as BN-d sample, towards propane ODH reaction, however, at higher temperatures (around 180°C higher). The reaction started above 600°C. The conversion of propane over BN-d@Au was around 42% and the propene selectivity

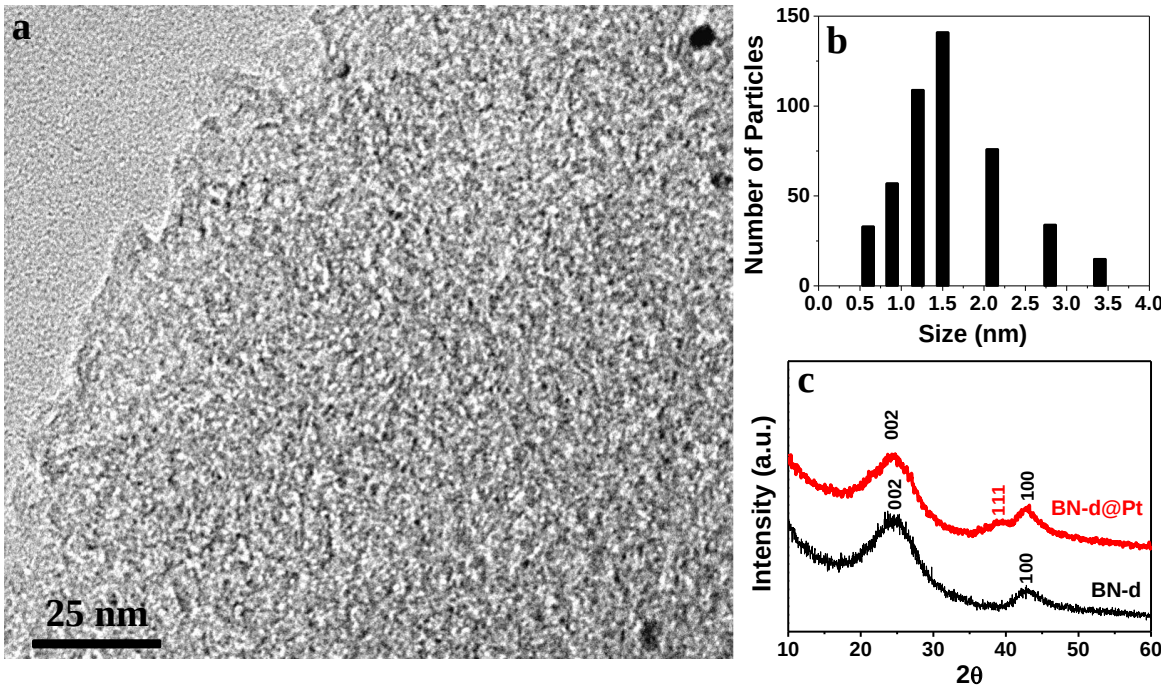

Figure 22: Characterization of BN-d@Pt sample. a) TEM image, b) histogram showing particles size distribution for gold nanoparticles (measured from TEM images), and c) XRD pattern.

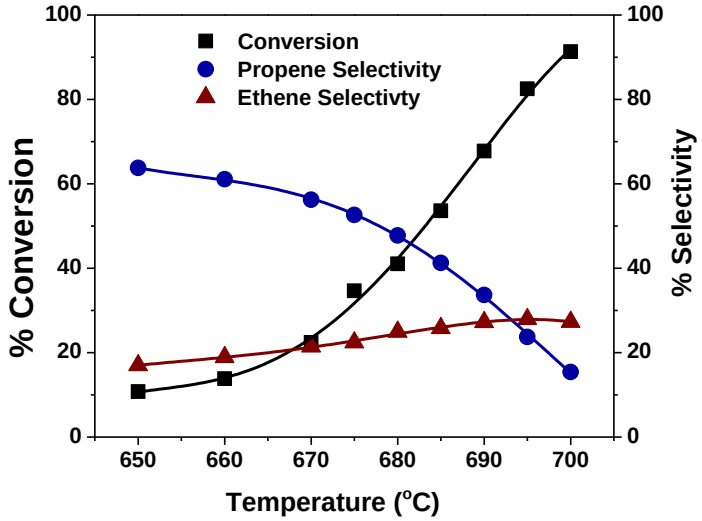

Figure 23: Propane oxidative dehydrogenation reactions over BN-d@Au catalyst. For this reaction 100 mg of the catalyst was used, the total flow was 20 sccm, and the ratio of propane and oxygen was 0.02.

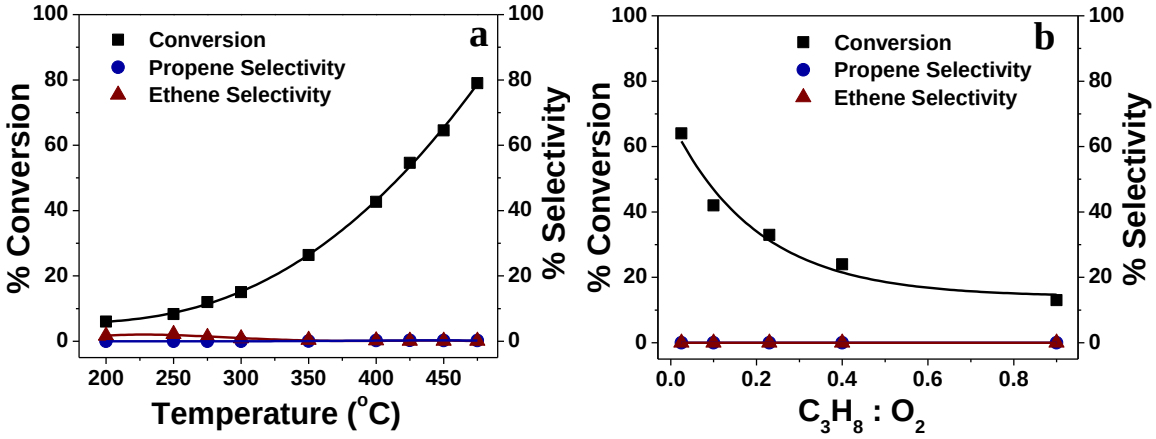

Figure 24: Propane oxidative dehydrogenation reactions over BN-d@Pt catalyst. a) Catalytic behavior with increasing temperature *i.e.* conversion/selectivity *vs* temperature. For this reaction 100 mg of the catalyst was used, the total gas flow rate was 20 sccm, and the ratio of propane and oxygen was 0.02. b) Catalytic behavior, at 400°C, with increasing propane to oxygen ratio. For this reaction 100 mg of the catalyst was used, the total gas flow rate was 20 sccm,

observed was about 48% at 680°C. The ethylene selectivity was around 28% at this temperature (Figure 23). For BN-d@Pt catalyst the ODH reaction for propane started at

comparatively very low temperature around 200^{o}C and the conversion reached nearly 80% at temperature value of 475^{o}C (Figure 24a). However, the only product observed was carbon dioxide with no observable unsaturated hydrocarbons, suggesting complete burning of propane. We have also carried out the reaction with lower proportions of oxygen. As it can be seen in figure 24b, with increasing propane to oxygen ratio, the conversion progressively decreased, though no improvement in the olefin selectivity was observed. Thus, towards propane ODH reaction, BN-d@Au showed similar catalytic activity as BN-d but at higher temperature, whereas BN-d@Pt showed complete conversion of propane to CO_2 with no olefin selectivity, clearly indicating superior catalytic property of BN-d.

5.5 Conclusions:

In conclusion, in this chapter we present, for the first time, the catalytic behavior of a generally received inert material, hexagonal boron nitride, for propane oxidative dehydrogenation reaction. Catalytic performance of boron nitride materials improved with increase in their specific surface area or in other worlds, with increase in the edge and dangling B-N bonds. The catalytic activity of these materials was found to be stable for nearly 5 hours after which it decreases. However, the activity of the catalyst could be regained by regenerating the catalyst in ammonia flow at elevated temperature. Oxidation of the dangling B-N bonds at the edges and in the nanopores was found to be responsible for the diminished catalytic activity, which reduced back to its original form on heating in ammonia flow. This suggested that the surface B-N bonds could be the active catalytic centers for the propane ODH reaction. Incorporating metal (Au and Pt) nanoparticles with the boron nitride didn't show any promising improvement in the catalysts activity. The boron nitride catalysts could prove to be very competent as metal free catalysts and could be explored for various reactions, such as oxidative dehydrogenation, oxidation, epoxidation in which oxidation is the major step, over relatively a wide range of reaction conditions compared to the metal free carbon catalysts.

5.6 References:

1. Plotkin, J. S., The changing dynamics of olefin supply/demand. *Catalysis Today* **2005,** *106*, 10-14.
2. University of York. The Essential Chemical Online: Propene. http://www.essentialchemicalindustry.org/chemicals/propene.html (accessed March 4, 2015).
3. Carrero, C. A.; Schloegl, R.; Wachs, I. E.; Schomaecker, R., Critical Literature Review of the Kinetics for the Oxidative Dehydrogenation of Propane over Well-Defined Supported Vanadium Oxide Catalysts. *ACS Catal.* **2014**, *4*, 3357-3380.
4. Evolving Propylene Sources Solution to Supply Shortages? http://thinking.nexant.com/sites/default/files/report/field_attachment_prospectus/201201/STMC11_Evolving_Propylene_Pros.pdf.
5. Cavani, F.; Ballarini, N.; Cericola, A., Oxidative dehydrogenation of ethane and propane: How far from commercial implementation? *Catal. Today* **2007**, *127*, 113-131.
6. How Shale Gas Is Changing Propylene. http://plasticsengineeringblog.com/2013/02/20/how-shale-gas-is-changing-propylene/.
7. Sattler, J. J. H. B.; Gonzalez-Jimenez, I. D.; Luo, L.; Stears, B. A.; Malek, A.; Barton, D. G.; Kilos, B. A.; Kaminsky, M. P.; Verhoeven, T. W. G. M.; Koers, E. J.; Baldus, M.; Weckhuysen, B. M., Platinum-Promoted Ga/Al_2O_3 as Highly Active, Selective, and Stable Catalyst for the Dehydrogenation of Propane. *Angew. Chem. Int. Ed.* **2014,** *126*, 9405-9410.

8. Lin, Y.; Connell, J. W., Advances in 2D boron nitride nanostructures: nanosheets, nanoribbons, nanomeshes, and hybrids with graphene. *Nanoscale* **2012,** *4*, 6908-6939.
9. Tang, Q.; Zhou, Z., Graphene-analogous low-dimensional materials. *Prog. Mater. Sci.* **2013,** *58*, 1244-1315.
10. Xu, M.; Liang, T.; Shi, M.; Chen, H., Graphene-Like Two-Dimensional Materials. *Chem. Rev.* **2013,** *113*, 3766-3798.
11. Hod, O., Graphite and Hexagonal Boron-Nitride have the Same Interlayer Distance. Why? *J. Chem. The. Comput.* **2012,** *8*, 1360-1369.
12. Pakdel, A.; Bando, Y.; Golberg, D., Nano boron nitride flatland. *Chem. Soc. Rev.* **2014,** *43*, 934-959.
13. Li, J.; Xiao, X.; Xu, X.; Lin, J.; Huang, Y.; Xue, Y.; Jin, P.; Zou, J.; Tang, C., Activated boron nitride as an effective adsorbent for metal ions and organic pollutants. *Sci. Rep.* **2013,** *3*.
14. Pakdel, A.; Zhi, C.; Bando, Y.; Nakayama, T.; Golberg, D., Boron Nitride Nanosheet Coatings with Controllable Water Repellency. *ACS Nano* **2011,** *5*, 6507-6515.
15. Weng, Q.; Wang, B.; Wang, X.; Hanagata, N.; Li, X.; Liu, D.; Wang, X.; Jiang, X.; Bando, Y.; Golberg, D., Highly Water-Soluble, Porous, and Biocompatible Boron Nitrides for Anticancer Drug Delivery. *ACS Nano* **2014,** *8*, 6123-6130.
16. Zhi, C.; Bando, Y.; Tang, C.; Golberg, D., Immobilization of Proteins on Boron Nitride Nanotubes. *J. Am. Chem. Soc.* **2005,** *127*, 17144-17145.
17. Lei, W.; Portehault, D.; Liu, D.; Qin, S.; Chen, Y., Porous boron nitride nanosheets for effective water cleaning. *Nat. Commun.* **2013,** *4*, 1777.

18. Liu, D.; Lei, W.; Qin, S.; Chen, Y., Template-Free Synthesis of Functional 3D BN architecture for removal of dyes from water. *Sci. Rep.* **2014,** *4*.

19. Wu, J. C. S.; Chou, H.-C., Bimetallic Rh–Ni/BN catalyst for methane reforming with CO_2. *Chem. Eng. J.* **2009,** *148*, 539-545.

20. Meyer, N.; Bekaert, K.; Pirson, D.; Devillers, M.; Hermans, S., Boron nitride as an alternative support of Pd catalysts for the selective oxidation of lactose. *Catal. Comm.* **2012,** *29*, 170-174.

21. Gao, M.; Lyalin, A.; Taketsugu, T., Catalytic Activity of Au and Au_2 on the h-BN Surface: Adsorption and Activation of O_2. *J. Phy. Chem. C* **2012,** *116*, 9054-9062.

22. Gao, M.; Lyalin, A.; Taketsugu, T., CO oxidation on h-BN supported Au atom. *J. Chem. Phy.* **2013,** *138*, 034701.

23. Postole, G.; Caldararu, M.; Bonnetot, B.; Auroux, A., Influence of the Support Surface Chemistry on the Catalytic Performances of PdO/BN Catalysts. *J. Phy. Chem. C* **2008,** *112*, 11385-11393.

24. Postole, G.; Gervasini, A.; Caldararu, M.; Bonnetot, B.; Auroux, A., Is BN an appropriate support for metal oxide catalysts? *App. Catal. A: Gen.* **2007,** *325*, 227-236.

25. Gao, M.; Lyalin, A.; Taketsugu, T., Oxygen activation and dissociation on h-BN supported Au atoms. *Int. J. Quan. Chem.* **2013,** *113*, 443-452.

26. Huang, C.; Chen, C.; Ye, X.; Ye, W.; Hu, J.; Xu, C.; Qiu, X., Stable colloidal boron nitride nanosheet dispersion and its potential application in catalysis. *J. Mater. Chem. A* **2013,** *1*, 12192-12197.

27. Lin, L.; Li, Z.; Zheng, Y.; Wei, K., Synthesis and Application in the CO Oxidation Conversion Reaction of Hexagonal Boron Nitride with High Surface Area. *J. Am. Chem. Soc.* **2009,** *92*, 1347-1349.
28. Gao, M.; Lyalin, A.; Taketsugu, T., The h-BN surface effect on CO oxidation reaction catalyzed by supported gold atom. *J. Phys.: Conf. Ser.* **2013,** *438*, 012003.
29. Qi, W.; Su, D., Metal-Free Carbon Catalysts for Oxidative Dehydrogenation Reactions. *ACS Catal.* **2014,** *4*, 3212-3218.
30. Yu, D.; Nagelli, E.; Du, F.; Dai, L., Metal-Free Carbon Nanomaterials Become More Active than Metal Catalysts and Last Longer. *J. Phy. Chem. Lett.* **2010,** *1*, 2165-2173.
31. Su , D. S.; Zhang, J.; Frank, B.; Thomas, A.; Wang, X.; Paraknowitsch, J.; Schlögl, R., Metal-Free Heterogeneous Catalysis for Sustainable Chemistry. *ChemSusChem* **2010,** *3*, 169-180.
32. Chen, D.; Holmen, A.; Sui, Z.; Zhou, X., Carbon mediated catalysis: A review on oxidative dehydrogenation. *Chinese Journal of Catalysis* **2014,** *35*, 824-841.
33. Su, D. S.; Perathoner, S.; Centi, G., Nanocarbons for the Development of Advanced Catalysts. *Chem. Rev.* **2013,** *113*, 5782-5816.
34. Frank, B.; Wrabetz, S.; Khavryuchenko, O. V.; Blume, R.; Trunschke, A.; Schlögl, R., Calorimetric Study of Propane and Propylene Adsorption on the Active Surface of Multiwalled Carbon Nanotube Catalysts. *ChemPhysChem* **2011,** *12*, 2709-2713.
35. Liu, X.; Frank, B.; Zhang, W.; Cotter, T. P.; Schlögl, R.; Su, D. S., Carbon-Catalyzed Oxidative Dehydrogenation of n-Butane: Selective Site Formation

during sp3-to-sp2 Lattice Rearrangement. *Angew. Chem. Int. Ed.* **2011,** *50*, 3318-3322.

36. Frank, B.; Morassutto, M.; Schomäcker, R.; Schlögl, R.; Su, D. S., Oxidative Dehydrogenation of Ethane over Multiwalled Carbon Nanotubes. *ChemCatChem* **2010,** *2*, 644-648.
37. Chen, C.; Zhang, J.; Zhang, B.; Yu, C.; Peng, F.; Su, D., Revealing the enhanced catalytic activity of nitrogen-doped carbon nanotubes for oxidative dehydrogenation of propane. *Chem. Comm.* **2013,** *49*, 8151-8153.
38. Zhang, J.; Liu, X.; Blume, R.; Zhang, A.; Schlögl, R.; Su, D. S., Surface-Modified Carbon Nanotubes Catalyze Oxidative Dehydrogenation of n-Butane. *Science* **2008,** *322*, 73-77.
39. Cataldo, F., A Study on the thermal stability to 1000°C of various carbon allotropes and carbonaceous matter both under nitrogen and in air. *Fullerenes, Nanotubes and Carbon Nanostructures* **2002,** *10*, 293-311.
40. Eftekhari, A.; Jafarkhani, P., Curly Graphene with Specious Interlayers Displaying Superior Capacity for Hydrogen Storage. *J. Phy. Chem. C* **2013,** *117*, 25845-25851.
41. Thostenson, E. T.; Li, C.; Chou, T.-W., Nanocomposites in context. *Compo. Sci. Technol.* **2005,** *65*, 491-516.
42. Mahajan, A.; Kingon, A.; Kukovecz, Á.; Konya, Z.; Vilarinho, P. M., Studies on the thermal decomposition of multiwall carbon nanotubes under different atmospheres. *Mater. Lett.* **2013,** *90*, 165-168.
43. Yamada, Y.; Murota, K.; Fujita, R.; Kim, J.; Watanabe, A.; Nakamura, M.; Sato, S.; Hata, K.; Ercius, P.; Ciston, J.; Song, C. Y.; Kim, K.; Regan, W.; Gannett, W.;

Zettl, A., Subnanometer Vacancy Defects Introduced on Graphene by Oxygen Gas. *J. Am. Chem. Soc.* **2014,** *136*, 2232-2235.

44. Musumeci, A. W.; Silva, G. G.; Martens, W. N.; Waclawik, E. R.; Frost, R. L., Thermal decomposition and electron microscopy studies of single-walled carbon nanotubes. *J. Therm. Anal. Calorim.* **2007,** *88*, 885-891.
45. Nag, A.; Raidongia, K.; Hembram, K. P. S. S.; Datta, R.; Waghmare, U. V.; Rao, C. N. R., Graphene Analogues of BN: Novel Synthesis and Properties. *ACS Nano* **2010,** *4*, 1539-1544.
46. Weng, Q.; Wang, X.; Zhi, C.; Bando, Y.; Golberg, D., Boron Nitride Porous Microbelts for Hydrogen Storage. *ACS Nano* **2013,** *7*, 1558-1565.
47. Weng, Q.; Wang, X.; Bando, Y.; Golberg, D., One-Step Template-Free Synthesis of Highly Porous Boron Nitride Microsponges for Hydrogen Storage. *Adv. Energy Mater.* **2014,** *4* (7), 1-8.
48. Wu, J. C. S.; Chen, W.-C., A novel BN supported bi-metal catalyst for selective hydrogenation of crotonaldehyde. *App. Catal. A: Gen.* **2005,** *289*, 179-185.
49. Wu, J. C. S.; Lin, Z.-A.; Pan, J.-W.; Rei, M.-H., A novel boron nitride supported Pt catalyst for VOC incineration. *App. Catal. A: Gen.* **2001,** *219*, 117-124.
50. Burch, R.; Crabb, E. M., Homogeneous and heterogeneous contributions to the oxidative dehydrogenation of propane on oxide catalysts. *App. Catal. A: Gen.* **1993,** *100*, 111-130.
51. Thomas, J.; Weston, N. E.; O'Connor, T. E., Turbostratic1 Boron Nitride, Thermal Transformation to Ordered-layer-lattice Boron Nitride. *J. Am. Chem. Soc.* **1962,** *84*, 4619-4622.

52. Li, J.; Xiao, X.; Xu, X.; Lin, J.; Huang, Y.; Xue, Y.; Jin, P.; Zou, J.; Tang, C., Activated boron nitride as an effective adsorbent for metal ions and organic pollutants. *Sci. Rep.* **2013,** *3*.

53. Gu, Y.; Zheng, M.; Liu, Y.; Xu, Z., Low-Temperature Synthesis and Growth of Hexagonal Boron-Nitride in a Lithium Bromide Melt. *J. Am. Ceram. Soc.* **2007,** *90*, 1589-1591.

54. Huang, C.; Chen, C.; Ye, X.; Ye, W.; Hu, J.; Xu, C.; Qiu, X., Stable colloidal boron nitride nanosheet dispersion and its potential application in catalysis. *J. Mater. Chem. A* **2013,** *1*, 12192-12197.

55. Liu, D.; Lei, W.; Qin, S.; Chen, Y., Template-Free Synthesis of Functional 3D BN architecture for removal of dyes from water. *Sci. Rep.* **2014,** *4*.

56. Haruta, M.; Daté, M., Advances in the catalysis of Au nanoparticles. *App. Catal. A: Gen.* **2001,** *222*, 427-437.

57. Turner, M.; Golovko, V. B.; Vaughan, O. P. H.; Abdulkin, P.; Berenguer-Murcia, A.; Tikhov, M. S.; Johnson, B. F. G.; Lambert, R. M., Selective oxidation with dioxygen by gold nanoparticle catalysts derived from 55-atom clusters. *Nature* **2008,** *454*, 981-983.

58. Haruta, M., Size- and support-dependency in the catalysis of gold. *Catal. Today* **1997,** *36*, 153-166.

59. Yu, W.; Porosoff, M. D.; Chen, J. G., Review of Pt-Based Bimetallic Catalysis: From Model Surfaces to Supported Catalysts. *Chem. Rev.* **2012,** *112*, 5780-5817.

60. Vajda, S.; Pellin, M. J.; Greeley, J. P.; Marshall, C. L.; Curtiss, L. A.; Ballentine, G. A.; Elam, J. W.; Catillon-Mucherie, S.; Redfern, P. C.; Mehmood, F.; Zapol,

P., Subnanometre platinum clusters as highly active and selective catalysts for the oxidative dehydrogenation of propane. *Nat. Mater.* **2009,** *8,* 213-216.

61. Yu, C.; Ge, Q.; Xu, H.; Li, W., Propane dehydrogenation to propylene over Pt-based catalysts. *Catal. Lett.* **2006,** *112,* 197-201.
62. Biloen, P.; Dautzenberg, F. M.; Sachtler, W. M. H., Catalytic dehydrogenation of propane to propene over platinum and platinum-gold alloys. *J. Catal.* **1977,** *50,* 77-86.
63. Rioux, R. M.; Song, H.; Hoefelmeyer, J. D.; Yang, P.; Somorjai, G. A., High-Surface-Area Catalyst Design: Synthesis, Characterization, and Reaction Studies of Platinum Nanoparticles in Mesoporous SBA-15 Silica†. *J. Phy. Chem. B* **2005,** *109,* 2192-2202.

LIST OF PUBLICATIONS

From Thesis:

1. *"pH Sensitive Breathing of Clay Within the Polyelectrolyte Matrix"* **Piyush Chaturbedy**, Dinesh Jagadeesan, Muthusamy Eswaramoorthy*, *ACS Nano* **2010**, 4, 5921-5929.
2. *"Multifunctional carbon nanospheres with magnetic and luminescent probes: Probable brain theranostic agents"* **Piyush Chaturbedy**, Snehajyoti Chatterjee, Ruthrotha B Selvi, Akshay Bhat, M K Kavitha, Vivek Tiwari, Anant B Patel, Tapas K Kundu*, Tapas K Maji*, Muthusamy Eswaramoothy*, *J. Mater. Chem. B* **2013**, 1, 939-945 (Highlighted on the front cover of the journal issue).
3. *"Shape-Directed In Vivo Compartmentalized Delivery of Drug-Nanoparticle Conjugates in the Brain Cells"* **Piyush Chaturbedy,** Manoj Kumar, Krishnachary Salikolimi, Sadhan Das, Sarmistha Kundu, Snehajyoti chatterjee, B. S. Suma, Tapas K Kundu*, Muthusamy Eswaramoorthy*, *Manuscript Submitted* **2015**.
4. *"Oxidative Dehydrogenation of Propane over Boron Nitride and Boron Nitride Supported Metal Catalysts"* **Piyush Chaturbedy**, Muthusamy Eswaramoorthy*, *Manuscript under preparation* **2015**.

Miscellaneous:

1. *"Self-assembly of C_{60}, SWNTs and few-layer graphene and their binary composites at the organic-aqueous interface"* **Piyush Chaturbedy,** H S S Ramakrishna Matte, Rakesh Voggu, A Govindaraj, C N R Rao*, *Journal of colloid and interface science* **2011**, 360, 249-255.
2. *"Remarkable Uptake of CO_2 and CH_4 by Graphene-Like Borocarbonitrides, BxCyNz"* Nitesh Kumar, K S Subrahmanyam, **Piyush Chaturbedy,** Kalyan Raidongia,

Achutharao Govindaraj, Kailash P S S Hembram, Abhishek K Mishra, Umesh V Waghmare, C N R Rao*, *ChemSusChem* **2011**, 4, 1662-1670.

3. *"ATP driven Clathrin dependent entry of Carbon nanospheres prefer Cells with Glucose Receptors"* Ruthrotha B Selvi, Snehajyoti Chatterjee, Dinesh Jagadeesan, **Piyush Chaturbedy,** B S Suma, Muthusamy Eswaramoorthy* and Tapas K Kundu*, *Journal of Nanobiotechnology* **2012**, doi:10.1186/1477-3155-10-35.
4. *"Hydrodesulfurization of Thiophene over Few-Layer MoS_2 Covered with Cobalt and Nickel Nanoparticles"* Bolla Govind Rao, HSS Ramakrishna Matte, **Piyush Chaturbedy,** C N R Rao*, *Chempluschem* **2013**, 78, 419-422.
5. *"Clay-antigen composites for antigen cross-presentation"* **Piyush Chaturbedy**[!], Prabhu SA[!], Ranga U Kumar*, Muthusamy Eswaramoorthy*, *Manuscript under preparation* **2015**.
6. *"Efficient composite catalysts for CO oxidative over wide temperature range"* Sisir Maithy, **Piyush Chaturbedy**, Muthusamy Eswaramoorthy*, *Manuscript under preparation* **2015**.

[!] Equal Contributions